Accessing the kinetics of the supra-τ_C range via relaxation dispersion NMR spectroscopy

Dissertation

for the award of the degree

"Doctor of Philosophy"
Division of Mathematics and Natural Sciences

of the Georg-August-Universität Göttingen

within the doctoral program *Biomolecules: Structure, Function, and Dynamics*

of the Georg-August University School of Science (GAUSS)

submitted by

David Ban

from New York, United States of America

Göttingen 2013

Thesis Committee

Prof. Dr. Christian Griesinger,
NMR-based Structural Biology, Max Planck Institute for Biophysical Chemistry

Prof. Dr. Bert de Groot,
Computational Biomolecular Dynamics, Max Planck Institute for Biophysical Chemistry

Prof. Dr. Kai Tittmann,
Bioanalytik, Georg-August-Universität Göttingen

Members of the Examination Committee

Prof. Dr. Christian Griesinger,
NMR-based Structural Biology, Max Planck Institute for Biophysical Chemistry

Prof. Dr. Bert de Groot,
Computational Biomolecular Dynamics, Max Planck Institute for Biophysical Chemistry

Prof. Dr. Kai Tittmann,
Bioanalytik, Georg-August-Universität Göttingen

Other Members of the Examination Committee

Prof. Dr. Markus Zweckstetter
Protein Structure Determination by NMR, Max Planck Institute for Biophysical Chemistry

Prof. Dr. Helmut Grubmüller
Theoretical and Computational Biophysics, Max Planck Institute for Biophysical Chemistry

Dr. Lars T. Kuhn
NMR Spectroscopy, European Neuroscience Institute

Date of Examination: August 12th 2013

Affidavit

I hereby declare that this thesis has been written independently and with no other sources and aids other than quoted.

-It's 106 miles to Chicago. We've got a full tank of gas, half a pack of cigarettes, it's dark, and we're wearing sunglasses.

- Hit it.

"Jake and Elwood Blues"

Acknowledgements

I would initially like to give my sincere thanks to Prof. Dr. Christian Griesinger for not only allowing me to perform my doctoral work under his supervision, but for his constant guidance and input that helped drive the projects in an always forward direction while providing an outstanding educational environment.

I would like to thank the members of my Thesis Committee, Prof. Dr. Bert de Groot and Prof. Dr. Kai Tittmann for constructive critique of the projects as they progressed with time. Additionally, thank you to the other examination members for taking the time to evaluate my dissertation.

I also wish to express my thanks to Dr. Donghan Lee whose consistent mentorship constantly challenged my own limits, his critical evaluation that made us do "our best", and for sharing his knowledge with me through the years.

Dr. Stefan Becker and Karin Giller for the sample preparation as without it this work could not have been realized.

Dr. Alvar Gossert who told us about how his cryo-probehead survived and Drs. Helena Kovacs, Roberto Seydoux, Klemens Kessler, Rainer Kümmerle at Bruker BioSpin for giving insight into the details and possibilities of cryo-probehead technology.

Dr. Adam Mazur who never failed to answer any of my questions and for always willing to discuss anything at anytime.

Dr. Michael T. Sabo with whom I was fortunate to constantly collaborate with and have many far reaching discussions.

Dr. Colin Smith whose diligence and comprehensive views allowed for a fruitful collaboration.

Dr. Luigi Russo for the late night lab companionship and discussions.

Fellow members of The Cubic, including you Pablo, for creating one of the greatest work environments.

Antoine, Bibow and other friends from the "family" for giving a proper balance to Göttingen life.

Also thank you to all of the people I have been lucky to come in contact with throughout my doctoral work.

Very importantly, I am completely indebted and grateful to my parents and Vanessa for their unyielding support for my endeavors abroad. Thank you!

Table of Contents

Introduction

1.1 Protein Dynamics: Why do we care and why is it important?

Within a multicellular organism the cell is considered to be its basic building block [1]. But the cell itself is composed of a complex compartmentalized soup filled with proteins, small molecules, and cofactors that form organized interaction networks that allow the cell to carry out its function [2,3]. Macromolecular entities that exist within the cell serve to signal and respond to external or internal stimuli thereby changing its composition [1]. Even with this broad concoction these elements must interact and communicate in some fashion in order for the macroscopic cell to survive and carry out its function. Internally molecular communication is largely governed by recognition between these components [4,5]. Upon forming intermolecular contacts some proteins can change their shape allowing the exposure of new surfaces that can lead to new or abrogated function [6]. For homeostatic purposes this can be up or down regulated via controlling the cellular concentrations of these components. However, how do these systems actually communicate? How are structural changes from different interactions propagated towards a particular function or response? Coupled with increasing numbers of examples in which malformed proteins or discontinuous communication pathways can lead to nonfunctioning cells and can ultimately to disease [6,7] purports heightened importance in understanding the deficiencies in macromolecules like proteins.

In order to gain a detailed understanding of these molecular machines knowledge of their spatial coordinates is imperative. There are a variety of techniques that can give this information with atomic resolution. X-ray crystallography has provided immense visualizations of large macromolecules at atomic resolution. Yet, information pertaining to the time dependent

perturbation of their structural coordinates, or kinetics, is missed which can be a pivotal aspect in describing a protein's function. An exquisite example comes from studies involving antibodies which are capable of binding a diverse amount of antigens [8]. The authors found that even with distinct structural states that were identified by X-ray crystallography, the conformational diversity of antibodies could only be explained when kinetic data that was used to distinguish the isomerization of the free antibodies [8]. In some cases a given crystal can also contain several low energy states [8,9], or comparison of many X-ray structures of a given system can be used to ascertain its structural variance [10,11]. Time resolved X-ray has been used to observe rapid reorganizations (nanoseconds – 1 μs) like in the case for photoactivated ligand dissociation from heme groups [12,13], but X-ray which is a high energy based technique can cause sample heating or radiation damage [14,15]. But an emerging technique in which free electron lasers are used to generate an X-ray source are able to collect the diffraction data before any harm can come to the sample [16,17]. Still, some large amplitude motions may be quenched due to spatial restriction (or prevent crystallization) in the solid environment and crystal packing forces can perturb the native state of a protein [18]. Therefore, techniques in which the system can be studied in solution are desirable in order to study it in a more natural environment.

Fluorescence intensity decays from a given fluorophore have been used to report on rotational diffusion of molecules (pico- to nanosecond) [19,20], and stop-flow based techniques with rapid mixing of ligands can be used to attain binding kinetics information [21].. But these approaches rely on the number of observable probes that can give a signal, and is usually limited in number or requires mutation of residues to a tryptophan or via ligation of a fluorophore [21]. Additionally, analysis of information from a fluorophore involves careful model selection and frequently requires additional structural data in order to verify the choice of model [22]. Another

technique that can also provide atomic resolution is Nuclear Magnetic Resonance spectroscopy (NMR). Given that the sample is tractable for NMR studies, the system can be explored in the solution without having to make chemical modification while maintaining atomic resolution. NMR spectroscopy has even been applied to the study of systems in complete cellular environments [23-25]. Most importantly however is the fact that, NMR based observables are timescale sensitive, and a wide range of NMR experiments have been developed that report on a broad range of timescales from pico-seconds to real time (Figure 1) [26,27]. NMR might be a powerful tool to be used to detect not only structural, but kinetic effects for systems in which deficient communication could lead to disease [6].

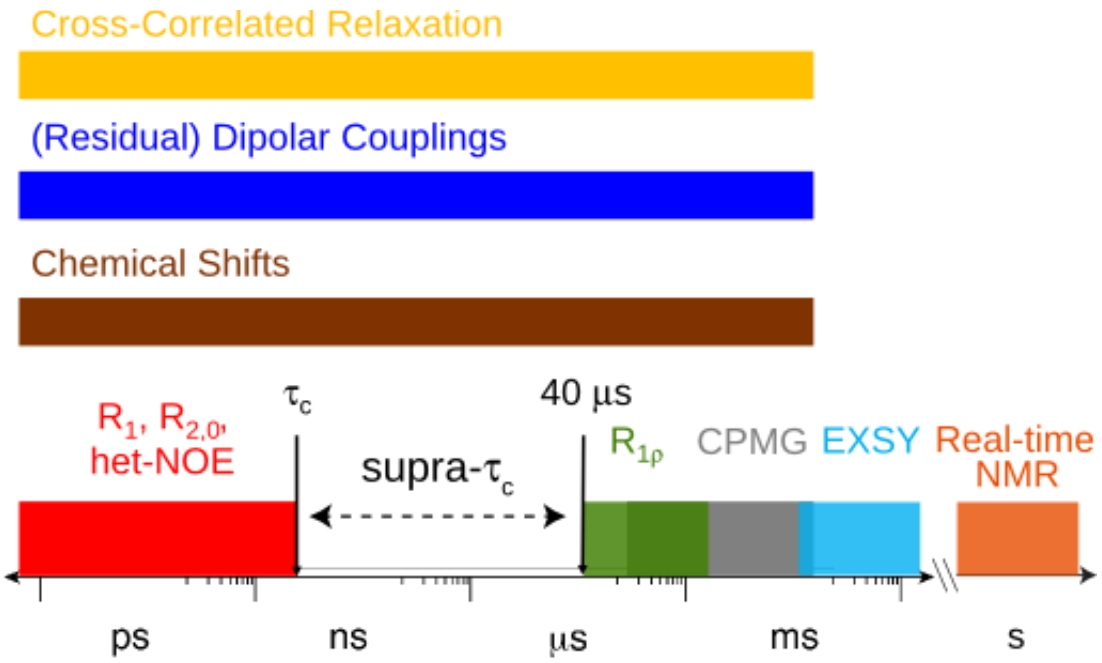

Figure 1 Examples of NMR experiments and the timescales of motion they are sensitive to.

Briefly, as a more extensive discussion follows, throughout the years of methodological development in NMR a variety of techniques exist that can probe motion across an entire spectrum of timescales that ranges from picoseconds to real time (Figure 1). A routinely applied

method is the analysis of relaxation data that uses conventional longitudinal relaxation (R_1), transverse relaxation (R_2) rates and heteronuclear NOE (het-NOE) [28]. These techniques are limited to the overall rotational tumbling time of a molecule which is demarcated as τ_C. Transverse-rotating frame spectroscopy ($R_{1\rho}$) [29] and Carr-Purcell-Meiboom-Gill sequences (CPMG) [30,31] have gained increased popularity and function by exploiting the phenomenon of chemical exchange (*vide infra*) [32,33]. Slower processes like aromatic ring flips [34] can be tracked using Exchange Spectroscopy (EXSY) [35] that are sensitive to milliseconds to seconds, and correlation spectra can be repeatedly recorded in real-time to identify slow processes from seconds and greater [36,37]. The use of chemical shifts as a metric for protein dynamics also provides a way to gain insight into sub-states sampled by proteins [38-41]. This dissertation is heavily rooted with the techniques that section under the name of relaxation dispersion (RD) which consist of $R_{1\rho}$ and CPMG experiments [32,33]. Although, other methods to perform RD have been reported [42-44]. The mechanism by which this technique functions is fundamentally different from experiments that focus on faster motions [32] (R_1, R_2, het-NOE). A brief presentation will be given on how these mechanisms are fundamentally different. Many great monographs [45-47] and reviews [27,32,33,48-50] have been written on this subject and the derivation below follows them.

1.2 Basic Theoretical Concepts

NMR active nuclei contain the intrinsic property of spin angular momentum. Nuclear spin angular momentum is vector whose magnitude is given by

$$\left|\vec{I}\right| = \frac{h}{2\pi}\sqrt{I\left(I+1\right)} \qquad \text{(Eq - 1.2.1)}$$

where *h* is Planck's constant and *I* is the spin angular momentum number. Since spin angular momentum is treated as a quantum mechanical parameter, the magnitude of $\vec{I}$ is constant and deemed to be quantized. Namely, its eigenvalues are discretized into only their z components

$$I_z = \frac{h}{2\pi} m \qquad \text{(Eq - 1.2.2)}$$

and can take on the azimuthal quantum numbers of *m* (*m* = -1/2, 0, +1/2) [51]. Please note that we restrict ourselves to the discussion of nuclei whose spin angular momentum quantum number equals 1/2 (i.e. ^{1}H, ^{13}C, and ^{15}N nuclei) [46]. Importantly, a nucleus that has non-zero spin angular momentum also possesses a magnetic moment ($\vec{\mu}$)

$$\vec{\mu} = \gamma \vec{I}$$
$$\mu_z = \gamma I_z = \gamma \frac{h}{2\pi} m \qquad \text{(Eq - 1.2.3)}$$

that is collinear to its spin angular momentum vector and where γ is the gyromagnetic ratio for the nucleus in question. Outside of any static magnetic field ($\vec{B}$) the magnetic moment will have a random orientation. The static magnetic field is a vector quantity that is aligned by definition along the z axis in Cartesian space. Upon introduction of nuclear spin to $\vec{B} = B_0 \vec{e_z}$ the magnetic moment will be reoriented by some amount θ and has an energy requirement of

$$E = \int \Gamma \, d\theta \qquad \text{(Eq - 1.2.4)}$$

The nuclear spins therefore effectively experience a torque (Γ) of that gives the required energy to be

$$E = \int \left(\vec{\mu} \times \vec{B} \right) d\theta = \int \left|\mu\right|\left|B\right| \sin\left(\theta\right) d\theta = -\left|\mu\right|\left|B\right| \cos\left(\theta\right) = -\vec{\mu} \cdot \vec{B} \qquad \text{(Eq - 1.2.5)}$$

Since a given nuclear spin can assume a spin up (m = +1/2) or spin down (m = -1/2) a magnetic moment can have two different energies ($E_{\pm} = \pm \frac{1}{2}\left(\frac{h}{2\pi}\right)\gamma B_0$; B_0 is the magnetic field strength in the z direction). And under equilibrium conditions, the energy difference of

$$\Delta E = +\frac{1}{2}\left(\frac{h}{2\pi}\right)\gamma B_0 - \left(-\frac{1}{2}\left(\frac{h}{2\pi}\right)\gamma B_0\right) = \left(\frac{h}{2\pi}\right)\gamma B_0 \quad \text{(Eq - 1.2.6)}$$

within a static magnetic field will cause an unequal population difference between spins states that is given by a Boltzmann distribution. Unfortunately, even at a B_0 of 14.1 T only 1 out of approximately every 10,000 proton spins will have a different orientation rendering the requirement for higher B_0 fields and samples that are of higher concentration (more magnetic moments). Additionally at this point we can see that we have only magnetization along the z-axis and the spins have no x and y component by computing the quantum mechanical expectation value for each Cartesian component of the magnetization (M_i; i = x, y, and z)

$$\langle M_i \rangle = tr\left(\mathbf{I_i}\boldsymbol{\sigma}\right) \qquad \text{(Eq - 1.2.7)}$$

in which the *tr* is the trace of the product between matrices $\boldsymbol{\sigma}$ and $\mathbf{I_i}$ (I = x, y, and z). $\boldsymbol{\sigma}$ which is the density matrix takes on the form $\mathbf{I_z}$ which is the Pauli spin matrix that describes the potentially assumed populations of a spin or the starting conditions, and $\mathbf{I_i}$ are operators (another spin matrix) projected out from $\mathbf{I_z}$ [52]. Applying the spin matrices for each $\mathbf{I_x}$ and $\mathbf{I_y}$ which are found in many texts [45,46,52] we find that the only nonzero magnetization is along the z-axis.

$$\langle M_x \rangle = \frac{\gamma h}{2\pi} tr\left(\mathbf{I_x I_z}\right) = \left(\frac{\gamma h}{8\pi}\right) tr\left(\begin{bmatrix} 0 & 1 \\ 1 & 0 \end{bmatrix}\begin{bmatrix} 1 & 0 \\ 0 & -1 \end{bmatrix}\right) = 0$$

$$\langle M_y \rangle = \frac{\gamma h}{2\pi} tr\left(\mathbf{I_y I_z}\right) = \left(\frac{\gamma h}{8\pi}\right) tr\left(\begin{bmatrix} 0 & -i \\ i & 0 \end{bmatrix}\begin{bmatrix} 1 & 0 \\ 0 & -1 \end{bmatrix}\right) = 0 \qquad \text{(Eq - 1.2.8)}$$

$$\langle M_z \rangle = \frac{\gamma h}{2\pi} tr\left(\mathbf{I_z I_z}\right) = \left(\frac{\gamma h}{8\pi}\right) tr\left(\begin{bmatrix} 1 & 0 \\ 0 & -1 \end{bmatrix}\begin{bmatrix} 1 & 0 \\ 0 & -1 \end{bmatrix}\right) = \frac{\gamma h}{4\pi}$$

The relative energy differences between populated spin states can also be used to calculate the precessional frequency or Larmor frequency around the z-axis and is given by

$$\frac{2\pi\,\Delta E}{h} = \omega = \gamma B_0 \qquad \text{(Eq - 1.2.9).}$$

If an orthogonal magnetic field is applied to the nuclei in the sample that are oriented along the static magnetic field whose energy matches ΔE then, similar to other types of spectroscopy, the resonance condition will be fulfilled and a transition or coherence is created (generation of off-diagonal terms in the density matrix formalism [45,46,52]). In NMR this is achieved by using linearly polarized radio-frequency waves as the electromagnetic radiation source ($\nu = \frac{\gamma B_0}{2\pi}$). Upon application of ν the bulk magnetization will transition to x-y plane and begin to precess around the z-axis.

This magnetization does not precess forever in the transverse plane, it will return to its equilibrium distribution with its original orientation along the static magnetic field. However, unlike other spectroscopic techniques, like optical based techniques which largely rely on stimulated and spontaneous emission mechanisms for the signal decay, spontaneous emission is not effective in causing NMR signal relaxation. This can be considered by comparing the probability per unit time for a transition between energy levels by spontaneous emission ($A \propto \nu^3$

). For example, the spontaneous emission with visible green light ($\lambda \sim 500$ nm; $\nu = 6 \cdot 10^{14}$ Hz) as compared to a ^{1}H Larmor frequency of $600 \cdot 10^{6}$ Hz would place spontaneous emission to be $\sim 10^{18}$ times more effective for the optical based technique! Ultimately NMR perturbations relax much slower and give us time to study them. What causes the decay of an NMR signal is instead due to random and thermal motions of or within a molecule that cause transitions and that push the nuclei back to equilibrium.

1.3 NMR relaxation

Time variant local oscillating magnetic fields that occur at particular frequencies can create transitions back to equilibrium that are effective at causing an NMR signal to decay. These random oscillating fields which are typically broken into longitudinal and transverse components depend on two facets, their amplitude and if they are resonant with any transitions or populations (i.e. frequency 0) [45,46]. Let us assume we have some time dependent interaction, $q(t)$ that is a stochastic process undergoing Brownian motion, whose mean value centers around zero (Figure 2) [53]. As *t* approaches large values $q(t)$ will average to zero ($\langle q(t) \rangle = 0$). However, the amplitude of this interaction is given by the variance of its time dependence ($q(t)^2$) and this does not average to zero ($\langle q(t)^2 \rangle \neq 0$).

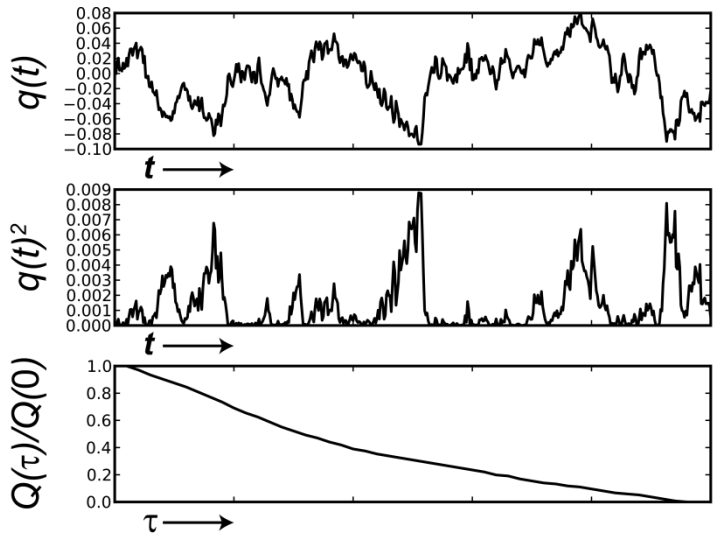

Figure 2 Interaction $q(t)$ is a stochastic process whose fluctuations center around zero. When the variance is considered $q(t)^2$ it no longer averages to zero. The auto-correlation function ($Q(\tau)$) reports on some process that decays with some characteristic time constant.

What was very astutely recognized early on in NMR relaxation theory [45,54] is that the pattern from the fluctuating $q(t)$ can be disseminated by evaluating the auto-correlation of a given interaction. The auto-correlation is given by

$$Q(\tau) = \langle q(t)q(t+\tau) \rangle \quad \text{(Eq - 1.3.1)}$$

where $\langle \ \rangle$ is the ensemble average over all entities experiencing interaction $q(t)$ and serves as the paramount equation to evaluate the effect of any source that can cause relaxation. The evaluation of $Q(\tau)$ is conducted with several assumptions. Since the process is stochastic, $q(t)$ can be determined at any time *t*, $t+\tau$ *(*τ*=t-t'; t'* is some time step*)*, and if *t=t'* then $Q(0)$ equals the variance of the interaction or the amplitude. But as τ increases what occurred the step before is forgotten since it is a stochastic process undergoing Brownian motion. The system begins to lose the memory of the prior step and should therefore follow $\lim_{\tau \to \infty} Q(\tau) = 0$ (Figure 2). Finally,

the auto-correlation of time dependent interaction $q(t)$ decays with some characteristic time constant which is related to the time required for a molecule to reorient and is referred to as the overall tumbling time, τ_C and is usually on the order of nanoseconds for most proteins. At $\tau = 0$, $q(t)$ assumes its maximum variance (amplitude of the process which is related to physical constants that depend on the interaction) and is formally expressed as

$$Q(\tau) = \left\langle q(0)^2 \right\rangle e^{-\frac{\tau}{\tau_C}} \qquad \text{(Eq - 1.3.2).}$$

This is the fundamental step for evaluating NMR relaxation phenomenon. Still, we want to know at what frequencies nuclei are driven back to equilibrium. This is accomplished by essentially performing a Fourier analysis on the auto-correlation function which will result in the power spectral density function and the characteristic frequencies at which transitions are made to restore the system to equilibrium [46,49]. Upon Fourier transform of the correlation functions, we attain a power spectral density function (J(ω)) which reports on the distribution of frequencies that can cause relaxation. From there, the frequency dependence of relaxation rates (R) can be calculated.

$$R = \left\langle q(0)^2 \right\rangle \int_0^\infty e^{-\frac{\tau}{\tau_C}} e^{-i\omega\tau} d\tau \qquad \text{(Eq - 1.3.3)}$$

The real part of the integral in equation 1.3.3 is proportional to $\left| q(0)^2 \right| \frac{\tau_C}{1 + (\omega\tau_C)^2}$ whereas the imaginary component of the integral yields terms that lead to the dynamic frequency shift [45,46]. In addition to the spectral density functions, which end up in the relaxation rates as a sum of Lorentzians, the spin part of the time dependent Hamiltonian needs to be evaluated by computing the double commutators between different spin-operators across all eigenfrequencies

which are subsequently summed to give the relaxation rate [45,46]. However, in some situations, upon evaluation of the double commutators some eigenfrequenices can be found to be not capable of causing transitions. The physical constants and operators as well as eigenfrequencies in a given external magnetic field that describe these interactions and their expressions are given in many texts [45,46,49,50] and are not reiterated here.

1.4 Sub-τ_C relaxation techniques

^{15}N nuclei are the most frequently probed nuclei with NMR based techniques [27] and we will limit our discussion to them. The major sources of relaxation stem from the through space interaction between two dipoles (dipole-dipole interactions (DD)) with respect to B_0 in which here the dipolar interaction is between the ^{15}N nucleus with its attached ^{1}H. And local magnetic fields that are created because of the unique orientation of a nucleus's electrons (chemical shift anisotropy (CSA)) with respect to B_0 [46]. We can also have perturbations of the isotropic chemical shift value because of changes in a nucleus's surrounding environment due to motion (conformational exchange or chemical exchange) [55], but we will see that the characteristic time and amplitude for this is different.

We can now begin to discern between different NMR experiments that measure the relaxation rates of a given nuclei. The relaxation that is intrinsic for ^{15}N nuclei is composed of the DD and CSA effects. As the dipolar and the induced chemical shift fields are reoriented by molecular tumbling in solution, time dependent local magnetic fields are generated. When the interactions are tabulated using the above protocol, we find that the decay of their auto-correlation functions is governed by the characteristic time constant commonly known as τ_C, or the overall rotational correlation time [46]. This is found to be on the order of nanoseconds for most proteins [46]. This source of relaxation is broken down into two components; the spin-

lattice interactions which are referred to as longitudinal relaxation (R_1) and spin-spin interactions commonly known as transverse relaxation (R_2). These rates differ in the frequencies at which they can cause transitions. R_2 is dominated with the spectral density term J(0) and is therefore directly dependent on τ_C. R_1 reports on high frequency motions and is made up of spectral density terms where frequencies $\omega_H \pm \omega_N$ and ω_N and as τ_C increases the longitudinal relaxation lifetime ($T_1 = 1/R_1$) can become quite long [56]. From Figure 1 the accessibility for R_1 and R_2 experiments is limited to motions up to τ_C (sub-τ_C) precisely because these measured relaxation rates report only on the frequency of motions that occur from DD and CSA effects which are modulated by molecular tumbling. Since relaxation rates can be determined site specifically a plethora of information can be attained by carrying out such experiments.

The ratio between R_2/R_1 is a facile method for determining τ_C [28]. Furthermore, measurement of these quantities can also be used to infer about the relative flexibility of an ^{15}N and $^{1}H^{N}$ attached pair. The Lipari-Szabo Model-Free formalism is one such way in which the DD component to the relaxation rate is considered and is effectively scaled by the flexibility of the ^{15}N-^{1}H internuclear vector by some constant S^2_{LS}, the Lipari-Szabo order parameter [19]. S^2_{LS} reports on the relative spatial flexibility of a given internuclear vector within the sub-τ_C window and can be used as a proxy for conformational entropy [57-59]. Additionally, this can also be expanded to include internal motions by assuming a product of two correlation functions (correlation function is biexponentional) that is typically known as the extended Model-Free analysis [60]. Het-NOE data reports on high frequency motions with transition frequencies at the sum and difference between the precessional frequency for ^{15}N and ^{1}H ($\omega_H - \omega_N$ and $\omega_H + \omega_N$) and can be useful in identifying nuclei in flexible regions of a protein [61]. Rotational anisotropy can also be ascertained with conventional relaxation measurements [62,63]. Transverse and

longitudinal cross relaxation has also been combined used to report on sub-τ_C motions [64,65]. Here, the mechanism of relaxation is a cross-correlation between DD and CSA interactions. R_2 is also the major contributor to the line width of a resonance in an NMR spectrum because the NMR signal is dampened by R_2 [46].

1.5 Relaxation by Conformational Exchange

Earlier, another relaxation mechanism, conformational exchange, was mentioned. It is ascribed to events in which the electronic environment of a nucleus is changed either by its motion, or from movement of its surroundings which then causes a modulation in the isotropic chemical shift (ω) of that nucleus [32,55]. This depends on the overall interconversion of this process (kinetics) and the structural differences between the populated states ($\Delta\omega$). Unlike sub-τ_C relaxation, the mechanism for conformational exchange is due to time dependent perturbations of the chemical shift, which is a rotation around the z-axis and is a perturbation that affects transverse relaxation [50]. However, the same steps in deriving this effect on relaxation are the same as above. Assume a situation in which a nucleus exchanges between two states given as

$$A \underset{k_B}{\overset{k_A}{\rightleftharpoons}} B$$

where the populations are $p_A = k_B/k_{ex}$ and $p_B = 1 - p_A$ ($k_{ex} = k_A + k_B$). NMR based kinetic perturbations are observed at equilibrium, therefore the time dependent change in the populations are zero and the kinetic matrix (**K**) takes the form of

$$\frac{d}{dt}\mathbf{P} = \mathbf{K}\mathbf{P} = \begin{bmatrix} -k_{ex}p_B & k_{ex}p_A \\ k_{ex}p_B & -k_{ex}p_A \end{bmatrix}\begin{bmatrix} p_A \\ p_B \end{bmatrix} = 0 \qquad \text{(Eq - 1.5.1).}$$

Ultimately, we want to derive an expression that correlates time dependent fluctuations (Eq. 1.3.1) in which a single ω value is observed and that has some characteristic decay time which is given by the interconversion rate between populated magnetization coherences. The correlation function (*C(t)*) in this case relies on knowing the a priori probabilities and conditional probabilities for a particular ω value when the state is assumed (two state interconversion from **K**) and can be given as

$$C(t) = \langle \omega(0)\,\omega(t) \rangle = \int dl \int dm \;\; p(l)\, p(m,t \mid l,0)\, \omega_l \omega_m \qquad \text{(Eq - 1.5.2)}$$

where the integration is performed over *l*, *m* which embodies the states A and B. Again, equation 1.5.2 depends on the conditional probabilities ($p(m,t \mid l,0)$) and a priori probabilities ($p(l)$). Following the illustrative derivation of Luginbühl et al. [50] we can evaluate the conditional probabilities using Green's function

$$p(m,t \mid l,0) = \sum_{n}^{2} \Lambda_{mn} \Lambda_{nl}^{-1} e^{\lambda_n t} \qquad \text{(Eq - 1.5.3)}$$

in which Λ contains columns of eigenvectors of **K**, the inverse of the eigenvectors is given by Λ^{-1}, and λ are the eigenvalues of the kinetic matrix. Due to detailed-balance criteria we always have one degenerate eigenvalue ($\lambda_1 = 0, \lambda_2 = -k_{ex}$) and the summation in 1.5.3 is run over *n* number of eigenvalues [45,46,52]. Equation 1.5.3 formally states that given that at time equal to zero starting at state *l* what is the probability that at a later time *t* we are at state *m*. The *m* rows of Λ and *l* columns of Λ^{-1} correspond to values of 1 and 2 in which they are equal to state A and B, respectively. Λ and Λ^{-1} take the form of

$$\Lambda = \begin{bmatrix} \frac{p_A}{p_B} & -1 \\ 1 & 1 \end{bmatrix}, \Lambda^{-1} = \begin{bmatrix} p_B & p_B \\ -p_B & p_A \end{bmatrix} \quad \text{(Eq - 1.5.4)}$$

from which the conditional probabilities (Eq. - 1.5.3) are equal to

$$\begin{aligned} p(A,t \mid A,0) &= p_A + p_B e^{-k_{ex}t} \\ p(A,t \mid B,0) &= p_A - p_A e^{-k_{ex}t} \\ p(B,t \mid A,0) &= p_B - p_B e^{-k_{ex}t} \\ p(B,t \mid B,0) &= p_B + p_A e^{-k_{ex}t} \end{aligned} \qquad \text{(Eq - 1.5.5)}$$

and the a priori probabilities ($p(l) = \lim_{t\to\infty} p(m,t \mid l,0)$) are found to be

$$\begin{aligned} p(A) &= \lim_{t\to\infty} p(A,t \mid A,0) = \lim_{t\to\infty} p(A,t \mid B,0) = p_A \\ p(B) &= \lim_{t\to\infty} p(B,t \mid A,0) = \lim_{t\to\infty} p(B,t \mid B,0) = p_B \end{aligned} \qquad \text{(Eq. - 1.5.6).}$$

The integration is merely a summation over the entire probability distribution and conditional probabilities multiplied by the modulation of chemical shifts between state A (ω_A) and state B (ω_B) therefore substituting back into equation 1.5.2:

$$C(t) = \langle \omega(0)\omega(t) \rangle = \sum_{l,m=1}^{2} p(l) \left(\sum_{n}^{2} \Lambda_{mn} \Lambda_{nl}^{-1} e^{\lambda_n t} \right) \omega_l \, \omega_m \qquad \text{(Eq - 1.5.7).}$$

Performing the required summations and simplifying we find

$$C(t) = \left(p_A \omega_A + p_B \omega_B \right)^2 + p_A p_B \Delta\omega^2 e^{-k_{ex}t} \qquad \text{(Eq - 1.5.8)}$$

where $\Delta\omega$ equals $\omega_A - \omega_B$. We can already disregard the first term from equation 1.5.8 which is time invariant and ineffective in causing relaxation. We are interested in determining at what

frequencies the relaxation is efficient therefore we need to calculate the spectral density ($J(\varpi)$) form of equation 1.5.8. After Fourier transform we retain the following

$$J(\varpi) = R_{ex} = p_A p_B \Delta\omega^2 \frac{k_{ex}}{k_{ex}^2 + \varpi^2} \qquad \text{(Eq - 1.5.9).}$$

This is the power spectral density function for nuclei experiencing conformational exchange in the fast regime. The amplitude of this process, unlike sub-τ_C motion, is governed by distinctly populated magnetization coherences that have a phase separation of $\Delta\omega$. The ϖ at which $J(\varpi)$ is evaluated depends on the interaction frame that is considered [49,66]. This is configured based on the experiment that is used. For example in $R_{1\rho}$ experiments the populated magnetization coherences are rotated into a doubly-tilted frame in which magnetization can be locked by a radio frequency pulse from the transverse plane [49,66]. Then ϖ becomes dependent on the radio frequency field that locks the coherence of interest and the precessional frequency ω of the queried nucleus. Overall, conformational exchange gives an apparent dephasing of the intended coherence in question where a contribution of exchange acts as an addendum to the intrinsic R_2 ($R_{2,0}$; reports on τ_C and not τ_{ex}) creating an effective transverse relaxation rate ($R_{2,eff} = R_{2,0} + R_{ex}$). During a period of free precession ($\varpi = 0$) R_{ex} still has a contribution of $R_{ex} = p_A p_B \Delta\omega^2 / k_{ex}$ and therefore the residual line width of a peak will be impacted by this amount [32]. It is interesting to note that the time invariant term in equation 1.5.6 retains the square of the average observed chemical shift. This is what we expect in the fast exchange regime in which the observed resonance is a population weight of both states. The characteristic time or exchange lifetime is given by τ_{ex} ($\tau_{ex} = 1/k_{ex}$) and the prefactor of the Lorentzian, $\Phi_{ex} = p_A p_B \Delta\omega^2$, can both be measured using RD experiments [32,66].

RD experiments have attained their widespread use for the ability to extract kinetic and structural information about lowly populated intermediates (> 0.5 %) [67-70]. They have been successfully used to probe many biologically relevant processes such as protein folding events [68,71-73], binding interactions [69,74,75] and enzymatic turnover events [67,76,77]. In addition, the development of RD experiments has been quite extensive to the point that most backbone and side chain atoms of a protein can be probed [78-88]. RD functions by monitoring the dependence of $R_{2,eff}$ by manipulating its observable exchange contribution. The dispersion is created by using radio-frequency pulses and/or frequency offsets that are varied in order to observe a change in $R_{2,eff}$ (Figure 3) [32]. If an exchange event is occurring $R_{2,eff}$ decreases to the $R_{2,0}$ or to the point where the contribution of exchange has been removed. Since additionally populated magnetization coherences cause a dephasing in the transverse plane this can be limited by rapid refocusing of the magnetization.

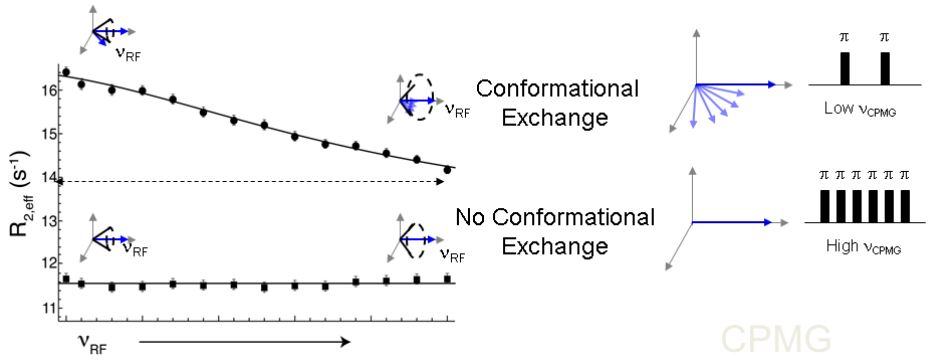

Figure 3 Illustration depicting the effect of conformational exchange (R_{ex}) on the effective transverse relaxation rate ($R_{2,eff} = R_{2,0} + R_{ex}$). Spin-lock ($\nu_{RF}$) based $R_{1\rho}$ is depicted on the left while an illustration for CPMG experiments is shown on the right where π is a 180° pulse and its inter-pulse delay is varied (ν_{CPMG}).The dashed line indicates the base-line of exchange which is $R_{2,0}$. The expected dependence for a nuclei that displays no exchange event should be flat as $R_{2,eff}$ should not change as a function of ν_{RF} or ν_{CPMG}. The plot of $R_{2,eff}$ versus ν_{RF} is from experimental values for two residues in ubiquitin at 277 K (Chapter 3). The solid black line for the top curve is a fit from Eq. 1.5.9 that included $R_{2,0}$ and the solid black line below is a fit that only considered $R_{2,0}$ as a parameter.

The two types of experiments that are most commonly used are $R_{1\rho}$ [29] and CPMG [30,31] (Figure 1). $R_{1\rho}$ RD is based on using RF pulses that lock the magnetization given that the nutation frequency of the dephasing coherences can be covered [33]. CPMG experiments functions by varying the inter-pulse delay between 180° pulses [79]. The dependence of exchange with respect to the two techniques is comparable [89], but the detailed dependence is different and will be demonstrated throughout this monograph. Although in some limiting cases like when spin-lock pulses are large in magnitude or inter-pulse delays are very short, they can be identical [90]. A major difference is that $R_{1\rho}$, if not performed on-resonance, contains a dependence on the tilt angle ($\theta = \tan^{-1}(\nu_{RF}/\Omega)$). The tilt angle is given by the offset frequency ($\Omega = \nu_0-\nu_{SL}$) of the probed nucleus and the amplitude of the spin-lock pulse (ν_{RF}) that is employed (Figure 3). If the tilt angle is not 90° then there will also be a contribution of R_1 relaxation. The fastest processes that can be probed directly relate to the amplitude of the spin-lock pulse or frequency of applied 180° pulses (ν_{CPMG}) for $R_{1\rho}$ and CPMG experiments, respectively [91]. This concept will be addressed and highlighted throughout this dissertation, and as this dissertation involved the use of a variety of NMR based relaxation methods each chapter contains its own unique materials and methods section in order to provide the reader a clear way to discern the different experimental approaches that have been taken.

Kinetics of Conformational Sampling in Ubiquitin

2.1 Motion from the supra-τ_C range dictates conformational sampling as a mechanism for ubiquitin interactions

So far we have only addressed motion within the sub-τ_C and up to the RD limit of 40 μs. There is still a blind spot that spans four orders of magnitude between τ_C and this 40 μs limit, deemed the supra-τ_C range. Therefore a large question that remains is to what/if any is the amplitude and kinetics of motion within this time window? Throughout the past decades RD based studies have been able to illuminate functional millisecond to second motions for binding events[69,89], turn-over rates in catalytic cycles [67,77], and the existence of folding intermediates[68]. This has been possible because the ones listed above are amenable to study as they rest within a timescale that can be accessed by the aforementioned RD type experiments. Up to now, the motional amplitudes within the supra-τ_C range have been identified for systems such as TAR-RNA [92,93], GB3 [94,95], and ubiquitin [11,96-98]. In the case of TAR-RNA and ubiquitin structural data and motional amplitudes from the supra-τ_C range has been linked to molecular recognition.

Structural variances from the supra-τ_c range have been made possible via the acquisition of residual dipolar couplings (RDCs) [99]. In solution, the dipolar coupling averages to zero since due to rotational diffusion all orientations can be assumed, but by introducing anisotropic conditions some preferred vector orientations can be achieved by steric and electrostatic

interactions driven by the alignment media. This in turn forces a sampling of some preferred orientations for a given internuclear vector (i.e. ^{15}N-$^{1}H^{N}$). The "restoration" of a dipolar coupling manifests itself as an apparent coupling value that can be disentangled from measurements of scalar couplings [100]. A tremendous outcome was realized in that RDCs also report on the motion of a given internuclear vector from milliseconds and faster [101]. Given that the five dimensional space that describes an internuclear vector's orientation is sufficiently sampled using distinct alignment conditions, motional amplitudes of a given bond vector's fluctuations, reported in the form of order parameters (S^2_{RDC}), from the supra-τ_c range can be isolated once motions from the sub-τ_c are accounted for [96,102].

For ubiquitin free in solution, an extensive set of alignment conditions have been measured for the amide backbone and methyl side chain positions [96,98,102]. An ensemble refinement protocol that enforces the RDC information retained an ensemble of structures that reports on the structural variance of motions that includes the conformational amplitudes from the supra-τ_c range [11]. From which, the heterogeneity of the free ubiquitin structures overlapped with the structures of ubiquitin bound to its variety of interacting partners. More importantly, the mimicry of free ubiquitin structures to that of ubiquitin structures in complex only originates when information from the supra-τ_c range is included [11]. This purports the concept that free ubiquitin samples different conformations, compliant with a conformational selection type binding mechanism, through motion within the supra-τ_c range. It has been hypothesized that the sampling or interconversion between different structural conformers may be a limiting factor for protein-protein recognition [103-105]. Therefore a question that requires answering is to address the situation that if ubiquitin samples all of these different conformations then what is the actual rate of interconversion between conformers.

Since for other systems, such as enzymes, have catalytic turn-over events that are 100-1000 times slower, RD type experiments has become an established method for their kinetic characterization [106]. However, due to technical limitations, which have since been lifted (*vide infra*) RD type experiments were limited to kinetic processes with a lifetime of about 40 μs [91,107], and therefore were inaccessible to the four orders of magnitude window that is the supra-τ_c range. In principle RD experiments could be used to detect motions from this timescale. However, at room temperature conventional RD experiments have not been able to identify any exchange driven fluctuations in ubiquitin (Appendix Figure 1) [108,109]. We therefore postulated that if this motion was occurring with a lifetime less than the RD limit of 40 μs at higher temperatures then by lowering the temperature this supra-τ_c motion could be pushed into the detectable range for RD experiments.

2.2 Super-cooled RD detects conformer interconversion

Off-resonance transverse rotating frame ($R_{1\rho}$) experiments were conducted initially at 265 K for ^{15}N backbone nuclei in super-cooled conditions. This type of RD experiment was chosen because maximum effective fields attainable are larger than the maximum refocusing fields as compared to alternative RD type experiments. The employed sequence was a ^{15}N $R_{1\rho}$ experiment with a TROSY readout [110] in order to account for the increased tumbling time of ubiquitin at lower temperatures and to reduce the effective heating via the prevention of having to apply decoupling sequence during acquisition. The full pulse code and acquisition parameters can be found in the section titled Pulse Programs. At 265 K significant exchange was detected for four residues: Ile13, Ile23, Asn25, and Val70 (Figure 4).

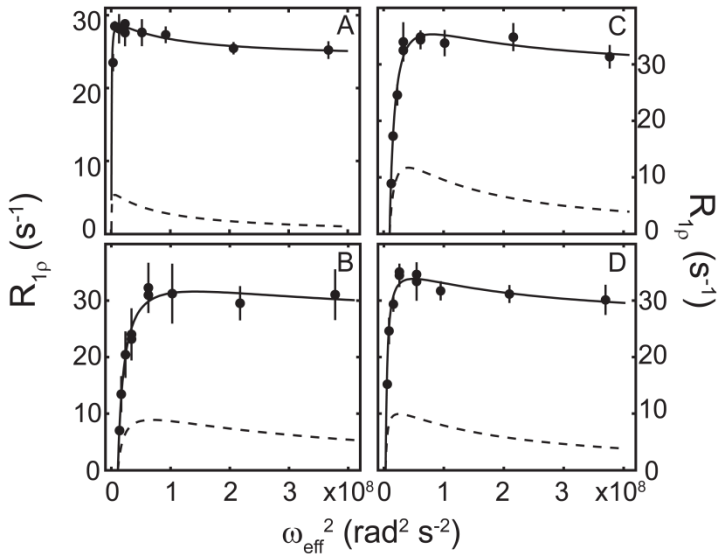

Figure 4 Off-resonance $R_{1\rho}$ dispersion curves for Ile13 (A), Ile23 (B), Asn25 (C), and Val70 (D) at 265 K plotted with respect to the effective spin-lock field strength (ω_{eff}^2). The solid and dashed curve in each plot represent the fitting the measured data, and the contribution from exchange, respectively to a model that assumes fast exchange.

Of which, Ile13 had not been detected before while Val70 although not explained has been previously observed at 260 and 280 K [108,109]. Previous observation of dispersion for Ile23 and Asn25 at 280 K was accounted for due to a hydrogen-bond reordering process involving Arg54 and Thr55 (see previous interpretations of kinetic measurements on ubiquitin) [108]. Exchange lifetimes (τ_{ex}) for Ile13 and Val70 at this temperature were 122 $\pm$ 40 μs and 90 $\pm$ 30 μs, respectively. Following which a temperature dependence from 265 K to 277 K (Figure 5) was conducted, (Appendix Table 1) in which τ_{ex} shortened to 61 $\pm$ 20 μs and 67 $\pm$ 10 μs for Ile13 and Val70, respectively at 277 K. For Figure 5, the same experimental approach was taken as in Figure 4. In Figure 5 however, the experimental curves are reformulated by only showing their contribution of R_{ex} with respect to their dependence on the employed effective field (ω_{eff} = $((2\pi\Omega)^2 + (2\pi\nu_1)^2)^{1/2}$; Ω is the frequency offset for a given nucleus and the applied spin-lock field and ν_1 is the amplitude of the spin-lock field strength). The utilized value of ω_{eff} creates a tilt-

angle of θ (sin(θ)=(2πν$_1$)/ω$_{eff}$). In Figure 5, the intrinsic relaxation rates, determined via fitting (Appendix Table 1), were subtracted from $R_{1\rho}$ to produce only $R_{ex}\sin^2(\theta)$ after full fitting of the dispersion curves (see Materials and Methods). Therefore, as ω_{eff} increases sin(θ) approaches one and $R_{1\rho}$ mostly reports on the transverse relaxation component ($R_{2,eff} = R_{2,0} + R_{ex}$). Indeed, at lower temperatures there is still a significant contribution of R_{ex} to $R_{1\rho}$.

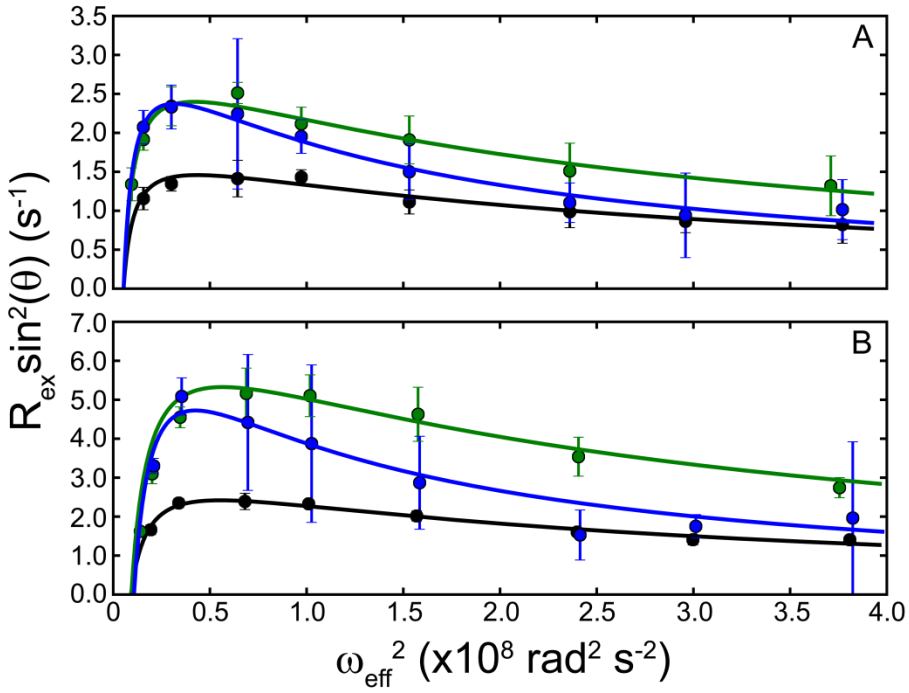

Figure 5 The exchange contribution (R_{ex}) from temperature dependent super-cooled $R_{1\rho}$ experiments for Ile13 (A) and Val70 (B). Dispersion curves for three temperatures measured at 269, 273, and 277 K are depicted as the blue, green, and black curves, respectively. Errors were propagated from the fitted parameters and $R_{1\rho}$ values.

Following τ_{ex} across this temperature range allows for an Arrhenius extrapolation that renders the exchange lifetime to be 10 ± 9 μs (Figure 6) at physiological conditions (309 K). The large error in τ_{ex} at 309 K is due to the extrapolation from the narrow range of temperatures that could be used for the super-cooled RD experiments. In addition, similar activation energies of 37

$\pm$ 7 kJ mol^{-1} and 32 $\pm$ 8 kJ mol^{-1} for Ile13 and Val70, respectively, were extracted from the Arrhenius fitting.

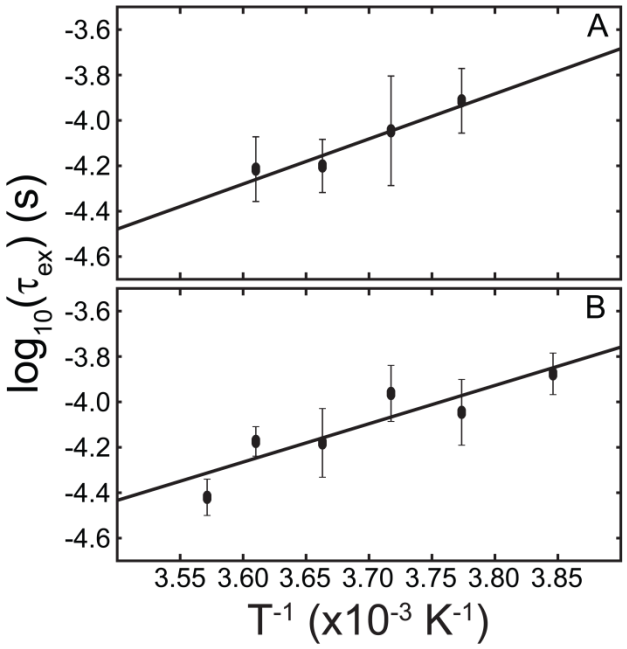

Figure 6 Temperature dependence of τ_{ex} for Ile13 (A) and Val70 (B) plotted with parameters from the fit to an Arrhenius equation as the black line. At physiological temperatures τ_{ex} = 10 ± 9 μs.

From, the significant amplitudes and complementary activation energies for Ile13 and Val70 we attribute their lifetime to the rate of interconversion between different ubiquitin conformers. As a form of corroboration we turn to the RDC-derived ensembles. Since, relaxation dispersion experiments rely on two parameters, τ_{ex} and the conformational amplitude of the motion (Φ_{ex}), RDC-derived ensembles [11,111,112], which encode the structural variances from motions originating from the same timescale detected by the super-cooled RD experiments, could maybe then also be used to calculate ensemble based conformational amplitudes ($\Phi_{ensemble}$) as a means of corroboration when compared to the super-cooled RD measurements.

2.3 Structural variances from RDC-derived ensembles

The RDC-derived ensembles represent ground state ensembles of ubiquitin and were constructed under the assumption that every conformer is equally probable to exist in solution [11]. They also contain the spread of conformations sampled by free ubiquitin. Therefore, under this presumption, the $\Phi_{ensemble}$ calculations also contend that if the conformers interconvert between each other this rate should also be equal (see $\Phi_{ensemble}$ calculation). Therefore, the application of an N-site jump model yields an upper-limit for any expected chemical shift variance. Alternatively, if an assumption was made regarding to a deviation in the kinetics such as a blocking of certain pathways which does not adhere under the pretenses of the RDC-derived ensembles, the expected variances would only decrease. $\Phi_{ensemble}$ was calculated on three ensembles of free ubiquitin using three different chemical shift prediction programs, SHIFTX [113], SHIFTS [114], and SPARTA [115]. Only residues that were one standard deviation greater than the average were considered to be significant. In all nine instances only Ile13 and Val70 fulfilled the above criterion. Even at two standard deviations from the mean, Ile13 and Val70 still demonstrated the largest $\Phi_{ensemble}$ values except in only one situation (Figure 7B) where the EROS ensemble was calculated with the SHIFTS program.

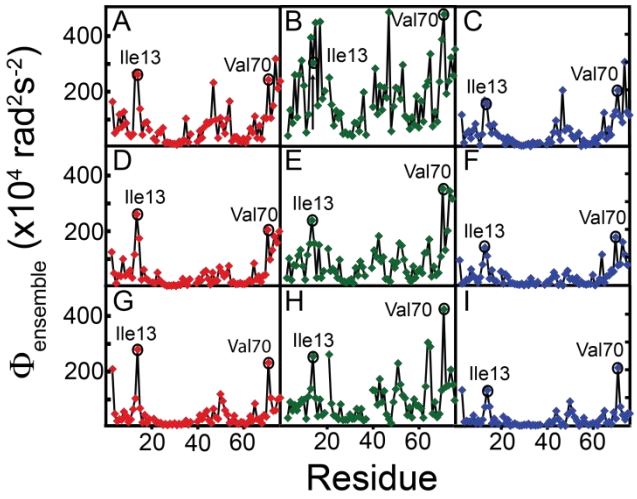

Figure 7 Chemical shift variances ($\Phi_{ensemble}$) predicted from the RDC-derived ensembles. The EROS (A-C) [11], EROSII (D-F) [112], and ERNST (G-I) [111] were used for the calculations. All members within an ensemble were used for the calculations with chemical shift programs, SHIFTX (A, D, and G), SHIFTS (B, E, and H) and SPARTA (C, F, and I) in red, green and blue, respectively.

Random selection of 50% of the members from each ensemble did not change that Ile13 and Val70 continued to show the most significant $\Phi_{ensemble}$ values. Despite the fact that Ile13 and Val70 show the largest $\Phi_{ensemble}$, there are eight backbone amides that report increased mobility on the supra-τ_c timescale (Appendix Figure 2). These eight amides have S^2_{LS}/S^2_{RDC} greater than Val70 where S^2_{LS} is the Lipari-Szabo order parameter (motion up to τ_c) [116]. Therefore, it can be expected that other residues might show dispersion, but their motion is either faster or the amplitudes of their motion smaller. Still only Ile13 and Val70 at this time using the current experimental procedure showed sufficient chemical shift variations such that RD was observed.

A connection can now be made with the microsecond motions detected from the super-cooled RD experiments between 265 and 277 K and the ensembles that reflect the structural variances from motion within the supra-τ_c range both identify Ile13 and Val70 as showing the largest conformational amplitudes that originate from conformer interconversion. Thus, the RDC-

derived ensembles correctly predict the NMR RD results in super-cooled solution. Additionally, this indicates that there is predictive power in RDC-derived ensembles as a tool for estimating residues that may display motion detectable by RD experiments given that their chemical shift variations are sufficiently large.

2.4 Discussion and Conclusion

Super-cooled RD could be used to obtain site specific kinetics for two residues whose experimentally determined lifetimes can be attributed to the time constant for conformer interconversion (Figure 4 and 5). The temperature dependence of their exchange lifetimes places the conformer interconversion to be fast at 309 K with a lifetime of 10 ± 9 μs (Figure 6). This experimental observation also agrees with a long MD trajectory of BPTI where backbone fluctuations also coincided with the microsecond timescale [117]. Additionally, through the use of ensembles that capture the motional variances from this timescale calculated motional amplitudes were the largest for the same two residues across all RDC-derived ensembles (Figure 7). An independent experimental approach was also utilized to verify the kinetics that had been detected.

The site specifically resolved kinetics for ubiquitin were also tested using an independent method that does require extrapolation of the extracted lifetimes and can be probed directly at 309 K. The employed technique was dielectric relaxation (DR) spectroscopy. DR is sensitive to motions that originate from changes of the electric dipole moment of solutes, solvent, and ions in solution [118]. Generally in DR, motions are broken down into different regimes α, β and γ which correspond to motions from conductivity of small ions in solution, dipole relaxation processes, and bond librations as well as the rearrangement of water dipoles, respectively. DR was measured on free ubiquitin in solution and at 309 K the β peak correctly corresponded to the

τ_c for ubiquitin. Once the effect of relaxation due to ionic charge transport is removed from the measured permittivity, the dielectric loss spectrum presented a new peak [112]. Deemed the sub-β, its resonant frequency was less than β peak. The mean value for this peak centers around 1 μs at 309 K providing independent validation for the super-cooled RD based Arrhenius extrapolation [112]. This peak was also reproduced at different temperatures and with different choices of ions in solution [112].

Kinetics from the supra-τ_c range, which spans four orders of magnitude, has remained elusive until now. We could narrow down this range and identify that for ubiquitin the lifetime for interconversion is around 10 μs at physiological temperatures. Via super-cooled RD we could obtain site specific kinetics whose amplitudes were also verified by ensembles that report on the motional variance of ubiquitin within the same timescale. In addition, NMR relaxation dispersion before has not been used to provide kinetic characterization of ground-state fluctuations from a protein. This motion was also identified by an independent experimental technique, namely solution DR. These studies also allow for this motion to be studied under solution conditions without having to make chemical modifications to the system itself. The combination of super-cooled RD, RDC-derived ensembles, and solution DR spectroscopy will open the doors for future investigations that should be applicable to a wide range of systems in order to elucidate motions from the supra-τ_c range.

2.5 Materials and Methods

Super-cooled off-resonance $R_{1\rho}$ NMR samples for measurements below the freezing point of water were conducted by filling 1 mm capillaries in which twelve could then be placed into one 5 mm NMR sample tube. ^{15}N labeled ubiquitin at a concentration of 6 mM was in a buffer composed of 100 mM NaCl, 50 mM sodium phosphate at pH 6.5. Dynamic light scattering was used to confirm that ubiquitin still existed as a single monomeric species at the employed concentrations. Off-resonance $R_{1\rho}$ experiments were conducted at 265, 269, 273, and 277 K with a TROSY based sequence similar to Kempf et al [110,119]. A TROSY [120] block was used not only to prevent sample heating during decoupling applied in the direct dimension, but also to account for the decrease in sensitivity due to the slower tumbling of ubiquitin at lower temperatures. Water handling was also optimized for the employed gradient based Echo-Antiecho readout used for frequency discrimination. Each spectrum was recorded with 512 and 128 complex points in the direct (t_2) and indirect (t_1) dimensions, respectively, with 24 transients per t_1 increment. The $t_{1,max}$ and $t_{2,max}$ were 81.4 and 65.5 ms, respectively. At each temperature eight spin-lock field strengths (ν_1) were used and varied between 265 to 3050 Hz. The spin-lock carrier frequency was set outside of the spectral range to 134 ppm. For each ν_1, a relaxation series was conducted by changing the length of the applied spin-lock between 20 to 240 ms. All spectra were acquired on a Bruker Avance III spectrometer operating at a ^1H Larmor frequency of 600 MHz. All data were processed with the NMRPipe sotware package [121] and visualized with the CARA program [122].

$R_{1\rho}$ rates were determined by fitting each relaxation series to the function $I_0=\exp(-R_{1\rho}T)$. Assessment of conformational exchange with respect to the effective fields (ω_{eff}) that were used were ascertained by fits to a fast exchange model of

$R_{1\rho} = R_1 \cos^2(\theta) + \left(R_{2,0} + \frac{\Phi_{ex}\tau_{ex}}{1+(\omega_{eff}\tau_{ex})^2} \right) \sin^2(\theta)$ in which R_1, $R_{2,0}$, Φ_{ex}, and τ_{ex} are the longitudinal relaxation rate, intrinsic inphase transverse relaxation rate, the conformational amplitude, and the exchange time constant, respectively. All data fitting routines were carried out using Mathematica (Wolfram Research). Errors in the fitted parameters were determined by Monte-Carlo simulations run with 500 iterations that used the base-plane noise as the standard deviation for a given intensity value. All parameters that describe exchange can be found in Appendix Table 1. Temperature dependent time constants were fit to an Arrhenius type exchange of the form $\log_{10}(\tau_{ex}) = \frac{E_a}{RT \ln 10} - \log_{10}\left(\frac{1}{A}\right)$ where A and E_a, are the attempt frequency and activation energy, respectively. Errors in A and E_a were determined from error propagation.

$\Phi_{ensemble}$ calculation The RDC-derived ensembles are non-canonical and therefore each conformer has an equal probability of existing and that all conformers interconvert with the same rate (k). The time dependent change in the populations is given by

$$\frac{dp_i(t)}{dt} = -\sum_{j=1}^{N} k_{ij} p_j(t) \qquad \text{(Eq - 2.5.1)}$$

The equation above is a first-order rate equation, but in NMR observables are made at equilibrium therefore $KP = 0$. Where the kinetic matrix (K) follows the formalism for an N-site jump model [123] and takes the form:

$$K = \begin{bmatrix} -r & \cdots & k \\ \vdots & \ddots & \vdots \\ k & \cdots & -r \end{bmatrix} \qquad \text{(Eq - 2.5.2)}$$

where $r = (N-1)k$ and the P matrix is a column vector with the form of $P^T = [p_1, p_2, \ldots p_N]$. The conditional probabilities are given by

$$p(j,t \mid i,0) = \frac{1}{N} + \left(\delta_{ij} - \frac{1}{N}\right) e^{-Nkt} \qquad \text{(Eq - 2.5.3)}$$

δ_{ij} is the Kronecker delta. For the N-site jump model the probability at t=0 is $p_i = 1/N$. The correlation function takes the form

$$C(t) = \left\langle \omega(0)\omega(t) \right\rangle = \sum_{i,j=1}^{N} p_i p(j,t \mid i,0) \omega_i \omega_j \quad \text{(Eq - 2.5.4)}$$

where ω is the precession frequency for a nucleus in a given state. After substitution of equation 2.5.3, into equation 2.5.4 yields

$$C(t) = \sum_{i,j=1}^{N} \frac{1}{N}\left(\frac{1}{N} + \left(\delta_{ij} - \frac{1}{N}\right) e^{-Nkt}\right) \omega_i \omega_j \qquad \text{(Eq - 2.5.5).}$$

Separation of the time-invariant, which do not cause relaxation, and time variant terms gives

$$C(t) = \frac{1}{N^2} \sum_{i,j=1}^{N} \omega_i \omega_j + \frac{e^{-Nkt}}{N^2} \sum_{i,j=1}^{N} \left(N\delta_{ij} - 1\right) \omega_i \omega_j \qquad \text{(Eq - 2.5.6)}$$

The first term in equation 2.5.6 is time independent and ineffective in causing relaxation. Focusing on the time-variant component we can expand the summation into two components in which

$$C(t) = \frac{e^{-Nkt}}{N^2}\left(\sum_{i=1}^{N} (N-1)\omega_i^2 + \sum_{i,j=1}^{N} (-1)\omega_i \omega_j\right) \quad \text{(Eq - 2.5.7).}$$

Equation 2.5.7 is a series that is the expanded form for the square difference between states *i* and *j* and simplifies to

$$C(t) = \frac{e^{-Nkt}}{2N^2} \sum_{i,j=1}^{N} \left(\omega_i - \omega_j\right)^2 \qquad \text{(Eq - 2.5.8)}$$

Equation 2.5.8 is reduced by a factor of two because the summation is performed for jumps between states *i* to *j* and *j* to *i*, but whose squared difference is equal in magnitude. The NMR observable form of equation 2.5.8 comes after Fourier transform which in the case of exchange in the fast limit becomes

$$R_{ex} = \frac{1}{2N^2} \sum_{i,j=1}^{N} \left(\omega_i - \omega_j\right)^2 \frac{\tau}{1 + \left(\tau\omega_{eff}\right)^2} \quad \text{(Eq - 2.5.9)}$$

where $\tau = (Nkt)^{-1}$, ω_{eff} is the experimentally employed frequency offset and spin-lock field. The term preceding the Lorentzian is the amplitude of the motion or structural variances reported by the ensembles

$$\Phi_{ensemble} = \frac{1}{2N^2} \sum_{i,j=1}^{N} \left(\omega_i - \omega_j\right)^2 \text{ (Eq - 2.5.10).}$$

Exceeding the kinetic limit for dynamic studies of biomolecules

3.1 Additional ^{15}N nuclei that have motion in the supra-τ_c range

Until now, the kinetics for conformational sampling within ubiquitin could be determined from super-cooled RD for two residues [112]. However, the motion which is fast, between 1 and 19 μs at 309 K, was not accessible to conventional $R_{1\rho}$ experiments because they are limited to a direction observation of motion around 40 μs [91,124]. This exchange event was also reported by an independent experimental technique that did not require any extrapolation, and the RDC-derived ensembles also identified their motional variance. Interestingly there are other residues that also display increased motion from the supra-τ_c range (Appendix Figure 2 and 6) other than Ile13 and Val70. Residues whose ratio between the Lipari-Szabo and RDC order parameter is greater than one, serves as an indicator for the amount of motion originating from timescales slower than the overall tumbling time (Appendix Figure 5). With the employed conventional experimental setups, those residues may have remained dispersion silent because they experience smaller amplitudes of motion, or their motion is faster than the 40 μs which is beyond the current detectable limit for $R_{1\rho}$ experiments. We therefore sought to extend the accessible kinetic range of these experiments.

As described in the introduction sections (Chapter 1), RD experiments monitor an effective transverse relaxation rate ($R_{2,eff}$). Namely, the intrinsic relaxation rate ($R_{2,0}$) is overlapped with a source of relaxation when a nuclei exchanges between distinct chemical sites ($R_{2eff} = R_{2,0} + R_{ex}$) [32]. The observation of this exchange event is predicated not only by the

amplitude, but at which lifetime a given magnetization coherence exchanges between the populated states. In order to quench or refocus this event, leading to the removal of the exchange component, the employed refocusing or spin-lock field strengths (ν_1) have to be on the order of the process's exchange lifetime. If the exchange event is in the fast regime, the natural line width of a Lorentzian ($\tau_{ex} \Big/ 1 + (\tau_{ex} 2\pi\nu_{RF})^2$) governs the minimum field strength required to observe the exchange event ($\tau_{ex} \approx 1/(2\ \pi\ \nu_1)$). This process is also scaled by the amplitude of its motion. $R_{1\rho}$ experiments are ideally suited to probe exchange processes whose lifetimes are shorter than 150 μs because larger average rotation frequencies can be generated [33]. However, due to technical limitations this has been limited to the observation of processes ~40 μs ($\nu_1 \approx 4$ kHz) [107]. We have been able to surpass the technical limitation by utilizing a cryogenically cooled probehead [125] (cryo-probehead).

3.2 Large ν_1 for ^{15}N nuclei on a cryo-probehead

We investigated the limit of a cryo-probehead (Bruker QCI S3) by measuring the largest amplitude spin-lock field that could be generated without endangering the probe. Off-resonance continuous wave decoupling during the acquisition time ($t_{2,max}$=122.1 ms) [33,66] in a [^{15}N, ^{1}H]-HSQC was used to determine ^{15}N spin-lock field strengths (Figure 8). Initially, we tested a spin-lock field strength that is suggested [126] for cryo-probeheads, approximately 2 kHz (Figure 8; black line) which only corresponds to a time resolution of 80 μs.

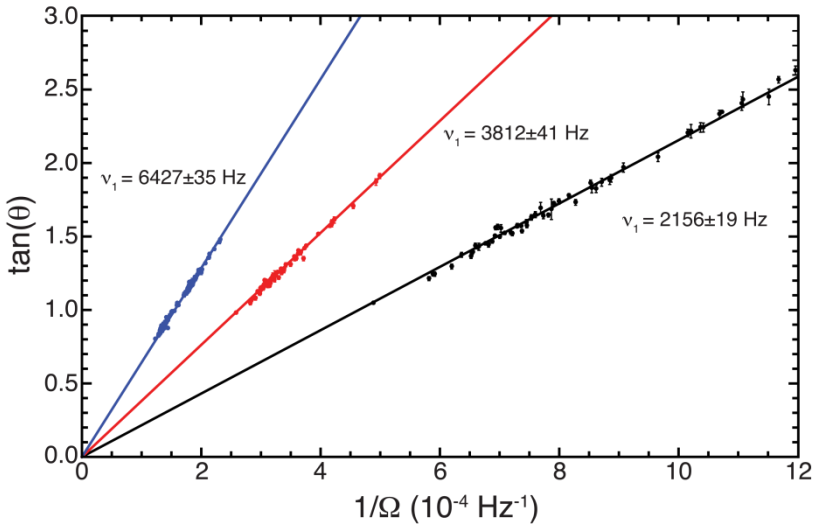

Figure 8 Spin-lock amplitudes (ν_1) for ^{15}N nuclei. For each field strength the tilt angle (tan(θ)) is plotted with respect to the inverse of the frequency difference between a given resonance and the position of the applied CW-field (Ω). Experimental procedures of these experiments are outlined in this section's Materials and Methods. Previously specified cryo-probehead (~2 kHz) and room-temperature probehead (~4 kHz) limits are plotted in black and red, respectively. The newly achieved field strength (6.4 kHz) appears in blue.

The structural integrity of the cryo-probehead was ensured by maintaining the power reserve for the preamp to be over 5%, which ensures enough power to continue regulation of the cold preamp's temperature, and that the temperature of the NMR coil was not deviating during application of the spin-lock pulse. Following that criteria we could safely reach a ν_1 of 6.4 kHz (Figure 8; blue line) which would permit a time resolution for kinetic processes up to 25 μs. Remarkably, this also exceeded the specified recommendations for room temperature probeheads which corresponds to a ν_1 of 4 kHz (Figure 8; red line). This limitation in room temperature probeheads is most likely caused due to the fact that the NMR coil itself sits at ambient temperature, whereas cryo-probehead NMR coils have superior cooling where the coil's temperature is between 15 to 20 K. RD experiments rely on the inherent sensitivity of the measurement. Therefore, a major advantage to cryo-probeheads is the increase in the signal-to-noise ratio, due to a reduction in the noise of the preamp and coil, which provides an

improvement in the signal-to-noise by a factor of 2-3 [127]. Thus, we have to compare the 6.4 kHz with the so far specified value of 2 kHz for cryo-probeheads which constitutes a 3.2 fold increase in the achievable field strength.

3.3 Validation of large amplitude spin-lock fields for RD experiments

With the identification that a ν_1 of 6.4 kHz can be created without endangering the intactness of a cryo-probehead it is important to establish its practical use for $R_{1\rho}$ experiments. We chose to implement an on-resonance $R_{1\rho}$ experiment that utilizes a selective heteronuclear Hartmann-Hahn transfer (HEHAHA-$R_{1\rho}$) [128]. In this experiment a single resonance is queried at a time (Figure 13) and only the amplitude of the spin-lock field is varied in order to modulate the exchange contribution. Therefore, with a ν_1 of this magnitude processes up to 25 μs are accessible without any contributions from the tilt-angle and longitudinal relaxation rate.

We utilized this HEHAHA-$R_{1\rho}$ experiment on ^{15}N labeled ubiquitin at 277 K for three residues whose exchange parameters have been determined before using off-resonance $R_{1\rho}$ techniques (Chapter 2 [44,108,112,129]). Figure 9 displays the results for Ile13, Thr55, and Val70 from the HEHAHA-$R_{1\rho}$ experiment where field strengths were varied from 1 to 6 kHz. Fitting the observed dispersion across all employed ν_1 values to a fast exchange model yielded τ_{ex} (Φ_{ex}) values of 50 ± 9 μs (29 ± 7 x10^3 rad^2 s^{-2}), 51 ± 5 μs (53 ± 7 x10^3 rad^2 s^{-2}), and 33 ± 5 μs (112 ± 38 x10^3 rad^2 s^{-2}) for Ile13, Thr55, and Val70, respectively and are in agreement with what has been presented in the literature (Figure 9). Using the specified limits for cryo-probeheads of only 2 kHz yields $R_{2,eff}^{1kHz}$-$R_{2,eff}^{2kHz}$ = 0.26, 0.64, and 0.43 s^{-1} for Ile13, Thr55, and Val70, respectively give only small changes in $R_{2,eff}$ (Figure 9; hatched box).

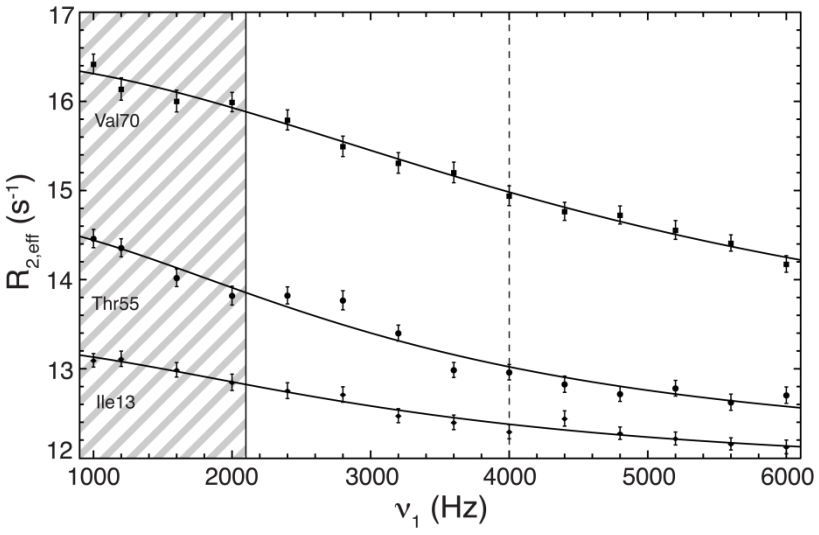

Figure 9 On-resonance HEHAHA-$R_{1\rho}$ dispersion curves for residues Ile13 (diamonds), Thr55 (circles), and Val70 (squares) using a ^{15}N labeled sample of ubiquitin at 277 K. Black curves correspond to fits using a fast exchange model. The hatched box up to 2 kHz indicates the previously specified limit for cryo-probeheads. The dashed line at 4 kHz indicates the limit for $R_{1\rho}$ experiments conducted on room temperature probeheads.

Additional advantages are immediately recognized with respect to the level of precision that dispersion curves can be measured by utilizing $R_{1\rho}$ experiments with large amplitude spin-lock field strengths. To evaluate the increase in precision with respect to the determination of the parameters that define exchange we measured a dispersion curve of Val70 with 51 different ν_1 values between 1 and 6 kHz (Figure 10). The uncertaintity in the extracted parameters was calculated by performing Monte-Carlo simulations with 300 iterations. Fitting the dispersion data with field strengths up to

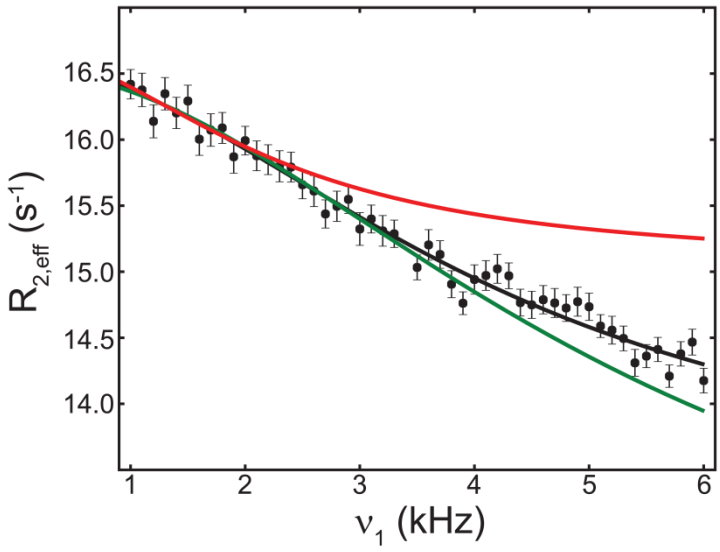

Figure 10 Effect of fitting on-resonance HEHAHA-$R_{1\rho}$ data for Val70 using ν_1 values up to 2 kHz (red curve), 4 kHz (green curve), and 6 kHz (black curve). For fitting at 2 kHz it is important to note that from the MC error ~50% of the calculations produced results in which there was no contribution from exchange.

	ν_1 = 2 kHz	**ν_1 = 4 kHz**	**ν_1 = 6 kHz**
τ_{ex} (μs)	72 ± 68	31 ± 10	38 ± 4
Φ_{ex} (x10^3 rad^2 s^{-2})	23 ± 80	148 ± 127	87 ± 13
$R_{2,0}$ (s^{-1})	15.1 ± 2.0	12.0 ± 1.9	13.2 ± 0.2

Table 1 Exchange parameters derived from fitting dispersion data aquired for Val70 using points up to the previously specified limits for ν_1 on cryo-probeheads (2 kHz), room-temperature (4 kHz) and the newly determined limit (6 kHz).

2 kHz (11 data point; red curve in Figure 10), although yielded a result, actually produced incorrect exchange parameters with large errors that could be understood with a model which describes no chemical exchange. This is an expected result considering the change in $R_{2,eff}$ is too small to extract reliable exchange parameters and that the Lorentzian profile is largely underestimated. Using data points up to the room-temperature probehead limit of 4 kHz (green curve in Figure 10) began to reproduce fits from the literature (Table 1) [44,108,112,129]. The exchange lifetime can be determined with ν_1 values up to 4 kHz because τ_{ex} is encoded in the decay profile of the Lorentzian, but the Φ_{ex} values still have large uncertantities due to the fact

that the Lorentzian profile is not as well sampled as with data measured up to 6 kHz. Evidently, using dispersion data measured with ν_1 up to 6 kHz increases the precision in parameters extracted from $R_{1\rho}$ data (Table 1) because the exchange contribution is explored more completely. Jacknife simulations in which eleven field strengths up to 2, 4, and 6 kHz were randomly selected 500 times and then subsequently refit produced the same observation as in Table 1 [129].

3.4 Application to the accurate determination of intrinsic transverse relaxation rates

Typically, $R_{2,0}$ measurements in conjunction with longitudinal relaxation rates and heteronuclear NOE data are used to determine the tumbling time of a protein, correlation times of motions faster than τ_c, and constants that describe rotational diffusion [26,28,62,63]. However, relaxation rates that report a contributuion from exchange (R_{ex}) must be excluded from the analysis because they disturb the fitting procedure by overestimating certain parameters [130]. Therefore it is highly desirable to have an experimental setup that can more efficiently remove R_{ex}. It is important to note that conventional relaxation techniques [27] monitor pure inhpase magnetization ($N_{x,y}$) of ^{15}N nuclei, and this is the same coherence that is tracked in the HEHAHA-$R_{1\rho}$ experiment. We compared the $R_{2,eff}$ values measured at 1 kHz where only motions up to 80 μs are removed to the 6 kHz data where motions up to 25 μs can be refocused.

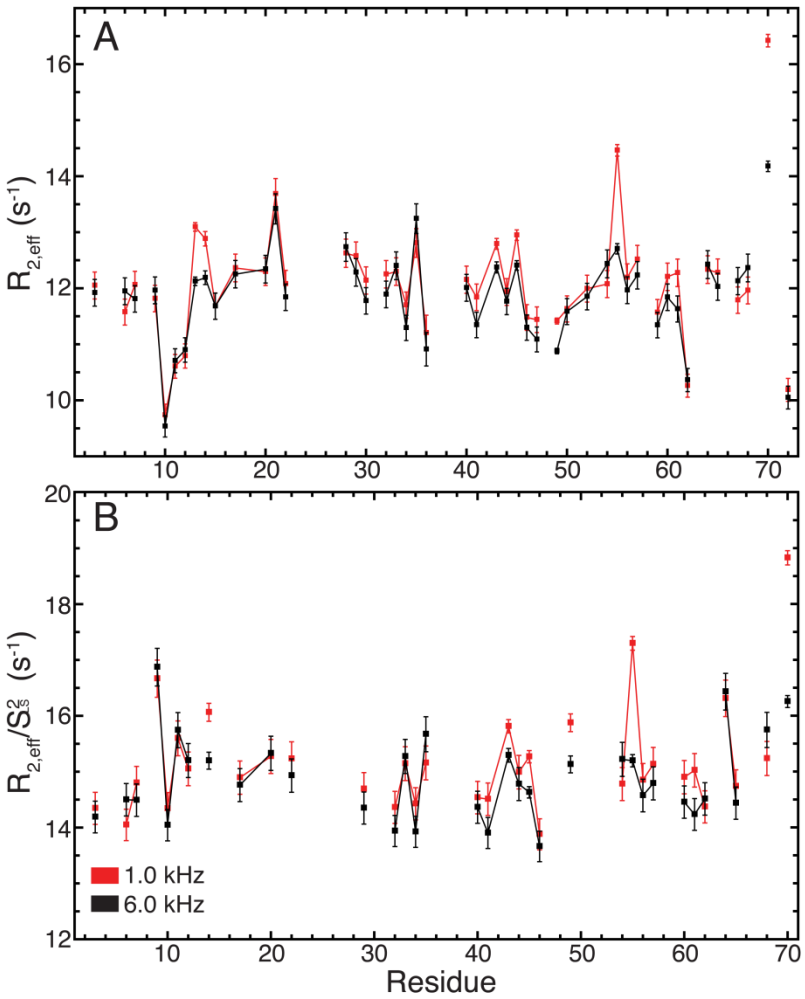

Figure 11 In A, $R_{2,eff}$ measured with a ν_1 of 1 (red points) and 6 (black points) kHz across all residues that could be queried from the HEHAHA-$R_{1\rho}$ experiment. Whereas in B residues are scaled by S^2_{LS} [116] and depict $R_{2,eff}$ without the impact of fast motions (faster than overall tumbling). In B residues are shown for ^{15}N sites across ubiquitin excluding the flexible C-terminal tail. All experiments were acquired with a ^{15}N labeled sample of ubiquitin at 277 K. In addition a tumbling time of 10.3 ± 0.1 ns was extracted, and agrees well with a recent study in which transverse cross-correlated relaxation was used to determine the tumbling time [131].

From Figure 11A, out of 72 observable resonances 46 gave sufficient intensity and frequency separation in either ^1H or ^{15}N dimensions that they could be probed [128,132] by the selective on-resonance HEHAHA-$R_{1\rho}$ experiment. Figure 11B shows the same $R_{2,eff}$ values as scaled by their respective S^2_{LS} [63] reporting $R_{2,eff}$ without the impact of motion faster than the tumbling time. Scaling by just S^2_{LS} does not take diffusion anisotropy or motion described by the

extended model-free formalism, but for ubiquitin's rotational diffusion tensor has been found to have a small amount of anisotropy [63]. Still the variances of $R_{2,eff}/S^2_{LS}$ using 6 kHz (0.57 s^{-2}) and 1 kHz (0.95 s^{-2}) spin-lock field strengths show a reduction by 40% (Figure 11B). Thus, the utilization of a spin-lock field with an amplitude of 6 kHz displays a greater efficiency in the removal of exchange.

3.5 Detection of ^{15}N nuclei that undergo small amplitude motion

Off-resonance $R_{1\rho}$ in theory can be used to generate larger effective fields whereby faster lifetimes could be quantified. However, a major hindrance is that the amplitude of motion would have to be large enough to detect any contribution of exchange because at large offsets the $R_{1\rho}$ rate will be dominated by the longitudinal relaxation rate (R_1) ($R_{1\rho} = R_1 \cdot \cos^2(\theta) + R_{2,eff} \cdot \sin^2(\theta)$; $\tan(\theta) = \nu_1/\Omega$). So for residues that display smaller motional amplitudes the on-resonance HEHAHA-$R_{1\rho}$ becomes an ideal method to be track small changes in $R_{2,eff}$ when large spin-lock amplitudes are used on a cryo-probehead because not only is the sampling of exchange greater to $R_{1\rho}$, but the increased signal-to-noise allows for greater precision in monitoring these small changes.

In Figure 11 there are four residues that show $\delta R_{2,eff}^{R1\rho}$ ($R_{2,eff}^{1\ kHz} - R_{2,eff}^{6\ kHz}$) greater 0.4 s^{-1} whose changes could be tracked and fitted to a fast exchange model (for the rates refer to Table 2). Dispersion curves for residues Thr14, Leu43, Phe45, and Gln49, which have not been detected before, are shown in Figure 12 and their extracted τ_{ex} and Φ_{ex} values are summarized in Table 2. The small changes in $R_{2,eff}$ can be realized from the small Φ_{ex} values that were extracted. For example, $\delta R_{2,eff}^{R1\rho}$ for Val70 is a factor of approximately four times larger than that of Gln49 which is the smallest (Figure 12D). Given that their changes are small the observation of

these residues would been precluded from complete observation without the use of the approach described above again highlighting the advantages of high powered spin-lock fields on cryogenically cooled probeheads.

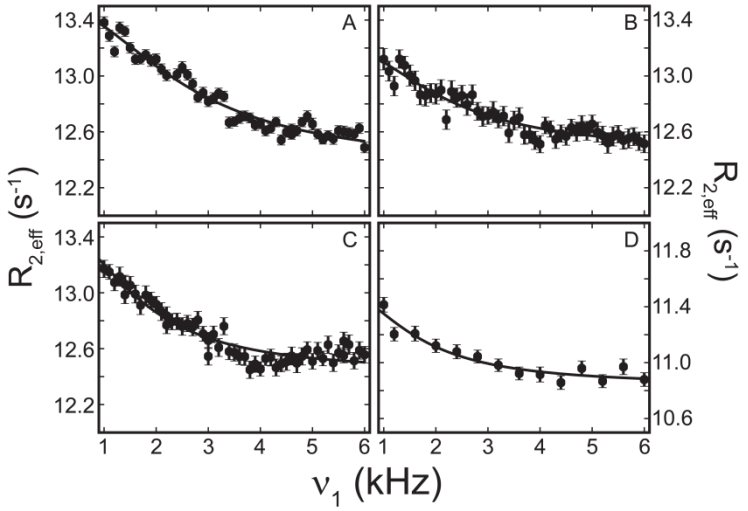

Figure 12 Additional ^{15}N backbone nuclei detected to have microsecond motion at 277 K using large amplitude spin-lock fields for Thr14 (A), Leu43 (B), Phe45 (C), and Gln49 (D) plotted is the dependence of $R_{2,eff}$ with respect to ν_1. Solid black curves represent fits to a fast exchange model.

	Thr14	**Leu43**	**Phe45**	**Gln49**
τ_{ex} (μs)	62 ± 6	75 ± 10	82 ± 12	101 ± 32
Φ_{ex} (x10^3 rad^2 s^{-2})	19 ± 2	11 ± 1	12 ± 1	7.1 ± 1.2
$R_{2,0}$ (s^{-1})	12.35 ± 0.04	12.45 ± 0.03	12.39 ± 0.03	10.84 ± 0.06

Table 2 Exchange parameters for ^{15}N nuclei that display small conformational amplitudes.

3.6 Conclusions

We have shown that cryo-probeheads can be safely used to exceed the time resolution limit for kinetic measurements conducted with $R_{1\rho}$ relaxation dispersion experiments. Compared to the previously specified limits for cryo-probeheads we have increased the fastest motion that can be detected by a factor of 3.2 and is now set to a life time of 25 μs for ^{15}N nuclei. The use of these large amplitude spin-lock fields was tested on ^{15}N labeled ubiquitin at 277 K and could

reproduce the exchange parameters [129] for three residues (Figure 9) that have been previously observed [44,108,112]. In addition, the increased sensitivity with a cryo-prohead, in conjunction with an on-resonance HEHAHA-$R_{1\rho}$ experiment in which only ν_1 is varied allowed for the observation for four residues that have not been identified before (Figure 12) and report small amplitude motions that, earlier, appeared to be relaxation silent. The large amplitude spin-lock fields presented here can remove motions up to 25 μs thereby suppressing chemical exchange that are inherent to the transverse relaxation rates and also opens an avenue for the determination of more veracious inphase intrinsic transverse relaxation rates (Figure 11). Besides providing greater access to motion displayed by ^{15}N nuclei from the supra-τ_c range this approach can also be extended to nuclei with larger gyromagnetic ratios.

3.7 Materials and Methods

^{15}N field strength measurements For all experiments a 2.5 mM U-^{15}N labeled ubiquitin sample was used at 277 K. All measurements were conducted on a Bruker Avance I spectrometer operating at a Larmor frequency of 600 MHz. The cryo-prohead used to generate the large amplitude field strengths was a Bruker CryoProbe QCI S3. The amplitudes of the ^{15}N field strengths were measured by applying off-resonance CW decoupling in an [^1H, ^{15}N]-HSQC experiment [32,46,66]. In this case, incomplete decoupling from the off-resonance CW field arises in an effective scalar coupling (J_{eff}^{NH}) value for $^1H^N$, ^{15}N coupled resonances. Another experiment was then performed in which no CW-decoupling is applied therefore giving the unperturbed coupling value (J_0^{NH}). A given nuclei's tilt angle ($\tan(\theta) = \nu_1/\Omega$) can be calculated as

$$\tan(\theta) = \sqrt{\left(\frac{J_0^{NH}}{J_{eff}^{NH}}\right)^2 - 1} \qquad \text{(Eq - 3.7.1).}$$

Ω is the frequency difference between an observed ^{15}N resonance the frequency at which the CW decoupling is applied. A plot (Figure 8) of tan(θ) versus Ω yields a linear correlation whose slope is ν_1. All experiments were acquired with 1024 ($t_{2,max}$ = 122.1 ms) and 256 ($t_{1,max}$ = 140.3 ms) complex points in the direct and indirect dimensions, respectively. The recycle delay was kept long enough that they duty cycle did not exceed 2.4%. When applying large amplitude fields it is imperative to monitor deviations in the NMR coil's temperature and cold preamp's power reserve. Here, we ensured that the preamp power reserve did not drop below 5%. Errors in measured J_{eff}^{NH} were acquired from the line width at half-height of coupled peaks divided by their signal to noise ratio, and errors in ν_1 were determined by error propagation. The pulse program used for measurement of ν_1 for ^{15}N nuclei is available in the Pulse Program section.

On-resonance Selective Hartmann-Hahn $R_{1\rho}$ (HEHAHA-$R_{1\rho}$) The pulse scheme used here was adapted from Korzhnev et al. [128] and details can be found in the caption of Figure 13. All experiments were acquired with 128 transients and a 3 second recycle delay between each transient was used. Spectra were recorded in which the length of the spin-lock delay (T_{RELAX}) was set to 125 ms and then the amplitude of the spin-lock field was varied. A reference experiment was recorded for each resonance with the T_{RELAX} period omitted from the pulse scheme. $R_{2,eff}$ was calculated as

$$R_{2,eff} = -\frac{1}{T_{RELAX}} \ln\left(\frac{I(\nu_1)}{I(0)}\right) \quad \text{(Eq - 3.7.2)}$$

where $I(\nu_1)$ and $I(0)$ are the peak amplitudes from the given spectra with the applied spin-lock and the reference spectrum, respectively. This method greatly facilitated the rapid measurement

of dispersion data where a complete 14 point dispersion curve (Figure 9) was acquired in 1.5 hours. The error in $R_{2,eff}$ was propagated from the base-plane noise in each spectrum.

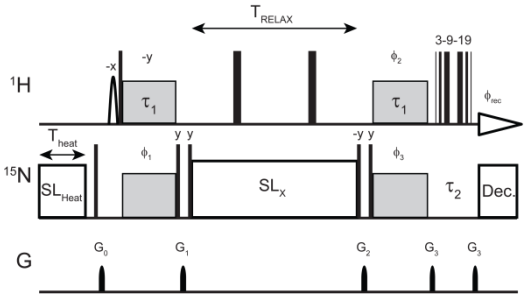

Figure 13 Pulse schematic for the HEHAHA-$R_{1\rho}$ experiment. All ^{1}H and ^{15}N 90° and 180° rectangular pulses are represented by narrow and wide black bars, respectively, and were applied at 31.3 kHz and 12.5 kHz for ^{1}H and ^{15}N, respectively. The shaped ^{1}H 90° water selective pulses after the Boltzmann purging gradient represents a Gaussian shaped pulse and was applied for a duration of 1.5 ms in order to flip water magnetization down which is then subsequently returned to the +z axis for the rest of the pulse sequence. Gray colored boxes designate the matched weak field heteronuclear Hartmann-Hahn transfer periods that are applied with field strengths of $\omega_{transfer} \sim 90$ Hz on proton and nitrogen channels [132]. These fields were applied for a length of 10.8 ms (τ_1). Calibration of these weak fields required an iterative approach as the ^{1}H amplifier on the employed 600 MHz Avance I spectrometer displayed non-linear tendencies with respect to the expected power output. Suppression of cross-correlated dipole-dipole/CSA relaxation was done via the application of two ^{1}H 180° pulses at $T_{RELAX}/4$ and $3T_{RELAX}/4$ [133]. Temperature compensation was achieved by using a scheme in which the length of T_{HEAT} was varied based on the amplitude and length of a given spin-lock (SL_x) period [134]. However, since a two-point sampling scheme was used T_{HEAT} simplifies to $T_{HEAT} = T_{RELAX}^{MAX} - \left(\frac{\omega_{SL_x}^{RF}}{\omega_{SL_x}^{MAX}} \right)^2 T_{RELAX}$ in which T_{RELAX}^{MAX}, $\omega_{SL_x}^{RF}$, $\omega_{SL_x}^{MAX}$ was 125 ms, a given $2\pi\nu_1$ value, and $2\pi\nu_1^{MAX}$ set at $37.7 \cdot 10^3$ rad s^{-1}. The heat compensation block was applied 25 kHz upfield from the resonance of interest. After the Gaussian pulse, the transmitter frequency for ^{1}H and ^{15}N were set to the resonance of interest and then the ^{1}H transmitter frequency was later returned to water for the application of the binomial pulse. Additional water suppression was achieved by using a 3-9-19 binomial pulse [135] where τ_2 was 238 μs. ^{15}N decoupling during acquisition was done with a WALTZ16 composite pulse with a field strength of 2 kHz [136]. A phase scheme of ϕ_1 = (x, -x), ϕ_2 = (4x, -4x), ϕ_3 = (2x, -2x) and ϕ_{rec} = ([x, -x, -x, x], 2[-x, x, x, -x], [x, -x, -x, x]), and x phase unless otherwise indicated. Gradients with strengths (length) of G_0 = 43 G/cm (1 ms), G_1 = 10 G/cm (0.5 ms), G_2 = 8.0 G/cm (0.5 ms), G_3 = 17 G/cm (0.5 ms) were used.

An estimation of the overall heating effect from the use of large amplitude spin-lock fields during the HEHAHA-$R_{1\rho}$ experiment was monitored by comparing a given amide proton's temperature

coefficient. In this case, the temperature deviation was found to be small at a maximum of ~0.7 K. In addition, the heat compensation block utilized here was effective in controlling the temperature as flat dispersion curves did not display a decrease in $R_{2,eff}$ as the amplitude of the spin-lock was increased (Appendix Figure 6).

The HEHAHA-$R_{1\rho}$ experiment uses weak matched field strengths on both ^{1}H and ^{15}N nuclei to transfer inphase proton magnetization directly to inphase nitrogen magnetization. It has been shown [132] that cross-polarization is possible and can be selective if the magnitude of applied matched fields are implemented with a field strength of $\omega_{transfer}/2\pi$ (Hz) set close to J, where J is the scalar coupling value between amide protons and backbone nitrogen sites (~-93 Hz), and applied for a length of 1/|J| (Figure 13; τ_1 = 10.8 ms). In order to preserve this selectivity, resonances must have a frequency separation of at least $\frac{3}{4\pi}\omega_{transfer}$ (Hz) in either the proton or nitrogen dimensions [128]. The pulse program HEHAHA-$R_{1\rho}$ can be found in the Pulse Program section. Examples of the HEHAHA-$R_{1\rho}$ experiment are shown in Figure 14.

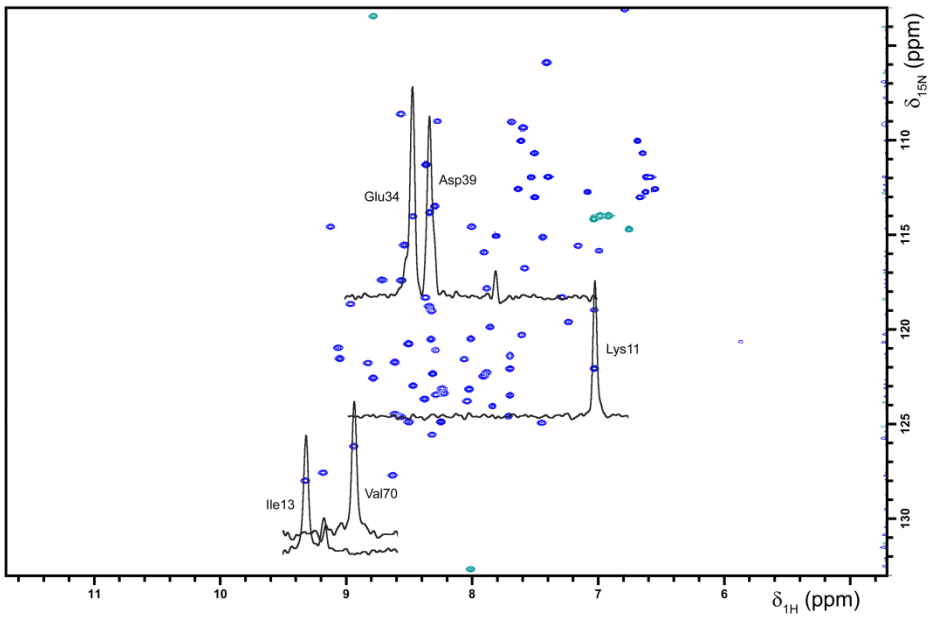

Figure 14 Overlay of the 1D HEHAHA-$R_{1\rho}$ experiments acquired at a single ν_1 value with a [^{1}H, ^{15}N]-HSQC spectrum of ubiquitin at 277 K. A total of 46 resonances could be quantified with the HEHAHA-$R_{1\rho}$ experiment. Positive and negative contours in the HSQC are in blue, and cyan, respectively. Ala46 and Gly47 are folded in this spectrum.

Large amplitude $R_{1\rho}$ detects concerted motion in ubiquitin

4.1 Towards the detection of motions faster than 25 μs

In the previous section, it was demonstrated that spin-lock amplitudes up to 6.4 kHz on ^{15}N nuclei could be safely generated on cryo-probeheads while maintaining the structural integrity of the equipment (Figure 8) [129]. In addition, the large field strengths were also tested and validated for use in relaxation dispersion experiments for the extraction of parameters that define conformational exchange (Figure 9) [129]. An additional advantage in the increased sensitivity from cryo-probeheads was also identified by the measurement of residues (Figure 12) that depicted small conformational amplitudes. However, the detectable time window is still limited with $1/(2\pi\nu_1) = 25$ μs. In principle, this limit could be alleviated by using different nuclei with larger gyromagnetic ratios (γ), such as ^{13}C and ^{1}H, and in this chapter, the applicability of the high spin-lock field strength on these nuclei for the detection of faster motions than 25 μs is discussed.

The amplitude of a spin-lock is given by the relationship $\omega_1 = \gamma B_1$ in which ω_1 is $2\pi\nu_1$ [46]. Since, the B_1 field that is produced is directly related to the voltage produced by the RF coil the attainable value of ν_1 scales by γ. Therefore, not only are larger spin-lock amplitudes possible with nuclei of larger gyromagnetic ratios, but the field strengths achieved before could be attained with reduced output from the amplifiers ($\nu_1 = \gamma B_1/(2\pi) \approx \sqrt{P}$; since $P = V^2/R$ where P, V, and R is the power (Watt), voltage, and resistance, respectively). In order to exploit this benefit, we measured ^{13}C and ^{1}H spin-lock field strengths using the same approach as what was

outlined in the Materials and Methods section of the previous chapter. The sample for these experiments was a selectively ^{13}C labeled sample of ubiquitin in a heavily deuterated background in which only Ileδ, Valγ1/γ2, and Leuδ1/δ2 resonances are ^{13}C labeled and the methyl groups consist two deuterons and one proton ($^{13}CHD_2$) [137]. We could achieve large increases than what was previously specified to be the maximum attainable ν_1 for ^{13}C and ^{1}H nuclei (Figure 15).

Values for tan(θ) were quantified by monitoring a resonance's effective splitting ($^{1}J_{eff}^{CH}$) using [^{1}H,^{13}C]-HSQC with CW decoupling applied in either during direct dimension acquisition (t_2) or during indirect dimension chemical shift labeling (t_1) for ^{13}C and ^{1}H field strengths determination, respectively. Pulse programs employed for the field strength calibrations on ^{13}C and ^{1}H nuclei are located in the section titled Pulse Programs. In Figure 14, the linear correlations between the tan(θ) for all observable methyl groups at their respective offsets are plotted.

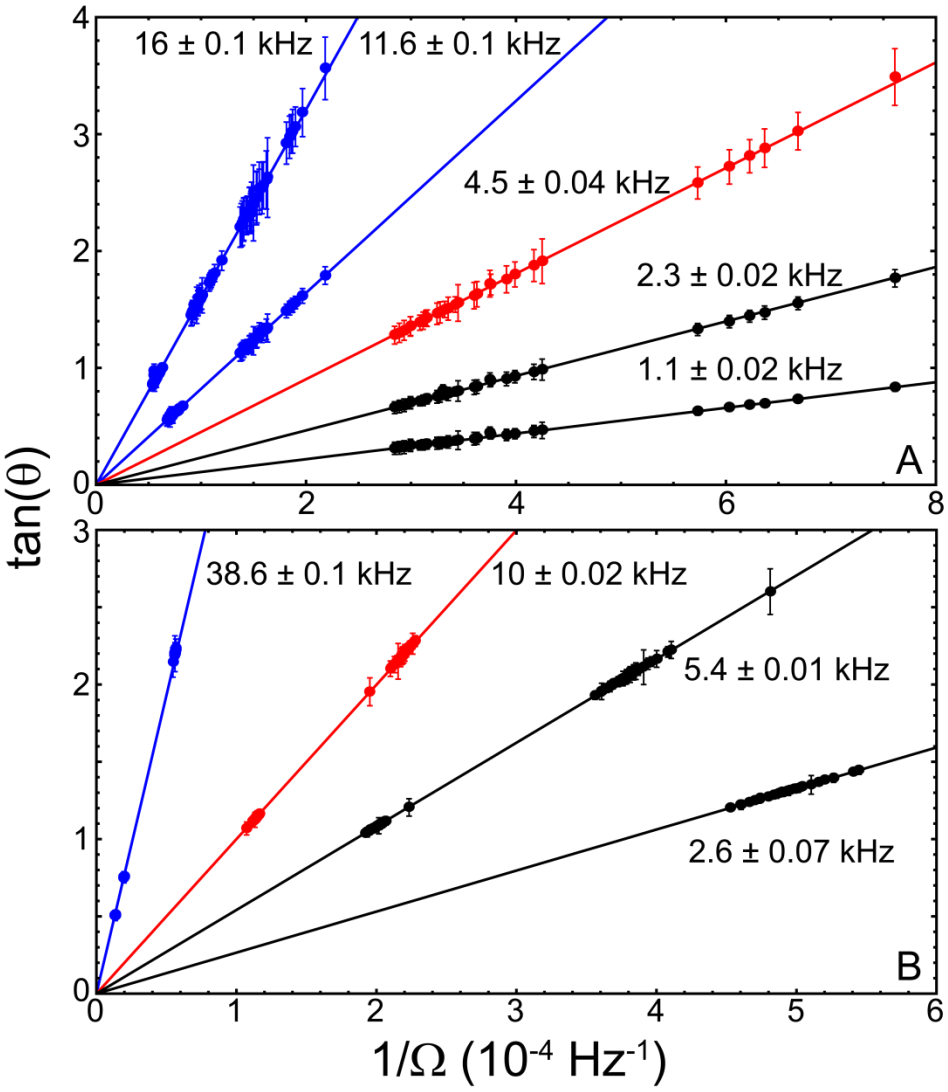

Figure 15 Plots of tan(θ) versus a resonances offset Ω ($\Omega = \Omega_{resonance} - \Omega_{CW-field}$) for spin-lock amplitude (straight lines) determination for ^{13}C (A) and ^{1}H (B) nuclei. In both A and B, lines and points in black, red, and blue represent conventional, specified limits, and the newly attained ν_1 values, respectively. With the $^{13}CHD_2$ sample of ubiquitin, only 33 methyl group correlations are present in each [^{1}H,^{13}C]-HSQC. Therefore for all experiments in which ν_1 was greater than 4 kHz multiple experiments were acquired with the same ν_1 value, but CW-decoupling field was placed at different positions. Deuterium decoupling was also applied during the indirect dimension in order to eliminate ^{13}C-D coupling. For the measurement of ^{1}H spin-lock strengths the CW-decoupling field was applied during t_1 chemical shift labeling thus, the $^{1}J_{eff}^{CH}$ for C-H correlations was observed in the indirect dimension.

Initially, marginal spin-lock amplitudes were employed (Figure 15; black), and specified limits suggested for cryo-probeheads (Figure 15; red) for both nuclei [126]. While adhering to a

minimum preamp power reserve level of 5% and a duty cycle ~3% we could achieve values of ν_1 up to 16 kHz and 38.6 kHz for ^{13}C and ^{1}H nuclei (Figure 15; blue), respectively. These large amplitude field strengths could also be applied for sufficiently long durations that allows for relaxation measurements (^{13}C; $t_{2,max}$ = 142 ms and ^{1}H; $t_{1,max}$ = 136 ms). Compared to ^{15}N nuclei where a ν_1 of 6.4 kHz (Figure 8) can be used to resolve motions up to 25 μs, ^{13}C and ^{1}H nuclei push this limit even further to where motions up to 10 and 4 μs, respectively, could theoretically [138] be probed. This leads to an even greater increase in time resolution by a factor of 2.5 and 6.3 for ^{13}C and ^{1}H nuclei, respectively, as compared to ^{15}N.

4.2 Implementation of RD for ^{13}C and ^{1}H nuclei

In order to ascertain the benefit of large spin-lock fields for ^{13}C nuclei, we performed methyl $R_{1\rho}$ RD on a selectively $^{13}CHD_2$ labeled sample at 277 K (Figure 16). This labeling scheme greatly simplifies the required possible experimental approaches as Hartmann-Hahn matching conditions, which for $R_{1\rho}$ experiments can be problematic with changes in the Ω, are minimized to adjacent carbon nuclei, and cross-correlated dipolar relaxation between the methyl carbon and its attached protons is eliminated rendering its behavior comparable to an AX spin system instead of an AX_3 spin system [137,139]. The pulse sequence used here is comparable to the one used by Brath et al. [139], details are given in the Materials and Methods of this chapter and the pulse code for Bruker instruments is placed in the Pulse Program section. A clear benefit can be seen in Figure 16. Similar to what was observed in Figure 9 a significant improvement as compared to the previously specified limits (Figure 16; hatched box) is achieved with these large spin-lock fields. If only ν_1 values up to the conventional limit [138] would have been used still ~20% of the exchange contribution for L50δ2 would not have been measured. More importantly, as compared to ^{15}N nuclei, which have a lower gyromagnetic ratio, the larger employed ν_1 values

allow for even further sampling of the exchange contribution to $R_{1\rho}$ as the complete tail of the Lorentzian is also sufficiently sampled and directly observed (Figure 16).

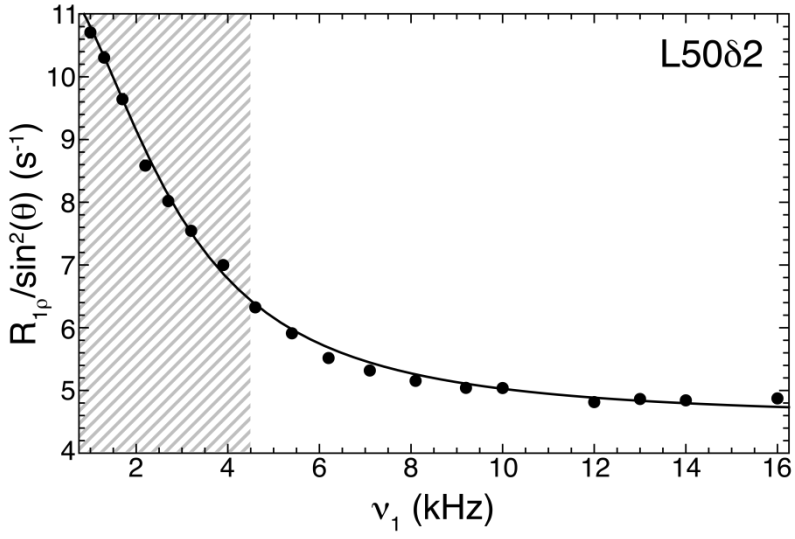

Figure 16 Example RD curve for L50δ2 in selectively methyl $^{13}CHD_2$ labeled ubiquitin measured at 277 K. The hatched box is drawn up to 4.5 kHz which designates the previously specified limit [138]. Compared to previous ^{13}C-$R_{1\rho}$ experiments, relaxation rates can be probed with an increased factor of 3.6. The black curve represents a fit to a fast exchange model that also takes into consideration intrinsic relaxation parameters. The error in $R_{1\rho}$ was propagated from the noise in each spectrum.

We have now been able to test these large amplitude fields for ^{13}C nuclei, but what is of great interest is the observation of a significant exchange (Φ_{ex} = 122.3 ± 9.1 ·10^3 rad^2s^{-2}) to a methyl ^{13}C probe in ubiquitin. For L50δ2, an exchange lifetime (τ_{ex}) of 58 ± 4 μs (Figure 16; black curve) was extracted. In order to identify all possible ^{13}C methyl sites that may show dispersion an extensive set of $R_{1\rho}$ experiments were conducted using a large variety of Ω values with ν_1 varied from 0.5 to 16 kHz. Here, Ω is the difference between the resonance of interest and the position where ν_1 was applied. Out of all 33 observable ^{13}C methyl resonances 10 residues gave appreciable and statistically significant dispersion that their exchange parameters could be extracted (see Materials and Methods). Backbone $^1H^N$ and methyl ^1H RD data on

ubiquitin at 277 K has also been collected up to maximum field strengths that would permit resolution of motion down to 4 μs. However, this work was done in direct collaboration with Dr. Colin Smith (MPI-BPC, Dept. Theoretical and Compuational Biophsyics) but was not acquired by the author of this Dissertation. Additional backbone $^{1}H^{N}$ RD data was observed for eleven resonances, yielding a total of 31 nuclei that show conformational exchange at 277 K (Appendix Figure 8) that center with a τ_{ex} between 55-60 μs. Motion faster than 55 μs and up to 4 μs were not detected. Also, the existence of microsecond motions within atoms of side chain moieties at this temperature have not been experimentally observed before. Although previous RDC based methyl order parameters for ubiquitin have shown that there is some amplitude of motion from the supra-τ_c range [98], the timescale of this motion for side chain moieties was not predicted to exist from a recent long 1 ms MD trajectory of BPTI [117].

4.3 Common time scale motions of the backbone and the side chain were detected

The individual lifetimes for the methyl nuclei apparently cluster around an exchange lifetime of about ~60 μs (Figure 17; Appendix Table 2). Indeed, when all methyl dispersion data were fit together (total number of data points (N) was 209), assuming that all the residues report on the same process the global lifetime of this exchange event is 61 ± 1 μs (Figure 18; blue lines). The quality of the global fits is excellent and can be assessed in Figure 17 where the global fits are plotted as red curves.

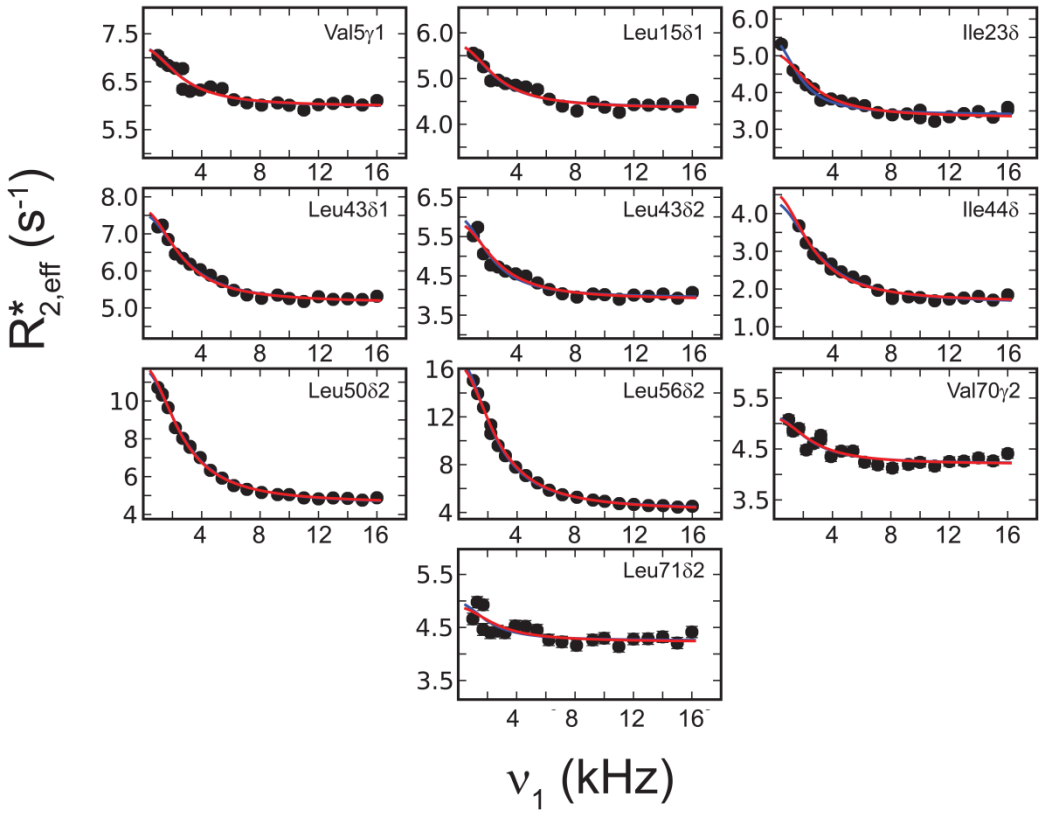

Figure 17 The dependence of $R^{*}_{2,eff}$ on ν_1 for methyl ^{13}C nuclei that displayed a contribution of exchange to $R^{*}_{2,eff}$. Plotted curves in blue and red represent individual fits and global fits that included all ten residues, respectively. All exchange parameters are reported in Appendix Table 2. A complete outline as to the methods used to acquire ^{13}C methyl RD data and how the data was analyzed is given in the Materials in Methods section.

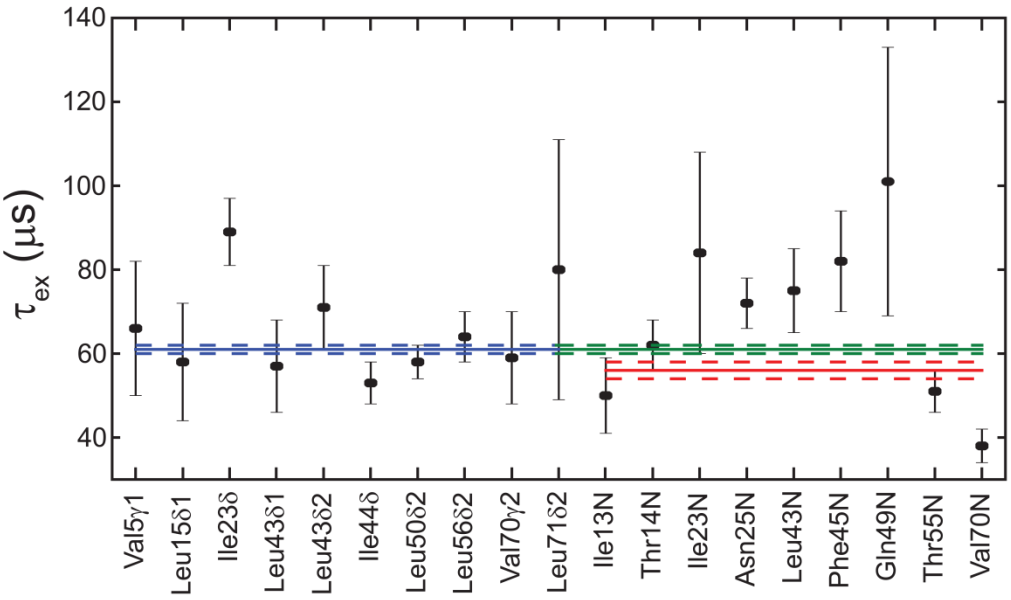

Figure 18 All extracted exchange lifetimes for ^{13}C methyl resonances and ^{15}N backbone nuclei. Global fits to the dispersion data are given by the straight lines and the error in τ_{ex} for each fit is given by the dashed lines that are above and below their respective solid lines. Globally fitting only the methyl and ^{15}N backbone data with a single lifetime yielded a τ_{ex} of 61 ± 1 μs (blue line) and 56 ± 2 μs (red line), respectively. When the ^{13}C methyl and ^{15}N backbone were fit together the global τ_{ex} was 61 ± 1 μs. All of the extracted parameters from all fits can be found in Appendix Table 2. The error in τ_{ex} was determined from Monte Carlo simulations with 1000 (individual fits) or 100 (global fits) iterations.

Given that the ^{13}C nuclei are well fit together we also conducted a global analysis of ^{15}N resonances that have shown dispersion using the high power techniques discussed previously. From the 9 ^{15}N nuclei a global τ_{ex} of 56 ± 2 μs was determined (Figure 18; red line) and is very similar to the 61 ± 1 μs determined for methyl ^{13}C resonances. Fitting all methyl ^{13}C and backbone ^{15}N dispersion data (N = 467) together yields a τ_{ex} of 61 ± 1 μs (Figure 18; green curve and Appendix Figure 7). The observation of these kinetics was expected to exist from earlier determined methyl RDC order parameters [117]. When the amide proton relaxation dispersion data was included into the analysis of the dispersion data the global exchange lifetime became 55 μs (Appendix Figure 8). All resonances that report on exchange are also distributed throughout

the structure of ubiquitin and are not locally conserved within the structure (Appendix Figure 8). Evidently, ubiquitin's backbone and side chain moieties undergo a global exchange process with a common timescale. Out of the different types of nuclei that were measured here, only backbone ^{15}N, $^{1}H^{N}$ and methyl ^{13}C nuclei report on this concerted process. The methyl ^{1}H sites were measured (courtesy Dr. Colin Smith, MPI-BPC) but reported no detectable motion even up to the accessible time limit of 4 μs.

4.4 Observable methyl dispersion does not follow a discrete exchange model

As mentioned above the methyl ^{1}H RD experiments reported a direct absence of dispersion, except for one site, that produced a small amplitude of motion from the methyl ^{1}H of Leu50δ2. The source of this observed dispersion is most likely due to ring current fluctuations from the spatially close aromatic ring of Tyr59 while its attached ^{13}C nucleus also exhibits motion. Therefore, the standing question is what can be the possible reasons for many sites showing methyl ^{13}C dispersion on the microsecond timescale, but not from their attached methyl ^{1}H? Some major sources that can perturb a chemical shift value stem from magnetic anisotropy [115] namely the close spatial proximity of one nucleus to a charged group and fluctuating ring currents from residues with aromatic rings [140]. Contributions from electric fields of certain nuclei have been found to have a small contribution to the overall chemical shift value for methyl sites [141]. Generally protons are exquisite probes for local structural changes as their gyromagnetic ratio is the highest [88]. Therefore, one would expect that if the above sources were the cause for the observed methyl carbon dispersion the Φ_{ex} values for methyl proton sites should be larger by a factor of approximately 16 ($(\gamma_H/\gamma_C)^2$) for the same magnetically induced changes as compared to methyl carbon sites. However, since there is a direct absence of methyl proton dispersion the only source that can affect methyl carbon resonances as opposed to methyl proton

sites would be from dihedral angle changes of methyl ^{13}C sites. Dihedral changes from methyl group bearing amino acids such as Valine (χ_1) or Leucine/Isoleucine (χ_2) are directly linked to population changes of a given rotameric state. For ^{13}C methyl groups a change in the methyl related dihedral angle results in the observation of the γ-gauche effect which can modify a ^{13}C chemical shift value of a given methyl nuclei by 5 ppm due to effects of neighboring methyl groups in their different rotameric states, trans (t), gauche(+) (g^+), or gauche(-) (g^-) [142,143].

To date for Leucine, Isoleucine, and Valine semi-quantitative models have been created that use their respective ^{13}C chemical shift values to obtain insights into the populations of rotameric states assumed by their methyl groups [144-146]. In the case of Leucine it has been shown that the predominately populated rotamers are the t and g^+ states [147]. From which a simple model was constructed by Mulder in which the difference between HSQC based ^{13}C chemical shifts between $\delta1$ and $\delta2$ can be used to deduce the rotamer populatiosn of t (p_t) or g^+ (p_{g+}) states [144]. Since Φ_{ex} for a discrete two-state process is described by the product between the major and minor populations times the square of the chemical shift difference ($p_t p_{g+} \Delta\omega^2$) we can use these models to calculate a conformational amplitude ($\Phi_{calc}^{2-state}$) (Table 4) to see if they concur with measured values. This calculation assumes that the microsecond interconversion process is due to discrete rotamer jumps, that follow an "excited states" model for ^{13}C methyl nuclei. The $\Phi_{calc}^{2-state}$ for Leucines in all cases overestimate the experimental Φ_{ex} by at least one order of magnitude (Figure 19). For Leu56$\delta2$, indicated by the red star in Figure 19, the model failed to predict the rotamer populations because the $\delta1$ and $\delta2$ chemical shift difference exceeded the model's range of validity. Therefore, a discrete two-state χ_2 rotameric jump occurring within the microsecond regime cannot be used to reconcile the observed dispersion for Leucine groups.

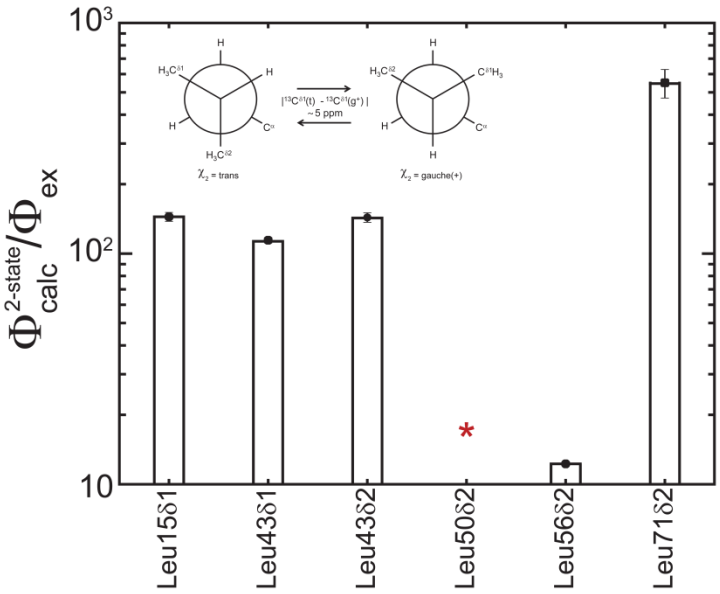

Figure 19 The use of a discrete two-state model greatly overestimates the experimental Φ_{ex} values for Leucine carbon nuclei in the delta position that experience conformational exchange. The populations p_t and p_{g+} was determined using the relation derived by Mulder and $\Delta\omega$ was taken to be 5 ppm because of the γ-gauche effect [143,144]. The inset in the plot presents the Newman projections for Leucine in the most common t or g^+ rotamer conformation.

A similar model using the δ chemical shift of Isoleucine residues has also been developed. Similar to the model above the correlation was established using DFT calculations that were cross-validated with measured three bond scalar coupling values between $^{13}C\delta1$ and $^{13}C\alpha$ resonances [145]. From which, the chemical shift value of Ileδ can be used to derive the predominate χ_2 rotameric state for Isoleucine which have been shown to exist in either t or g^- positions (< 2% in the g^+ rotamer) [145]. However, similar to the case for Leucine this model predicted that Ile23δ and Ile44δ only populate the t state and again cannot reconcile the experimental Φ_{ex} values for those methyl ^{13}C sites. Valines have to be considered differently as they have been shown to be able to populate three different χ_1 rotamers. We constructed an analytical three-state jump model (Materials and Methods) and used the populations derived from the RDCs and scalar couplings in conjunction with a DFT based hypersurface [146] for the

estimation of the chemical shifts for a given χ_1 rotamer in order to back calculate the conformational amplitudes (Table 5). This rendered a large overestimation in cases that include ideal and deviations from ideally staggered rotamers. It can be seen that discrete models that assume that the microsecond motion is due to the γ-gauche effect are not sufficient to understand the conformational amplitudes for the methyl moieties in free ubiquitin.

4.5 Conformational amplitudes report on Population Shuffling

We instead can propose a new model that doesn't assume rotamer jumps occurring on the microsecond timescale, but place the rotamer jumps within the pico- to nanosecond range which is the generally accepted timescale for rotameric changes [148,149]. Here, the modulation of the methyl nuclei, which undergo a concerted process with a lifetime of τ_{ex}, is also masking fast motions that are $<<\tau_{ex}$. Analytically this can be represented using the following derivation. Starting from the Φ_{ex} calculation that was based on the N-site jump model (Chapter 2):

$$\Phi_{ex} = \frac{1}{2N^2} \sum_{i,j=1}^{N} \left(\omega_i - \omega_j \right)^2 \qquad \text{(Eq - 4.5.1)}$$

each interconversion event is associated with a unique chemical shift value ($\omega_{i,j}$) which can be expanded to incorporate the effect of fast ($<< \tau_{ex}$) rotamer hopping.

$$\omega_{i,j} = p_{t(i,j)}\omega_t + p_{g+(i,j)}\omega_{g+} \qquad \text{(Eq - 4.5.2)}$$

where ω_t, ω_{g+}, p_t, p_{g+} is the chemical shift for the trans and gauche(+) rotamer, and population of a methyl carbon in the trans and gauche(+) state for conformer *i* or *j*, respectively. Inserting equation 4.5.2 back into equation 4.5.1 yields

$$\Phi_{ex} = \frac{1}{2N^2}\sum_{i,j=1}^{N}\left(p_{t,i}\omega_t + p_{g+,i}\omega_{g+} - \left(p_{t,j}\omega_t + p_{g+,j}\omega_{g+}\right)\right)^2 \qquad \text{(Eq - 4.5.3)}$$

After simplification it can be seen that the squared difference between the populated states can be expressed

$$\Phi_{ex} = \frac{1}{2N^2}\sum_{i,j=1}^{N}\left(\left(p_{t,i} - p_{t,j}\right)\omega_t + \left(p_{g+,i} - p_{g+,j}\right)\omega_{g+}\right)^2 \qquad \text{(Eq - 4.5.4).}$$

Since $p_{t,i} - p_{t,j} = p_{g+,j} - p_{g+,i} = \Delta p_{i,j}$, equation 4.5.4 can be recast as

$$\Phi_{ex} = \frac{1}{2N^2}\sum_{i,j=1}^{N}\left(\Delta p_{i,j}\omega_t - \Delta p_{i,j}\omega_{g+}\right)^2 \qquad \text{(Eq – 4.5.5)}$$

or more concisely as

$$\Phi_{ex} = \frac{\left(\omega_t - \omega_{g+}\right)^2}{2N^2}\sum_{i,j=1}^{N}\Delta p_{i,j}^{\,2} \qquad \text{(Eq - 4.5.6).}$$

Therefore the Φ_{ex} for ^{13}C methyl nuclei, are reduced by the relative differences in populations for each sampled ubiquitin conformer whose chemical shift changes due to the γ-gauche effect. We can now begin to envision how large Δp is for the methyl carbons reporting on the observed relaxation dispersion (Figure 17).

Starting from equation 4.5.6 which assumes equal populations in ubiquitin conformers we can see how the Φ_{ex} for methyl nuclei are reduced by the relative population differences between the trans and gauche(+) states for Leucine and Isoleucine amino acids. Let us assume a simple scenario in which we have two distinct ubiquitin conformers (N = 2), conformer A and B, equation 4.5.6 becomes

$$\Phi_{ex} = \frac{\left(\omega_t - \omega_{g+}\right)^2}{4} \Delta p_{t,A\to B}{}^2 \qquad \text{(Eq. - 4.5.7)}$$

in which $\Delta p_{t,A\to B}$ is the relative population difference for trans rotamer between conformer A and B. Changes in gauche(+) follow with the reverse of the trans rotamer

$$\Delta p_{t,A\to B} = p_{t,A} - p_{t,B} = p_{g+,B} - p_{g+,A} \qquad \text{(Eq. - 4.5.8)}$$

because for methyl bearing residues who populate two rotameric states (Leucine and Isoleucine) results in that any change from a trans rotamer in state A to B follows with a change in the gauche(+) rotamer in state B to A. Therefore, $\Delta p_{t,A\to B}$ can be rewritten as

$$\Delta p_{t,A\to B} = \frac{2}{\left(\omega_t - \omega_{g+}\right)} \sqrt{\Phi_{ex}} \qquad \text{(Eq. - 4.5 9).}$$

Valine residues are degenerate in their gauche(+) and gauche(-) populations because they can populate all rotamer groups therefore $\Delta p_{t,A\to B}$ can be expanded as

$$\begin{aligned} \Delta p_{t,A\to B} &= \left(p_{g+,B} + p_{g-,B}\right) - \left(p_{g+,A} + p_{g-,A}\right) \\ \Delta p_{t,A\to B} &= \left(p_{g+,B} - p_{g+,A}\right) + \left(p_{g-,B} - p_{g-,A}\right) \qquad \text{(Eq. - 4.5.10)} \\ \Delta p_{t,A\to B} &= \Delta p_{g+,B\to A} + \Delta p_{g-,B\to A} \end{aligned}$$

Thus, unique determination of gauche(+) and gauche(-) for Valine is precluded from the current analysis. Assuming the 5 ppm for $\left(\omega_t - \omega_{g+}\right)$ due to the γ-gauche effect the $\Delta p_{t,A\to B}$ for all methyl nuclei that reported RD are found to be between 0.042 ± 0.003 to 0.191 ± 0.001 (Table 3). The magnitude of this shuffling event indicates that population shuffling is not a marginal effect. It is also important to note that the observation of population shuffling amongst methyl nuclei does not necessarily reflect in the same residue displaying detectable chemical shift variances for the

backbone (Appendix Figure 8, i.e. Val5N, Leu15N, Ile44N, Leu56N, and Leu71). This may occur because the nitrogen backbone nuclei's chemical shift variance is too small or motions from surrounding nuclei function to negate a detectable variance. Interestingly, the magnitude of $\Delta p_{t,A\to B}$ also shows no correlation with the accessibility to the solvent of these methyl groups (Appendix Figure 9) in which residues whose methyl groups are completely buried have $\Delta p_{t,A\to B}$ values between 0.06 to 0.19.

Nuclei	$\Delta p_{t,A\to B}$
Val5γ1	0.061 ± 0.002
Leu15δ1	0.063 ± 0.001
Ile23δ	0.071 ± 0.002
Leu43δ1	0.084 ± 0.001
Leu43δ2	0.075 ± 0.002
Ile44δ	0.093 ± 0.002
Leu50δ2	0.146 ± 0.001
Leu56δ2	0.191 ± 0.001
Val70γ2	0.055 ± 0.002
Leu71δ2	0.042 ± 0.003

Table 3 The relative population differences between the trans rotamer from two different conformers derived from methyl carbon motional amplitudes that report on population shuffling. Calculated assuming a spectrometer field strength of 14.1 T.

4.6 MD corroborates population shuffling

Again, the above data does not support a model where rotameric interconversion occurs on the microsecond timescale. Instead, rotamer jumps occurring on a faster timescale (pico- to nanosecond) that experience different weighting between various ubiquitin conformations, or population shuffling, can account for the reduced Φ_{ex} values. In order examine this situation a collection of molecular dynamics (MD) simulations that were conducted with free ubiquitin and ubiquitin in complex with its various binding partners were considered [150].

MD simulations were taken from a recent report in which a 1 μs simulation of unbound ubiquitin was compared to eleven simulations of ubiquitin in complex with different interaction partners [150]. An observation was made in which some binding partners constrict the sampling space of ubiquitin as compared to free ubiquitin across the same two major modes of motion (pincer-mode) [11] that was identified from the previous RDC based ensembles. The overall equilibration time of the MD trajectories are not on the same length of τ_{ex}, but the MD trajectories which were conducted up to 100 nanoseconds, could be used to asses the rotamer states assumed by a given ubiquitin conformation within each spatially restrained complex.

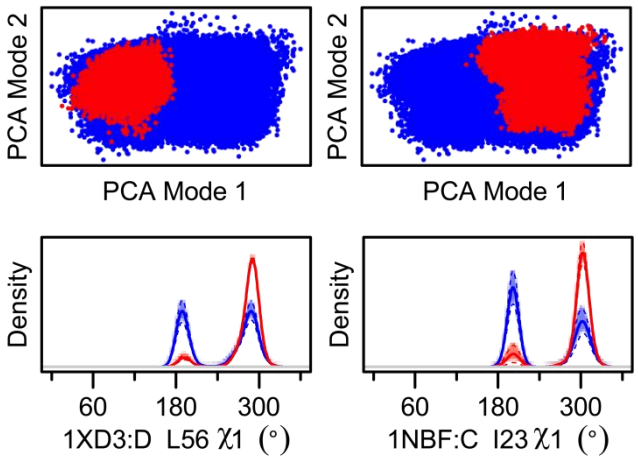

Figure 20 Comparison between free ubiquitin (blue points) and ubiquitin bound in complex (red points) show constriction in the sampled conformers. This restriction translates into large changes in the populations assumed by rotamer groups given by the plots displaying the density of a given χ_1 dihedral angle. Figure courtesy of Dr. Colin Smith (MPI-BPC, Dept. Theoretical and Computational Biophysics)

The determination of the RDC based structural ensembles highlighted that the largest structural variance occurs as a pincer like motion that involves the loop between first and second beta strands, the alpha helix and third beta strand, and the C-terminal tail of the helix in ubiquitin [11]. This is represented in PCA space (Figure 20) where the two largest modes, PCA 1 and 2 are plotted with respect to each other. Across these modes, free ubiquitin structures (Figure 20;

blue points) traverse between closed and open conformations. Two examples are given in Figure 20 in which a binding partner restricts the sampling of ubiquitin in either a closed (1NBF:C) [151] or open (1XD3:D) [152] conformational space. What can be surmised from this is that similar sites that display microsecond exchange also report on the largest redistribution in their rotamer populations (Figure 20; density plots between free ubiquitin (blue curve) and bound ubiquitin (red curve)). Given that rotamer redistribution occurs on a much faster timescale than the reorganization of the backbone and methyl nuclei a new model emerges in which depending on the fraction of openness that a ubiquitin conformer assumes, the backbone and methyl nuclei fluctuate in a concerted fashion that translates in a shuffling of the rotamer populations (Figure 21). Thus, the population shuffling between rotamers is predicated on the concerted microsecond backbone and side chain motion.

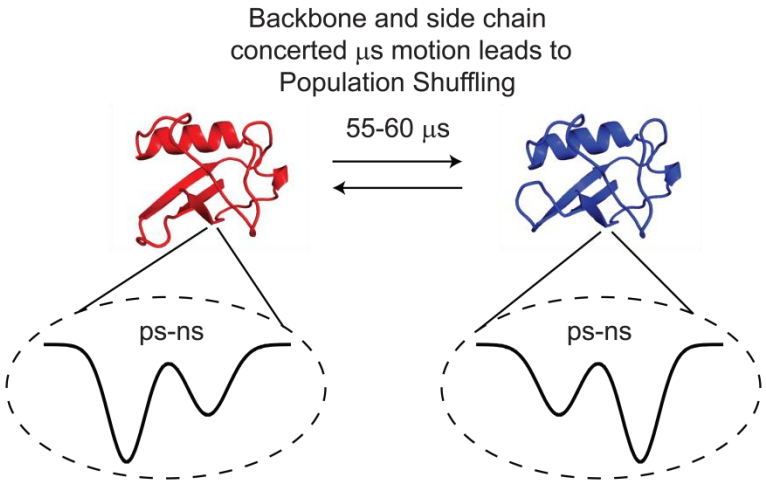

Figure 21 Proposed thermodynamic model. Structures are of free ubiquitin are from the two extremes between open (red) and closed (blue) free ubiquitin structures. Each ubiquitin conformer can contain different rotamer populations that occur on a timescale << τ_{ex}.

4.7 Conclusion

We have compiled the most extensive RD data set using large amplitude spin-lock field $R_{1\rho}$ for nuclei within ubiquitin (Figure 17 and Appendix Figure 7 and 8). In total thirty-one nuclei that span the sequence of ubiquitin display a common timescale of motion between 55-60 μs at 277 K (Figure 18). Importantly, this motion which coexists for both backbone and side chain nuclei has not been experimentally observed before. The use of high powered RD experiments also narrows the kinetic regime where this motion takes place. Namely, with the current time resolution of 10 μs and 4 μs for ^{13}C and ^{1}H, respectively, only a process between the 55-60 μs could be detected. Insights into the meaning of this side chain motion at this timescale could not be reconciled with discrete processes assuming rotamer interconversion in the microsecond regime (Figure 19). Rather comparison of various binding partners (Figure 20) [150] revealed that the major mode of motion that has been attributed to the same timescale for backbone interconversion causes the population shuffling of rotameric states depending on the degree of openness for a given ubiquitin conformer. Further work is being pursued in order to optimize the various modes from the PCA analysis that are cross-validated with the RD data in hopes of attaining mechanistic insight into the direct structural changes due to this concerted motion. Conformational sampling events within proteins have usually been limited to one set of nuclei [112,153]. However, the implications of this work can be far reaching where studying multiple types of nuclei can reveal a united behavior for the backbone and side chain moieties. However, the models required to describe the motion for each nuclei may be different. This work further extends our insight into the kinetics for conformational sampling in ubiquitin and potentially for other systems. The sampling of different conformers which for ubiquitin affects the binding to particular interaction partners appears to require a global concerted process that reorganizes the

backbone and side chain moieties differently. Additionally, the experimental and analytical tools laid out here should aid in establishing and/or quantitating this phenomenon for other systems of interest.

4.8 Materials and Methods

Methyl ^{13}C-$R_{1\rho}$ All were performed on a uniformly deuterated, selectively methyl labeled $^{13}CHD_2$ sample [137] in which only δ-Ile, δ1,δ2-Leu, and γ1,γ2-Val were labeled.. Experiments were collected at 277 K on a Bruker Avance I spectrometer operating at ^{1}H Larmor frequency of 600 MHz with samples that contained 50 mM phosphate and 100 mM NaCl at a pH of 6.5. ^{13}C field strengths were calibrated by measuring $^{1}J_{eff}^{CH}$ with a [^{1}H,^{13}C]-HSQC in which ^{13}C-CW decoupling was applied off-resonance during acquisition ($t_{2,max}$ = 142 ms). The larger errors in tan(θ) in Figure 14 (as compared to Figure 6) are due to the use of a Gaussian window function that remove distortions from truncation artifacts that effect the determination of $^{1}J_{eff}^{CH}$. The heavy background deuteration ($^{13}CHD_2$) greatly simplifies the experimental approach as this provides a simple AX spin system to probe methyl ^{13}C nuclei. The pulse schematic was adapted from Brath et al. [139], but was modified to handle the large ^{13}C ν_1 amplitudes as given in Figure 22. Additionally, neighboring carbons to the labeled methyl carbons are NMR silent so Hartmann-Hahn conditions are negligible allowing for a simple pulse scheme to be implemented and cross-correlated dipolar relaxation between the methyl carbon and its attached protons can be removed [139]. The pulse code in Figure 22 is appended to this dissertation under the section called Pulse Programs.

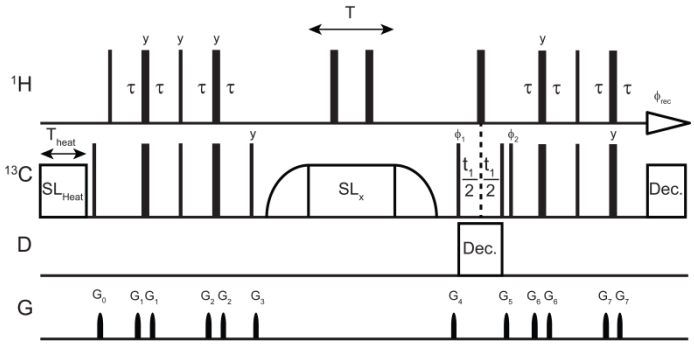

Figure 22 Pulse schematic for the methyl ^{13}C-$R_{1\rho}$ experiments. All ^{1}H and ^{13}C 90° and 180° are rectangular pulses are represented by narrow and wide black bars, respectively. All rectangular pulses were applied with field strengths of 37.8 and 25 kHz for ^{1}H and ^{13}C, respectively. The delay τ during the INEPT blocks was set to $1/4J_{CH}$ = 1.8 ms. The shaped pulses before and after the spin-lock period (T) are adiabatic ramping pulses whose maximum amplitude reached the employed ν_1 and were applied for a duration of 4 ms. Suppression of cross-correlated dipole-dipole/CSA relaxation was done via the application of two ^{1}H 180° pulses at T/4 and 3T/4 [133]. Temperature compensation was achieved by applying the maximum spin-lock amplitude (SL_{HEAT}) at a frequency of 60 kHz off-resonance on the ^{13}C channel during the recycle delay for a period of T_{HEAT}. T_{HEAT} was calculated using the following relation:

$$T_{HEAT} = \left(\frac{T_d + T}{T_d + T_{MAX}} \right) T_{MAX} - \left(\frac{\nu_{SL_x}^{RF}}{\nu_{SL_x}^{MAX}} \right)^2 T$$ in which T_{MAX}, T_d $\nu_{SL_x}^{RF}$, $\nu_{SL_x}^{MAX}$ were the maximum length a spin-lock period was applied, the recycle delay, a given ν_1 between 0.5 and 16 kHz, and the maximum ν_1 set at 16 kHz. Since, the carbon spectral range for the methyl range is narrow, with a sweep width of 2.7 kHz, WALTZ16 decoupling with a field strength of 2.1 kHz was applied during acquisition [136]. Decoupling on deuterium was also applied with the WALTZ16 scheme with a field strength of 1.6 kHz in order to remove ^{13}C-D splitting in the indirect dimension. A phase scheme of ϕ_1 = (x, -x), ϕ_2 = (y, y, -y -y), and ϕ_{rec} = (x, -x, -x, x), and x phase unless otherwise indicated. Gradients with strengths (length) of G_0 = 46 G/cm (0.3 ms), G_1 = 25 G/cm (0.75 ms), G_2 = 35 G/cm (0.8 ms), G_3 = 16 G/cm (0.75 ms), G_4 = 39 G/cm (1.0 ms), G_5 = 30 G/cm (1.0 ms), G_6 = 15 G/cm (0.75 ms), G_7 = 8 G/cm (0.75 ms) were used. Frequency discrimination was achieved using the States-TPPI scheme [154].

Initially, the scheme was tested using variable spin-lock lengths (T) in order to determine if monoexponential decay curves are observed thereby testing the assumption of a simple AX spin system. An example decay curve for Val5γ2 is given in Figure 23.

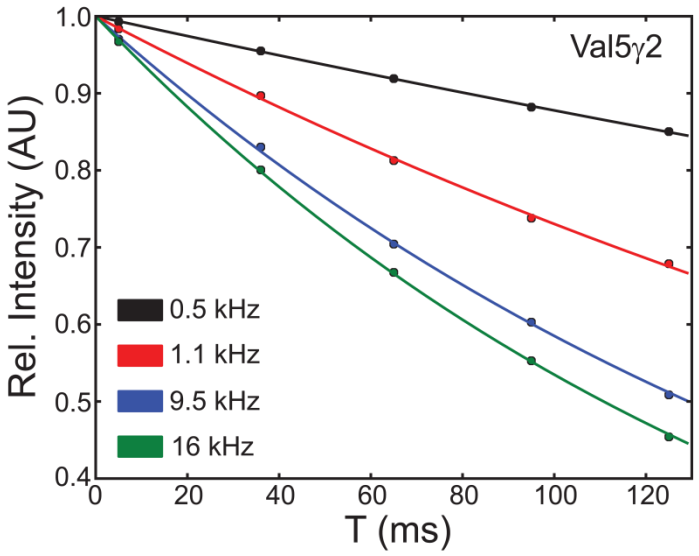

Figure 23 Example of a characteristic exponential decay curves from the methyl-$R_{1\rho}$ experiment used here. For each utilized ν_1 value, designated by their different colors, their relaxation time (T) was sampled between 5 and 125 ms. Solid lines indicates fits to the model $I(t) = I_0 \exp(-R_{1\rho}T)$ in which I_0 is the intensity at T = 0, and $R_{1\rho}$ is the relaxation rate.

The preservation of monoexponential decay behavior (Figure 23) greatly expedited the measurements and allowed for a two point sampling scheme to be applied in which for a given offset (Ω) and ν_1 value a decay rate was recorded with using relaxation times of 5 and 125 ms. The intensities ($I_{\nu_1,\Omega}(T)$) were then converted to $R_{1\rho}$ using $R_{1\rho} = \frac{1}{\Delta T} \ln \frac{I_{\nu_1,\Omega}(5\ ms)}{I_{\nu_1,\Omega}(125\ ms)}$ (ΔT = 0.120 ms). In total, 53 different combinations of Ω and ν_1 were acquired. Ω and ν_1 were varied between ± 10 ppm from the ^{13}C transmitter frequency, and between 0.5 and 16 kHz, respectively. Each spectrum was recorded with 128 ($t_{1,max}$ = 42.4 ms) and 1024 ($t_{2,max}$ = 142.5 ms) complex points in the indirect and direct dimension, respectively with four transients per point. If a given data point violated the adiabatic alignment condition given by reference [139] it was removed from further analysis. Additionally, in order to minimize the effect of R_1 only $R_{1\rho}$ values whose $\sin(\theta)$ were greater then 0.96 was accepted. This maintains the R_1 contribution to be less than 8%

to the observed $R_{1\rho}$ rate. This rendered a minimum of twenty points per dispersion curve. All spectra were processed and analyzed using the NMRPipe software package [121].

Determination of Exchange Parameters Initially, all 33 methyl resonances were individually fit to a two parameter (R_1, $R_{2,0}$) model that does not predict any exchange and a four parameter model (R_1, $R_{2,0}$, Φ_{ex}, τ_{ex}) that includes the effect of exchange. A residue was determined to have a statistically significant contribution of exchange based on a F-test with a confidence interval of 99% [155]. All fitted parameters are reported in Appendix Table 2. Analysis of individual fits yielded R_1 values of approximately 0 s^{-1} indicating that the contribution to $R_{1\rho}$ from longitudinal relaxation is negligible. In addition, fits of dispersion data to a model assuming complete on-resonance dependence of exchange did not change the fitted parameters. A total of ten ^{13}C methyl nuclei were retained totaling 209 data points (N).

As was presented in Figure 18 the clustering of exchange lifetimes permitted a global fitting of all ^{13}C methyl and ^{15}N backbone data. The global minimizations assumed that a single τ_{ex} value could be used to describe each nuclei. The starting point for all local parameters was set from the individual fits. At which point τ_{ex} was varied twenty times and all parameters were subsequently minimized together. The minimization which gave the lowest target function value, defined by a χ^2 function, was taken as the best solution. This procedure was done for the ^{13}C methyl (parameters = 31, N = 209) and ^{15}N backbone data (parameters = 21, N = 258) alone and with all RD data together (parameters = 51, N = 467) producing reduced χ^2 values of 1.82, 2.01, 1.76. Generally, a reduced χ^2 statistic should be around 1. In order to ascertain if the optimization proceeded to the wrong minimum, the error (weighting in the χ^2 function) for each point was increased in different gradients (between 2 and 10%) (effectively decreasing the barriers in the minimization landscape) and all optimization procedures were repeated. This

produced reduced χ^2 between 0.8 and 1.1 for all optimizations, but no changes, within error, were observed for the extracted parameters indicating the initial fits were in the correct minimum. Errors were evaluated by Monte-Carlo simulations with 1000 and 100 iterations for the individual and global optimizations, respectively. From here, all relaxation dispersion data was reformulated and is reported as $R_{2,eff}^{*} = \frac{R_{1\rho}}{\sin^2(\theta)} - R_1 \cot^2(\theta) = R_{2,0}^{13C} + \frac{\Phi_{ex}\tau_{ex}}{1+(\omega_{eff}\tau_{ex})^2}$. All fitting routines were implemented in Python using the SciPy libraries. Errors in $R_{1\rho}$ were derived either from the root mean square deviation in intensities from duplicate spectra, or from the residual error during the dispersion curve fitting and subsequently propagated when $R_{1\rho}$ was reported as $R_{2,eff}^{*}$.

Rotameric states Leucine methyl groups from the δ position chemical shifts Using the semi-quantitative models derived from previous publications [144-146] we can calculate the expected Φ_{ex} ($\Phi_{calc}^{2-state}$) if a discrete rotameric switch is the source of the observed dispersion.

Residue	p_t [a]	p_{g+}	$\Phi_{calc}^{2-state}$ (x10^6 rad^{2}s^{-2})[b]	δ1 CSV (ppm)[c]	δ2 CSV (ppm)[c]
Leu15δ1	0.82	0.18	3.25	23.309	20.068
Leu43δ1	0.72	0.28	4.55	22.594	20.414
Leu43δ2	0.72	0.28	4.55	22.594	20.414
Leu50δ2	1.00	0.00	0.00	22.143	15.6
Leu56δ2	0.87	0.13	2.50	22.947	19.227
Leu71δ2	0.59	0.41	5.45	21.094	20.233

Table 4 $\Phi_{calc}^{2-state}$ for Leucine residues that showed a contribution of exchange from the methyl ^{13}C-$R_{1\rho}$ experiments.

[a] Calculated using the relation [144] $^{13}C(\delta 1) - {}^{13}C(\delta 2) = -5 + 10\,p_t$

[b] Calculated assuming a spectrometer with a ^{1}H Larmor frequency of 600 MHz

[c] Chemical shift value (CSV) for Leucine methyl resonances at 277 K.

Rotameric states Isoleucine methyl groups from the δ position chemical shift The δ position from Ile23 and Ile44 showed a contribution of exchange from the above experiments. Hansen et

al. have derived a simple relationship for Isoleucine residues, which predominately populate the g^- and t rotamer states, that in which the p_{g-} can be deduced solely from the Ileδ chemical shift value [145]. The p_{g-} can be calculated as (14.8 ppm – $^{13}C(\delta)$)/5.5 ppm when the chemical shift for the Ileδ position is between 9.3 and 14.8 ppm. When the chemical shift value is less than 9.3 ppm or greater than 14.8 ppm p_{g-} takes the value of one and zero, respectively. Again we can use their relationship to check if the detected microsecond motion is due to a discrete two-state rotamer jump. However, at 277 K the chemical shift for Ile23δ and Ile44δ is 5.379 and 8.718 ppm, respectively. Therefore, these methyl groups are predicted to always be in the g- χ_2 state and again a discrete process cannot account for the exchange contribution for these residues. The authors report that the error in this estimation is on the order 0.2 for p_{g-} [145].

Expected Φ_{ex} for 3-state rotamer jumps of Valine For Valine three different rotameric states can exist in solution, the trans (t), gauche$^+$ (g_+), and gauche$^-$ (g_-). We are interested in distinguishing that the observed experimental conformational amplitudes for valine residues that show relaxation dispersion are not from discrete three-state rotameric jumps. The scheme will also serve for the distinction where any discrete three-state rotamer jump is possible. The kinetic scheme can be modeled as,

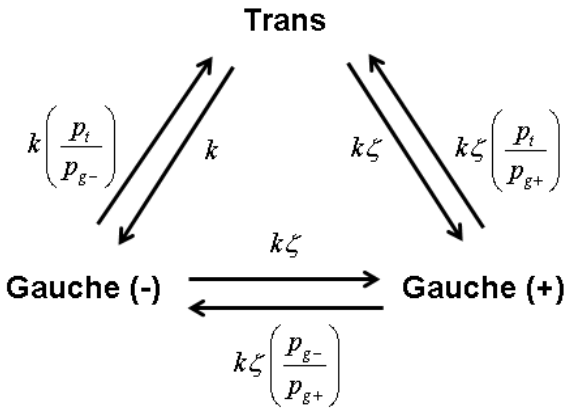

where *k* is the overall transition rate, and ζ is the term used to scale whether a step from one to the other is kinetically faster or slower than the other steps. The kinetic transition matrix (K) is

$$KP = \begin{pmatrix} -k(1+\zeta) & k\left(\frac{p_t}{p_{g-}}\right) & k\zeta\left(\frac{p_t}{p_{g+}}\right) \\ k & -k\left(\frac{p_t}{p_{g-}}+\zeta\right) & k\zeta\left(\frac{p_{g-}}{p_{g+}}\right) \\ k\zeta & k\zeta & -k\zeta\left(\frac{p_t+p_{g-}}{p_{g+}}\right) \end{pmatrix} \begin{pmatrix} p_t \\ p_{g-} \\ p_{g+} \end{pmatrix} \qquad \text{(Eq - 4.8.1)}$$

and whose eigenvalues (λ_{1-3}) are 0, $-k\zeta/p_{g+}$, and $-k(p_t/p_{g-} + (1+\zeta))$, respectively. The following steps in the derivation are similar to what was introduced in Chapter 2. The conditional probabilities can be evaluated as

$$P(m,t \mid l,0) = \sum_{n}^{3} \Lambda_{mn}\Lambda_{nl}^{-1} e^{\lambda_n t} \qquad \text{(Eq - 4.8.2)}$$

in which Λ is a matrix of eigenvectors and Λ^{-1} its inverse of the kinetic matrix, K. The a priori conditional probabilities are known from the initial conditions where

$P_a = \lim_{t\to\infty} P(a,t \mid b,0) \quad a,b \in [1,3]$. The correlation function is then given by

$$C(t) = \langle \omega(0)\omega(t) \rangle = \sum_{l,m=1}^{3} P_l \left(\sum_{n}^{3} \Lambda_{mn}\Lambda_{nl}^{-1} e^{\lambda_n t} \right) \omega_l\, \omega_m \qquad \text{(Eq - 4.8.3).}$$

Evaluation of 4.8.3 yields

$$\left(p_{g^-}\omega_{g^-} + p_{g^+}\omega_{g^+} + p_t\omega_t \right)^2 + \frac{p_{g^-}p_t\Delta\omega_{g^--t}^2}{p_{g^-}+p_t} e^{\lambda_2 t} + \frac{p_{g^+}\left(p_{g^-}\Delta\omega_{g^--g^+} + p_t\Delta\omega_{t-g^+} \right)}{p_{g^-}+p_t} e^{\lambda_3 t} \qquad \text{(Eq - 4.8.4)}$$

The first term corresponds to the square of the average chemical shift and is time invariant and does not cause relaxation. After Fourier transform we retain only the second and third terms from 4.8.4 which gives

$$R_{ex} = \frac{p_{g^-} p_t \Delta\omega^2_{g^- - t}}{p_{g^-} + p_t} \cdot \frac{\tau_2}{1 + (\gamma B_1 \tau_2)^2} + \frac{p_{g^+}\left(p_{g^-}\Delta\omega_{g^- - g^+} + p_t \Delta\omega_{t - g^+}\right)}{p_{g^-} + p_t} \cdot \frac{\tau_3}{1 + (\gamma B_1 \tau_3)^2} \qquad \text{(Eq - 4.8.5)}$$

In equation 4.8.5, τ_2 and τ_3 correspond to $1/\lambda_2$ and $1/\lambda_3$, γB_1 is the employed field strength for a given $R_{1\rho}$ experiment, p_{t,g^-,g^+} correspond to the populations in the trans, gauche$^-$, and gauche$^+$ conformations, and the term preceding the Lorentzians are the Φ values. From the kinetic matrix, ζ can set to match any desired exchange lifetime, and therefore does not affect the calculation of the expected conformational amplitudes. However, the least negative eigenvalue, whose lifetime is given by τ_3, will only contribute to observed dispersion and its prefactor will be the expected Φ_{ex}. We can now evaluate expected Φ_{ex} values for three-state discrete rotamer jumps using RDC and scalar coupling derived populations [30,98,146,156] and with chemical shifts derived from a DFT based hypersurface [146]. In Table S1, all calculated (Φ_{calc}) values still exceed the measured Φex for V5γ1 and V70γ2 indicating that discrete rotameric jumps cannot account for the observed dispersion.

Residue	Φ_{calc} populations from Ref.[c] ($x10^3$ rad^2s^{-2})	$\pm 30^o$ deviation from ideal geometry[a,b,c] ($x10^3$ rad^2s^{-2})	Φ_{calc}. populations from Ref.[d] ($x10^3$ rad^2s^{-2})	$\pm 30^o$ deviation from ideal geometry[a,b,d] ($x10^3$ rad^2s^{-2})	Φ_{ex} Experimental ($x10^3$ rad^2s^{-2})
Val5γ1	164	386-132	763	1082-857	20.6 ± 1.2
Val70γ2	348	484-64	210	1039-91	16.7 ± 1.1

Table 5 Comparison of calculated and experimental conformational amplitudes for observed valines.

[a] All values were calculated assuming a ^{1}H Larmor frequency of 600 MHz.

[b] The range represents the Φ_{calc} calculated with chemical shifts that deviate by $\pm 30^o$ from ideal geometry.

[c] Populations from Chou et al. [156]

[d] Populations from Fares et al. [146]

Enhanced accuracy for CT-CPMG experiments using $R_{1\rho}$

5.1 CT-CPMG as an RD type experiment

Nuclear magnetic resonance (NMR) is a key spectroscopic tool for investigating the different states that proteins can exist in. A particular unique phenomenon inherent to NMR is the ability to explore exchange. The two RD techniques that largely appear within the NMR community are the $R_{1\rho}$ [29,66] and Carr-Purcell-Meiboom-Gill (CPMG) [30,31] experiments. The two approaches contrast in the execution of these experiments, $R_{1\rho}$ through the application of spin-lock fields and CPMG the modulation of inter-pulse delays between 180° refocusing pulses. This ultimately leads to a different dependence in the description of exchange between the two techniques [89,90]. Although the fundamentals, kinetics (k_{ex}; $k_{ex} = 1/\tau_{ex}$), difference in chemical shifts of the populated states ($\Delta\omega$), and the intrinsic relaxation rates, that underlie these approaches are identical. Ultimately, both function by altering the degree of refocusing for a given populated magnetization coherence by probing an effective transverse relaxation rate ($R_{2,eff}$).

The implementation of CPMG sequences have received more attention as compared to the $R_{1\rho}$ approach, in which sparsely populated intermediates have been linked to enzymatic catalysis [67,76,77], folding intermediates [68,157], and molecular interactions [69,74]. A severe drawback with the use of CPMG sequences as an RD experiment was that the applied frequency (ν_{CPMG}) must be carefully considered to prevent generation of antiphase magnetization caused by scalar couplings and thus, only either a very short or low multiples of the scalar coupling (τ_{CPMG}

= $1/(4\nu_{CPMG})$ = n/J) could be applied as the inter-pulse delay between 180° pulses [158,159]. This drawback was alleviated by the seminal paper from Loria et al. by which contributions from inphase and antiphase magnetization were averaged ($R_{2,0}^{CT-CPMG}$) to $R_{2,0}$ [79]. This also allowed for RD experiments to be carried out in a constant-time (CT-CPMG) fashion, which dramatically reduces the measurement time and purports a larger collection of $R_{2,eff}$ rates at various ν_{CPMG} values [91,124,160]. For the RD experiments using the CT-CPMG sequence, the applied frequency within a given constant-time block is varied in order to measure the change in $R_{2,eff}$ as a function of ν_{CPMG}. For increasing ν_{CPMG}, populated magnetization coherences become more completely refocused and $R_{2,eff}$ decreases to $R_{2,0}^{CT-CPMG}$, or the point at which all exchange has been removed. However, typical ν_{CPMG} values for ^{15}N nuclei are limited to 1 kHz [91,138]. This constraint results in the inability to resolve fast kinetic processes since the exchange contribution that remains is not sampled and the overall exchange contribution ($R_{ex} = R_{2,eff}(\nu_{CPMG} \to 0) - R_{2,eff}(\nu_{CPMG} \to \infty)$) will be underestimated. Here, it is shown that the extraction of kinetic information by CT-CPMG can be hindered when $R_{2,0}^{CT-CPMG}$ is not known *a priori* and included in the analysis, but can be mitigated by using large amplitude transverse-rotating frame spin-lock fields (high powered ν_1 procedures described in Chapter 3) that are applied to same observables that are tracked during the CT-CPMG experiments. The proposed experimental procedure outlined below is also a critical aspect since $R_{2,0}^{CT-CPMG}$ is not the same as what is obtained from standard ^{15}N relaxation measurements [28,91] (*vide infra*).

5.2 Dramatic increases in accuracy and precision of k_{ex} if $R_{2,0}^{CT-CPMG}$ is known

In order to monitor the effects $R_{2,0}^{CT-CPMG}$ has on fitting CT-CPMG data , Monte-Carlo simulations were employed on synthetic data that were generated with various values of k_{ex} using a simple two-state exchange scenario, $A \underset{k_{-1}}{\overset{k_1}{\rightleftharpoons}} B$ where $k_1 + k_{-1} = k_{ex}$, (see Materials and Methods; Figure 24) that assumed a minor population of 0.05 and a $\Delta\omega$ of 2 ppm. These synthetic datasets were fitted to models described by the Bloch-McConnell equations [161] (BM; Figure 24A, B), and the Luz-Meiboom equation [162] (LM; Figure 24C, D), with $R_{2,0}^{CT-CPMG}$ either as a parameter to be fitted (green circle in Figure 24) or as a known parameter (blue circle in Figure 24). Details on the BM and LM models can be found in the Materials and Methods section of this chapter. The timescale of exchange is defined by the not only k_{ex}, but also the $\Delta\omega$ of the process. Therefore, demarcation between slow, intermediate, or fast exchange is defined by the ratio $k_{ex}/\Delta\omega$ (slow; $k_{ex}/\Delta\omega < 1$, intermediate; $k_{ex}/\Delta\omega \sim 1$, and fast; $k_{ex}/\Delta\omega > 1$) [158]. These definitions are used below.

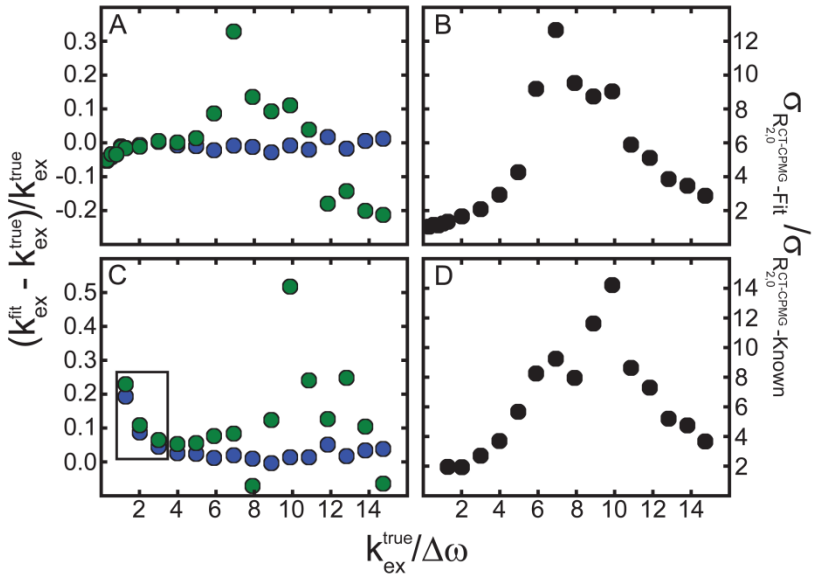

Figure 24 (A, C) Comparison of the errors in k_{ex}^{fit} as a fraction of k_{ex}^{true}. Synthetic CT-CPMG data were generated up to a maximum ν_{CPMG} of 1 kHz (details in Materials and Methods) and fitted to the Bloch-McConnell (BM; A and B) and the Luz-Meiboom (LM; C and D) equations with $R_{2,0}^{CT-CPMG}$ either as a fitting parameter (green circle in A and C) or a known parameter (blue circle in A and C). (B, D) The ratio between uncertainties in the determination of k_{ex}^{fit}, defined as the standard deviation from Monte-Carlo runs using $R_{2,0}^{CT-CPMG}$ as a fitting parameter ($\sigma_{R_{2,0}^{CT-CPMG}-Fit}$) and as a known parameter ($\sigma_{R_{2,0}^{CT-CPMG}-Known}$). Overestimation of k_{ex}^{fit} in C for $1 \leq k_{ex}^{true}/\Delta\omega < \sim 3$ due to the limitation of LM equation (Appendix Figure 10) are boxed. Additional details on the models used here can be found in the Materials and Methods section titled under "Fitting Models".

It is apparent from Figure 24 that the fractional error in the fitted exchange rate (k_{ex}^{fit}) relative to the true exchange rate (k_{ex}^{true} is the k_{ex} value used as input for the generation of the synthetic sets) were as large as ~30 and 50 % (in particular, when the exchange process is fast; $k_{ex}^{true}/\Delta\omega > \sim 4$) for the BM and LM models, respectively, when $R_{2,0}^{CT-CPMG}$ remained as a variable (green circles Figure 24). In contrast, when $R_{2,0}^{CT-CPMG}$ was included as a known parameter during the minimization of a given synthetic set, the error in k_{ex}^{fit} does not exceed more than 5 % over all ratios of $k_{ex}^{true}/\Delta\omega$ in the simulations. The $R_{2,0}^{CT-CPMG}$ included in this analysis can be obtained

from a different experiment, as suggested in this section. Further, the uncertainties of fitted k_{ex} (σ) were reduced by as much as 12-14 fold when $R_{2,0}^{CT-CPMG}$ is known compared to the situation where $R_{2,0}^{CT-CPMG}$ has to be fitted (Figure 24B, D). The pseudo Lorentzian profile from the reduction in $\sigma_{R_{2,0}^{CT-CPMG}-Known}$ beyond $k_{ex}^{true}/\Delta\omega > 8$ (Fig 24B, D) is due to the effect that as k_{ex}^{true} increases the overall contribution of exchange decreases for those synthetic sets (Appendix Figure 10) and introduces larger errors in k_{ex}^{fit}. The simulations here were conducted with dispersion curves created at two different spectrometer field strengths as this is frequently done to increase the precision in the extracted parameters [163]. However, even with measurements conducted at a single field using a known $R_{2,0}^{CT-CPMG}$ during the fitting procedure still constitutes an advantage over leaving $R_{2,0}^{CT-CPMG}$ as an adjustable parameter (Appendix Figure 11). Thus, it is clearly beneficial to directly measure $R_{2,0}^{CT-CPMG}$ and include this value as a known parameter for extracting accurate kinetic information from dispersion profiles.

5.3 Veracious $R_{2,0}^{CT-CPMG}$ for CT-CPMG by HEROINE

In principle, the ν_{CPMG} used during a CT-CPMG experiment must be much larger than k_{ex}, to quench the contribution from exchange in the measured $R_{2,eff}$ which then becomes $R_{2,0}^{CT-CPMG}$. However, the typical upper value of ν_{CPMG} that is utilized on conventional spectrometers, approximately 1 kHz for ^{15}N, is not large enough to suppress exchange processes faster than ~150 μs ($\tau_{ex} \approx 1/4\sqrt{3}\nu_{CPMG}$) [90,91]. What can be done to overcome this hindrance is to apply the high power transverse rotating frame relaxation experiments [129] that were demonstrated and validated for ^{15}N nuclei in Chapter 3. This can be used as an alternative for quenching exchange processes (Figure 10) since ν_1 values ($\nu_1 = \nu_{SL}$) in $R_{1\rho}$ experiments is larger than ν_{CPMG}. With ^{15}N

spin-lock fields up to 6 kHz yields a $R_{2,eff}$ that is free from an exchange process slower than 25 μs. Thus, we turn to develop the heteronuclear rotating-frame invasive nuclear exchange (HEROINE) experiment for measuring $R_{2,eff}$, utilizing the highest possible spin-lock field strength. The measured rate from HEROINE is included as currently the best measure of $R_{2,0}^{CT-CPMG}$ in order to improve the accuracy of model fitting data acquired from CT-CPMG experiments.

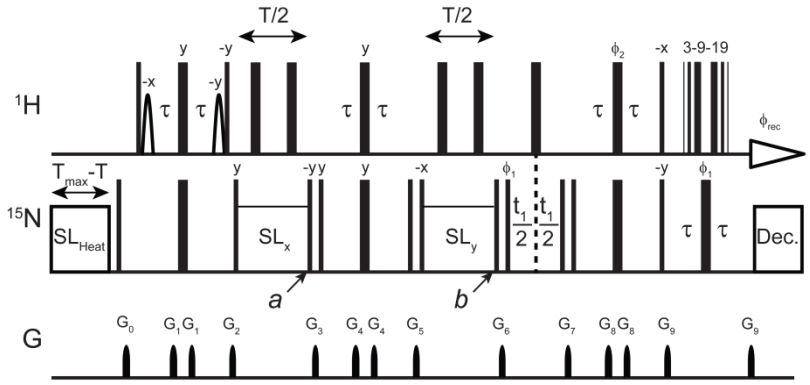

Figure 25 Pulse scheme of the HEROINE experiment for measuring $R_{2,eff}$ utilizing a high spin-lock field strength, which can be used as $R_{2,0}^{CT-CPMG}$ for improving the accuracy of model fitting CPMG data. All ^{1}H and ^{15}N 90° and 180° rectangular pulses are represented by narrow and wide black bars, respectively, and were applied at 35.7 kHz and 10.6 kHz for ^{1}H and ^{15}N, respectively. The shaped ^{1}H 90° water selective pulses within the first INEPT block represent Gaussian shaped pulses and were applied for a duration of 1.5 ms in order to maintain water magnetization along the +z axis before the spin-lock period. Analogous to the relaxation compensated constant time CPMG schemes [79,164], the relaxation delay (T) is split into two sections where $2H_zN_x$ and N_y coherences are each measured for a length of T/2 during the SL_x and SL_y spin-lock blocks, respectively. The field strength of the implemented SL field can be set to any value; here we used a large amplitude (ν_{SL} = 6 kHz) to ensure that resonances which are on-resonance had exchange processes with lifetimes up to 25 μs quenched. Only resonances that are on-resonance are considered for further analysis. Therefore, a hard 90° ^{15}N pulse suffices to place a target resonance within the transverse plane before the start of the spin-lock. Cross correlated relaxation between chemical shift anisotropy and dipolar coupling was suppressed by applying ^{1}H 180° rectangular pulses at T/8 and 3T/8 during a given SL period [133]. To ensure equal power deposition during all values of T, a linear temperature compensation scheme ($\nu_{SLheat} = \nu_{SL}$) was used in which SL_{Heat} is the difference between the longest relaxation delay (T_{max}) and the length

of a given total SL period (T). SL_{Heat} was applied at 28.4 kHz upfield from the transmitter frequency. Before purging the ^{15}N Boltzmann polarization, the ^{15}N transmitter frequency was placed back on-resonance. During acquisition ^{15}N decoupling was done with a WALTZ16 scheme at field strength of 2 kHz [136]. The delay τ was set to $1/4J_{NH}$ (2.7 ms). Frequency discrimination in the indirect dimension was achieved by States-TPPI quadrature detection [154] utilizing the following phase scheme: ϕ_1 = (x, -x, -x, x), ϕ_2 = (y, y, -y, -y), and ϕ_{rec} = (-x, x, x, -x). Phases for all pulses are x phase unless otherwise indicated. Gradients with strengths (length) of G_0 = 42 G/cm (1 ms), G_1 = 10 G/cm (0.5 ms), G_2 = 28 G/cm (0.5 ms), G_3 = 38 G/cm (0.5 ms), G_4 = 12 G/cm (0.5 ms), G_5 = 37 G/cm (0.5 ms), G_6 = 16 G/cm (0.5 ms), G_7 = 24 G/cm (0.5 ms), G_8 = 20 G/cm (0.5 ms), and G_9 = 35 G/cm (0.5 ms) were used. The pulse code for HEROINE can be found in the Pulse Programs section.

The pulse scheme of HEROINE (Figure 25) monitors the same coherence as in constant-time CT-CPMG experiments, namely averaged inphase and antiphase (1/2 (N_y + 2 H_zN_x)) magnetization. Using INEPT, antiphase coherence ($2H_zN_x$) is generated and its relaxation rate ($R_{1\rho}^{anti}$) is monitored by a spin-lock (SL_x) with a time of T/2 ($I_a \propto \exp\left(-\frac{1}{2}R_{1\rho}^{anti}T\right)$). After point *a* in Figure 25, the antiphase coherence is transferred to an inphase coherence (N_y), using a relaxation compensated element and the relaxation rate of the inphase ($R_{1\rho}^{in}$) is monitored by a spin-lock (SL_y) for a time of T/2. Thus, at time point *b* in Figure 25, the intensity is proportional to $I_b \propto \exp\left(-\frac{1}{2}R_{1\rho}^{anti}T\right)\exp\left(-\frac{1}{2}R_{1\rho}^{in}T\right) = \exp\left(-\frac{1}{2}\left(R_{1\rho}^{anti}+R_{1\rho}^{in}\right)T\right)$, compared with CT-CPMG ($\exp\left(-\frac{1}{2}\left(R_{2,eff}^{anti}+R_{2,eff}^{in}\right)T\right) = \exp\left(-R_{2,eff}T\right)$). Since we are using spin-lock fields the exponential function takes the form $I(T) = I_0\exp\left(-R_{1\rho,eff}T\right)$, where $R_{1\rho,eff}$ is $\exp\left(-\frac{1}{2}\left(R_{1\rho}^{anti}+R_{1\rho}^{in}\right)T\right)$, and retains a rate that is in the form of a conventional $R_{1\rho}$ experiment:

$R_{1\rho,eff} = R_1\cos^2(\theta) + \left(R_{2,0}^{\nu SL\to\infty} + R_{1\rho}^{ex}\right)\sin^2(\theta)$ where R_1, $R_{2,0}^{\nu SL\to\infty}$, $R_{1\rho}^{ex}$, and θ are the longitudinal

relaxation rate, the intrinsic transverse rotating-frame relaxation rate, contribution from exchange, and the tilt angle, respectively. Here, $R_{2,0}^{\nu SL\to\infty}$ is again the average between inphase and antiphase relaxation rates measured by transverse rotating-frame experiments. For the CT-CPMG measured rate, $R_{2,eff}$ can be expressed as $R_{2,eff} = R_{2,0}^{CT-CPMG} + R_{ex}^{CT-CPMG}$. For the on-resonance ($\theta=90^o$) HEROINE experiment, R_1 does not play a role and the difference in measured relaxation rates between the HEROINE and the CT-CPMG experiment is $R_{1\rho}^{ex}$ and $R_{ex}^{CT-CPMG}$. If ν_{SL} and ν_{CPMG} in the HEROINE and CT-CPMG experiments, respectively, are sufficiently large to suppress the contribution of exchange on the relaxation rate, namely that there is no difference $R_{1\rho}^{ex}$ and $R_{ex}^{CT-CPMG}$, the same intrinsic transverse relaxation rate will be achieved. However, the maximum attenuation of a given exchange event monitored during a CT-CPMG experiment is often not sufficient, given the relatively small refocusing frequency [91], and may introduce an error in the extraction of kinetic information as described earlier (Figure 24). In contrast, using the recent development of applying a high spin-lock field strength up to 6 kHz an exchange process slower than 25 μs can be quenched in HEROINE and a more veracious $R_{2,0}^{CT-CPMG}$ can be obtained (Chapter 3) [129]. For the off-resonance ($\theta<90°$) situation, complications caused by a contribution from R_1 due to the tilt angle will arise. However, in the current implementation (using a 6 kHz spin-lock field strength), only 2.2% contribution of R_1 is expected, even with an offset of 15 ppm on a 600 MHz spectrometer. Here, HEROINE was repeated at three different offsets and observed that R_1 had a negligible contribution (< 0.1%) to $R_{1\rho}$.

In order to validate whether HEROINE results in the same $R_{2,eff}$ observed in CT-CPMG, we performed HEROINE and CT-CPMG measurements at 298 K on ^{15}N labeled ubiquitin, since exchange slower than 25 μs would not contribute to the measurement of ^{15}N relaxation

(Appendix Figure 1). In Figure 26, typical HEROINE measurements for Ile23 and Lys39 are displayed showing that a monoexponential profile is retained and other effects from cross-correlated relaxation during the spin-lock period are removed. The correlation between $R_{2,eff}$ - measured by CT-CPMG at a ν_{CPMG} value of 1 kHz and HEROINE at a ν_{SL} value of 6 kHz is excellent with a Pearson correlation coefficient of 0.989 (Figure 26B).

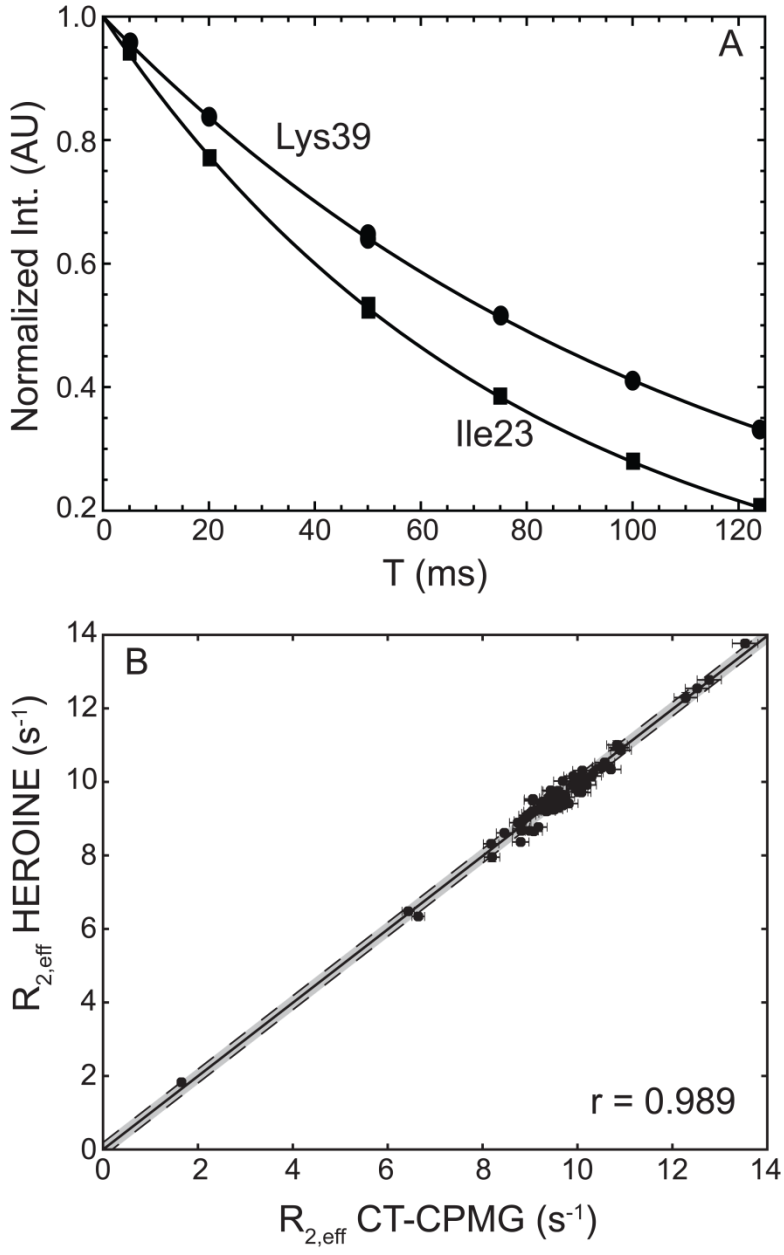

Figure 26 Validation of HEROINE experiment using ^{15}N labeled ubiquitin at 298 K, at which exchange process slower than 20 μs do not exist (Appendix Figure 1) and thus, $R_{2,eff}$ from CT-CPMG with 1 kHz ν_{CPMG} and 6 kHz HEROINE experiment should display similar values. (A) Example decay curves measured for residues Ile23 and Lys39 where points were sampled for 5 to 125 ms and fit to a monoexponential function. (B) Correlation between $R_{2,eff}$ measured with HEROINE and CT-CPMG using ν_{SL} and ν_{CPMG} values at 6 and 1 kHz, respectively. The solid line in B has a slope of 0.998 and the Pearson correlation coefficient (r) is also given in b with a root mean square deviation of 0.21 s^{-1}. The average error of the CT-CPMG experiment (0.19 s^{-1}) is represented by the gray shading with the black dashed line boundaries in B.

The RMSD between the data points is 0.21 s^{-1} and is comparable to the average error derived from the CT-CPMG experiment rendering the rates from both experiments nearly indistinguishable. Thus, HEROINE probes the same $R_{2,0}^{CT-CPMG}$ as in CT-CPMG, and therefore this value can be used in the fitting procedure described earlier.

5.4 Kinetic constants for OAA are underestimated without HEROINE

As an example of a protein that exhibits exchange processes in the fast regime we selected the *Oscillatoria aghardii agglutinin* (OAA) [165,166], a lectin that binds high mannose glycans on GP120, a protein linked to the entry of HIV into human cells [167]. HEROINE together with CT-CPMG measurements were performed. From the CT-CPMG experiments performed on OAA at 296 K, several residues in the carbohydrate binding pockets [165,166] undergo exchange. Among them, Trp77 and Asn99 exhibit the effect of a large (Figure 27A, B) and small (Figure 27C, D) underestimation in R_{ex}, respectively, for the CT-CPMG with ν_{CPMG} values up to 960 Hz compared to the HEROINE experiment that utilizes a ν_{SL} with an amplitude of 6 kHz. Differences in $R_{2,eff}$ ($\delta R_{2,eff} = R_{2,eff}^{CT\text{-}CPMG} - R_{2,eff}^{HEROINE}$) for Trp77 and Asn99 are 9.67 ± 1.07 and 3.60 ± 0.63 s^{-1}, respectively, hamper the accuracy of the determined kinetic values (Table 6).

For Trp77, if $R_{2,0}^{CT-CPMG}$ is not fixed when fitting the data using the BM formalism, minimized values differ by 66% for k_{ex}, compared to a fit when $R_{2,0}^{CT-CPMG}$ is known from HEROINE. In addition, Φ_{ex} could not be determined with any precision (Table 6). Such behavior, generally, would indicate that the BM model is inappropriate and instead the LM formalism should be used [158,168].

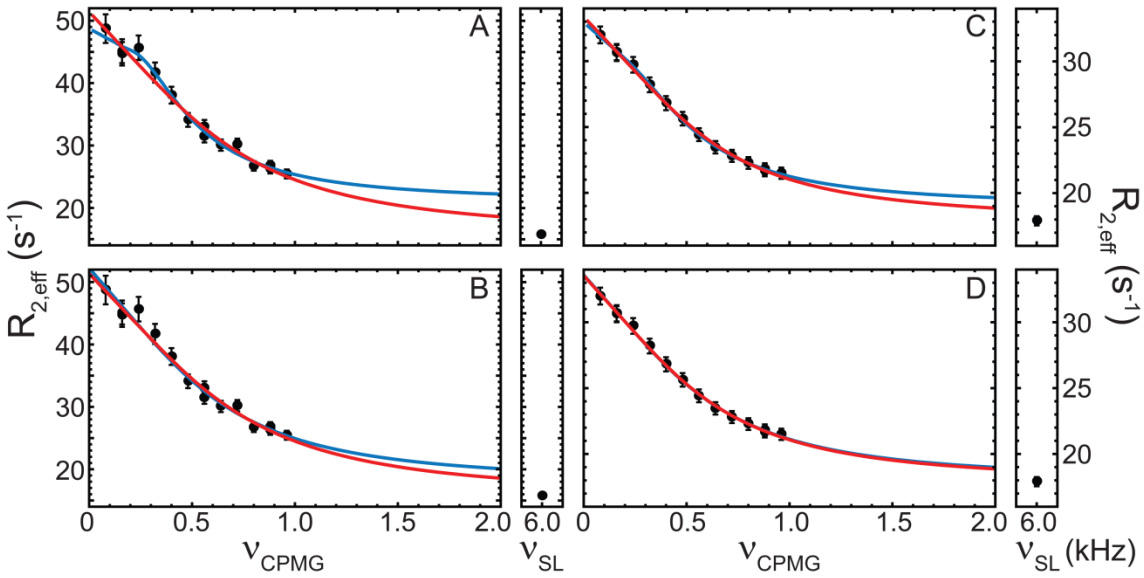

Figure 27 Application of HEROINE to OAA. CT-CPMG dispersion curves were measured for W77 (A, B) and N99 (C, D) and display exchange on a fast timescale at 296 K. For the CT-CPMG experiments on OAA, the maximum ν_{CPMG} was 960 Hz and represents a conventional value used in CT-CPMG experiments. In A and C data were fit using the BM model while in B and D the LM model was applied. Fitted dispersion curves in blue correspond to minimizations where $R_{2,0}^{CT-CPMG}$ was a fitting parameter while red curves represent fits curves using $R_{2,eff}$ from HEROINE as a known $R_{2,0}^{CT-CPMG}$. Strips next to the CT-CPMG data depict a given residue's measured $R_{2,eff}^{HEROINE}$. Two residues were selected since they represent situations where fits without *a priori* knowledge of $R_{2,0}^{CT-CPMG}$ result in large (W77; A 66%, B 12%) and small (N99; C 34%, 2% D) deviations from the more accurately determined k_{ex} when $R_{2,0}^{CT-CPMG}$ is known. Dispersion curves are plotted up to a ν_{CPMG} value of 2 kHz in order to readily detect the underestimation of the additional exchange contribution to $R_{2,eff}$, $\delta R_{2,eff}$ ($R_{2,eff}^{CT\text{-}CPMG} - R_{2,eff}^{HEROINE}$). (A, B) $\delta R_{2,eff}$ for W77 is 9.67 ± 1.07 s^{-1}, and for N99 (C, D) $\delta R_{2,eff}$ = 3.60 ± 0.63 s^{-1}. For a known $R_{2,0}^{CT-CPMG}$ a reduction in the errors of the fitted parameters is observed and convergence amongst the different models that are used to fit the data is reached (Table 6).

When the LM model is used to fit the data with $R_{2,0}^{CT-CPMG}$ as an adjustable parameter, an even faster k_{ex} is realized. More interestingly, as long as $R_{2,0}^{CT-CPMG}$ is kept fixed using the HEROINE measured value both BM and LM models converge to the same solution. In addition, as predicted from the simulations described above (Figure 24), the error in k_{ex} decreases by a factor of 6 and 2 for the BM and LM formalisms, respectively. Even for Asn99 (Fig. 28C, D) for which $\delta R_{2,eff}$ is smaller ($3.60 \pm 0.63\ s^{-1}$), k_{ex} determined from the BM approach while $R_{2,0}^{CT-CPMG}$ is kept as an adjustable parameter, within the error, gives a similar value like the other models. Again, the error associated with k_{ex} using the BM and LM formalism is reduced by a factor of 2 and 5, respectively when the HEROINE measured $R_{2,0}^{CT-CPMG}$ is included in the analysis. These experimental results reported here are in accordance with the observations from the Monte-Carlo simulations in Figure 24.

The analysis of RD data also depends on selecting the correct model that describes the exchange dependence. Generally, newly acquired CT-CPMG data is initially fit to models that are valid over all timescales (Carver-Richards and BM) or the fast exchange LM model and then fit statistics (χ^2) are used in conjunction with F-tests to confirm the applicability of a given model [168,169]. Instead, using HEROINE, a new protocol can be followed for handling data derived from CT-CPMG sequences. Once, $R_{2,0}^{CT-CPMG}$ is known, the BM and LM models converge to similar values, and therefore model selection becomes unnecessary. Thus, the BM model, which is valid over all timescales, can be used instead of the LM model. In particular, the HEROINE experiment may even provide the correct solution in the range where the LM model overestimates k_{ex} ($1 \leq k_{ex}^{true}/\Delta\omega < \sim 3$; square box in Figure 24; Appendix Figure 10 [170]). Since

the BM and LM models converge to similar solutions, the Akaike Information Criterion (AIC_c) was used to identify the model that has the highest probability of best representing the current data set [155]. In this case, for both Trp77 and Asn99 the LM model with $R_{2,0}^{CT-CPMG}$ determined from HEROINE (Table 6) was selected from the AIC_c analysis.

	$R_{2,0}^{CT-CPMG}$ **-Fit BM**	$R_{2,0}^{CT-CPMG}$ **- Known BM**	$R_{2,0}^{CT-CPMG}$ **- Fit LM**	$R_{2,0}^{CT-CPMG}$ **- Known LM**
Trp77				
k_{ex} (s^{-1})	1401±1039	4095±160	3590±447	4078±160
Φ_{ex} x10^3 (rad^2 s^{-2})	162±218	145±10	123±20	145±3
AIC_c	19.04	18.48	17.54	15.35
Asn99				
k_{ex} (s^{-1})	2195±896	3329±478	3521±744	3591±157
Φ_{ex} x10^3 (rad^2 s^{-2})	56.7±12.3	58.5±5.6	54.7±13.6	56.2±1.4
AIC_c	12.33	9.39	9.45	6.30

Table 6 Results from fits to CT-CPMG data measured on OAA with and without the HEROINE determined $R_{2,0}^{CT-CPMG}$.

Two examples were presented, Trp77 and Asn99 (Figure 27) to depict the effect of HEROINE applied to CT-CPMG data. However, in total twenty-five ^{15}N nuclei had an appreciable contribution of exchange for OAA at 296 K. This limit was demarcated that the difference between their $R_{2,eff}$ values measured at ν_{CPMG} of 80 and 960 Hz was greater than 2 s^{-1}. The same analysis above was applied for all 25 nuclei and all fitted results can be found in Appendix Table 3. From which, use of the BM and LM model without HEROINE on average produced an underestimation in the extracted kinetics by approximately 28 and 14 %, respectively. The use of HEROINE derived $R_{2,0}^{CT-CPMG}$ also provided a reduction in the error estimate for k_{ex} on average by a factor of 3 for both BM and LM models. The correlation between BM and LM models is excellent when HEROINE is included in the analysis for k_{ex} (Appendix Figure 12) highlighting the lack of requirement for statistically based methods to discern CT-

CPMG derived conformational exchange data. Although, a large improvement is attained in the increased precision and accuracy for kinetic information, extracted amplitude information for some residues (Φ_{ex} was less than $15x10^3$ rad^2s^{-2}) when the BM model is used (Appendix Table 3) maintained a large uncertainty even with HEROINE in the analysis. This occurred for two backbone ^{15}N nuclei, Asn18 and Gly26. This is not surprising for the BM model as the populations and $\Delta\omega$ are taken as separate parameters during minimization, but what can be retained is only the product and therefore a large number of fitted solutions will fulfill the same Φ_{ex} value. Additionally, all fitting procedures were performed taking each nuclei's data individually and at only one spectrometer field strength. Global fitting and multiple field strength measurements could further reduce the uncertainty in k_{ex} for those residues (Figure 24, [163]).

5.5 Comparison of other approaches

Conventional relaxation techniques focus on the determination of the inphase intrinsic relaxation rates of ^{15}N nuclei ($R_{2,0}^N$) [49,91,158]. This relaxation rate is composed of a contribution of dipolar relaxation of the nitrogen nuclei with its directly attached proton, relaxation due to the nitrogen's electron density orientation with the static magnetic field, and chemical exchange [46]. One approach was utilized in which four experiments are used and the relaxation rates are then linearly recombined and only the contribution of dipolar relaxation is retained [171]. Exchange free measures of $R_{2,0}^N$ have also been performed by measurements of het-NOE, transverse and longitudinal cross relaxation [64]. However, the imperative distinction is that for the CT-CPMG experiment does not provide a direct measure of $R_{2,0}^N$. As mentioned above $R_{2,0}^{CT-CPMG}$ is composed of the antiphase $2H_zN_x$ coherence which is sampled for a period of T/2 in Figure 24. $R_{2,0}^{CT-CPMG}$ also encounters a contribution from longitudinal remote proton

relaxation (R_H). The contribution of R_H can surmount to be quite large for folded proteins because a period R_1 for proton-proton interaction consists of an additional contributions of J(0) [65]. Excluding the high frequency components and CSA contribution of ^1H that add to R_H is proportional to

$$R_H \propto \sum_i^N \left(\frac{\mu_0 h \gamma_H^2}{8\pi^2 r_i^3} \right)^2 J(\omega_H - \omega_X) = \sum_i^N \left(\frac{\mu_0 h \gamma_H^2}{8\pi^2 r_i^3} \right)^2 J(0) \qquad \text{(Eq - 5.5.1)}$$

and extends over all remote protons that are close in space (< 5 Å) to the targeted nitrogen site [46,120]. Here, μ_0, h, γ_H, J(0), r_i are the permeability constant in vacuum, Planck's constant, the gyromagnetic ratio for ^1H, spectral density function, and distance between two nuclei, respectively. R_H is directly quantified by HEROINE without requirement of additional measurements and is directly applicable for CT-CPMG data. An alternative approach has also been reported where to account for R_H, CT-CPMG $R_{2,eff}$ is measured with a period where two spin order R_{2HzNz} is also recorded during the sequence [172], in order to make the derived $R_{2,eff}$ value approximately comparable to $R_{2,0}^N$. But only conventional values of ν_{CPMG} were considered which would not capture the exchange contribution for residues that are in the fast-regime (τ_{ex} < 150 μs) [90,172]. In contrast, HEROINE directly probes the actual magnetization that is used in CT-CPMG experiments and is acquired via a single mono-exponential decay profile as shown in Figure 26A and uses spin-lock fields where more efficient quenching of the exchange contribution can be attained.

5.6 Conclusion

We have demonstrated that if $R_{2,0}^{CT-CPMG}$ is known experimentally and therefore can be fixed during the analysis of CT-CPMG data, accurate kinetic parameters can be obtained over a

broad range of $k_{ex}/\Delta\omega$ ratios (Figure 24). In order to measure an accurate $R_{2,0}^{CT-CPMG}$ valid for CT-CPMG data, HEROINE was developed and validated (Figures 26 and 27) and shown to give access to this exchange free relaxation parameter in an unprecedentedly straight forward manner. HEROINE utilized large ν_{SL} to measure an $R_{2,eff}$ that represents a more true $R_{2,0}^{CT-CPMG}$ where motions up to 25 μs are removed from $R_{2,eff}$. If ν_{SL} values up to or exceeding 6 kHz cannot be achieved with a given hardware configuration, it is possible to use lower ν_{SL} values, although additional measurements at different offsets must be performed to maintain probed sites on-resonance. As shown for OAA, using the rate measured with HEROINE, as a way to constrain $R_{2,0}^{CT-CPMG}$, unifies different models that are frequently used to describe exchange (Table 6, Figure 27). In addition, if HEROINE was not implemented for OAA, leaving $R_{2,0}^{CT-CPMG}$ as an adjustable fit parameter would have resulted in gross underestimation of the kinetics.

Fast regime motions measured by CT-CPMG experiments contain a parameter correlation between the populations and Δω. HEROINE, in combination with a recent approach for breaking this correlation [173], using the difference in chemical shifts from single- and multiple quantum experiments, may further extend the limit at which populations and Δω information can be extracted. HEROINE could also be adapted for the study of molecules with higher molecular weight. Even though HEROINE was demonstrated on relatively small systems, ubiquitin (8.7 kDa) and OAA (14 kDa), this pulse sequence can be easily converted to incorporate a TROSY readout for macromolecules of higher molecular weight [120]. Additionally, if different nuclei are of interest the approach outlined above would still hold.

CT-CPMG experiments have come into widespread use for studying folding intermediates, enzymatic catalysis, and protein-ligand interactions. Therefore, the inclusion of

HEROINE with large ν_{SL} derived $R_{2,0}^{CT-CPMG}$ for analyzing CT-CPMG data will augment the current methodology, in order to improve the accuracy and reliability of kinetic data from the micro- to millisecond timescale.

5.7 Materials and Methods

Simulation The assessment of CT-CPMG data fitted with and without a known $R_{2,0}^{CT-CPMG}$ was performed on synthetic data sets created using the analytical Carver-Richards [174] equation that is valid over all timescales. Data was created for a single residue, with k_{ex} values between 300 and 15000 s^{-1} (defined in Figure 24 as k_{ex}^{true}), and $\Delta\omega$, p_b (the minor population), and $R_{2,0}^{CT-CPMG}$ were kept constant at 2 ppm, 0.05, and 10 s^{-1}, respectively. For each exchange scenario, 100 dispersion curves were created at two fields, 60.8 and 81 MHz for ^{15}N, with a 2 % error in $R_{2,eff}$. Each dispersion curve consisted of seventeen points and ν_{CPMG} varied between 40 and 1000 Hz. Two models were employed to fit the CT-CPMG data: the numerical description of magnetization across the CT-CPMG refocusing elements was used (Bloch-McConnell; BM) [161] or the fast exchange Luz-Meiboom equation (LM) [162] and are given below.

Fitting Models

Bloch-McConnell (BM) For the BM model magnetization through the CPMG pulse train is described by

$$M(4nt) = \left(\exp(At)\exp\left(A^{*}t\right)\exp\left(A^{*}t\right)\exp(At)\right)^{n} M(0) \qquad \text{(Eq - 5.7.1).}$$

In which

$$A = \begin{pmatrix} -R_{2,0}^{CT-CPMG} - k_1 & k_{-1} \\ k_1 & -R_{2,0}^{CT-CPMG} - k_{-1} + i\Delta\omega \end{pmatrix} \qquad \text{(Eq - 5.7.2)}$$

where k_1, k_{-1}, $\Delta\omega$ ($\Delta\omega = \omega_b - \omega_a$), $R_{2,0}^{CT-CPMG}$ are the forward and reverse rate ($k_{ex} = k_1 + k_{-1}$), the chemical shift difference between the populated states, and the intrinsic relaxation rate from the CT-CPMG experiment, respectively. A* is the complex conjugate of A that inverts the chemical shift evolution direction, which is the effect of the two 180° pulses after the first and before the fourth segment of length *t*. M(0) is a column matrix with the populations of states *a* and *b*. The interpulse delay and the number of refocusing elements in a given constant-time period is given by *n* and *t*, respectively. At which point $R_{2,eff}$ can be calculated as

$$R_{2,eff} = \left(-1/4nt\right)\ln\left(M_a(t)/M_a(0)\right) \quad \text{(Eq - 5.7.3)}$$

for the slow exchange case ($k_{ex}^{true}/\Delta\omega < 1$), or as the sum over both the *a* and *b* state,

$$R_{2,eff} = \left(-1/4nt\right)\ln\left(M_a(t) + M_b(t)\right) \quad \text{(Eq - 5.7.4)}$$

in the fast exchange regime ($k_{ex}^{true}/\Delta\omega > 1$). All optimization protocols were implemented in Python using the SciPy libraries.

Luz-Meiboom (LM) The functional form of the LM model comes from again realizing that a CPMG experiment functions by inverting the sense of precession for probed nuclei during the period *t* – 180° pulse – *t* and solving the eigenvalue problem for the Hermitian matrix [27, 170]

$$B = \exp\left(At\right)\exp\left(A^{*}t\right) \qquad \text{(Eq - 5.7.5)}$$

Taking into consideration that equation 5.7.2 is the summation of three components, the kinetic rate constants ($\mathbf{K} = k_{ex}\begin{bmatrix} -p_b & p_a \\ p_b & -p_a \end{bmatrix}$), intrinsic relaxation rates (intrinsic relaxation rates for each site is assumed to be equal) for all states, and their chemical shift information with respect to the observed peak ($\mathbf{\Omega} = \begin{bmatrix} \omega_a & 0 \\ 0 & \omega_b \end{bmatrix}$). The general solution has been derived by Luz and Meiboom [162] and later in greater generality by Allerhand and Gutowsky [170] using perturbation theory

in which the kinetic and intrinsic relaxation rates are assumed to be unperturbed zero-order contribution and $\Delta\omega$ is taken to be very small first-order perturbation following the fast exchange assumption ($k_{ex} >> \Delta\omega$). Allerhand and Gutowsky [170] arrived at a general solution for the relaxation rate of a single population averaged resonance which is recast from them using the above nomenclature

$$R_{2,eff} = R_{2,0}^{CT-CPMG} + \sum_{i=2}^{N} \frac{\left\langle \Lambda_1 \left| \mathbf{\Omega} \right| \Lambda_i \right\rangle^2}{\left|\lambda_i\right|} \left(1 - \frac{4\nu_{CPMG}}{\left|\lambda_i\right|} \tanh\left(\frac{\left|\lambda_i\right|}{4\nu_{CPMG}} \right) \right) \qquad \text{(Eq - 5.7.6)}$$

Where here *N* is the summation over all populated states. We are concerned with a two-state problem and therefore *N* = 2.

$$R_{2,eff} = R_{2,0}^{CT-CPMG} + \frac{\left\langle \Lambda_1 \left| \mathbf{\Omega} \right| \Lambda_2 \right\rangle^2}{\left|\lambda_2\right|} \left(1 - \frac{4\nu_{CPMG}}{\left|\lambda_2\right|} \tanh\left(\frac{\left|\lambda_2\right|}{4\nu_{CPMG}} \right) \right) \text{(Eq - 5.7.7)}$$

From equation 5.7.9, λ_i and Λ_i are the i-th eigenvalue and eigenvector from the symmetrized form of $\mathbf{K}$ ($\mathbf{K}'$)

$$\mathbf{K}' = \mathbf{S}\mathbf{K}\mathbf{S}^{-1} = \begin{bmatrix} p_a^{-1/2} & 0 \\ 0 & p_b^{-1/2} \end{bmatrix} k_{ex} \begin{bmatrix} -p_b & p_a \\ p_b & -p_a \end{bmatrix} \begin{bmatrix} p_a^{1/2} & 0 \\ 0 & p_b^{1/2} \end{bmatrix} \text{(Eq - 5.7.8)}$$

$$\mathbf{K}' = k_{ex} \begin{bmatrix} -p_b & p_a^{1/2} p_b^{1/2} \\ p_a^{1/2} p_b^{1/2} & -p_a \end{bmatrix}$$

The eigenvalues and eigenvectors of $\mathbf{K}'$ are

$$\lambda_1 = 0;\ \lambda_2 = -k_{ex}$$
$$\left\langle \Lambda_1 \right| = \begin{bmatrix} p_a^{1/2} & p_b^{1/2} \end{bmatrix};\ \left\langle \Lambda_2 \right| = \begin{bmatrix} -p_b^{1/2} & p_a^{1/2} \end{bmatrix} \qquad \text{(Eq - 5.7.9).}$$

Substituting back into equation 5.7.7 and performing the matrix algebra we arrive at

$$R_{2,eff} = R_{2,0}^{CT-CPMG} + \frac{\left(p_a^{1/2} p_b^{1/2} \left(\omega_b - \omega_b \right) \right)^2}{k_{ex}} \left(1 - \frac{4\nu_{CPMG}}{k_{ex}} \tanh\left(\frac{k_{ex}}{4\nu_{CPMG}} \right) \right) \text{(Eq - 5.7.10)}$$

And is further simplified to the functional form of the LM model as

$$R_{2,eff} = R_{2,0}^{CT-CPMG} + \frac{\Phi_{ex}}{k_{ex}}\left(1 - \frac{4\nu_{CPMG}}{k_{ex}}\tanh\left(\frac{k_{ex}}{4\nu_{CPMG}}\right)\right) \quad \text{(Eq – 5.7.11).}$$

Where in equation 5.7.11 Φ_{ex} is the product between the populations and the square of the chemical shift difference ($\Phi_{ex} = p_a p_b \Delta\omega^2$), ν_{CPMG} is a given CT-CPMG refocusing frequency and all other parameters are the same as defined above. From which, k_{ex}^{fit} was defined as the average k_{ex}, and σ was the standard deviation in k_{ex} of all minimizations in a given synthetic set.

NMR Spectroscopy Samples contained 2 mM ^{15}N labeled ubiquitin, in 50 mM sodium phosphate buffer, pH 6.5, 100 mM NaCl, 0.05% NaN_3, 5% D_2O/95% H_2O or 1 mM ^{15}N labeled OAA in 20 mM sodium acetate buffer, pH 5, 20 mM NaCl, 3 mM NaN_3, 5% D_2O/95% H_2O. CT-CPMG experiments are analogous to the scheme of Long et al. [164,175,176] and is presented in Figure 28.

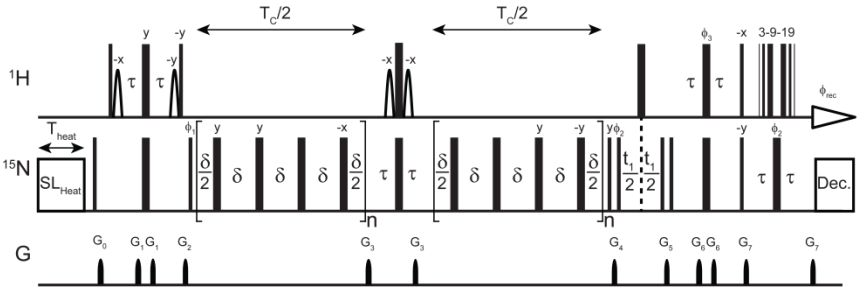

Figure 28 Constant-time Carr-Purcell-Meiboom-Gill (CT-CPMG) sequence that measures $R_{2,eff}$. 90° and 180° rectangular pulses are depicted by the narrow and wide black bars. Field strengths for ^{1}H and ^{15}N pulses were set at 31.6 and 10.8 kHz, respectively. All shaped pulses are of a Gaussian shape and are applied on-resonance with water for a period of 1.5 ms. T_c is the length of the constant-time block. This sequence employs a new temperature compensation block in order to match the temperature between the CT-CPMG and HEROINE experiments. SL_{Heat} was applied with the same ν_{SL} from the HEROINE experiment ($\nu_{SLheat} = \nu_{SL} = 6$ kHz) for a period of T_{Heat}. T_{Heat} was calculated as $T_{HEAT} = \frac{T_{max}^{HEROINE}\left(T_{RD}^{CT-CPMG} + T_C\right)}{T_{RD}^{HEROINE} + T_{max}^{HEROINE}} - \left(\frac{\nu_{CPMG}}{\nu_{SL}}\right)^2 T_P$ where $T_{max}^{HEROINE}$, $T_{RD}^{CT\text{-}CPMG}$, $T_{RD}^{HEROINE}$, T_P, and ν_{CPMG}, are the maximum relaxation delay in the HEROINE

experiment, recycle delay in the CT-CPMG experiment, recycle delay in the HEROINE experiment, the length that 180° pulses are applied during T_C for a given ν_{CPMG} ($T_P = 8\ n\ p^{15}N$; $p^{15}N$ is the 180° pulse length), and the field strength of the 180° pulses during T_C, respectively. SL_{Heat} was applied at 28.4 kHz upfield from the transmitter frequency. Before purging the ^{15}N Boltzmann polarization, the ^{15}N transmitter frequency was placed back on-resonance. During acquisition ^{15}N decoupling was done with a WALTZ16 scheme at field strength of 2 kHz [136]. The delay τ was set to $1/4J_{NH}$ (2.7 ms). The reference experiment was recorded using the same scheme only with the period T_C omitted [169]. Frequency discrimination in the indirect dimension was achieved by States-TPPI quadrature detection [154] utilizing the following phase scheme: $\phi_1 = 4(x), 4(-x)$, $\phi_2 = (x, -x, -x, x)$, $\phi_3 = (y, y, -y, -y)$ and $\phi_{rec} = (-x, x, x, -x)$. Phases for all pulses are x phase unless otherwise indicated. Gradients with strengths (length) of $G_0 = 42$ G/cm (1 ms), $G_1 = 10$ G/cm (0.5 ms), $G_2 = 32$ G/cm (0.5 ms), $G_3 = 14$ G/cm (0.5 ms), $G_4 = 25$ G/cm (0.5 ms), $G_5 = 8$ G/cm (0.5 ms), $G_6 = 17$ G/cm (0.5 ms), and $G_7 = 28$ G/cm (0.5 ms) were used. HEROINE pulse code for Bruker type instruments is found in the Pulse Programs section.

The phases of the ^{15}N pulses during the CT-CPMG blocks were alternated in order to minimize off-resonance effects [175,176]. Constant relaxation times (T_c) of 60 and 50 ms were used, and ν_{CPMG} values from 67 to 1000 Hz and 80 to 960 Hz were employed for ubiquitn and OAA, respectively. Three duplicates per dispersion profile were used for error estimation in $R_{2,eff}$. In total 80 ($t_{1,max}$=41.1 ms) and 512 ($t_{2,max}$ = 61 ms) complex points in the indirect and direct dimensions, respectively, were collected with 8 transients per point for ubiquitin. For OAA, 100 ($t_{1,max}$ = 48.4 ms) and 512 ($t_{2,max}$ = 61 ms) complex points in the indirect and direct dimensions, respectively, were acquired with 32 transients per point. Recycle delays of 2 and 1.5 seconds were used for ubiquitin and OAA, respectively. All spectra were processed and peak amplitudes determined using the NMRPipe software package [121]. Analysis of CT-CPMG data followed procedures set in the literature using the models described above. We utilized AIC_c since the compared models are not nested [155]. AIC_c was calculated as $\chi^2 + 2m\left(1 + \frac{m+1}{l-m-1}\right)$ where χ^2 is the target function value from a Least-Sqaures minimization [177], m the number of parameters in a given model, and l the total number of $R_{2,eff}$ values (l=15).

Only residues that are on-resonance with the applied ν_{SL} are considered for analysis. Analysis of resonances is facilitated by using the largest ν_{SL} possible in order to eliminate R_1 and offset effects. HEROINE was measured at three different offsets (Ω), reducing the maximum R_1 contribution to $R_{1\rho}$ to 0.1%. The application and calibration for a ν_{SL} strength of 6 kHz was carried out as described in Chapter 3. Decay profiles were recorded by varying the relaxation period, T, between 5 to 125 ms and 5 to 100 ms for ubiquitin and OAA, respectively. These profiles were subsequently fit to a monoexponential function ($I(T) = I_0 \exp(-R_{HEROINE}T)$). For ubiquitin, spectra were collected with 8 scans per point, for a total of 80 ($t_{1,max}$ = 41.1 ms) and 512 ($t_{2,max}$ = 61 ms) complex points in the indirect, and direction dimensions, respectively. For OAA, spectra were acquired with 90 ($t_{1,max}$ = 43.5 ms) and 512 ($t_{2,max}$ = 61 ms) complex points in the indirect and direct dimensions, respectively with 8 transients per point. The recycle delay used in experiments with ubiquitin and OAA were 3 and 2 seconds, respectively. Acquisition of all NMR data was on a Bruker Avance I spectrometer operating at a ^{1}H Larmor frequency of 600 MHz with a QCI cryo-probehead.

Accessing conformational interconversion during binding

6.1 Conformational sampling kinetics during binding

Communication in cellular processes is relayed via molecular interactions [3]. The way in which proteins and small molecules communicate is controlled by how they can recognize each other. For molecular recognition two different mechanisms, the induced-fit and the conformational selection model, are commonly enovked to describe these processes. The induced-fit binding mechnaism predicates that a loosely formed binding complex is formed, deemed the encounter complex, after which structural rearrangements are made that lead to the formation of the final bound complex. The conformational selection mechanism is governed by the internal dynamics of a given system in which a subset of configurations are sampled that mimic the final bound conformation. This small subset of correct boundable conformations then allows for the system to shift its distribution of sampled conformers to a more dominate bound form and has been refered to as the population shift mechanism [178,179]. The key limiting difference between the two binding models is that in the induced-fit case binding is diffusion-controlled and for conformational selection it is not limited, but diffusion associated. Recently, it was shown however that for a given system both models can be active and is given by the both the protein and its interaction partner's (ligand) concentrations (Figure 29) [104]. Namely, by controlling the relative concentrations of both the protein and ligand it could be possible to push a system in one pathway or the other.

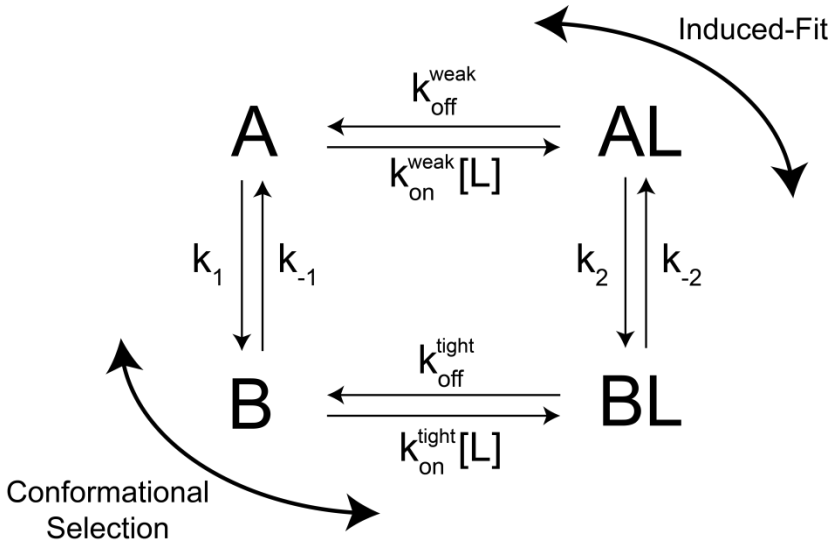

Figure 29 Four-state model in which both conformational selection and induced-fit can exist depending on the relative protein concentrations [104].

The interplay between both binding mechanisms can be represented as a four-state model (Figure 29) [104,180]. For conformational selection the free protein samples between non-boundable (A) and boundable conformations (Figure 29; state B) with rates of k_1 and k_{-1}. If the correct conformation is selected B binds with the diffusion associated rate of k_{on}^{tight} to form the final bound conformation (Figure 29; state BL). In the induced-fit pathway encounter complexes (Figure 29; state AL) are limited by k_{on}^{weak} and once formed final rearrangments to BL are dictated by k_2 and k_{-2}. This model can distinguish between both binding schemes because of the location of where the ligand dependence occurs. Therefore, if all of the rates that govern both pathways can be uniquely determined then at at any given the flux [$s \cdot M^{-1}$] through either conformational selection or induced-fit at any concentration could be calculated [104]. In order to quantify this proposed model a system of study must first be identified.

Since previously collected RDC information highlighted that free ubiquitin samples different conformations that mimic bound conformations a prevelance of conformational selection has been shown to exist [11]. And with the recent measurement of the kinetics for this

sampling process (Chapters 2, 3 & 4) ubiquitin with an interaction partner would be an ideal system to experimentally quantify the model in Figure 29. This would also provide insight as to if conformer sampling (k_1 and k_{-1}; Figure 29) can still be detected during an interaction event. Therfore, RD experiments could in principle be used to asses this model because if the differentially populated states from the above model exist in solution, they could potentially be diseminated via careful analysis of the acquired data. However, attaining insight into such a complex model requires the measurement of very accurate data and thus prefaces the imperative requirement of having experimental conditions that would allow for highly sensitive measurements (i.e. sufficient concentrations, monomeric interactions, detectable affinities). So before a systematic determination of the rate constants can be performed a binding partner for ubiquitin has to be identified that would adhere to such criteria. Currently, we have been pursuing two interaction partners: the ubiquitin associated (UBA) domain of Dsk2p (Dsk2) [181] and the SH3-C domain of CIN85 (SH3) [182,183].

6.2 Interaction of ubiquitin with Dsk2

Two-dimensional [^{1}H,^{15}N]-HSQC spectra provide a conventional but rigorous experimental technique that can verify interactions between molecules [184]. Since each peak in a [^{1}H, ^{15}N]-HSQC not only correspond to the unique frequency for and $^{1}H^{N}$ and ^{15}N nuclei pair it also serves a sensitive reporter of a nuclei's surrouding environment. Therefore, HSQC based titration experiments can be used to determine the efficacy (affinity) and location of binding between two systems by monitoring peak movements in each spectrum as a function of ligand and/or protein concentration [46]. The dependence of the chemical shift change ($\Delta\omega_N$) as a function of the titrant concentration can be fitted for the chemical shift value at saturation (bound

population of 100 %) for a given nuclei and the dissociation constant (K_D) for the interaction assuming a two-state binding process.

Dsk2p is a yeast protein whose function is the targeting of mono- and polyubiquitinated proteins that are ultimately shuttled to the proteasome for degradation [185]. Its UBA domain is a small 6.2 kDa three helix bundle whose solution NMR structure has been previously determined [181].

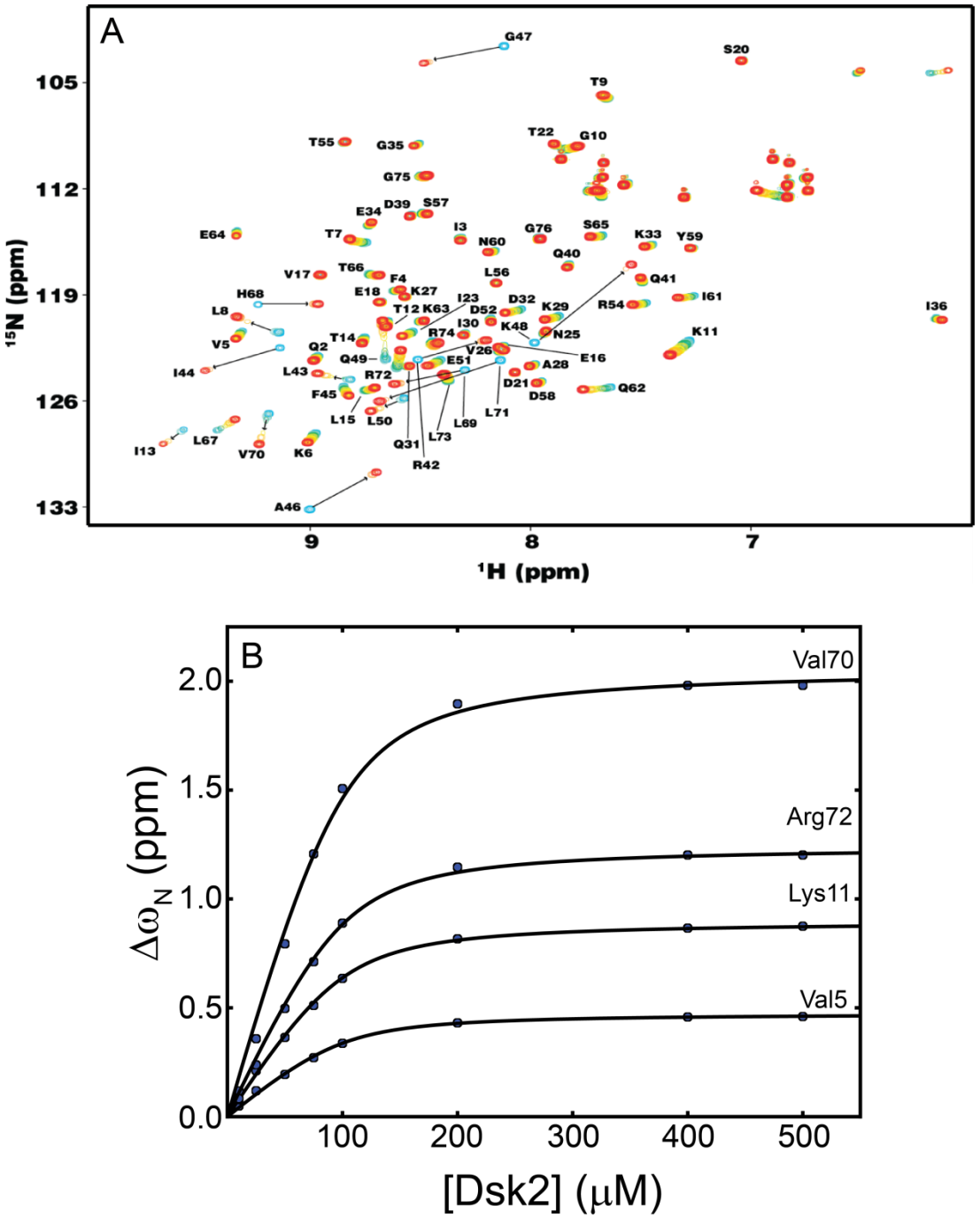

Figure 30 (A) [^{1}H,^{15}N]-HSQCs of ^{15}N labeled ubiquitin with increasing amounts of unlabeled Dsk2 at 298 K. Free ubiquitin (red) was titrated up to a ubiquitin/Dsk2 ratio of 5 (blue) using 8 increments. (B) Binding isotherms for 5 residues of ubiquitin. Global fitting of 25 ^{15}N nuclei yielded a two-state K_D of 12 ± 4 μM.

We carried out HSQC based titrations with 100 μM ^{15}N labeled ubiquitin and increasing amounts of unlabeled Dsk2 (Figure 30). From the HSQC series many peaks shift in a manner

characteristic of intermediate to fast exchange (Figure 30A) [46]. Chemical shift perturbations were quite large with a maximum of up to 5.4 ppm for Lys48 (Figure 30A; K48). In total 25 binding isotherms were fitted globally yielding an overall K_D of 12 ± 4 μM (solid curves Figure 30B) which agrees with the spectral patterns seen in Figure 30A and with previous observations [181]. Interestingly, Dsk2's UBA domain binds with an affinity that is an order of magnitude less than what has been seen for other UBA domains [186].

Given binding isotherms that displayed singular binding events (Figure 30B) we began to carry out CT-CPMG experiments. CT-CPMG experiments are well catered to probing timescale for binding (~500 μs at 298 K for the ubiquitin – Dsk2 interaction) and any lowly populated intermediates that may exist are more readily detected by these experiments than that of the titration derived K_D which is an apparent K_D. However, upon inspection of $R_{2,eff}$ profiles for two samples that were measured with the same ratio of ubiquitin and Dsk2 (1:5), with different protein concentrations revealed distinct profiles (Figure 31). At 298 K CT-CPMG experiments were measured on a sample of 165 μM ubiquitin with 830 μM Dsk2 (Figure 31; black points) and 400 μM ubiquitin with 2000 μM Dsk2 (Figure 31; blue points). Surprisingly, since these samples were measured using the same ratio, the apparent K_D renders the bound population to between 98 and 99 % for both of the samples. Still, even with the same ratio of protein it can be clearly seen that there is an average 5 s^{-1} in $R_{2,eff}$ between the sample with higher relative protein concentrations (Figure 31; blue points) than the sample with lower concentrations (Figure 31; black points).

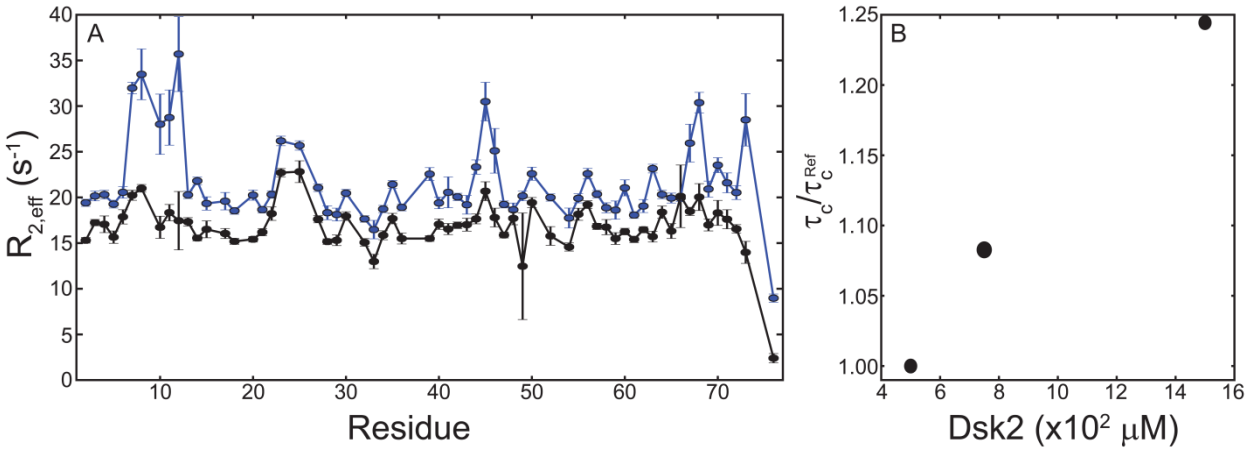

Figure 31 (A) $R_{2,eff}$ for ubiquitin in complex with Dsk2 plotted versus residue. Two samples with a ratio (ubiquitin/Dsk2) of 1:5 measured with concentrations of 165/830 μM (black points) and 400/2000 μM (blue points) are plotted for comparison. $R_{2,eff}$ was determined from CT-CPMG experiments (Chapter 4) measured at a ^{1}H Larmor frequency of 800 MHz. (B) Effective rotational correlation times (τ_c) determined via TRACT experiments [65] for three samples that had a ratio 1:5, but with different concentrations of ubiquitin and Dsk2. τ_C^{Ref} was the τ_C measured from the sample with the lowest concentration of ubiquitin (100 μM). Even though the ratios were kept constant the effective tumbling time increased up to ~25 % for ubiquitin.

In order to account for this discrepancy we must consider that $R_{2,eff}$ is directly sensitive to changes in the intrinsic relaxation of a given nucleus and from effects due to conformational exchange. It has been shown for dilute solutions that contain a solute volume fraction (ε) of less than 0.28 that the apparent viscosity (η) scales by $\eta = \eta_0(1+2.5\,\varepsilon)$ where η_0 is the viscosity of the solvent [187,188]. Given the sample conditions and the molecular weight of the unbound Dsk2 and ubiquitin-Dsk2 complex we can find ε to be $6.3\cdot10^{-3}$ and $1.52\cdot10^{-2}$ for the samples measured in Figure 31A. Therefore, η is 2.2 % larger in the sample with larger relative protein concentrations. Based on the Stokes-Einstein equation τ_C scales linearly with the viscosity and since $R_{2,eff}$ is mostly dominated at the spectral density function evaluated a zero frequency we expect that $R_{2,eff}$ would only differ by approximately 0.4 s^{-1} between the two samples in Figure 31. Thus, the increased η does not reconcile the 5 s^{-1} difference between the two samples (Figure 31A). Additionally, a 2.2 % change in τ_C does not concur with the 25 % change in τ_C observed in

Figure 31B. Further speculation can be made that residues in the N-terminus and C-terminus which have even further elevated rates from the mean of the higher concentrated sample (Figure 31A; blue points) may stem from additional sources of conformational exchange.

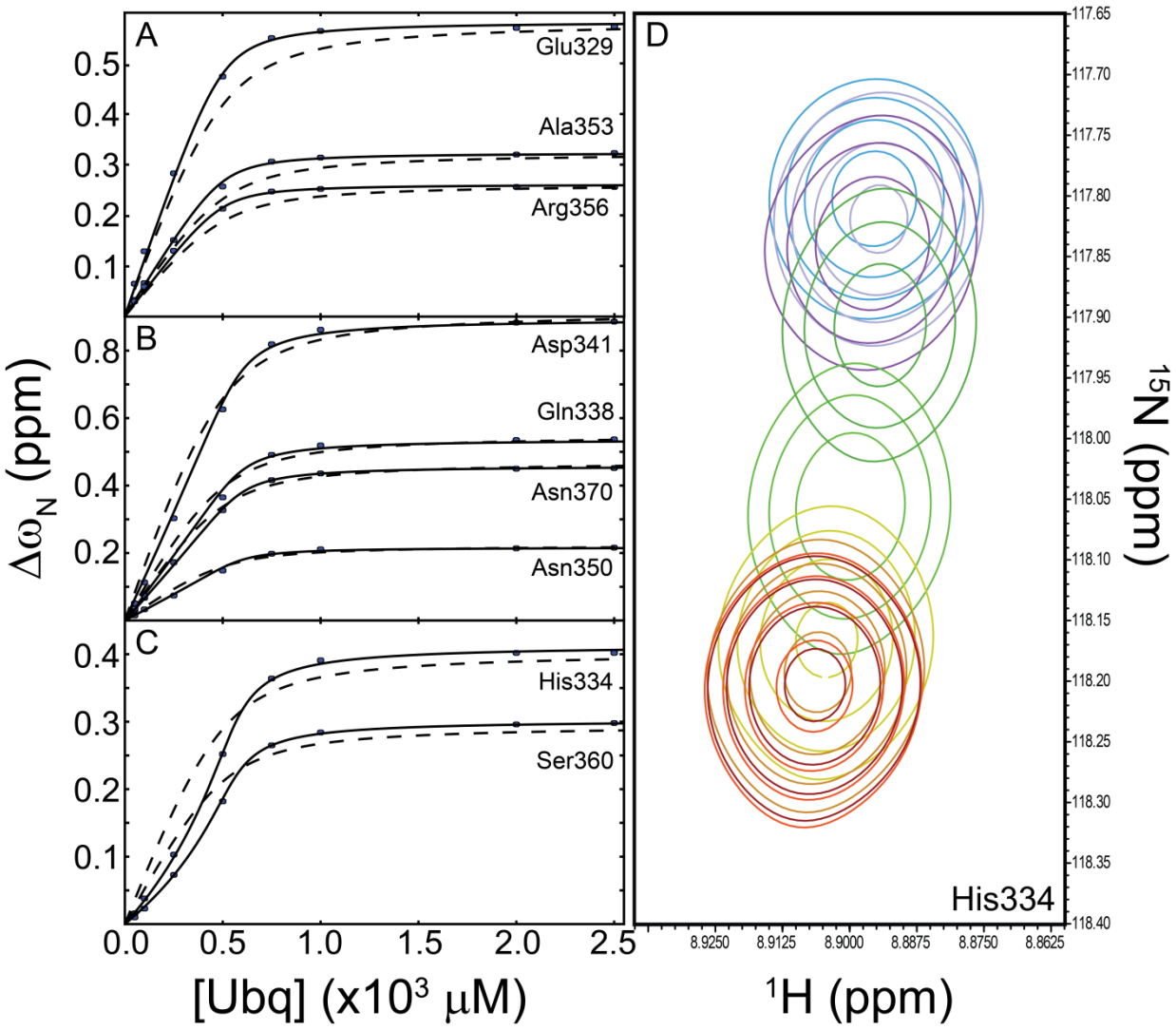

Figure 32 (A-C) Binding isotherms for ^{15}N labeled Dsk2 when increasing concentrations of unlabeled ubiquitin (Ubq) were added to the sample. For A-C the concentration of Dsk2 was kept constant at 500 μM and unlabeled ubiquitin was added up to 2500 μM. Dashed lines are from global fits of all residues to a two-state binding model. In A, residues that represented statistically better fits to a two-state model are shown with a solid black line, and in B and C residues that were reported to have statistically significant behavior that correspond to fits using a model that reports on two binding events are plotted with solid black curves (Materials and Methods). (D) Example of sigmoidal peak movements from the titration series for His334 of

Dsk2. Free Dsk2 is colored in blue increasing ubiquitin concentrations that culminates with a ubiquitin concentration 2500 μM is in red.

We also conducted the reverse titration in which ^{15}N labeled Dsk2 signals were observed as a function of increasing concentrations of unlabeled ubiquitin. This titration was conducted with higher relative protein concentrations with 500 μM Dsk2. A globally fitted two-state K_D was determined to be 56 ± 27 μM from fits of 21 binding isotherms (Figure 32A-C; dashed lines). However, further inspection of the back plotted theoretical curve for a two-state binding process with a K_D of 56 ± 27 μM clearly does not properly describe the chemical shift dependence for many of the residues. This is also reflected in the large uncertainty in the K_D. Instead three distinct profiles for binding isotherms emerged that did not corroborate with the two-state derived K_D (Figure 33A-C). Out of the 21 residues that displayed significant chemical shift perturbations, five residues reported single binding event titration curves (Figure 32A) with a K_D a factor of two less than the globally derived one (K_D = 20 ± 13 μM) and is similar to the K_D that was derived when the titration was performed when ubiquitin resonances were observed. Instead, other residues even display a sigmoidal behavior (Figure 32B and C). Residues were separated in Figure 32B and C based on their initial slope where $\Delta\omega_N$ was less than 0.1 at a Dsk2/ubiquitin ratio of 0.25 (Figure 32). This criterion was established based on the fit statistics (χ^2) value at which point the different models were compared with an F-test in order to determine if a singular or sigmoidal binding model was more applicable (Materials and Methods). Sigmoidal binding isotherms [189,190] infer two possibly different situations. Either the protein whose resonances' are being queried undergo two binding events or there is the existence of two independent binding sites for a given protein. Using a model [190] that describes this dependence we could extract a K_{D1} of 27 ± 16 μM (36 ± 20 μM) and a K_{D2} of 73 ± 58 μM (25 ± 12μM) for residues in Figure 32B (Figure 32C), respectively. The identification of a multiple modes of binding from

the reverse titration purports the necessity to investigate free Dsk2 alone in order to establish if there is potential interconversion kinetics amongst Dsk2 alone that could be used to define a binding scheme that might contradict or conform with the above titration results.

Since RD is sensitive to alternatively populated states, it can be used to shed light on whether there are other states sampled within free Dsk2 conformers. We conducted CT-CPMG experiments on ^{15}N nuclei at 283 K and detected significant exchange contribution to $R_{2,eff}$ for 13 residues in Dsk2 (Figure 33A). These 13 residues were fitted globally and a fast exchange event with a τ_{ex} of 178 ± 14 μs was realized and thus prevents the separation of populations from the structural information. An X-ray structure of Dsk2 has been reported in which Dsk2 monomers can form a multimeric chain [191]. Each native Dsk2 molecule contains an asymmetric dimer interface on both sides of a given Dsk2 monomer that ultimately appears as a polymer of multiple Dsk2 molecules. Interestingly, the same sites that reported the exchange event overlap with this interface (Figure 33B).

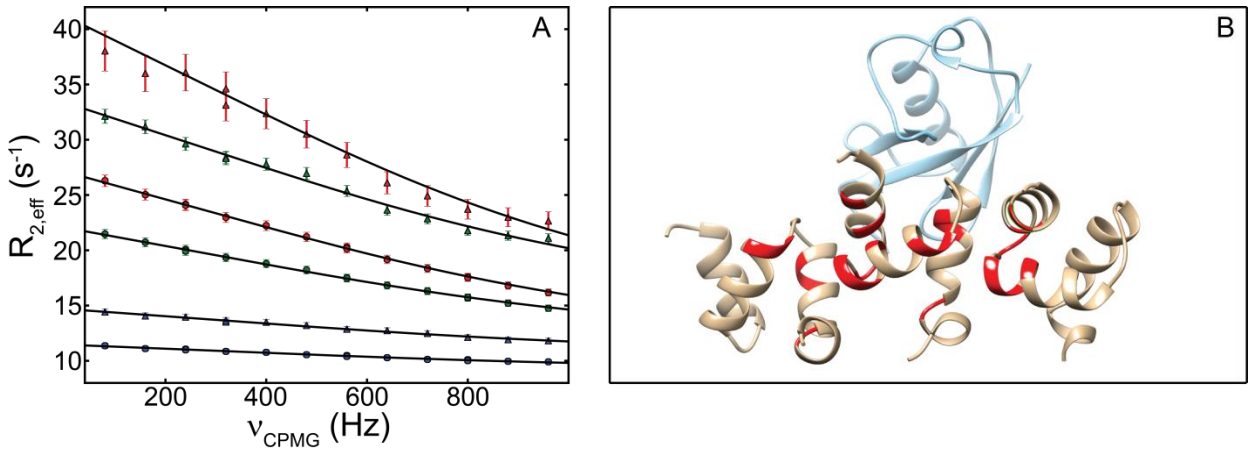

Figure 33 (A) The dependence of $R_{2,eff}$ on the ν_{CPMG} from a CT-CPMG experiment conducted on a 1 mM sample of native free Dsk2. Out of the 13 residues that displayed significant relaxation dispersion residues Tyr332 (green points), Asp348 (blue points), and Gly358 (red points) are depicted in A. All experiments were performed at 283 K using spectrometers operating at ^{1}H Larmor frequencies of 600 (circles) and 800 (triangles) MHz. (B) Ribbon representation of the Dsk2 multimeric structure (tan color; PDB: 2BWB [191]) superimposed with the solution NMR

structure of the ubiquitin/Dsk2 complex (ubiquitin structure blue color; PDB: 1WR1 [181]). Residues in red correspond to the thirteen residues for which exchange was detected. From the Dsk2 structure [191] chains B, C, and D are presented and residues identified from the CT-CPMG experiments are shown in red on both sides of the asymmetric interface between Dsk2 monomers. The binding interface for ubiquitin (blue) does not directly coincide with the multimerization interface between different Dsk2 monomers.

Taking this information together, we have a situation in which the observed behavior of Dsk2 as a function of ubiquitin concentration shows two binding modes (Figure 32). Now, coupled with the site-specific kinetic information (Figure 33) that correlates with an asymmetric self-interaction interface between Dsk2 monomers, we have to expand the kinetic scheme to be

$$D_1 - Ubq \underset{k_{on,1}[Ubq_{free}]}{\overset{k_{off,1}}{\rightleftharpoons}} D_1 \underset{k_{off,self}}{\overset{k_{on,self}[D_1]}{\rightleftharpoons}} D_2 \underset{k_{off,2}}{\overset{k_{on,2}[Ubq_{free}]}{\rightleftharpoons}} D_2 - Ubq$$

However, since the Dsk2 concentration was kept constant throughout the titration we can reform the kinetic scheme to involve a simple interconversion between two states of Dsk2 (D_1 and D_2) and that interconvert with k_1 and k_2 in the following:

$$D_1 - Ubq \underset{k_{on,1}[Ubq_{free}]}{\overset{k_{off,1}}{\rightleftharpoons}} D_1 \underset{k_1}{\overset{k_2}{\rightleftharpoons}} D_2 \underset{k_{off,2}}{\overset{k_{on,2}[Ubq_{free}]}{\rightleftharpoons}} D_2 - Ubq$$

We can derive a relation that relates the apparent two-state K_D (K_D^{app}) to this complex behavior observed in Figure 33.

$$K_D^{app} = \frac{([D_1] + [D_2])[Ubq_{free}]}{[D_1 - Ubq] + [D_2 - Ubq]} \qquad \text{(Eq - 6.2.1)}$$

Since, we measure under equilibrium conditions microscopic reversibility [170] holds so the concentrations of $[D_2]$, $[D_1 - Ubq]$ and $[D_2 - Ubq]$ are given by

$$[D_2] = \left(\frac{k_2}{k_1}\right)[D_1]$$

$$[D_1 - Ubq] = \frac{k_{on,1}[D_1][Ubq_{free}]}{k_{off,1}} = \frac{[D_1][Ubq_{free}]}{K_{D1}} \qquad \text{(Eq - 6.2.2).}$$

$$[D_2 - Ubq] = \frac{k_{on,2}[D_2][Ubq_{free}]}{k_{off,2}} = \frac{[D_2][Ubq_{free}]}{K_{D2}}$$

Upon substitution of equation 6.2.2 we find

$$K_D^{app} = \frac{\left(1 + \frac{k_2}{k_1}\right)K_{D1}K_{D2}}{K_{D2} + \left(\frac{k_2}{k_1}\right)K_{D1}} \qquad \text{(Eq - 6.2.3).}$$

Let us assume for a moment equal populations of D_1 and D_2, inserting what was found from the sigmoidal analysis of the Dsk2 titration (Figure 32C) is in qualitative agreement with 30 ± 15 μM (with the data from Figure 32B; 39 ± 25 μM) with the residues determined using the two-state apparent K_D (20 ± 14 μM). However, for accurate quantitation of this effect it would be necessary to uniquely determine the ratio of k_2/k_1 because the equilibrium between D_1 and D_2 will affect the calculation of the free ubiquitin concentration which is dependent on $[D_1 - Ubq]$ and $[D_2 - Ubq]$. This model could also be too simplistic as we can speculate that since the binding interface for ubiquitin is unique compared to the interaction surface for Dsk2 monomers the above scheme might have to be extended to allow for two ubiquitin binding sites within one Dsk2 dimer. Therefore, the inherent complexity of native Dsk2 and ubiquitin interaction measured at concentrations that are favorable for RD experiments are nontrivial. As measurements at higher relative concentrations of Dsk2 not only affected the measured $R_{2,eff}$ values from the ubiquitin side (Figure 31A), but also reported elevated τ_C values (Figure 31B), and multiple binding modes

were observed from the Dsk2 side (Figure 32). Although, the impact on the internal sampling dynamics of ubiquitin may not be affected by this; we have begun to take steps at abolishing the self-interaction surfaces of Dsk2 and further work with this complex is underway (Appendix Figure 13) to confine the kinetic scheme to the initial one of Figure 29. Initial work with a mutant of Dsk2 has also identified differences in the HSQC based titrations when the same ratios, but different relative protein concentrations are used (Appendix Figure 13). This is in accordance with the assumed K_D^{app} above (Eq. 6.2.3). Further analysis as to the exact multimerization state of Dsk2 should be evaluated and concentration dependent studies are required to find conditions where a singular species or high population of it would exist. Concentration or temperature dependent RD measurements of free Dsk2 could allow for the quantitation of its conformational equilibrium.

6.3 Interaction of ubiquitin with SH3

Since ubiquitin has many binding partners we have recently explored the applicability of its interaction with the SH3-C domain of CIN85 (SH3) [182,183]. An HSQC based titration (Figure 32A) revealed characteristic titration curves that are well described by the standard two-state binding model and gave an apparent K_D of 333 ± 50 μM (Figure 34B). For this titration the concentration of ubiquitin was kept constant at 400 μM as the SH3 concentration was increased. A global analysis using only the amide proton chemical shifts did not change the K_D value. From previous reports this K_D differs by a factor of two, but the construct utilized here differs by an extension of 7 and 5 residues on the N- and C- termini, respectively [182]. This extension has been shown to increase the stability of this SH3 domain and while maintaining a monomeric state in solution [182]. But how such an extension would affect the affinities for systems that share the

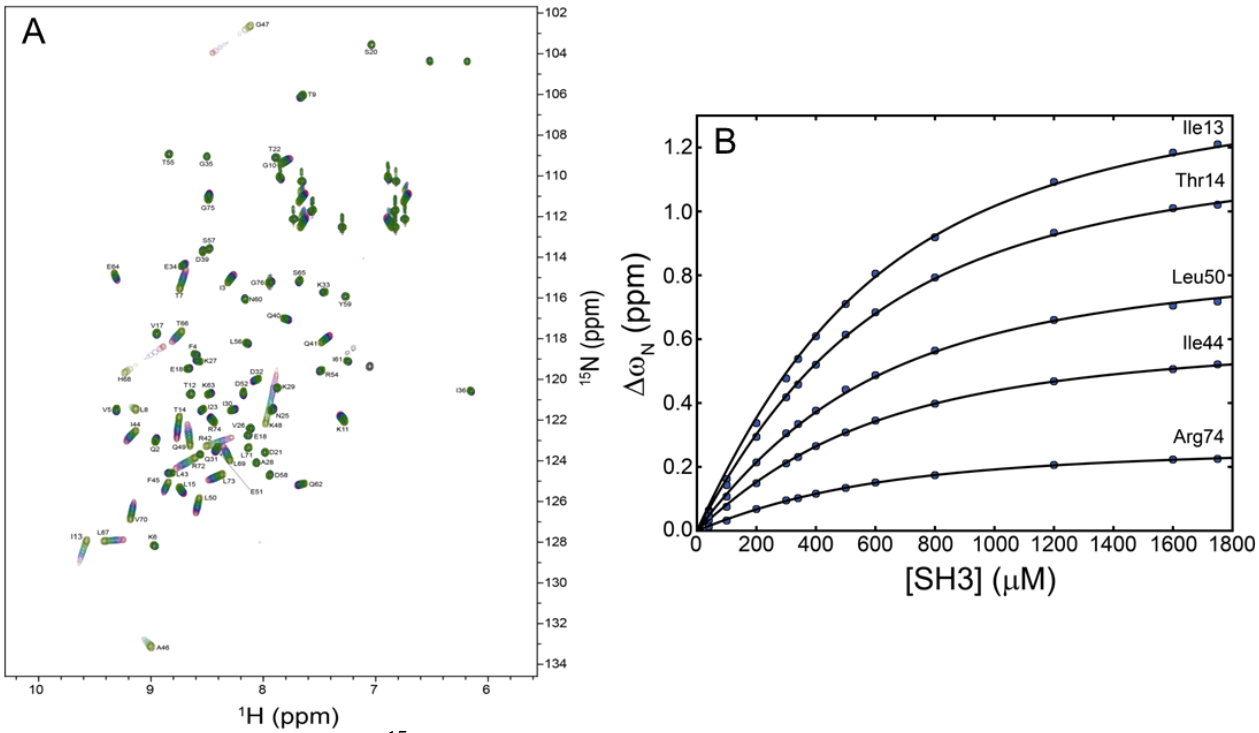

Figure 34 (A) Resonances of ^{15}N labeled ubiquitin are monitored via a series of HSQCs where the concentration of SH3 is increased. Free ubiquitin corresponds to the spectrum in green and the titrated solution that went up to an SH3/ubiquitin ratio of 4.4 is in red. (B) Binding isotherms of select residues as a function of increasing concentration of SH3. The ubiquitin concentration was kept constant at 400 μM and all experiments were conducted at 298 K.

same interaction surface as ubiquitin was not determined. This SH3 domain provides singular binding isotherms and appears to be a promising avenue as a system to explore the conformational sampling dynamics of ubiquitin (Figure 29) during a binding interaction.

6.4 Materials and Methods

HSQC based titrations For all titrations, stock solutions were prepared in which the ligand was kept at a high concentration and the protein concentration was kept constant. The acquisition parameters for each titration can be found in Table 7. Between each point the sample was given fifteen minutes to equilibrate in the magnet in order to ensure consistency between each point. All experiments employed sufficient dummy scans before the acquisition of any data and used recycle delays of one second. All spectra were processed using the NMRPipe software package

[121] and were visualized in CARA [122]. ^{15}N chemical shifts were used for the global analysis if the difference between the chemical shift value at the highest concentration of ligand and the free form exceeded 0.2 ppm [189]. All spectra zero-filled in both dimensions up with 8192 points.

	$t_{1,max}$ (complex points)	$t_{2,max}$ (complex points)
^{15}N ubiquitin – Dsk2	32 ms (100)	48 ms (512)
^{15}N Dsk2 – ubiquitin	83 ms (256)	48 ms (512)
^{15}N ubiquitin – SH3	55ms (150)	98 ms (1024)
^{15}N ubiquitin – Dsk2$^{R356\ (1)}$	77 ms (160)	61 ms (512)

Table 7 Experimental acquisition parameters for the aforementioned HSQC titrations (1) Acquisition details for Appendix Figure 13.

The models used for the two-state and sigmoidal ligand dependence were taken from the literature using references [46,74,189,190]. An F-test was used to ascertain the statistical significance between models in cases where the sigmoidal binding isotherms were analyzed [155]. The uncertainties in the fitted parameters were determined using a conservative approach suggested from [192]. An error of 10 % in the concentrations form the addition of ligand to the protein solution, or from the stock solution was assumed. This effectively shifts the data points along the abscissa. 1000 data sets were created using a normal distribution whose mean was centered at these shifted concentrations and then subsequently refit. The standard deviation from each minimization was used as the error in the extracted parameter. Assumed errors from both sources did not perturb the mean position of the K_D and gave similar error bars.

CT-CPMG and TRACT CT-CPMG experiments (Chapter 5) were performed using the sequence in Figure 28 with a TROSY readout for the measurements made at a lower temperature and the pulse code can be found in the Pulse Program section of this dissertation. Refocusing frequencies were varied between 80 and 960 Hz with several duplicates used for error estimation. The constant-time length of was set to 50 ms. Experiments were conducted using both 600 and

800 MHz spectrometers. Analysis of the data was done in an identical manner as was described in Chapter 5 and was fit using the LM model. The temperature was set to 283 K. All TRACT experiments were recorded at 298 K using a spectrometer operating at a ^{1}H Larmor frequency of 600 MHz. Delays for sampling the relaxation rate of the α and β state were varied between 2 and 220 ms. Integration was taken over a window of 6.5 to 9.0 ppm, but changing this window did not affect the determination of τ_C. The functions used to extract τ_C can be found in reference [65].

Summary

The supra-τ_C range which is a time window that spans four orders of magnitude [11] was not accessible by kinetic type measurements. Through the use of super-cooled RD [109,112] focused on ^{15}N nuclei, chemical shift variance calculations on RDC conformational ensembles, and solution DR we could elucidate kinetics within the ground-state ensemble of ubiquitin (Chapter 2). At physiological temperatures the conformer interconversion lifetime was found to be between 1 and 19 μs. It was also demonstrated that RDC based ensembles [11,111,112] can have predictive power for qualitative estimation of conformational amplitudes detectable by RD experiments. The high complementarity between solution DR and super-cooled RD outlined from Chapter 2 can open the doors for functional studies on other systems of interest that may display motion from the supra-τ_C range.

Experimental limitations rendered the observation of only two nuclei, one of which Ile13, that had not been observed before by RD experiments (Chapter 2). Since studies into the supra-τ_C range were restricted to 40 μs we focused on extending this border for ^{15}N nuclei. In order to achieve this we demonstrated that the use of cryogenically-cooled probeheads, a device found in many NMR based laboratories, could be safely applied to access motions up to 25 μs (Chapter 3). When compared to previous specified limitations this reflects an improvement by a factor of 3.2. Validation was provided by comparing previously published lifetimes [44,108,112] with the ones determined using large amplitude spin-lock fields. Additional advantages were realized not only in the increased level in quantitation of RD data, but by utilizing cryo-probeheads the increased sensitivity coupled with on-resonance experiments permitted the observation of resonances that displayed smaller conformational amplitudes (Chapter 3). We expanded on the use of large-

amplitude spin-lock fields by pursuing such measurements on ^{13}C and ^{1}H nuclei (Chapter 4). We could attain unprecedented increases that now place the minimum observable lifetimes to 10 and 4 μs for ^{13}C and ^{1}H, respectively. This approach was then applied to ^{13}C methyl nuclei in which 10 methyl carbon sites reported relaxation dispersion and interestingly, methyl ^{1}H sites were relaxation dispersion silent at 277 K with the maximum spin-lock strengths used here. The extracted exchange lifetimes for the methyl nuclei (Chapter 4) were similar to that of backbone nuclei (Chapter 2 & 3) in which global fitting of all nuclei revealed a common timescale of motion with a lifetime of 55- 60 μs at 277 K. The potential differences between methyl carbon and methyl proton sources of RD were analyzed and determined to stem dihedral changes of methyl carbon nuclei. However, rotamer jumps on the microsecond timescale could not reconcile the experimentally observed conformational amplitudes. Instead, upon analysis of MD simulations [150], which coincide with the timescale for rotameric jumps (pico- to nanosecond) [149], performed on ubiquitin in complex with a variety of binding partners revealed that depending on the motion experienced by the backbone and side chain elements predicated population shuffling between assumed rotamer states. A new model emerged that while depending on the degree of openness between the backbone and side chain the populations of rotameric states are shuffled (Chapter 4). Namely, that the relaxation dispersion from the methyl nuclei reported on the relative population differences and not just on discrete interconversion events.

From Chapter 5, an experimental approach for attaining enhanced accuracy of kinetics derived from the commonly used CT-CPMG was demonstrated. For ^{15}N nuclei, CT-CPMG experiments are typically limited to observing kinetic lifetimes up to 150 μs [90,91], and it was shown that within the fast-exchange regime the extraction of kinetic rate constants can be

compromised without knowledge of the intrinsic relaxation rate. An experiment was developed, HEROINE, which monitors the exact same coherences as in the CT-CPMG experiment. However, HEROINE uses large amplitude spin-lock fields (Chapter 3) to measure the relaxation rate at the end-point of the dispersion curve. The use of high powered spin-lock fields permits a more veracious relaxation rate in which motions up to 25 μs are removed. This was tested on two systems and in the case for OAA without the HEROINE determined rate kinetic rates would have been underestimated by 66 % (Chapter 5) in one example. Additionally in contrast to conventional relaxation measurements, which do not probe the same coherences as in CT-CPMG experiments, HEROINE provides a facile method that is directly comparable.

Recent endeavors towards the determination of conformer sampling events during an interaction event were presented in Chapter 6. So far two ubiquitin binding partners have been tested the UBA domain of Dsk2p [181] and the SH3-C domain of CIN85 [182,183]. Multiple binding modes were detected in the Dsk2 molecule and were confirmed by using reverse titrations with labeled Dsk2 and CT-CPMG experiments of just Dsk2 alone. Although this is not immediately favorable for understanding sampling kinetics in ubiquitin, further analysis and mutational work could resolve the nontrivial binding behavior that was observed for native Dsk2. Still this study underlies the strengths of NMR based approaches for monitoring binding events. HSQC based approaches allow for rapid determination of dissociation constants, but lowly populated intermediates observed via RD experiments can provide increased detail to complex binding mechanisms while maintaining atomic resolution. Alternatively, the SH3 system gave characteristic binding curves for a single binding mode. Further work will be necessary to completely ascertain ubiquitin's binding kinetics with SH3 in hopes of experimentally defining

the kinetic rates that dictate the interplay between conformational selection and the induced-fit binding mechanisms [104].

Relaxation dispersion has arisen as a powerful tool for the investigation of micro- to millisecond motions in proteins [27,32,33,68,69,106,112,128,139,157,193-195]. Their use and efficacy has been further extended in this dissertation. Even though a large dedication was given to the small protein, ubiquitin, kinetic measurements within the supra-τ_C range are now feasible [112] and can be probed with motions as fast as 25 (^{15}N nuclei) [129], 10 (^{13}C nuclei), and 4 (^{1}H nuclei) μs. As long as the system is tractable for solution NMR studies it can be done without having to work in the solid-state or having to make chemical modification to the system of interest therefore making it an ideal avenue for more physiologically relevant studies. As it becomes increasingly transparent that the dynamics of a system can govern its function, the experimental and theoretical approaches outlined here can help in validating, testing, or reinforcing our understanding of the complex and dynamic nature of systems of biological interest.

Appendix

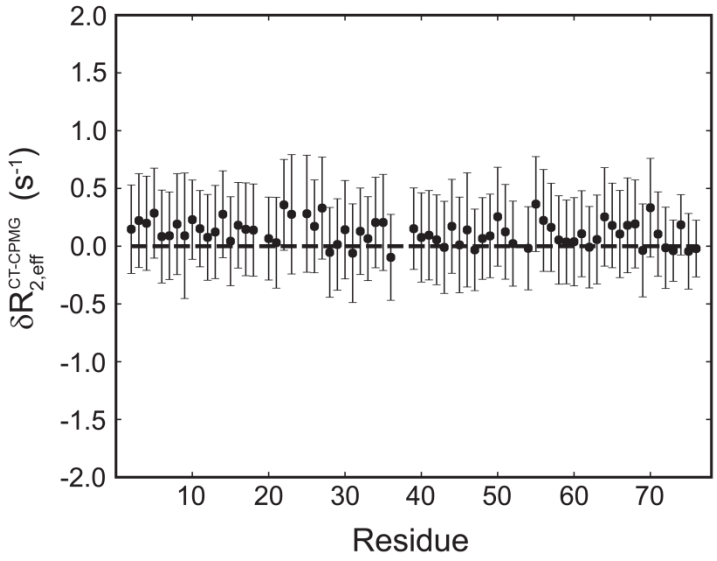

Appendix Figure 1 The difference between $R_{2,eff}$ at low (ν_{CPMG} = 67 Hz) and high (ν_{CPMG} = 1000 Hz) measured from a conventional CT-CPMG experiment. Data for 72 observable residues across ubiquitin measured at 298 K are represented. No residues gave statistically significant dispersion at this high temperature, and the dashed line is plotted at 0 s^{-1} to guide the eye. The errors in $\delta R_{2,eff}^{CT-CPMG}$ were propagated as the sum of the errors from the low and high frequency measurements.

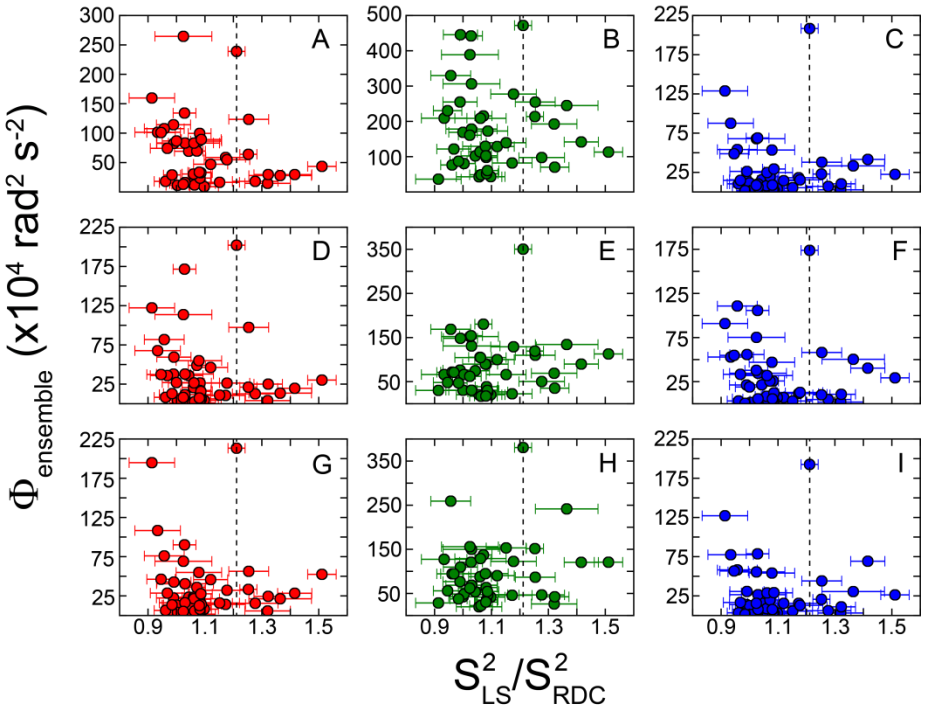

Appendix Figure 2 Scatter plots of the predicted chemical shift variance from the RDC-enforced ensembles compared to the ratio between internuclear vector fluctuations from motions up to τ_c (S^2_{LS}; Lipari-Szabo type order parameter [116]) and motions including the supra-τ_c range (S^2_{RDC}). $\Phi_{ensemble}$ was calculated for the EROS (A-C) [11], EROSII (D-F) [112], and ERNST (G-I) [111] ensembles using the SHIFTX [113], SHIFTS [114], and SPARTA [115] chemical shift prediction programs (red, green, and blue points, respectively). The dashed line drawn through each plot goes through Val70. Points after the dashed line indicate amides with greater mobility than Val70 from motions on the supra-τ_c range. The errors in S^2_{LS}/S^2_{RDC} are propagated from the error in S^2_{RDC} [102]. For Ile13, there is no reported S^2_{LS}.

Appendix Table 1 Conformational exchange parameters for ubiquitin residues probed by the super-cooled RD experiments

Residue		260 K[a]	265 K	269 K	273 K	277 K	280 K[b]
Ile13	τ_{ex} (μs)	-	122 ± 40[c]	90 ± 50[c]	63 ± 17[c]	61 ± 20[c]	-
	Φ_{ex} (10^3 rad^2 s^{-2})	-	48 ± 30	40 ± 36	51 ± 47	32 ± 28	-
Ile23	τ_{ex} (μs)	-	73 ± 20	-	101 ± 42	84 ± 24	43 ± 6
	Φ_{ex} (10^3 rad^2 s^{-2})	-	170 ± 40	-	102 ± 52	113 ± 41	117 ± 14
Asn25	τ_{ex} (μs)	-	100 ± 20	99 ± 33	80 ± 19	72 ± 6	43 ± 5
	Φ_{ex} (10^3 rad^2 s^{-2})	-	213 ± 30	245 ± 21	238 ± 123	185 ± 22	229 ± 32
Thr55	τ_{ex} (μs)	-	-	-	-	-	40 ± 13
	Φ_{ex} (10^3 rad^2 s^{-2})	-	-	-	-	-	59 ± 17
Val70	τ_{ex} (μs)	133 ± 28[d]	90 ± 30[d]	109 ± 31[d]	66 ± 23[d]	67 ± 10[d]	38 ± 7[d]
	Φ_{ex} (10^3 rad^2 s^{-2})	390 ± 80	120 ± 60	87 ± 27	120 ± 65	54 ± 14	85 ± 13

[a]measurements previously reported by Mills et al. [109]

[b]measurements previously reported by Massi et al. [108]

Previous interpretations of kinetic measurements on ubiquitin

Ubiquitin has been a system of focus for the development and testing of new NMR methodologies. That being said there are many other sources of information pertaining to its motion from a wide range of timescales [63,108,112,196]. Here, we will focus on other RD experiments that have been conducted on ubiquitin and that appear in the literature. An initial study by Massi and coworkers [108] reported microsecond motions for Ile23, Asn25, Thr55, and Val70 in ubiquitin. Observed RD was explained using a discrete two-state model. A minor population (p_B) of 0.02 was estimated from the random coil chemical shift for Valine (~6 ppm). This value for p_B was used under the presumptuous justification that all native contacts are lost for Val70 and is thus the cause for the observable dispersion. This is unlikely considering the stability of Val70's contacts, for example its hydrogen bonding with Arg42 has been shown to be extremely stable over a broad range of temperatures and pressures [197,198]. Still, this value for p_B was further used in their work to interpret the motions for Ile23, Asn25, and Thr55. From which, a discrete two-state hydrogen bond reordering process with a forward lifetime of $\tau_1 \approx 2$ milliseconds was determined. In order to check the observed dispersion at 280 K a back calculation was done assuming an expected upfield shift of 4.5 ppm for ^{15}N Threonine nuclei when a hydrogen bond is disrupted [108,199]. For reconciliation of the observed Φ_{ex} at 280 K for Ile23 a 1.5 ppm upfield shift was assumed for a disrupted hydrogen bond plus a χ_1 change from -60° to +60° (attributed with a 4.5~5.0 ppm change) was then used to back calculate Φ_{ex} for Ile23. Although, under their assumptions back calculations for Ile23 and Thr55 were within error, Asn25 would require an unrealistically large value of $\Delta\omega$ ~9 ppm to match the experimentally determined Φ_{ex}. No further interpretation was given for Asn25 and Val70 in their report.

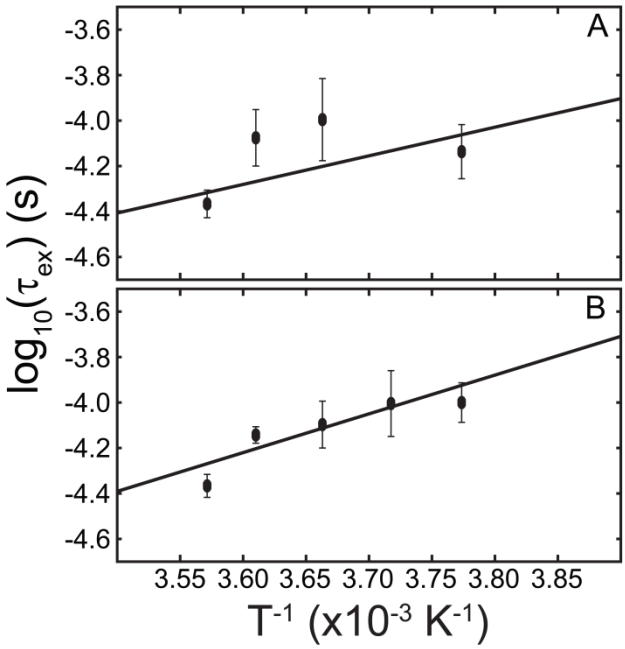

Appendix Figure 3 Arrhenius dependence for Ile23 (A) and Asn25 (B). Activation energies for Ile23 and Asn25 were 24 ± 19 and 33 ± 14 kJ/mol, respectively derived from the super-cooled $R_{1\rho}$ experiments.

However, from our temperature dependence of τ_{ex}, the Arrhenius extrapolation revealed a similar activation energy for Asn25 when compared to Ile13 and Val70 (Appendix Figure 3). Additional insight can be reached by looking at the temperature dependence of Φ_{ex} from the super-cooled RD.

In Appendix Figure 3, the Φ_{ex} values from the temperature dependent super-cooled $R_{1\rho}$ experiments are presented. With a pure two-state process one would expect that the Φ_{ex} values would decrease with decreasing temperature because p_B would decrease. From Appendix Figure 3, this is not the case especially for Asn25 (Appendix Figure 3C) where the error for the Φ_{ex} is the smallest, and no trend towards a diminishing Φ_{ex} can be seen as the temperature decreases. Therefore, the use of only a two-state model to describe the observed RD may not be a correct one, or is too simplistic to fully describe the exchange event. Additionally, the observed RD for

Asn25 may not stem solely from an excited state model, but might be overlapped with another process, namely the ground-state sampling of ubiquitin conformers, and is different to what was initially postulated from Massi and coworkers.

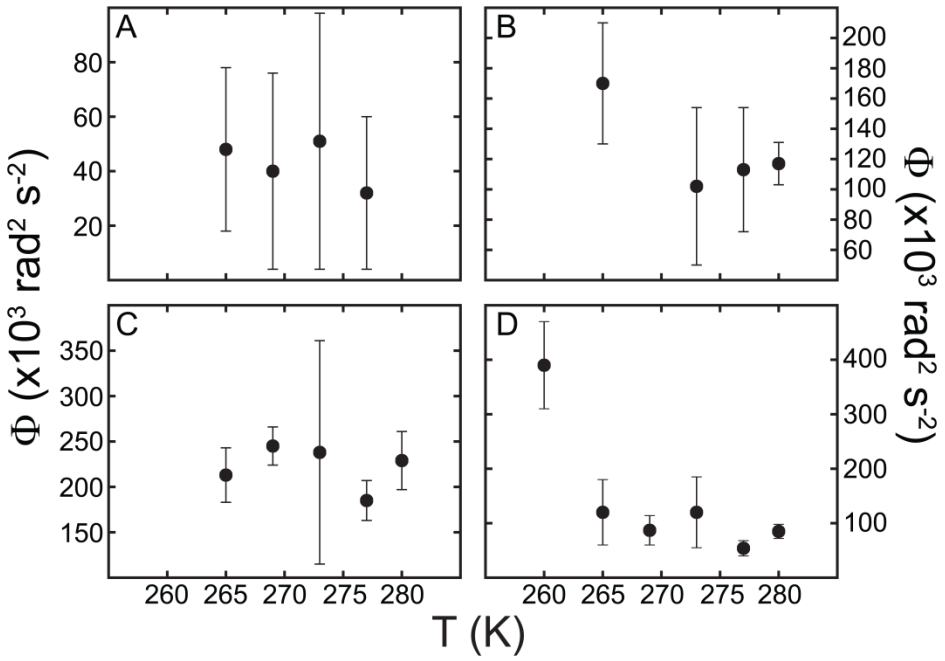

Appendix Figure 4 Experimentally determined Φ_{ex} from off-resonance $R_{1\rho}$ experiments (Chapter 2) conducted in super-cooled and low temperature conditions plotted for Ile13 (A), Ile23 (B), Asn25 (C), and Val70 (D).

A recent publication in which mutants of ubiquitin were made for Glu24 and Gly53, two resonances that are broadened beyond detection in a [^{1}H,^{15}N]-HSQC due to chemical exchange, were identified to produce a unique hydrogen bond that is formed between the side chain carboxyl group of Glu24 and the nitrogen backbone site of Gly53 [200]. Two mutants, Glu24Ala and Gly53Ala were created and then their exchange contributions from conventional relaxation measurements determined. Their Lipari-Szabo analysis was conducted at 278 K and found that by mutation of Glu24 to alanine the exchange contribution, determined from model fitting, for

Ile23, Asn25, and Thr55 vanished indicating that the large source of their observed exchange contribution may be predominately from the reordering between Glu24 and Gly53 [200]. Importantly, in their measurements, Val70 retained its exchange contribution even with the dissolution of the hydrogen bond reordering of Glu24 and Gly53 within the mutants. Thus, providing further evidence that Val70's exchange contribution does not arise from the previously stated hydrogen bond reordering process. The authors did not detect any exchange contribution via the conventional Lipari-Szabo data fitting routine for Ile13. The formation and breaking of this hydrogen bond has been attributed to cause a peptide bond flip in Asp52 which has been observed in several structures of ubiquitin in complex with binding partners [200,201]. This peptide bond flip also exists in the EROS and EROSII ensembles. At this point it is important to mention that lowly populated states are not expected to exist in the RDC-derived ensembles because a small population would hardly change the RDC values ($RDC_{obs} = \sum_{i}^{N} p_i RDC_i$). Indeed, Ile23, Asn25, and Thr55 did not show significant $\Phi_{ensemble}$ values when ^{15}N chemical shifts ($\delta_{15N}^{Predicted}$) were predicted from the RDC-derived ensembles (Figure 4). In the above measurements (Chapter 2), Thr55 did not show dispersion up to 260 K indicating that the effect of this process does not contribute in super-cooled conditions (Chapter 2; [109,112]).

However, even with the identification of the role Glu24 and Gly53 have on perturbing the chemical environments for Ile23, Asn25, and Thr55 [200] it is important to consider that the process may not be a discrete two-state event deriving solely from motion of their nitrogen sites. Further information may be attained into the complex behavior of these residues by performing in depth temperature dependent RD experiments using high-powered ^{1}H RD in order to visualize their Φ_{ex} values over a broad range of temperatures.

Cross-correlated relaxation rates measured for N-C_α, N-C', and C'-C_α have also been used to identify the same "hotspot" as described above, but lacked in any kinetic information [202,203]. After publication of reference [112], another report in which multiple quantum (MQ) coherences were probed in a transverse rotating frame experiment has retained similar kinetics for Ile23, Thr55 and Val70 at 277 K [44]. In the MQ-RD experiment, dispersion relies not only on the modulation of a single nucleus, as in the single quantum experiments carried out above, but on the chemical shift differences experienced by two nuclei. In the aforementioned MQ-RD experiments case auto and cross relaxation mechanisms between $^{15}N/^{1}H^{N}$ sites compound the measurement in addition to a contribution from chemical exchange. The amplitude of the dispersion is then proportional to chemical shift differences for both ^{15}N and $^{1}H^{N}$ and their respective change in the sign of the chemical shift. Although, the extracted kinetic information [44] was similar to what has been previously presented [112,133] an in-depth analysis into a mechanism for the motion was not pursued. It is interesting to comment that the same concept was employed by the same group, but weaker refocusing fields were implemented in the form of a CPMG experiment where the same sites were found, but their older determined timescales are lower by a factor of three [196]. Their new measurements using stronger refocusing fields are in accordance with the super-cooled RD measurements (Chapter 3).

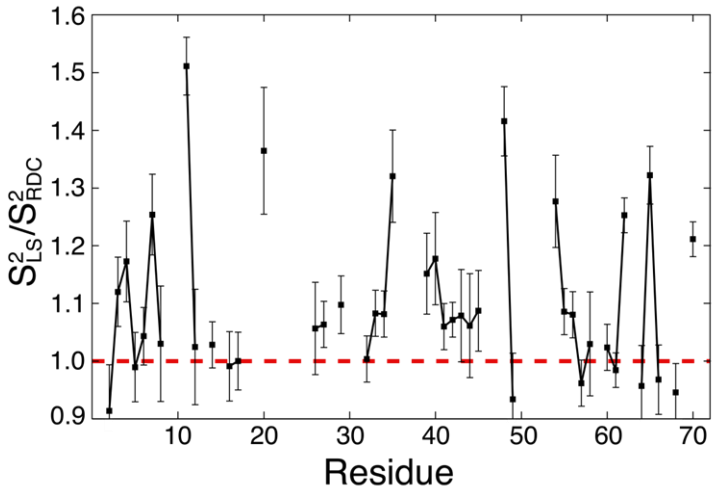

Appendix Figure 5 The ratio between S^2_{LS} and S^2_{RDC} for residues in ubiquitin where both order parameters have been determined. Residues with a ratio greater than one indicate additional modes of motion from within the supra-τ_c range. Lipari-Szabo and RDC order parameters come from Tjandra et al. and Lakomek et al. [102,116]. Val70 is the residue at the rightmost place on the plot.

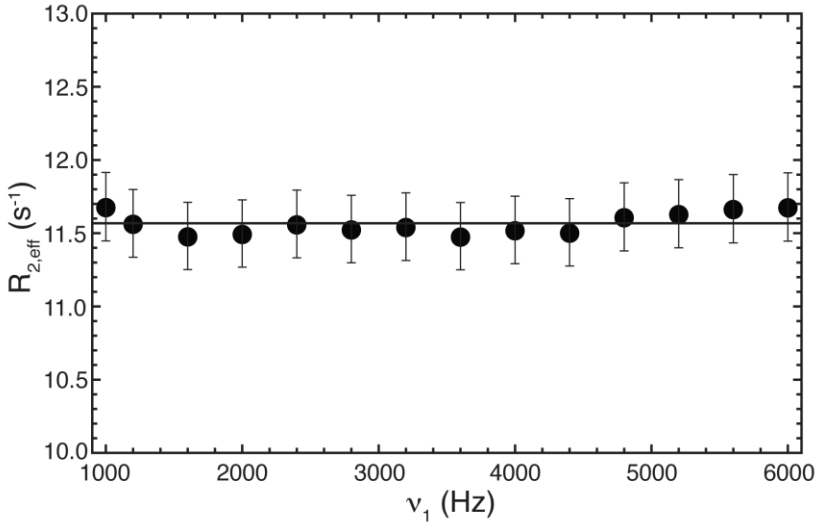

Appendix Figure 6 Dispersion curve for ^{15}N backbone site of Leu15 that shows no exchange contribution to $R_{2,eff}$. The dispersion curve was measured as described in the main text, and temperature fluctuations were effectively controlled as a flat dispersion curve was obtained.

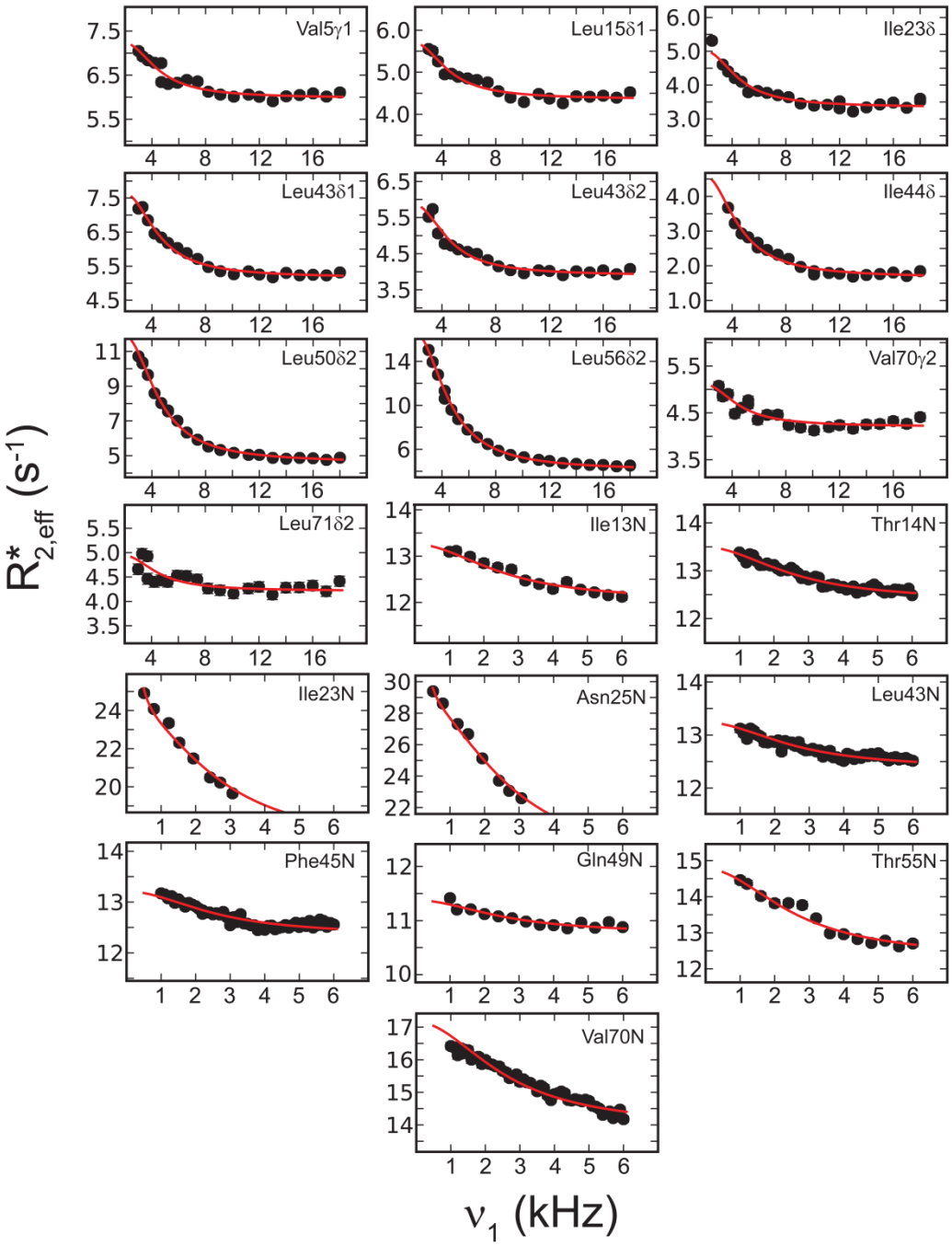

Appendix Figure 7 Global fits (red curves) to all acquired dispersion data for ^{13}C methyl and backbone ^{15}N nuclei plotted as a function of the utilized spin-lock strength (ν_1). For most data points the error bars are within the black data points.

Appendix Table 2 Exchange parameters that define the observed dispersion for methyl ^{13}C and ^{15}N backbone residues fitted individually, for each nucleus type, and then both ^{15}N and ^{13}C fitted globally.

	Individual $^{13}C/^{15}N$	Global: $^{13}C/^{15}N$	Global: ^{13}C & ^{15}N
Val5γ1			
τ_{ex} (μs)	66 ± 16	61 ± 1	61 ± 1
Φ_{ex} (x10^3 rad^{2}s^{-2})	18.8 ± 4.1	20.0 ± 1.1	20.6 ± 1.2
$R_{2,0}$ (s^{-1})	5.99 ± 0.05	5.98 ± 0.02	5.97 ± 0.03
R_1 (s^{-1})	0.00 ± 0.28	0.00 ± 0.00	0.00 ± 0.00
Leu15δ1			
τ_{ex} (μs)	58 ± 14	61 ± 1	61 ± 1
Φ_{ex} (x10^3 rad^{2}s^{-2})	23.2 ± 5.8	22.7 ± 1.0	22.5 ± 1.0
$R_{2,0}$ (s^{-1})	4.34 ± 0.06	4.34 ± 0.02	4.34 ± 0.03
R_1 (s^{-1})	0.09 ± 25.2	1.02 ± 1.95	0.88 ± 0.90
Ile23δ			
τ_{ex} (μs)	89 ± 8	61 ± 1	61 ± 1
Φ_{ex} (x10^3 rad^{2}s^{-2})	22.4 ± 1.4	28.6 ± 1.1	28.2 ± 1.2
$R_{2,0}$ (s^{-1})	3.41 ± 0.03	3.32 ± 0.03	3.32 ± 0.03
R_1 (s^{-1})	0.00 ± 0.05	0.00 ± 0.10	0.00 ± 0.09
Leu43δ1			
τ_{ex} (μs)	57 ± 11	61 ± 1	61 ± 1
Φ_{ex} (x10^3 rad^{2}s^{-2})	41.9 ± 6.8	41.1 ± 1	39.8 ± 1.1
$R_{2,0}$ (s^{-1})	5.14 ± 0.07	5.14 ± 0.02	5.16 ± 0.02
R_1 (s^{-1})	0.00 ± 13.4	0.00 ± 0.93	0.00 ± 1.12
Leu43δ2			
τ_{ex} (μs)	71 ± 10	61 ± 1	61 ± 1
Φ_{ex} (x10^3 rad^{2}s^{-2})	28.7 ± 2.9	31.7 ± 1.2	31.7 ± 1.5
$R_{2,0}$ (s^{-1})	3.94 ± 0.04	3.89 ± 0.03	3.89 ± 0.03
R_1 (s^{-1})	0.00 ± 0.46	0.00 ± 0.00	0.00 ± 0.00
Ile44δ			
τ_{ex} (μs)	53 ± 5	61 ± 1	61 ± 1
Φ_{ex} (x10^3 rad^{2}s^{-2})	49.4 ± 2.0	47.4 ± 1.3	48.8 ± 1.6
$R_{2,0}$ (s^{-1})	1.62 ± 0.04	1.65 ± 0.02	1.63 ± 0.03
R_1 (s^{-1})	0.00 ± 0.04	0.00 ± 0.00	0.00 ± 0.00
Leu50δ2			
τ_{ex} (μs)	58 ± 4	61 ± 1	61 ± 1
Φ_{ex} (x10^3 rad^{2}s^{-2})	122.3 ± 9.1	119.5 ± 0.8	118.9 ± 1.0
$R_{2,0}$ (s^{-1})	4.53 ± 0.11	4.57 ± 0.02	4.57 ± 0.02
R_1 (s^{-1})	0.00 ± 1.87	0.00 ± 0.02	0.00 ± 0.02
Leu56δ2			

τ_{ex} (μs)	64 ± 6	61 ± 1	61 ± 1
Φ_{ex} (x10^3 rad^{2}s^{-2})	194.5 ± 16.2	200.2 ± 1.7	203.9 ± 1.9
$R_{2,0}$ (s^{-1})	4.19 ± 0.21	4.11 ± 0.04	4.05 ± 0.05
R_1 (s^{-1})	0.00 ± 5.76	0.00 ± 0.04	0.00 ± 0.00
Val70γ2			
τ_{ex} (μs)	59 ± 11	61 ± 1	61 ± 1
Φ_{ex} (x10^3 rad^{2}s^{-2})	15.1 ± 2.0	14.8 ± 1.0	16.7 ± 1.1
$R_{2,0}$ (s^{-1})	4.20 ± 0.04	4.20 ± 0.03	4.17 ± 0.03
R_1 (s^{-1})	0.00 ± 0.06	0.00 ± 0.00	0.00 ± 0.01
Leu71δ2			
τ_{ex} (μs)	80 ± 31	61 ± 1	61 ± 1
Φ_{ex} (x10^3 rad^{2}s^{-2})	8.9 ± 2.2	10.7 ± 1.3	9.9 ± 1.4
$R_{2,0}$ (s^{-1})	4.27 ± 0.04	4.23 ± 0.03	4.24 ± 0.03
R_1 (s^{-1})	0.00 ± 0.12	0.00 ± 0.00	0.00 ± 0.00
Ile13N			
τ_{ex} (μs)	50 ± 9	56 ± 2	61 ± 1
Φ_{ex} (x10^3 rad^{2}s^{-2})	28.9 ± 7.1	22.3 ± 2.0	24.1 ± 1.4
$R_{2,0}$ (s^{-1})	11.82 ± 0.14	11.97 ± 0.06	11.92 ± 0.05
Thr14N			
τ_{ex} (μs)	62 ± 6	56 ± 2	61 ± 1
Φ_{ex} (x10^3 rad^{2}s^{-2})	18.5 ± 2.0	20.3 ± 0.8	18.9 ± 0.4
$R_{2,0}$ (s^{-1})	12.35 ± 0.04	12.31 ± 0.02	12.35 ± 0.01
Ile23N			
τ_{ex} (μs)	84 ± 24	56 ± 2	61 ± 1
Φ_{ex} (x10^3 rad^{2}s^{-2})	113 ± 41	143.1 ± 4.2	133.6 ± 3.5
$R_{2,0}$ (s^{-1})	16.82 ± 1.17	16.23 ± 0.18	16.48 ± 0.14
R_1 (s^{-1})	0.16 ± 1.37	0.67 ± 0.11	0.57 ± 0.08
Asn25N			
τ_{ex} (μs)	72 ± 6	56 ± 2	61 ± 1
Φ_{ex} (x10^3 rad^{2}s^{-2})	185 ± 22	196.5 ± 5.6	197.7 ± 3.7
$R_{2,0}$ (s^{-1})	18.15 ± 0.71	17.87 ± 0.21	17.74 ± 0.13
R_1 (s^{-1})	0.02 ± 1.62	0.76 ± 0.13	0.47 ± 0.07
Leu43N			
τ_{ex} (μs)	75 ± 10	56 ± 2	61 ± 1
Φ_{ex} (x10^3 rad^{2}s^{-2})	10.6 ± 1.0	14.9 ± 1.2	12.7 ± 0.8
$R_{2,0}$ (s^{-1})	12.45 ± 0.03	12.34 ± 0.03	12.40 ± 0.02
Phe45N			
τ_{ex} (μs)	82 ± 12	56 ± 2	61 ± 1
Φ_{ex} (x10^3 rad^{2}s^{-2})	12.2 ± 1.0	13.8 ± 1.0	14.6 ± 0.4
$R_{2,0}$ (s^{-1})	12.39 ± 0.03	12.35 ± 0.03	12.33 ± 0.01
Gln49N			
τ_{ex} (μs)	101 ± 32	56 ± 2	61 ± 1

Φ_{ex} ($x10^3$ rad^2s^{-2})	7.1 ± 1.2	11.8 ± 1.1	9.4 ± 0.9
$R_{2,0}$ (s^{-1})	10.84 ± 0.06	10.72 ± 0.03	10.78 ± 0.03
Thr55N			
τ_{ex} (μs)	51 ± 5	56 ± 2	61 ± 1
Φ_{ex} ($x10^3$ rad^2s^{-2})	52.7 ± 7.0	48.8 ± 2.3	45.5 ± 1.8
$R_{2,0}$ (s^{-1})	12.01 ± 0.15	12.08 ± 0.08	12.16 ± 0.05
Val70N[1]			
τ_{ex} (μs)	38 ± 4	56 ± 2	61 ± 1
Φ_{ex} ($x10^3$ rad^2s^{-2})	87.0 ± 13.0	62.1 ± 3.7	52.7 ± 1.3
$R_{2,0}$ (s^{-1})	13.2 ± 0.56	13.69 ± 0.10	13.90 ± 0.03

[1] Val70N was fit with the full dispersion curve composed of 51 different field strengths.

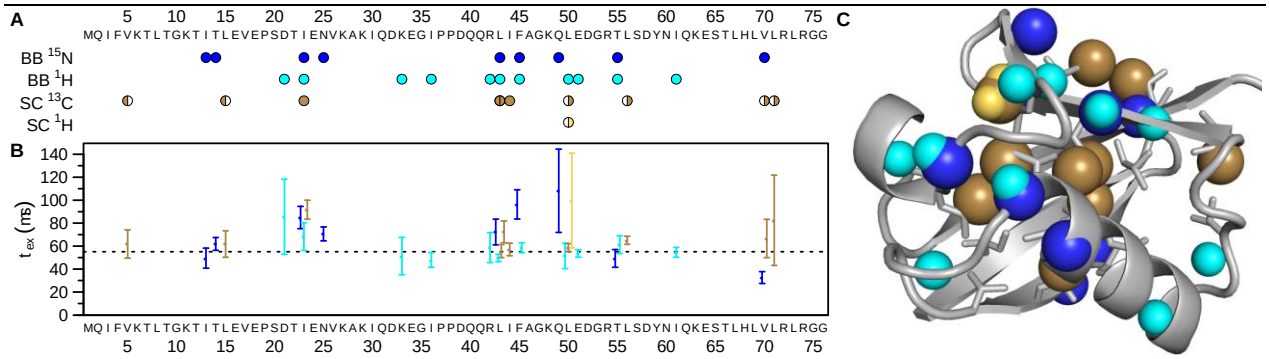

Appendix Figure 8 (A) 31 nuclei in total that have been detected to undergo an exchange event are plotted across the residue number. The individual fits to all nuclei (B) indicate a common timescale of motion that was determined globally to be a τ_{ex} of 55 μs (B; dashed line). The sites that have been measured are not locally conserved, but are spread throughout the structure of ubiquitin (C). In blue, cyan, brown, and yellow are the backbone ^{15}N, backbone $^{1}H^{N}$, methyl ^{13}C, and methyl ^{1}H nuclei, respectively. Figure courtesy of Dr. Colin Smith (MPI-BPC, Dept. Theoretical and Computational Biophysics)

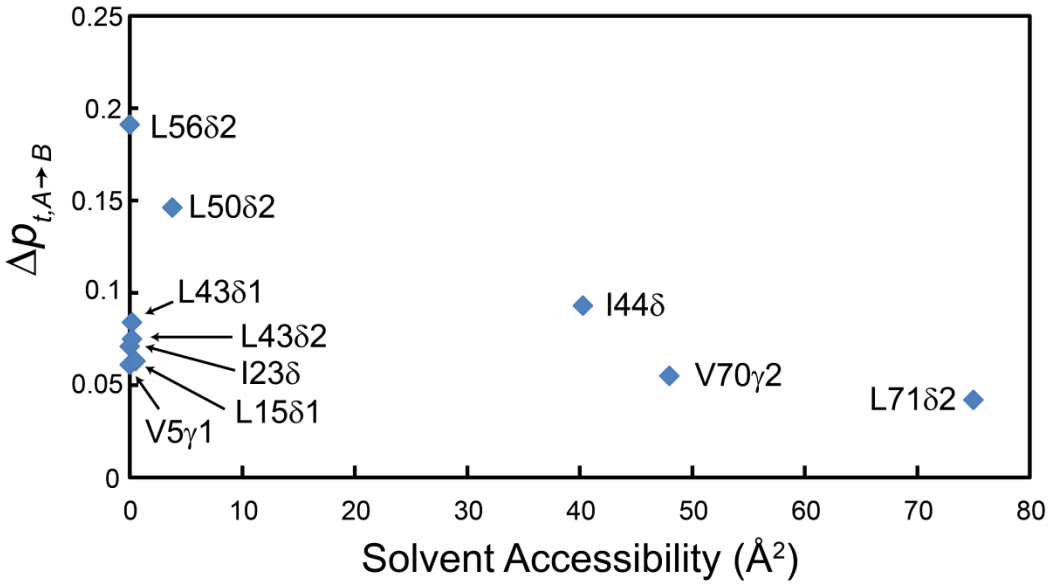

Appendix Figure 9 Solvent accessibility for all methyl groups that reported on having microsecond fluctuations at 277 K compared with their calculated relative population changes to the trans position ($\Delta p_{t,A\rightarrow B}$). There is no clear correlation between the population shuffling of methyl groups and their accessibility with the solvent. The Pearson correlation coefficient was 0.41. The solvent accessibility was calculated using the PYMOL program.

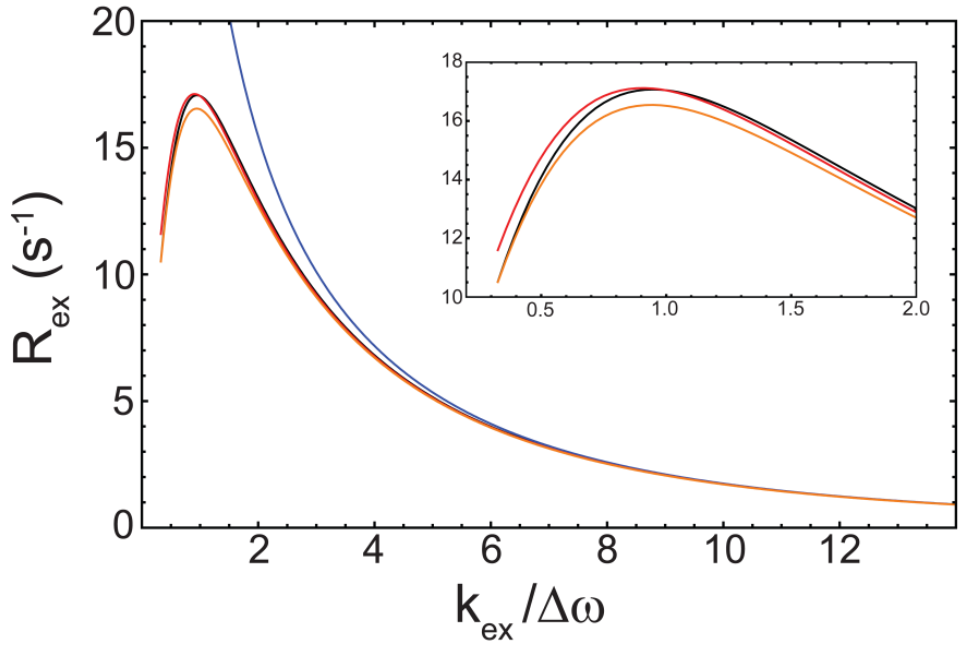

Appendix Figure 10 Dependence of chemical exchange (R_{ex}) on $k_{ex}/\Delta\omega$ using the simulation parameters in Figure 24 of Chapter 4. The analytical Carver-Richards equation [174], that is valid over all timescales is plotted as the black curve. Bloch-McConnell (BM) [161] equations with $R_{2,eff}$ calculated over the major state (p_a) and summed over both major and minor states are shown in orange and red, respectively. The Luz-Meiboom (LM) [162] equation is presented as the blue curve. For the LM model, overestimation in R_{ex} produces an asymptotic profile in Figure 1 when $k_{ex}/\Delta\omega$ < ~3 and leads to a larger fractional error in k_{ex} from the simulations in Figure 1. At $k_{ex}/\Delta\omega$ ~3 there is only a 5% difference in R_{ex} calculated with the LM formalism as compared to the Carver-Richards equation. The BM model is a numerical solution and is also valid over all timescales like the Carver-Richards equation. As shown in the inset, the numerical model leads to a small 2-5% deviations in R_{ex} from the Carver-Richards solution over all ratios of $k_{ex}/\Delta\omega$. In the inset, the abscissa and ordinate are $k_{ex}/\Delta\omega$ and R_{ex}, respectively.

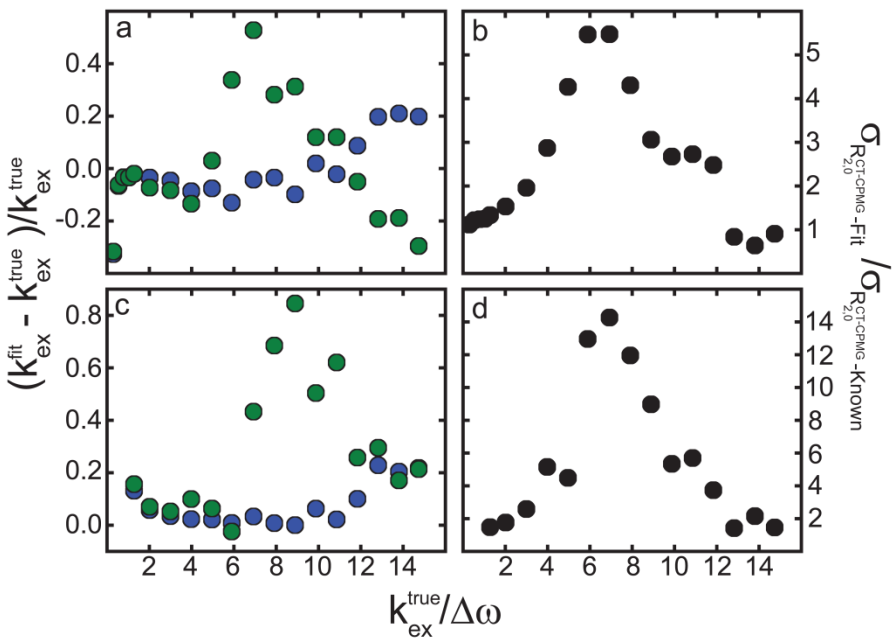

Appendix Figure 11 (a, c) Comparison of the fractional error in the exchange rate used to generate the synthetic data (k_{ex}^{true}). In a and c data sets were fit with $R_{2,0}^{CT-CPMG}$ taken as a known (blue circles) or fitted (green circles) parameters, respectively. (b, d) The extracted error in k_{ex}^{fit}, defined as the standard deviation (σ) of all minimizations for a given set, is plotted as the ratio in σ for a known $R_{2,0}^{CT-CPMG}$ ($\sigma_{R_{2,0}^{CT-CPMG}-Known}$) or as an adjustable parameter ($\sigma_{R_{2,0}^{CT-CPMG}-Fit}$) for fits to both BM (b) and LM (d) models. All synthetic data sets were created for a Larmor frequency of 60.8 MHz for ^{15}N.

Appendix Table 3 For OAA, 25 different ^{15}N nuclei gave appreciable exchange $R_{ex} \sim 2.0\ s^{-1}$. Their dispersion curves were fitted to the Bloch-McConnell (BM) and Luz-Meiboom (LM) models (see Chapter 5 for details) with and without the HEROINE determined $R_{2,0}^{CT-CPMG}$.

	$R_{2,0}^{CT-CPMG}$ **-Fit BM**	$R_{2,0}^{CT-CPMG}$ **- Known BM**	$R_{2,0}^{CT-CPMG}$ **- Fit LM**	$R_{2,0}^{CT-CPMG}$ **- Known LM**
Gln9				
k_{ex} (s^{-1})	493±1071	2427±1006	1966±809	2434±431
Φ_{ex} x10^3 (rad^2 s^{-2})	14.9±485	8.4±106	6.6±3.4	8.3±0.8
Trp10				
k_{ex} (s^{-1})	2178±1134	4834±484	2836±717	4837±356
Φ_{ex} x10^3 (rad^2 s^{-2})	16.7±92.5	33.4±2.4	16.0±6.1	33.2±1.5
Gly11				
k_{ex} (s^{-1})	2632±708	3685±146	2890±372	3686±147
Φ_{ex} x10^3 (rad^2 s^{-2})	29.9±54.6	40.3±1.2	29.5±4.3	40.2±1.0
Asn18				
k_{ex} (s^{-1})	2935±1016	1025±1010	2396±721	2942±401
Φ_{ex} x10^3 (rad^2 s^{-2})	10.3±104	11.7±167	8.0±3.3	10.2±0.9
Gly26				
k_{ex} (s^{-1})	2356±662	1192±393	2447±344	1856±116
Φ_{ex} x10^3 (rad^2 s^{-2})	21.1±16.5	21.3±20.7	20.7±3.2	15.4±0.6
Ser27				
k_{ex} (s^{-1})	2495±533	2656±266	2491±339	2660±136
Φ_{ex} x10^3 (rad^2 s^{-2})	25.9±5.8	27.8±2.9	25.7±3.7	27.7±0.9
Arg28				
k_{ex} (s^{-1})	1459±412	2350±330	2049±235	2355±148
Φ_{ex} x10^3 (rad^2 s^{-2})	21.1±31.9	21.4±2.9	18.3±1.9	21.2±0.7
Ser29				
k_{ex} (s^{-1})	2034±1097	2950±623	2559±590	2957±285
Φ_{ex} x10^3 (rad^2 s^{-2})	11.4±49.6	13.0±5.5	10.9±3.1	13.0±0.7
Gln31				
k_{ex} (s^{-1})	1700±578	2792±158	2320±229	2795±129
Φ_{ex} x10^3 (rad^2 s^{-2})	25.9±23.0	29.1±1.2	23.5±2.4	29.0±0.7
Asn32				
k_{ex} (s^{-1})	1444±716	2355±457	2066±461	2362±254
Φ_{ex} x10^3 (rad^2 s^{-2})	12.0±68.7	12.2±3.3	10.5±2.0	12.1±0.7
Val34				
k_{ex} (s^{-1})	2493±988	2776±466	2658±553	2781±220
Φ_{ex} x10^3 (rad^2 s^{-2})	23.0±63.8	24.1±6.6	22.7±5.6	23.9±1.1
Met51				
k_{ex} (s^{-1})	2450±4445	3849±721	2450±6854	3855±579
Φ_{ex} x10^3 (rad^2 s^{-2})	8.0±264	13.9±2.8	7.9±14.7	13.9±1.2

Gly55				
k_{ex} (s^{-1})	2333±718	2479±426	2334±482	2486±181
Φ_{ex} x10^3 (rad^2 s^{-2})	15.3±68.3	16.3±4.9	15.1±3.5	16.2±0.8
Gly60				
k_{ex} (s^{-1})	2179±1039	3033±252	2180±447	3039±220
Φ_{ex} x10^3 (rad^2 s^{-2})	15.7±6.5	22.7±1.2	15.6±5.0	22.6±1.0
Asn75				
k_{ex} (s^{-1})	2082±712	3385±233	2106±416	3389±233
Φ_{ex} x10^3 (rad^2 s^{-2})	15.4±32.0	26.1±1.0	15.2±2.7	26.0±1.0
Gln76				
k_{ex} (s^{-1})	618±1005	2322±819	1911±570	2330±392
Φ_{ex} x10^3 (rad^2 s^{-2})	15.2±247	10.4±73	8.4±2.4	10.3±0.9
Trp77				
k_{ex} (s^{-1})	1401±1039	4095±397	3590±447	4078±160
Φ_{ex} x10^3 (rad^2 s^{-2})	162±218	145±10	123±20	145±3
Gly78				
k_{ex} (s^{-1})	2751±650	4006±175	2746±365	4007±175
Φ_{ex} x10^3 (rad^2 s^{-2})	26.3±7.6	42.3±1.1	26.0±3.9	42.1±1.1
Asp80				
k_{ex} (s^{-1})	2083±469	2998±99	2540±188	2998±95
Φ_{ex} x10^3 (rad^2 s^{-2})	38.4±4.7	44.4±0.8	36.6±2.8	44.2±0.8
Trp84				
k_{ex} (s^{-1})	2592±903	3240±547	2630±697	3246±278
Φ_{ex} x10^3 (rad^2 s^{-2})	13.1±27.6	16.9±2.9	13.0±4.4	16.8±0.9
Glu96				
k_{ex} (s^{-1})	2350±1006	2442±555	2839±621	2743±210
Φ_{ex} x10^3 (rad^2 s^{-2})	19.8±40.3	19.8±4.8	19.3±5.9	18.5±0.8
Gln98				
k_{ex} (s^{-1})	722±1122	3362±889	2615±587	3368±343
Φ_{ex} x10^3 (rad^2 s^{-2})	16.4±241	12.0±80.6	8.7±2.5	12.0±0.7
Asn99				
k_{ex} (s^{-1})	2195±896	3329±478	3521±744	3591±157
Φ_{ex} x10^3 (rad^2 s^{-2})	56.7±12.3	58.5±5.6	54.7±13.6	56.2±1.4
Val101				
k_{ex} (s^{-1})	2242±2864	1328±622	2246±3608	1688±349
Φ_{ex} x10^3 (rad^2 s^{-2})	9±326	8±300	9±73	6.6±0.8
Gly122				
k_{ex} (s^{-1})	2104±1129	3138±432	2109±953	3146±422
Φ_{ex} x10^3 (rad^2 s^{-2})	8±25	12.7±1.1	8.1±5.5	12.7±1.0

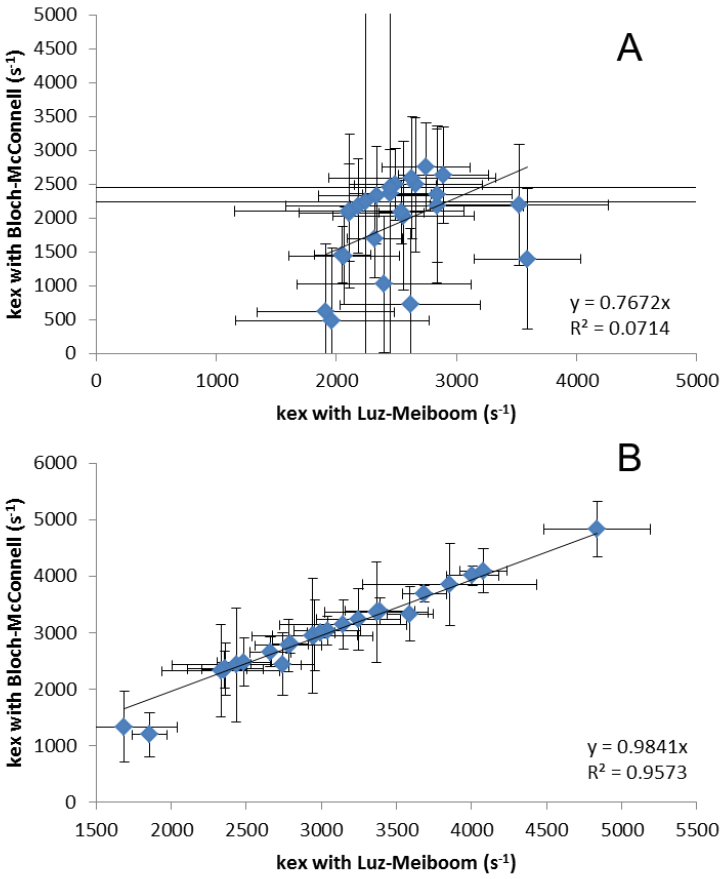

Appendix Figure 12 Effect of HEROINE on all 25 nuclei that showed relaxation dispersion for OAA at 296 K. the kinetic rate (k_{ex}) is compared between fits to the Bloch-McConnell equations (BM) and Luz-Meiboom (LM) models when HEROINE derived rates were not included (A) and were included (B) in the analysis. Upon the introduction of HEROINE for CT-CPMG data analysis the extracted kinetics agree between both the BM and LM models. R is the Pearson correlation coefficient.

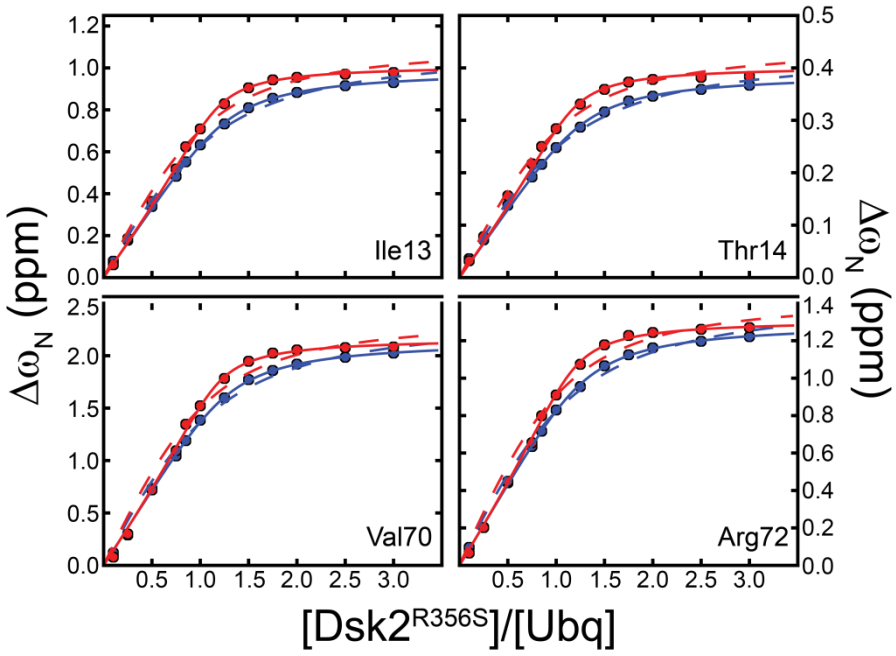

Appendix Figure 13 Titration studies with ^{15}N labeled ubiquitin and the R356 mutant of Dsk2 (Dsk2^{R356}). HSQC based titrations were performed with constant concentrations of 100 μM (blue points) and 500 μM (red points) ubiquitin at 298 K. Dsk2^{R356S} was designed in hopes of destabilizing one side of the asymmetric interface between Dsk2 monomers. The same ratios (Dsk2^{R356}/Ubq) were used for both titrations. Back plotted curves are based on fits to two-state binding models (dashed curves) and a multiple binding modes model (solid curves). The different dependencies in the titration at two different concentrations of ubiquitin may stem from the different populations between multimeric states within Dsk2 (Figure 33). This is also represented in the differences between the chemical shifts extracted at saturation and extracted two-state K_Ds (dashed curves) which were 32 ±14 μM and 112 ±53 μM for the 100 μM and 500 μM samples, respectively. All residues reported statistically significant better fits to the sigmoidal model than the two-state model based on an F-test. Applying the multiple binding modes model K_{D1} (K_{D2}) was found to be 13 ± 6 μM (35 ± 24 μM) and 31 ± 9 μM (65 ± 39 μM) for the 100 and 500 μM titrations, respectively. Although, within the error the extracted K_Ds are similar this fitting procedure does not take into account the conformational equilibrium between Dsk2 molecules which can affect the free ligand calculation (Chapter 6).

References

1. Alberts, B.; Johnson, A.; Lewis, J.; Raff, M.; Roberts, K.; Walter, P., *Molecular Biology of the Cell*. 5 ed.; Garland Science: 2007.
2. Voet, D.; Voet, J.G., *Biochemistry*. 2nd ed.; Wiley.
3. Pawson, T., Protein modules and signalling networks. *Nature* **1995**, *373*.
4. McCammon, J.A., Theory of biomolecular recognition. *Curr. Opin. Struct. Biol.* **1998**, *8*, 245-249.
5. Nussinov, R.; Tsai, C.; Ma, B., The underappreciated role of allostery in the cellular network. *Annu. Rev. Biophys.* **2013**, *6*, 169-189.
6. Nussinov, R.; Tsai, C., Allostery in disease and in druge discovery. *Cell* **2013**, *153*, 293-305.
7. Tsai, C.; Nussinov, R., The molecular basis of targeting protein kinases in cancer therapeutics. *Semin. Cancer. Biol.* **2013**.
8. James, L.C.; Roversi, P.; Tawfik, D.S., Antibody multispecificity mediated by conformational diversity. *Science* **2003**, *299*, 1362-1367.
9. Petegem, F.V.; Chatelain, F.C.; Minor, D.L.J., Insights into voltage-gated calcium channel regulation from the structure of the Cav.1.2 IQ domain-Ca2+/calmodulin complex. *Nat. Struct. Biol.* **2005**, *12*, 1108-1115.
10. Best, R.B.; Lindorff-Larsen, K.; DePristo, M.A.; Vendruscolo, M., Relation between native ensembles and experimental structures of proteins. *Proc. Natl. Acad. Sci. U. S. A.* **2006**, *103*, 10901-10906.
11. Lange, O.F.; Lakomek, N.A.; Fares, C.; Schröder, G.F.; Walter, K.F.; Becker, S.; Meiler, J.; Grubmüller, H.; Griesinger, C.; de Groot, B.L., Recognition dynamics up to microseconds revealed from an RDC-derived ubiquitin ensemble in solution. *Science* **2008**, *320*, 1471-1475.
12. Bourgeois, D.; Vallone, B.; Arcovito, A.; Sciara, G.; Schotte, F.; Anfinrud, P.A.; Brunori, M., Extended subnanosecond structural dynamics of myoglobin revealed by Laue crystallography. *Proc. Natl. Acad. Sci. U. S. A.* **2006**, *103*, 4924-4929.

13. Srajer, V.; Royer, W.E.J., Time-resolved x-ray crystallography of heme proteins. *Methods Enzymol.* **2008**, *437*, 379-395.
14. Fraser, J.S.; van den Bedem, H.; Samelson, A.J.; Lang, P.T.; Holton, J.M.; Echols, N.; Alber, T., Accessing protein conformational ensembles using room-temperature X-ray crystallography. *Proc. Natl. Acad. Sci. U. S. A.* **2011**, *108*, 16247-16252.
15. Dauter, Z.; Jaskolski, M.; Wlodawer, A., Impact of synchrotron radiation on macromolecular crystallography: a personal view. *J. Synchrotron Radiat.* **2010**, *17*, 433-444.
16. Chapman, H.N.; Fromme, P.; Barty, A.; White, T.A.; Kirian, R.A.; Aquila, A.; Hunter, M.S.; Schulz, J.; DePonte, D.P.; Weierstall, U., *et al.*, Femtosecond X-ray protein nanocrystallography. *Nature* **2011**, *470*, 73-U81.
17. Aquila, A.; Hunter, M.S.; Doak, R.B.; Kirian, R.A.; Fromme, P.; White, T.A.; Andreasson, J.; Arnlund, D.; Bajt, S.; Barends, T.R.M., *et al.*, Time-resolved protein nanocrystallography using an X-ray free-electron laser. *Opt. Express* **2012**, *20*, 2706-2716.
18. Fraser, J.S.; Clarkson, M.W.; Degnan, S.C.; Erion, R.; Kern, D.; Alber, T., Hidden alternative structures of proline isomerase essential for catalysis. *Nature* **2009**, *462*, 669-673.
19. Szabo, A.; Rayner, D.M., Fluorescence decay of tryptophan conformers in aqueous solution. *J. Am. Chem. Soc.* **1980**, *102*, 554-563.
20. Palmer, A.G., 3rd; Hochstrasser, R.A.; Millar, D.P.; Rance, M.; Wright, P.E., Characterization of Amino Acid Side Chain Dynamics in a Zinc-Finger Peptide Using 13C NMR Spectroscopy and Time-Resolved Fluorescence Spectroscopy. *J. Am. Chem. Soc.* **1993**, *115*, 6333-6345.
21. Fersht, A., *Structure and Mechanism in Protein Science: A Guide to Enzyme Catalysis and Protein Folding*. 1st ed.; W. H. Freeman: 1998.
22. Moncrieffe, M.C.; Juranic, N.; Kemple, M.D.; Potter, J.D.; Macura, S.; Predergas, F.G., Structure-Fluorescence Correlations in a Single Tryptophan Mutant of Carp Parvalbumin: Solution, Structure, Backbone and Side-chain Dynamics. *J. Mol. Biol.* **2000**, *297*, 147-163.

23. Sakakibara, D.; Sasaki, A.; Ikeya, T.; Hamatsu, J.; Hanashima, T.; Mishima, M.; Yoshimasu, M.; Hayashi, N.; TMikawa, T.; Walchli, M., *et al.*, Protein structure determination in living cells by in-cell NMR spectroscopy. *Nature* **2009**, *458*, 102-105.
24. Serber, Z.; Keatinge-Clay, A.T.; Ledwidge, R.; Kelly, A.E.; Miller, S.M.; Dötsch, V., High-Resolution Macromolecular NMR Spectroscopy Inside Living Cells. *J. Am. Chem. Soc.* **2001**, *123*, 2446-2447.
25. Banci, L.; Barbieri, L.; Bertini, I.; Luchinat, E.; Secci, E.; Zhao, Y.; Aricescu, A.R., Atomic-resolution monitoring of protein maturation in live human cells by NMR. *Nat. Chem. Biol.* **2013**, *9*, 297-299.
26. Palmer, A.G., 3rd, NMR probes of molecular dynamics: Overview and comparison with other techniques. *Annu. Rev. Biophys. Biomol. Struct.* **2001**, *30*, 129-155.
27. Palmer, A.G., 3rd, NMR characterization of the dynamics of biomacromolecules. *Chem. Rev.* **2004**, *104*, 3623-3640.
28. Kay, L.E.; Torchia, D.A.; Bax, A., Backbone Dynamics of Proteins as Studied by ^{15}N Inverse Detected Heteronuclear NMR Spectroscopy: Application to Staphylococcal Nuclease. *Biochemistry* **1989**, *28*, 8972-8979.
29. Deverell, C.; Morgan, R.E.; Strange, J.H., Studies of chemical exchange by nuclear magnetic relaxation in the rotating frame. *Mol. Phys.* **1970**, *18*, 553-559.
30. Carr, H.Y.; Purcell, E.M., Effects of Diffusion on Free Precession in Nuclear Magnetic Resonance Experiments. *Phys. Rev.* **1954**, *54*, 630-638.
31. Meiboom, S.; Gill, S., Modified Spin-Echo Method for Measuring Nuclear Relaxation Times. *Rev. Sci. Instrum.* **1958**, *29*, 688-691.
32. Palmer, A.G., 3rd; Kroenke, C.D.; Loria, J.P., Nuclear magnetic resonance methods for quantifying microsecond-to-millisecond motions in biological macromolecules. *Methods Enzymol.* **2001**, *339*, 204-238.
33. Palmer, A.G., 3rd; Massi, F., Characterization of the dynamics of biomacromolecules using rotating-frame spin relaxation NMR spectroscopy. *Chem. Rev.* **2006**, *106*, 1700-1719.
34. Wagner, G.; Bodenhausen, G.; Müller, N.; Rance, M.; Sorensen, O.W.; Ernst, R.R., Exchange of two-spin order in nuclear magnetic resonance: Separation of exchange and cross-relaxation processes. *J. Am. Chem. Soc.* **1985**, *107*, 6440-6446.

35. Bodenhausen, G.; Wagner, G.; Rance, M.; Sorensen, O.W.; Wüthrich, K.; Ernst, R.R., Longitudinal two-spin order in 2d exchange spectroscopy. *J. Magn. Reson.* **1984**, *59*, 542-550.

36. Haupt, C.; Patzschke, R.; Weininger, U.; Groger, S.; Kovermann, M.; Balbach, J., Transient enzyme-substrate recognition monitored by real-time NMR. *J. Am. Chem. Soc.* **2011**, *133*, 11154-11162.

37. Zeeb, M.; Balbach, J., Protein folding studied by real-time NMR spectroscopy. *Methods Enzymol.* **2004**, *34*, 65-74.

38. Berjanskii, M.V.; Wishart, D.S., A Simple Method To Predict Protein Flexibility Using Secondary Chemical Shifts. *J. Am. Chem. Soc.* **2005**, *127*, 14970-14971.

39. Li, D.W.; Brüschweiler, R., Certification of Molecular Dynamics Trajectories with NMR Chemical Shifts. *J. Chem. Phys. Lett.* **2009**, *1*, 246-248.

40. Robustelli, P.; Stafford, K.A.; Palmer, A.G., 3rd, Interpreting Protein Structural Dynamics from NMR Chemical Shifts. *J. Am. Chem. Soc.* **2012**, *134*, 6365-6374.

41. Xue, Y.; Ward, J.M.; Yuwen, T.; Podkorytov, I.S.; Skrynnikov, N.R., Microsecond Time-Scale Conformational Exchange in Proteins: Using Long Molecular Dynamics Trajectory To Simulate NMR Relaxation Dispersion Data. *J. Am. Chem. Soc.* **2012**, *134*, 2555-2562.

42. Mangia, S.; Traaseth, N.J.; Veglia, G.; Garwood, M.; Michaeli, S., Probing slow protein dynamics by adiabatic $R_{1\rho}$ and $R_{2\rho}$ NMR experiments. *J. Am. Chem. Soc.* **2010**, *132*, 9979-9981.

43. Traaseth, N.J.; Chao, F.; Masterson, L.R.; Mangia, S.; Garwood, M.; Michaeli, S.; Seelig, B.; Veglia, G., Heteronuclear adiabatic relaxation dispersion (HARD) for quantitative analysis of conformational dynamics in proteins. *J. Magn. Reson.* **2012**, *219*, 75-82.

44. Salvi, N.; Ulzega, S.; Ferrage, F.; Bodenhausen, G., Timescales of Slow Motions in Ubiquitin Explored by Heteronuclear Double Resonance. *J. Am. Chem. Soc.* **2012**, *134*, 2481-2484.

45. Abragam, A., Principles in Nuclear Magnetism. Oxford University Press: 1961.

46. Cavanagh, J.; Fairbrother, W.J.; Palmer, A.G., 3rd; Rance, M.; Skelton, N.J., *Principles and Practice: Protein NMR Spectroscopy*. 2nd ed.; Elsevier: 2007.

47. Rule, G.S.; Hitchens, T.K., *Fundamentals of Protein NMR Spectroscopy*. Springer: 2006; Vol. 5.

48. Daragan, V.A.; Mayo, K.H., Motional model analyses of protein and peptide dynamics using ^{13}C and ^{15}N NMR relaxation. *Prog. in Nuc. Mag. Res.* **1997**, *31*, 63-105.
49. Korzhnev, D.M.; Billeter, M.; Arseniev, A.S.; Orekhov, V.Y., NMR studies of Brownian tumbling and internal motions in proteins. *Prog. in Nuc. Mag. Res.* **2001**, *38*, 197-266.
50. Lüginbuhl, P.; Wüthrich, K., Semi-classical nuclear spin relaxation theory revisted for use with biological macromolecules. *Prog. in Nuc. Mag. Res.* **2002**, *40*, 199-247.
51. Liboff, R., *Introductory Quantum Mechanics*. 4th ed.; Peasron Education: 2002.
52. Ernst, R.R.; Bodenhausen, G.; Wokaun, A., *Principles of Nuclear Magnetic Resonance in One and Two Dimensions*. Oxford Science Publications: United Kingdom, 1987.
53. Kruk, D., *Theory of Evolution and Relaxation of Multi-spin Systems: Application to Nuclear Magnetic Resonance and Electron Spin Resonance*. Arima Publishing: 2007.
54. Redfield, A.G., In *Advances in Magnetic Resonance*, Waugh, J.S., Ed. Academic Press: New York, 1965; Vol. 1.
55. Wennerström, H., Nuclear magnetic relaxation induced by chemical exchange. *Mol. Phys.* **1972**, *24*, 69-80.
56. Wang, C.; Rance, M.; Palmer, A.G., 3rd, Mapping Chemical Exchange in Proteins with MW > 50 kD. *J. Am. Chem. Soc.* **2003**, *125*, 8968-8969.
57. Akke, M.; Brüschweiler, R.; Palmer, A.G., 3rd, NMR order parameters and free energy: an analytical approach and its application to cooperative Ca2+ binding by calbindin D9k. *J. Am. Chem. Soc.* **1993**, *115*, 9832-9833.
58. Lee, A.L.; Kinnear, S.A.; Wand, A.J., Redistribution and loss of side chain entropy upon formation of a calmodulin-peptide complex. *Nat. Struct. Biol.* **2000**, *7*, 72-77.
59. Yang, D.; Kay, L.E., Contributions to conformational entropy arising from bond vector fluctuations measured from NMR-derived order parameters: application to protein folding. *J. Mol. Biol.* **1996**, *263*, 369-382.
60. Clore, G.M.; Szabo, A.; Bax, A.; Kay, L.E.; Driscoll, P.C.; Gronenborn, A.M., Deviations from the simple two-paramter model-free approach to the interpretation of nitrogen-15 nuclear magnetic relaxation of proteins. *J. Am. Chem. Soc.* **1990**, *112*, 4989-4991.
61. Farrow, N.A.; Muhandiram, R.; Singer, A.U.; Pascal, S.M.; Kay, C.M.; Gish, G.; Shoelson, S.E.; Pawson, T.; Forman-Kay, J.D.; Kay, L.E., Backbone dynamics of a free and phosphopeptide-complexed Src homology 2 domain studied by ^{15}N NMR relaxation. *Biochemistry* **1994**, *33*, 5984-6003.

62. Brüschweiler, R.; Liao, X.; Wright, P.E., Long-range motional restrictions in a multidomain zinc-finger protein from anisotropic tumbling. *Science* **1995**, *268*, 886-889.
63. Tjandra, N.; Feller, S.E.; Pastor, R.W.; Bax, A., Rotational diffusion anisotropy of human ubiquitin from ^{15}N NMR relaxation. *J. Am. Chem. Soc.* **1995**, *117*, 12562-12566.
64. Kroenke, C.D.; Loria, J.P.; Lee, L.K.; Rance, M.; Palmer, A.G., 3rd, Longitudinal and Transverse ^{1}H-^{15}N Dipolar/^{15}N Chemical Shift Anisotropy Relaxation Interference: Unambiguous Determination of Rotational diffusion Tensors and Chemical Exchange Effects in Biological Macromolecules. *J. Am. Chem. Soc.* **1998**, *120*, 7905-7915.
65. Lee, D.; Hilty, C.; Wider, G.; Wüthrich, K., Effective rotational correlation times of proteins from NMR relaxation interference. *J. Magn. Reson.* **2006**, *178*, 72-76.
66. Desvaux, H.; Berthault, P., Study of dynamic processes in liquids using off-resonance rf irradiation. *Prog. in Nuc. Mag. Res.* **1999**, *35*, 295-340.
67. Eisenmesser, E.Z.; Millet, O.; Labeikovsky, W.; Korzhnev, D.M.; Wolf-Watz, M.; Bosco, D.A.; Skalicky, J.J.; Kay, L.E.; Kern, D., Intrinsic dynamics of an enzyme underlies catalysis. *Nature* **2005**, *438*, 117-121.
68. Korzhnev, D.M.; Salvatella, X.; Vendruscolo, M.; Di Nardo, A.A.; Davidson, A.R.; Dobson, C.M.; Kay, L.E., Low-populated folding intermediates of Fyn SH3 characterized by relaxation dispersion NMR. *Nature* **2004**, *430*, 586-590.
69. Sugase, K.; Dyson, H.J.; Wright, P.E., Mechanism of coupled folding and binding of an intrinsically disordered protein. *Nature* **2007**, *447*, 1021-1025.
70. Szyperski, T.; Lüginbuhl, P.; Otting, G.; Güntert, P.; Wüthrich, K., Protein dynamics studied by rotating frame 15N spin relaxation times. *J. Biomol. NMR* **1993**, *3*, 151-164.
71. Korzhnev, D.M.; Religa, T.L.; Lundström, P.; Fersht, A.R.; Kay, L.E., The folding pathway of an FF domain: characterization of an on-pathway intermediate state under folding conditions by ^{15}N, ^{13}Cα and ^{13}C-methyl relaxation dispersion and ^{1}H/^{2}H-exchange NMR spectroscopy. *J. Mol. Biol.* **2007**, *372*, 497-512.
72. Vugmeyster, L.; Kroenke, C.D.; Picart, F.; Palmer, A.G., 3rd; Raleigh, P., ^{15}N $R_{1\rho}$ measurements allow the determination of ultrafast protein folding rates. *J. Am. Chem. Soc.* **2000**, *122*, 5387-5388.

73. Korzhnev, D.M.; Kay, L.E., Probing Invisible, Low-Populated States of Protein Molecules by Relaxation Dispersion NMR Spectroscopy: An Application to Protein Folding. *Acc. Chem. Res.* **2008**, *41*, 442-451.
74. Korzhnev, D.M.; Bezsonova, I.; Lee, S.; Chalikian, T.V.; Kay, L.E., Alternate binding modes for a ubiquitin-SH3 domain interaction studied by NMR spectroscopy. *J. Mol. Biol.* **2009**, *386*, 391-405.
75. Tolkatchev, D.; Xu, P.; Ni, F., Probing the Kinetic Landscape of Transient Peptide-Protein Interactions by Use of Peptide ^{15}N NMR Relaxation Dispersion Spectroscopy: Binding of an Antithrombin Peptide to Human Prothrombin. *J. Am. Chem. Soc.* **2003**, *125*, 12432-12442.
76. Bhabha, G.; Lee, J.; Ekiert, D.C.; Gam, J.; Wilson, I.A.; Dyson, H.J.; Benkovic, S.J.; Wright, P.E., A dynamic knockout reveals that conformational fluctuations influence the chemical step of enzyme catalysis. *Science* **2011**, *332*, 234-238.
77. Boehr, D.D.; McElheny, D.; Dyson, H.J.; Wright, P.E., The dynamic energy landscape of dihydrofolate reductase catalysis. *Science* **2006**, *313*, 1638-1642.
78. Hansen, D.F.; Vallurupalli, P.; Lundström, P.; Neudecker, P.; Kay, L.E., Probing Chemical Shifts of Invisble States of Proteins with Relaxation Dispersion NMR Spectroscopy: How Well Can We Do? *J. Am. Chem. Soc.* **2008**, *130*, 2667-2675.
79. Loria, J.P.; Rance, M.; Palmer, A.G., 3rd, A Relaxation-Compensated Carr-Purcell-Meiboom-Gill Sequence for Characterizing Chemical Exchange by NMR Spectroscopy. *J. Am. Chem. Soc.* **1999**, *121*, 2331-2332.
80. Lundström, P.; Hansen, D.F.; Vallurupalli, P.; Kay, L.E., Accurate Measurement of Alpha Proton Chemical Shifts of Excited Protein States by Relaxation Dispersion NMR Spectroscopy. *J. Am. Chem. Soc.* **2009**, *131*, 1915-1926.
81. Korzhnev, D.M.; Kloiber, K.; Kay, L.E., Multiple-Quantum Relaxation Dispersion NMR Spectroscopy Probing Millisecond Time-Scale Dynamics in Proteins: Theory and Application. *J. Am. Chem. Soc.* **2004**, *126*, 7320-7329.
82. Korzhnev, D.M.; Kloiber, K.; Kanelis, V.; Tugarinov, V.; Kay, L.E., Probing Slow Dynamics in High Molecular Weight Proteins by Methyl-TROSY NMR Spectroscopy: Application to a 723-Residue Enzyme. *J. Am. Chem. Soc.* **2004**, *126*, 3964-3973.

83. Ishima, R.; Baber, J.L.; Louis, J.M.; Torchia, D.A., Carbonyl carbon transverse relaxation dispersion measurements and milli- to microsecond timescale motion in a protein hydrogen bond network. *J. Biomol. NMR* **2004**, *29*, 187-198.
84. Ishima, R.; Torchia, D.A., Extending the range of amide proton relaxation dispersion experiments in proteins using a constant-time relaxation-compensated CPMG approach. *J. Biomol. NMR* **2003**, *25*, 243-248.
85. Lundström, P.; Hansen, D.F.; Kay, L.E., Measurement of carbonyl chemical shifts of excited protein states by relaxation dispersion NMR spectroscopy: comparison between uniformly and selectively 13C labeled samples. *J. Biomol. NMR* **2008**, *42*, 35-47.
86. Lundström, P.; Lin, H.; Kay, L.E., Measuring ^{13}C beta chemical shifts of invisble excited states in proteins by relaxation dispersion NMR spectroscopy. *J. Biomol. NMR* **2009**, *44*, 139-155.
87. Lundström, P.; Vallurupalli, P.; Religa, T.L.; Dahlquist, F.W.; Kay, L.E., A single-quantum methyl 13C-relaxation dispersion experiment with improved sensitivity. *J. Biomol. NMR* **2007**, *38*, 79-88.
88. Hansen, A.L.; Lundström, P.; Velyvis, A.; Kay, L.E., Quantifying millisecond exchange dynamics in proteins by CPMG relaxation dispersion NMR using side-chain ^{1}H probes. *J. Am. Chem. Soc.* **2012**, *134*, 3178-3189.
89. Davis, D.G.; Perlman, M.E.; London, R.E., Direct measurements of the dissociation-rate constant for inhibitor-enzyme complexes via the $T_{1\rho}$ and T_2 (CPMG) methods. *J. Magn. Reson.* **1994**, *104*, 266-275.
90. Ishima, R.; Torchia, D.A., Estimating the time scale of chemical exchange of proteins from measurements of transverse relaxation rates in solution. *J. Biomol. NMR* **1999**, *14*, 369-372.
91. Ishima, R., Recent developments in ^{15}N NMR relaxation studies that probe protein backbone dynamics. *Top. Curr. Chem.* **2012**, *326*, 99-122.
92. Zhang, Q.; Al-Hashimi, H.M., Domain-elongation NMR spectroscopy yields new insights into RNA dynamics and adaptive recognition. *RNA* **2009**, *15*, 1941-1948.
93. Zhang, Q.; Stelzer, A.C.; Fisher, C.K.; Al-Hashimi, H.M., Visualizing spatially correlated dynamics that directs RNA conformational transitions. *Nature* **2007**, *450*, 1263-1267.
94. Bouvignies, G.; Bernado, P.; Meier, S.; Cho, K.; Grzesiek, S.; Brüschweiler, R.; Blackledge, M., Identification of slow correlated motions in proteins using residual

dipolar and hydrogen-bond scalar couplings. *Proc. Natl. Acad. Sci. U. S. A.* **2005**, *102*, 13885-13890.

95. Yao, L.; Vogeli, B.; Torchia, D.A.; Bax, A., Simultaneous NMR study of protein structure and dynamics using conservative mutagenesis. *J. Phys. Chem. B* **2008**, *112*, 6045-6056.
96. Lakomek, N.A.; Carlomagno, T.; Becker, S.; Griesinger, C.; Meiler, J., A thorough dynamic interpretation of residual dipolar couplings in ubiquitin. *J. Biomol. NMR* **2006**, *34*, 101-115.
97. Meiler, J.; Peti, W.; Griesinger, C., Dipolar couplings in multiple alignments suggest alpha helical motion in ubiquitin. *J. Am. Chem. Soc.* **2003**, *125*, 8072-8073.
98. Fares, C.; Lakomek, N.A.; Walter, K.F.; Frank, B.T.; Meiler, J.; Becker, S.; Griesinger, C., Accessing ns-microsecond side chain dynamics in ubiquitin with methyl RDCs. *J. Biomol. NMR* **2009**, *45*, 23-44.
99. Tolman, J.R.; Flanagan, J.M.; Kennedy, M.A.; Prestegard, J.H., Nuclear magnetic dipole interactions in field-oriented proteins: information for structure determination in solution. *Proc. Natl. Acad. Sci. U. S. A.* **1995**, *92*, 9279-9283.
100. Bax, A.; Kontaxis, G.; Tjandra, N., Dipolar Couplings in Macromolecular Structure Determination. *Methods Enzymol.* **2001**, *339*, 127-174.
101. Meiler, J.; Prompers, J.J.; Peti, W.; Griesinger, C.; Brüschweiler, R., Model-free approach to the dynamic interpretation of residual dipolar couplings in globular proteins. *J. Am. Chem. Soc.* **2001**, *123*, 6098-6107.
102. Lakomek, N.A.; Walter, K.F.; Fares, C.; Lange, O.F.; De Groot, B.L.; Grubmüller, H.; Brüschweiler, R.; Munk, A.; Becker, S.; Meiler, J., *et al.*, Self-consistent residual dipolar coupling based model-free analysis for the robust determination of nanosecond to microsecond protein dynamics. *J. Biomol. NMR* **2008**, *41*, 139-155.
103. Zhou, H.X., From the induced fit to the conformational selection: a continuum of binding mechanism controlled by the timescale of conformational transitions. *Biophys. J.* **2010**, *98*, L15-L17.
104. Hammes, G.G.; Chang, Y.C.; Oas, T.G., Conformational selection or induced fit: a flux description of reaction mechanism. *Proc. Natl. Acad. Sci. U. S. A.* **2009**, *106*, 13737-13741.

105. Wlodarski, T.; Zagrovic, B., Conformational selection and induced fit mechanism underlie specificity in noncovalent interactions with ubiquitin. *Proc. Natl. Acad. Sci. U. S. A.* **2009**, *106*, 19346-19351.

106. Boehr, D.D.; Dyson, H.J.; Wright, P.E., An NMR perspective on enzyme catalysis. *Chem. Rev.* **2006**, *106*, 3055-3079.

107. Mulder, F.A.; van Tilborg, P.J.; Kaptein, R.; Boelens, R., Microsecond time scale dynamics in the RXR DNA-binding domain from a combination of spin-echo and off-resonance rotating frame relaxation measurements. *J. Biomol. NMR* **1999**, *13*, 275-288.

108. Massi, F.; Grey, M.J.; Palmer, A.G., 3rd, Microsecond timescale backbone conformational dynamics in ubiquitin studied with NMR $R_{1\rho}$ relaxation experiments. *Protein Sci.* **2005**, *14*, 735-742.

109. Mills, J.L.; Szyperski, T., Protein dynamics in supercooled water: the search for slow motional modes. *J. Biomol. NMR* **2002**, *23*, 63-67.

110. Kempf, J.G.; Jung, J.; Sampson, N.S.; Loria, J.P., Off-resonance TROSY ($R_{1\rho}$-R_1) for quantitation of fast exchange processes in large proteins. *J. Am. Chem. Soc.* **2003**, *125*, 12064-12065.

111. Fenwick, R.B.; Esteban-Martin, S.; Richter, B.; Lee, D.; Walter, K.F.; Milovanovic, D.; Becker, S.; Lakomek, N.A.; Griesinger, C.; Salvatella, X., Weak long-range correlated motions in a surface patch of ubiquitin involved in molecular recognition. *J. Am. Chem. Soc.* **2011**, *133*, 10336-10339.

112. Ban, D.; Funk, M.; Gulich, R.; Egger, D.; Sabo, T.M.; Walter, K.F.; Fenwick, R.B.; Giller, K.; Pichierri, F.; de Groot, B.L., *et al.*, Kinetics of conformational sampling in ubiquitin. *Angew. Chem. Int. Ed. Engl.* **2011**, *50*, 11437-11440.

113. Neal, S.; Nip, A.M.; Zhang, H.; Wishart, D.S., Rapid and accurate calculation of protein ^{1}H, ^{13}C, and ^{15}N chemical shifts. *J. Biomol. NMR* **2003**, *26*, 215-240.

114. Xu, X.P.; Case, D.A., Automated prediction of ^{15}N, $^{13}C\alpha$, $^{13}C\beta$, and $^{13}C'$ chemical shifts in proteins using a density functional database. *J. Biomol. NMR* **2001**, *21*, 321-333.

115. Shen, Y.; Bax, A., Protein backbone chemical shifts predicted from searching a database for torsion angle and sequence homology. *J. Biomol. NMR* **2007**, *38*, 289-302.

116. Chang, S.L.; Tjandra, N., Temperature dependence of protein backbone motion from carbonyl ^{13}C and amide ^{15}N NMR relaxation. *J. Magn Reson.* **2005**, *174*, 43-53.

117. Shaw, D.E.; Maragakis, P.; Lindorff-Larsen, K.; Piana, S.; Dror, R.O.; Eastwood, M.P.; Bank, J.A.; Jumper, J.M.; Salmon, J.K.; Shan, Y., *et al.*, Atomic-Level Characterization of the Structural Dynamics of Proteins. *Science* **2010**, *330*, 341-346.

118. Knocks, A.; Weingartner, H., The Dielectric Spectrum of Ubiquitin in Aqueous Solution. *J. Phys. Chem. B* **2001**, *105*, 3635-3638.

119. Nietlispach, D., Suppression of anti-TROSY lines in a sensitivity enhanced gradient selection TROSY scheme. *J. Biomol. NMR* **2005**, *31*, 161-166.

120. Pervushin, K.; Riek, R.; Wider, G.; Wüthrich, K., Attenuated T2 relaxation by mutual cancellation of dipole-dipole coupling and chemical shift anisotropy indicates an avenue to NMR structures of very large biological macromolecules in solution. *Proc. Natl. Acad. Sci. U. S. A.* **1997**, *94*, 12366-12371.

121. Delaglio, F.; Grzesiek, S.; Vuister, G.W.; Zhu, G.; Pfeifer, J.; Bax, A., NMRPipe: a multidimensional spectral processing system based on UNIX pipes. *J. Biomol. NMR* **1995**, *6*, 277-293.

122. Keller, R. Optimizing the process of nuclear magnetic resonance spectrum analysis and computer aided resonance assignment. ETH, 2004.

123. Tropp, J., Dipolar relaxation and nuclear Overhauser effects in nonrigid molecules: The effect of fluctuating internuclear distances. *J. Chem. Phys.* **1980**, *72*, 6035-6043.

124. Mulder, F.A.A.; Skrynnikov, N.R.; Hon, B.; Dahlquist, F.W.; Kay, L.E., Measurement of slow (micro- to millisecond) time scale dynamics in protein side chains by ^{15}N relaxation dispersion NMR spectroscopy: Application to Asn and Gln residues in a cavity mutant of T4 lysozyme. *J. Am. Chem. Soc.* **2001**, *123*, 967-975.

125. Styles, P.; Soffe, N.F.; Scott, C.A.; Cragg, D.A.; Row, F.; White, D.J.; White, P.C., A high-resolution NMR probe in which the coil and preamplifier are cooled with liquid helium. *J. Magn. Reson.* **1984**, *60*, 497-404.

126. Bruker, B., *NMR CryoProbe Limitation Sheet*. 2007.

127. Kovacs, H.; Moskau, D.; Spraul, M., Cryogenically cooled probes - a leap in NMR technology. *Prog. in Nuc. Mag. Res.* **2005**, *46*, 131-155.

128. Korzhnev, D.M.; Orekhov, V.Y.; Kay, L.E., Off-resonance $R_{1\rho}$ NMR studies of exchange dynamics in proteins with low spin-lock fields: an application to a Fyn SH3 domain. *J. Am. Chem. Soc.* **2005**, *127*, 713-721.

129. Ban, D.; Gossert, A.D.; Giller, K.; Becker, S.; Griesinger, C.; Lee, D., Exceeding the limit of dynamics studies on biomolecules using high spin-lock field strengths with a cryogenically cooled probehead. *J. Magn. Reson.* **2012**, *221*, 1-4.

130. Lee, A.L.; Wand, A.J., Assessing potential bias in the determination of rotational correlation times of proteins by NMR relaxation. *J. Biomol. NMR* **1999**, *13*, 101-112.

131. Sabo, T.M.; Bakhtiari, D.; Walter, K.F.; McFeeters, R.L.; Giller, K.; Becker, S.; Griesinger, C.; Lee, D., Thermal coefficients of the methyl groups within ubiquitin. *Protein Sci.* **2012**, *21*, 562-570.

132. Pelupessy, P.; Chiarparin, E., Hartmann-Hahn polarization transfer in liquids: An ideal tool for selective experiments. *Concepts Magn. Reson.* **2000**, *12*, 103-124.

133. Massi, F.; Johnson, E.; Wang, C.; Rance, M.; Palmer, A.G., 3rd, NMR $R_{1\rho}$ rotating-frame relaxatin with weak radio-frequency fields. *J. Am. Chem. Soc.* **2004**, *126*, 2247-2256.

134. Wang, A.C.; Bax, A., Minimizing the effects of radio-frequency heating in multidimensional NMR experiments. *J. Biomol. NMR* **1993**, *3*, 715-720.

135. Sklenar, V.; Piotto, M.; Saudek, L.V., Gradient-Tailored Water Suppression for ^{1}H-^{15}N HSQC Experiments Optimized to Retain Full Sensitivity. *J. Magn. Reson.* **1993**, *102*, 241-245.

136. Shaka, A.J.; Keeler, J.; Frenkiel, T.; Freeman, R., An improved sequence for broadband decoupling: WALTZ-16. *J. Magn. Reson.* **1983**, *52*, 335-338.

137. Tugarinov, V.; Kanelis, V.; Kay, L.E., Isotope labeling strategies for the stuyd of high-molecular-weight proteins by solution NMR spectroscopy. *Nat. Protoc.* **2006**, *1*, 749-754.

138. Lundström, P.; Akke, M., Off-resonance rotating-frame amide proton spin relaxation experiments measuring microsecond chemical exchange in proteins. *J. Biomol. NMR* **2005**, *32*, 163-173.

139. Brath, U.; Akke, M.; Yang, D.; Kay, L.E.; Mulder, F.A., Functional dynamics of human FKBP12 revealed by methyl 13C rotating frame relaxation dispersion NMR spectroscopy. *J. Am. Chem. Soc.* **2006**, *128*, 5718-5727.

140. Boyd, J.; Skrynnikov, N.R., Calculations of the Contribution of Ring Currents to the Chemical Shielding Anisotropy. *J. Am. Chem. Soc.* **2002**, *124*, 1832-1833.

141. Li, D.W.; Brüschweiler, R., PPM: a side-chain and backbone chemical shift predictor for the assessment of protein conformational ensembles. *J. Biomol. NMR* **2012**, *54*, 257-265.

142. Grant, D.M.; Paul, E.G., Carbon-13 Magnetic Resonance. II. Chemical Shift Data for the Alkanes. *J. Am. Chem. Soc.* **1964**, *86*, 2984-2990.
143. Tonelli, A.E.; Schilling, F.C., Calculated Carbon-13 Nuclear Magnetic Resonance Chemical Shifts for Ethylene-Vinyl Chloride Copolymers. *Macromolecules* **1981**, *14*, 74-76.
144. Mulder, F.A.A., Leucine Side-Chain Conformation and Dynamics in Proteins from 13C NMR Chemical Shifts. *ChemBioChem* **2009**, *10*, 1477-1479.
145. Hansen, D.F.; Neudecker, P.; Kay, L.E., Determination of Isoleucine Side-Chain Conformations in Ground and Excited States of Proteins from Chemical Shifts. *J. Am. Chem. Soc.* **2010**, *132*, 7589-7591.
146. Hansen, D.F.; Kay, L.E., Determining Valine Side-Chain Rotamer Conformations in Proteins from Methyl 13C Chemical Shifts: Application to the 360 kDa Half-Proteasome. *J. Am. Chem. Soc.* **2011**, *133*.
147. Lovell, S.C.; Word, M.J.; Richardson, J.S.; Richardson, D.C., The penultimate rotamer library. *Proteins Struct. Funct. Bioinf.* **2000**, *40*, 389-408.
148. Millet, O.; Mittermaier, A.; Baker, D.; Kay, L.E., The effects of mutations on motions of side-chains in protein L studied by 2H NMR dynamics and scalar couplings. *J. Mol. Biol.* **2003**, *329*, 551-563.
149. Skrynnikov, N.R.; Millet, O.; Kay, L.E., Deuterium spin probes of side-chain dynamics in proteins. 2. Spectral density mapping and identification of nanosecond time-scale side-chain motions. *J. Am. Chem. Soc.* **2002**, *124*, 6449-6460.
150. Peters, J.H.; De Groot, B.L., Ubiquitin Dynamics in Complexes Reveal Molecular Recognition Mechanisms Beyond Induced Fit and Conformational Selection. *PLoS Comput. Biol.* **2012**, *8*, e1002704.
151. Hu, M.; Li, P.; Li, M.; Li, W.; Yao, T.; Wu, J.W.; Gu, W.; Cohen, R.E.; Shi, Y., Crystal structure of a UBP-family deubiquitinating enzyme in isolation and in complex with ubiquitin aldehyde. *Cell* **2002**, *111*, 1041-1054.
152. Misaghi, S.; Galardy, P.J.; Meester, W.J.N.; Ovaa, H.; Ploegh, H.L.; Gaudet, R., Structure of the ubiquitin hydrolase UCH-L3 complexed with a suicide substrate. *J. Biol. Chem.* **2005**, *280*, 1512-1520.
153. Dethoff, E.A.; Petzold, K.; Chugh, J.; Casiano-Negroni, A.; Al-Hashimi, H.M., Visualizing transient low-populated structures of RNA. *Nature* **2012**, *491*, 724-728.

154. Marion, D.; Ikura, M.; Tschudin, R.; Bax, A., Rapid recording of 2D NMR spectra without phase cycling. Application to the study of hydrogen exchange in proteins. *J. Am. Chem. Soc.* **1989**, *85*, 393-399.

155. Burnham, K.P.; Anderson, D.R., *Model Selection and Multi-Model Inference*. Springer: 2002.

156. Chou, J.J.; Case, D.A.; Bax, A., Insights into the mobility of methyl-bearing side chains in proteins from 3JCC and 3JCN couplings. *J. Am. Chem. Soc.* **2003**, *125*, 8959-8966.

157. Korzhnev, D.M.; Religa, T.L.; Banachewicz, W.; Fersht, A.R.; Kay, L.E., A transient and low-populated protein-folding intermediate at atomic resolution. *Science* **2010**, *329*, 1312-1316.

158. Millet, O.; Loria, J.P.; Kroenke, C.D.; Pons, M.; Palmer, A.G., 3rd, The Static Magnetic Field Dependence of Chemical Exchange Linebroadening Defines the NMR Chemical Shift Time Scale. *J. Am. Chem. Soc.* **2000**, *122*, 2867-2877.

159. Palmer, A.G., 3rd; Skelton, N.J.; Chazin, W.J.; Wright, P.E.; Rance, M., Suppression of the effects of cross-correlation between dipolar and anisotropic chemical shift relaxation mechanisms in the measurement of spin-spin relaxation rates. *Mol. Phys.* **1992**, *75*, 699-711.

160. Tollinger, M.; Skrynnikov, N.R.; Mulder, F.A.; Forman-Kay, J.D.; Kay, L.E., Slow dynamics in folded and unfolded states of an SH3 domain. *J. Am. Chem. Soc.* **2001**, *123*, 11341-11352.

161. McConnell, H.M., Reaction rates by nuclear magnetic resonance. *J. Chem. Phys.* **1958**, *28*, 430-431.

162. Luz, Z.; Meiboom, S., Nuclear Magnetic Resonance Study of the Protolysis of Trimethylammonium Ion in Aqueous Solution-Order of the Reaction with Respect to Solvent. *J. Chem. Phys.* **1963**, *39*, 366-370.

163. Kovrigin, E.L.; Kempf, J.G.; Grey, M.J.; Loria, J.P., Faithful estimation of dynamics parameters from CPMG relaxation dispersion measurements. *J. Magn. Reson.* **2006**, *180*, 93-104.

164. Long, D.; Yang, D., Millisecond timescale dynamics of human liver fatty acid binding protein: testing of its relevance to the ligand entry process. *Biophys. J.* **2010**, *98*, 3054-3061.

165. Koharudin, L.M.; Furey, W.; Gronenborn, A.M., Novel fold and carbohydrate specificity of the potent anti-HIV cyanobacterial lectin from Oscillatoria agardhii. *J. Biol. Chem.* **2011**, *286*, 1588-1597.
166. Koharudin, L.M.; Gronenborn, A.M., Structural basis of the anti-HIV activity of the cyanobacterial Oscillatoria Agardhii agglutinin. *Structure* **2011**, *19*, 1170-1181.
167. Chan, D.C.; Kim, P.S., HIV entry and its inhibition. *Cell* **1998**, *93*, 681-684.
168. Mulder, F.A.; Mittermaier, A.; Hon, B.; Dahlquist, F.W.; Kay, L.E., Studying excited states of proteins by NMR spectroscopy. *Nat. Struct. Biol.* **2001**, *8*, 932-935.
169. Skrynnikov, N.R.; Mulder, F.A.; Hon, B.; Dahlquist, F.W.; Kay, L.E., Probing slow time scale dynamics at methyl-containing side chains in proteins by relaxation dispersion NMR measurements: application to methionine residues in a cavity mutant of T4 lysozyme. *J. Am. Chem. Soc.* **2001**, *123*, 4556-4566.
170. Allerhand, A.; Gutowsky, H.S., Spin-Echo Studies of Chemical Exchange. II. Closed Formulas for Two Sites. *J. Chem. Phys.* **1964**, *42*, 1587-1599.
171. Hansen, D.F.; Yang, D.; Feng, H.; Zhou, Z.; Wiesner, S.; Bai, Y.; Kay, L.E., An Exchange-Free Measure of ^{15}N Transverse Relaxation: An NMR Spectroscopy Application to the Study of Folding Intermediate with Pervasive Chemical Exchange. *J. Am. Chem. Soc.* **2007**, *129*, 11468-11479.
172. Wang, C.; Grey, M.J.; Palmer, A.G., 3rd, CPMG sequences with enhanced sensitivity to chemical exchange. *J. Biomol. NMR* **2001**, *21*, 361-366.
173. Vallurupalli, P.; Bouvignies, G.; Kay, L.E., Increasing the exchange time-scale that can be probed by CPMG relaxation dispersion NMR. *J. Phys. Chem. B* **2011**, *115*, 14891-14900.
174. Carver, J.P.; Richards, R.E., A general two-site solution for the chemical exchange produced dependence of T2 upon the Carr-Purcell pulse separation. *J. Magn. Reson.* **1972**, *6*, 89-105.
175. Yip, G.N.; Zuiderweg, E.R., A phase cycle scheme that significantly suppresses offset-dependent artifacts in the R2-CPMG 15N relaxation experiment. *J. Magn. Reson.* **2004**, *171*, 25-36.
176. Long, D.; Liu, M.; Yang, D., Accurately Probing Slow Motions on Millisecond timescales with a Robust NMR Relaxation Experiment. *J. Am. Chem. Soc.* **2008**, *130*, 17629.

177. Press, W.H.; Teukolsky, S.A.; Vetterling, W.T.; Flannery, B.P., *Numerical Recipes in C++: The art of Scientific Computing*. Cambridge University Press: 2002.
178. Ma, B.; Kumar, S.; Tsai, C.; Nussinov, R., Folding funnels and binding mechanisms. *Prot. Eng.* **1999**, *12*, 713-720.
179. Tsai, C.; Kumar, S.; Ma, B.; Nussinov, R., Folding funnels, binding funnels, and protein function. *Protein Sci.* **1999**, *8*, 1181-1190.
180. Bosshard, H.R., Molecular Recognition by Induced Fit: How Fit is the Concept? *Physiology* **2001**, *16*, 171-173.
181. Ohno, A.; Jee, J.; Fujiwara, K.; Tenno, T.; Goda, N.; Tochio, H.; Kobayashi, H.; Hiroaki, H.; Shirakawa, M., Structure of the UBA domain of Dsk2p in complex with ubiquitin molecular determinants for ubiquitin recognition. *Structure* **2005**, *13*, 521-532.
182. Phillipe, D.; Ababou, X.; Yang, R.; Ghost, R.; Daviter, T.; Ladbury, J.E.; Pfuhl, M., Making Ends Meet: The Importance of the N- and C- Termini for the Structure, Stability, and Function of the Third SH3 Domain of CIN85. *Biochemistry* **2011**, *50*, 3649-3659.
183. Bezsonova, I.; Bruce, C.; Wiesner, S.; Lin, H.; Rotin, D.; Forman-Kay, J.D., Interactions between the Three CIN85 SH3 Domains and Ubiquitin: Implications for CIN85 Ubiquitination. *Biochemistry* **2008**, *47*, 8937-8949.
184. Shuker, S.B.; Hajduk, P.J.; Meadows, R.P.; Fesik, S.W., Discovering High-Affinity Ligands for Proteins: SAR by NMR. *Science* **1996**, *274*, 1531-1534.
185. Biggins, S.; Ivanovska, I.; Rose, D.M., Yeast ubiquitin-like genes are involved in duplication of the microtubule organizing center. *J. Cell Biol.* **1996**, *133*, 1331-1346.
186. Mueller, T.D.; Kamionka, M.; Feigon, J., Specificity of the interaction between ubiquitin-associated domains and ubiquitin. *J. Biol. Chem.* **2004**, *279*, 11926-11936.
187. Maude, A.D., The viscosity of a suspension of spheres. *J. Fluid Mech.* **1960**, *7*, 230-236.
188. Einstein, A., Eine neue Bestimmung der Molekuldimensionen. *Ann. Physik Lpz.* **1906**, *19*, 289-306.
189. Arai, M.; Ferreon, J.C.; Wright, P.E., Quantitative Analysis of Multisite Protein-Ligand Interactions by NMR: Binding of Intrinsically Disordered p53 Transactivation Subdomains with the TAZ2 Domain of CBP. *J. Am. Chem. Soc.* **2012**, *134*, 3792-3803.
190. Wang, Z.X.; Jiang, R.F., A novel two-site binding equation presented in terms of the total ligand concentration. *FEBS Lett.* **1996**, *392*, 245-249.

191. Lowe, E.D.; Hasan, N.; Trempe, J.F.; Fonso, L.; Noble, M.E.M.; Endicott, J.A.; Johnson, L.N.; Brown, N.R., Structures of the Dsk2 UBL and UBA domains and their complex. *Acta Crystallogr. D* **2006**, *62*, 177-188.

192. Markin, C.J.; Spyracopoulos, L., Increased precision for analysis of protein-ligand dissociation constants determined from chemical shift titrations. *J. Biomol. NMR* **2012**, *53*, 125-138.

193. Akke, M.; Liu, J.; Cavanagh, J.; Erickson, H.P.; Palmer, A.G., 3rd, Pervasive conformational fluctuations on microsecond time scales in a fibronectin type III domain. *Nat. Struct. Biol.* **1998**, *5*, 55-59.

194. Korzhnev, D.M.; Orekhov, V.Y.; Dahlquist, F.W.; Kay, L.E., Off-resonance $R_{1\rho}$ relaxation outside of the fast exchange limit: An experimental study of a cavity mutant of T4 lysozyme. *J. Biomol. NMR* **2003**, *26*, 39-48.

195. Vallurupalli, P.; Hansen, D.F.; Stollar, E.; Meirovitch, E.; Kay, L.E., Measurement of bond vector orientations in invisible excited states of proteins. *Proc. Natl. Acad. Sci. U. S. A.* **2007**, *104*, 18473-18477.

196. Dittmer, J.; Bodenhausen, G., Evidence for slow motion in proteins by multiple refocusing of heteronuclear nitrogen/proton multiple quantum coherences in NMR. *J. Am. Chem. Soc.* **2004**, *126*, 1314-1315.

197. Nisius, L.; Grzesiek, S., Key stabilizing elements of protein structure identified through pressure and temperature perturbation of its hydrogen bond network. *Nat. Chem.* **2012**, *4*, 711-717.

198. Kitahara, R.; Yokoyama, S.; Akasaka, K., NMR Snapshots of a Fluctuating Protein Structure: Ubiquitin at 30 bar - 3 kbar. *J. Mol. Biol.* **2005**, *347*, 277-285.

199. Xu, X.P.; Case, D.A., Probing multiple effects on 15N, 13Ca, 13Cb, 13C' chemical shifts in peptide using density functional theory. *Biopolymers* **2002**, *65*, 408-423.

200. Sidhu, A.; Surolia, A.; Robertson, A.D.; Sundd, M., A Hydrogen Bond Regulates Slow Motions in Ubiquitin by Modulating a Beta-turn Flip. *J. Mol. Biol.* **2011**, *411*, 1037-1048.

201. Huang, K.Y.; Amodea, G.A.; Tong, L.; McDermott, A., The structure of human ubiquitin in 2-methyl-2,4-pentanediol: A new conformational switch. *Protein Sci.* **2011**, *20*, 630-639.

202. Majumdar, A.; Ghose, R., Probing Slow Backbone Dynamics in Proteins Using TROSY-Based Experiments to Detect Cross-Correlated Time-Modulation of Isotropic Chemical Shifts. *J. Biomol. NMR* **2004**, *28*, 213-227.

203. Carlomagno, T.; Maurer, M.; Hennig, M.; Griesinger, C., Ubiquitin Backbone Motion Studied via ^{N}HN-C'Cα Dipolar-Dipolar and C'-C'Cα/^{N}HN CSA-Dipolar Cross-Correlated Relaxation. *J. Am. Chem. Soc.* **2000**, *122*, 5105-5113.

Pulse Programs

The following section contains all pulse programs and schematics that were mentioned in the preceding chapters. They are written in programming language that can be interpreted by Bruker instruments.

^{15}N off-resonance $R_{1\rho}$ experiments performed in super-cooled conditions (Chapter 2)

Sample: ^{15}N labeled

```
;optimization of water flip back:
;- optimize water flip up (sp1,ph17)
;- optimize water flip dow (sp2,ph18)

;K. Pervushin et al., PNAS, 94, 12366 (1997)
;D. Nietlispach, JBNMR, 31 (2005)

;Has adiabatic spin lock but not random number generation
;for the proton decoupling during spin lock (Korzhnev et al., JACS, 2003)

;pl1   : power for 1H
;pl2   : power for 13C
;pl3   : power for 15N

;sp1   : water flip up power
;sp2   : water flip down power
;spnam1: gauss128_5
;spnam2: gauss128_5

;p1    : 90 degree hard pulse 1H
;p3    : 90 degree hard pulse 13C
;p4    : 180 degree hard pulse 13C (225d for 5/600)
;p5    : 90 degree hard pulse 15N
;p11   : water flipback pulse (1.5m)


;cnst11 : 8 ppm
;cnst12 : o1p
;cnst15 : ppm value of off-res CW frequency
;cnst16 : ppm value of on-res frequency
;cnst21 : ppm value for temp correction block

;sp15   : power for begin adiabadic pulse
;sp16   : power for end adiabadic pulse
;pl11   : power for proton pulse during CW (4 kHz)
;pl16   : power for 15N CW
;spnam15: begin adiabadic pulse (LtoH - frequency sweep)
```

```
;spnam16: end adiabadic pulse (HtoL – frequency sweep)


;p15   : 4000 (adiabatic pulses)
;p16   : 10m (pulse for H during CW)
;p20   : 1000u (Gradient after d1)
;p24   : 500u (Gradient in first INEPT)
;p25   : 800u (Gradient in first INEPT)
;p26   : 300u (Gradient in second INEPT)
;p28   : 500u (Gradient before spin lock)
;p29   : 500u (Gradient after spin locl)
;gpz4 : 27%
;gpz5 : 28%
;gpz8 : 65%
;gpz9 : 17%

;d8   : relaxation delay (2 ms to 240 ms)
;d9   : total relaxation delay (250 ms)


;p21   : 500u (Gradient in first INEPT)
;p22   : 500u (Gradient in second INEPT)
;p23   : 900u (Gradient in watergate)
;gpz0  : 80%
;gpz1  : 19%
;gpz2  : 15%
;gpz3  : 32%
;gpz27 : 80%
;gpz26 : 16.2%

;d1    : relaxation delay
;d2    : INEPT delay (~2.7ms)
;in0   : 1/(2 SW) (Hz)

define delay INEPT1
define delay INEPT21
define delay INEPT22
define delay INEPT3
define delay DELTA

define list<gradient> EA=<EA>

#include <Avance_dl.incl>

#define GRADIENT0   10u p20:gp0 200u
#define GRADIENT1   10u p21:gp1 200u
#define GRADIENT2   10u p22:gp2 200u
#define GRADIENT3   10u p23:gp3 200u
#define GRADIENT4   10u p24:gp4 200u
#define GRADIENT5   10u p25:gp5 200u
#define GRADIENT8   10u p28:gp8 200u
#define GRADIENT9   10u p29:gp9 200u

"p2=2*p1"
"p6=2*p5"

"in0=inf1/2"
"d0=in0/2"
```

```
"d12=p26+210u"

"d13 = 2u + (2u+p16*2)*l8"
"d11=d1-d9+d13"
"d14=d9-d13-2u"

"INEPT1=d2-(p21+210u)"
"INEPT21=d2-(p22+p11+210u)-10u"
"INEPT22=d2-(p22+210u)"
"INEPT3=d2-(p23+210u)"
"DELTA=d2-(p25+210u)"


1  10u ze
2  1m
   2u pl16:f3
   2u fq=cnst21 (bf ppm):f3
   d11
   2u cw:f3
   d14
   2u do:f3
   4u
   10u pl1:f1
   20u pl2:f2
   20u pl3:f3
   20u LOCKH_ON
   5u fq=cnst16 (bf ppm):f3
   5u
   (p5 ph20):f3
   GRADIENT0
   1m
;---------------------------------------first INEPT
5  10u
   (p1 ph20):f1
   GRADIENT1
   INEPT1 pl1:f1
   (center(p2 ph20):f1 (p6 ph20):f3)
   GRADIENT1
   INEPT1
   (p1 ph21):f1
   GRADIENT4
   (p5 ph20):f3
   GRADIENT5
   DELTA
   (center(p2 ph20):f1 (p6 ph20):f3)
   GRADIENT5
   DELTA
   (p5 ph4):f3
   GRADIENT8
;---------------------------------------off spin-lock
   3u fq=cnst11 (bf ppm):f1
   3u fq=cnst15 (bf ppm):f3
   (p15:sp15 ph20):f3
   2u pl11:f1
   2u pl16:f3
   2u cw:f3 ph20
;---------------------------------------x-x alternation on H
7  1u
```

```
   (p16 ph20):f1
   (p16 ph22):f1
   1u
lo to 7 times l8
   2u do:f3
   2u pl1:f1
   2u
   (p15:sp16 ph20):f3
   2u fq=cnst12 (bf ppm):f1
   2u pl3:f3
   2u fq=cnst16 (bf ppm):f3
   GRADIENT9
;----------------------------------------------------------------------
;---------------------------------------15N evolution
31 (p5 ph1):f3
32 d0
   d0
   10u
   p26:gp27*-1*EA
   200u
   (p6 ph2):f3
   10u
   p26:gp27*EA
   200u
;---------------------------------------second INEPT
   (center (p1 ph20):f1 (p5 ph3):f3)
   10u
   (p11:sp2 ph18:r):f1
   GRADIENT2
   INEPT21 pl1:f1
   (center(p2 ph20):f1 (p6 ph20):f3)
   GRADIENT2
   INEPT22
   (center(p1 ph21):f1 (p5 ph20):f3)
;---------------------------------------third INEPT
   GRADIENT3
   INEPT3
   (center(p2 ph20):f1 (p6 ph20):f3)
   GRADIENT3
   INEPT3
   (center (p1 ph21):f1 (p5 ph21):f3)
   d12
   (p2 ph20):f1
   10u
   p26:gp26
   200u LOCKH_OFF
;---------------------------------------acquisition
   go=2 ph31
   1m mc #0 to 2 F1EA(igrad EA & ip3 & ip3 & ip31 & ip31,id0)
10u do:f1
10u do:f2
10u do:f3
10u LOCKH_OFF
exit

ph1 =0 2
ph2 =0 0 0 0 2 2 2 2
ph3 =2
```

```
ph4 =1 1 3 3
ph31=0 2 2 0

ph17=2
ph18=0

ph20=0
ph21=1
ph22=2
ph23=3
```

Off-resonance CW decoupling for ^{15}N ν_1 calibration (Chapter 3)

Sample: ^{15}N labeled

```
;15N-1H HSQC correlations without water saturation
;The delay for 3-9-19 watergate (d5) should be matched
;with 1/d;d=distance of next null point (in Hz).

;built upon a fast-HSQC
;S. Mori et al, JMR B108, 94-98 (1995)

;cnst3 : o3p
;cnst13: off-res CW decouple pos (ppm)

;pl1   : power for 1H
;pl2   : power for 13C
;pl3   : power for 15N
;pl13  : power for 15N CW decoupling

;p1    : 90 degree hard pulse 1H
;p3    : 90 degree hard pulse 13C
;p4    : 180 degree hard 13C pulse (225d for 5/600)
;p5    : 90 degree hard pulse 15N
;pcpd3 : 90 deg cpd-pulse15N(waltz16,160u)

;d1    : relaxation delay
;d2    : INEPT delay (~2.7m)
;d5    : delay for 3-9-19=1/(Hz between nulls)
;in0   : 1/(2 SW) (Hz)

;p21   : 500u (Gradient in first INEPT)
;p22   : 500u (Gradient for z-filter)
;p23   : 1m (Gradient for second INEPT)
;gpz1  : 19%
;gpz2  : 30%
;gpz3  : 65%


#include <Avance.incl>
```

```
define delay INEPT_W
define delay INEPT_D

#define GRADIENT1  10u p21:gp1 200u
#define GRADIENT2  10u p22:gp2 200u
#define GRADIENT3  10u p23:gp3 200u

"p2=2*p1"
"p6=2*p5"

"in0=inf1/2"

"d0=in0/2-p5*2/3.14159-p1"
"d3=d5/2-p5"
"INEPT_D=d2-p21-210u"
"INEPT_W=d2-(p23+210u+p1*2.3846+d5*2.5)-10u"


1  10u ze
2  1m do:f3
   d1
   10u fq=cnst3 (bf ppm):f3
   10u pl1:f1
   10u pl2:f2
   20u pl3:f3
   20u LOCKH_ON
;----------------------------------------first INEPT
   (p1 ph20):f1
   GRADIENT1
   INEPT_D
   (center(p2 ph21):f1 (p6 ph1):f3)
   GRADIENT1
   INEPT_D
   (p1 ph21):f1
   GRADIENT2
;----------------------------------------15N evolution
   (refalign (p5 ph1 d0 d0 p5 ph20):f3 center (p2 ph23):f1 center (p3 ph20
1.5u p4 ph21 1.5u p3 ph20):f2)
;-----------------------uncomment for non 13C labeled system
;   (p5 ph1):f3
;   (d0 p2 ph23 d0):f1
;   (p5 ph20):f3
   GRADIENT2
;----------------------------------------second INEPT
   (p1 ph22):f1
   GRADIENT3
   INEPT_W
   10u
   (p1*0.2308 ph21 d5 p1*0.6923 ph21 d5 p1*1.4615 ph21):f1
   (d3 p6 ph1 d3):f3
   (p1*1.4615 ph23 d5 p1*0.6923 ph23 d5 p1*0.2308 ph23):f1
   GRADIENT3
   10u fq=cnst13 (bf ppm):f3
   INEPT_W pl13:f3 LOCKH_OFF
;---------------------------------------acquisition
   go=2 ph31 cw:f3
   1m do:f3 mc #0 to 2 F1PH(ip1,id0)
10u do:f1
```

```
10u do:f2
10u do:f3
10u LOCKH_OFF
exit

ph1 =0 2
ph31=2 0

ph20=0
ph21=1
ph22=2
ph23=3
```

^{15}N HEHAHA-$R_{1\rho}$: on-resonance $R_{1\rho}$ used during large amplitude spin-lock experiments (Chapter 3)

Sample: ^{15}N labeled

```
;see paper Korz et al., JACS (2005)

;d1    : relaxation delay and water suppression
;pl1   : power for 1H
;p21   : 1 ms (Gradient before acquisition)
;gpz1  : 50 %

;p1    : 90 degree hard pulse 1H
;p10   : 1.5ms gaussian
;p11   : 1/J (NH - 10.8 ms)
;p16   : SL pulse (T_relax)
;cnst1 : O1p
;cnst3 : O3p
;cnst5 : water lock Hz
;cnst6 : spin-lock N Hz
;cnst7  : wRF MAX <=2000Hz
;cnst8  : wRF desired
;cnst11: on-resonance proton ppm
;cnst13: on-resonance nitrogen ppm
;cnst14: how far off nitrogen Hz
;cnst20: zeta offset (Hz)
;cnst21: 15N temp corr placement (ppm)
;d5    : delay for 3-9-19=1/(Hz between nulls)
;d9    : total relax delay (!!probe dependent!!)
;p16   : T_relax
;pl15  : max spin lock power for temp-corr
;pl16  : spin lock power
;pl6   : matched 15N field strength (~90 Hz)
;pl5   : mathced 1H field strength (~90 Hz)
;d14   : var temp corr
```

```
;l8    : equals cnst20
;d20   : dephasing period for undesired signals

;SINE GRADIENTS
#define GRADIENT0  10u p20:gp0 200u
#define GRADIENT1  10u p21:gp1 200u
#define GRADIENT2  10u p22:gp2 200u
#define GRADIENT3  10u p23:gp3 200u



#include <Avance.incl>
"p2 = 2*p1"
"d11=d1-d14"
"d13=1/cnst7"
"d17=1/cnst8"
"p15=p16/2"

"d20=(3.1415927)/(2*cnst20)"

"d11=d1-d14"

"l8=cnst20"

1 ze
  d13
  d17
  d9

2 2u
  10u LOCKH_OFF
;----------------------------variable temp correction + xfboltzmann
  2u pl15:f3
  2u fq=cnst21 (bf ppm):f3
  2u cw:f3
  d14
  2u do:f3
  4u
  d11
  10u pl1:f1
  10u pl3:f3
  10u LOCKH_ON
  10u fq=cnst1 (bf ppm):f1
  10u fq=cnst13 (bf ppm):f3
  (p5 ph20):f3
  GRADIENT0
  10m
;------------------------------HEHAHA
  (p10:sp1 ph18:r):f1
  5u
  2u pl1:f1
  3u
  (p1 ph20):f1
  2u fq=cnst11 (bf ppm):f1
  2u pl6:f3
  2u pl5:f1
  (p11 ph1):f1 (p11 ph2):f3
  2u pl1:f1 pl3:f3
```

```
  (p5 ph21):f3
;------------------------------cleaning PFG
  GRADIENT1
;------------------------------spin-lock
if (l8 > 1)
{
  (p5 ph21):f3
  2u pl16:f3
  (center (p15 ph20):f3 (p2 ph20):f1)
  (center (p15 ph20):f3 (p2 ph20):f1)
  2u pl3:f3
  (p5 ph7):f3
;  2u
;------------------------------zeta
  2u
  (p5 ph23):f3
  2u pl3:f3
  d20
  2u
  (p5 ph21):f3
  2u pl1:f1
}
else
{
  (p5 ph21):f3
  2u pl16:f3
  (center (p15 ph20):f3 (p2 ph20):f1)
  (center (p15 ph20):f3 (p2 ph20):f1)
  2u pl3:f3
  (p5 ph7):f3
;  2u
}
;------------------------------
  GRADIENT2
;------------------------------HEHAHA back
  (p5 ph21):f3
  2u pl5:f1
  2u pl6:f3
  (p11 ph5):f1 (p11 ph6):f3
  2u fq=cnst1 (bf ppm):f1
;--------------------------------3-9-19
  2u pl1:f1
  2u pl3:f3
  GRADIENT3
  (p1*0.2308 ph21 d5 p1*0.6923 ph21 d5 p1*1.4615 ph21):f1
  d5
  (p1*1.4615 ph23 d5 p1*0.6923 ph23 d5 p1*0.2308 ph23):f1
  GRADIENT3
  4u pl13:f3 LOCKH_OFF
;---------------------------------------acquisition
  go=2 ph31 cpd3:f3
  100u do:f3 wr #0
  10u LOCKH_OFF
exit


ph1= 1 1 1 1 1 1 1 1
     3 3 3 3 3 3 3 3
```

```
ph2= 2 0
ph3= 1
ph4= 3
ph5= 0 0 0 0 2 2 2 2
ph6= 0 0 2 2
ph7= 3 3 3 3 3 3 3 3
     3 3 3 3 3 3 3 3
;for testing
;     1 1 1 1 1 1 1 1
;     1 1 1 1 1 1 1 1
ph31=0 2 2 0 2 0 0 2
     2 0 0 2 0 2 2 0
;for testing
;     2 0 0 2 0 2 2 0
;     0 2 2 0 2 0 0 2



ph18=2

ph20=0
ph21=1
ph22=2
ph23=3
```

^{15}N HEHAHA-$R_{1\rho}$ Reference Experiment: on-resonance $R_{1\rho}$ used during large amplitude spin-lock experiments (Chapter 3)

Sample: ^{15}N labeled

```
;see paper Korz et al., JACS (2005)

;d1    : relaxation delay and water suppression
;pl1   : power for 1H
;p21   : 1 ms (Gradient before acquisition)
;gpz1  : 50 %

;p1    : 90 degree hard pulse 1H
;p10   : 1.5ms gaussian
;p11   : 1/J (NH - 10.8 ms)
;p16   : SL pulse (T_relax)
;cnst1 : O1p
;cnst3 : O3p
;cnst5 : water lock Hz
;cnst6 : spin-lock N Hz
;cnst7  : wRF MAX <=2000Hz
;cnst8  : wRF desired
;cnst11: on-resonance proton ppm
;cnst13: on-resonance nitrogen ppm
;cnst14: how far off nitrogen Hz
;cnst20: zeta offset (Hz)
```

```
;cnst21: 15N temp corr placement (ppm)
;d5    : delay for 3-9-19=1/(Hz between nulls)
;d9    : total relax delay (!!probe dependent!!)
;p16   : T_relax
;pl15  : max spin lock power for temp-corr
;pl16  : spin lock power
;pl6   : matched 15N field strength (~90 Hz)
;pl5   : mathced 1H field strength (~90 Hz)
;d14   : var temp corr
;l8    : equals cnst20
;d20   : dephasing period for undesired signals

;SINE GRADIENTS
#define GRADIENT0  10u p20:gp0 200u
#define GRADIENT1  10u p21:gp1 200u
#define GRADIENT2  10u p22:gp2 200u
#define GRADIENT3  10u p23:gp3 200u



#include <Avance.incl>
"p2 = 2*p1"
"d11=d1-d14"
"d13=1/cnst7"
"d17=1/cnst8"
"p15=p16/2"

"d20=(3.1415927)/(2*cnst20)"

"d11=d1-d14"

"l8=cnst20"

1 ze
  d13
  d17
  d9

2 2u
  10u LOCKH_OFF
;----------------------------variable temp correction + xfboltzmann
  2u pl15:f3
  2u fq=cnst21 (bf ppm):f3
  2u cw:f3
  d14
  2u do:f3
  4u
  d11
  10u pl1:f1
  10u pl3:f3
  10u LOCKH_ON
  10u fq=cnst1 (bf ppm):f1
  10u fq=cnst13 (bf ppm):f3
  (p5 ph20):f3
  GRADIENT0
  10m
;------------------------------HEHAHA
  (p10:sp1 ph18:r):f1
```

```
  5u
  2u pl1:f1
  3u
  (p1 ph20):f1
  2u fq=cnst11 (bf ppm):f1
  2u pl6:f3
  2u pl5:f1
  (p11 ph1):f1 (p11 ph2):f3
  2u pl1:f1 pl3:f3
  (p5 ph21):f3
;-------------------------------cleaning PFG
  GRADIENT1
;-------------------------------HEHAHA back
  (p5 ph21):f3
  2u pl5:f1
  2u pl6:f3
  (p11 ph5):f1 (p11 ph6):f3
  2u fq=cnst1 (bf ppm):f1
;--------------------------------3-9-19
  2u pl1:f1
  2u pl3:f3
  GRADIENT3
  (p1*0.2308 ph21 d5 p1*0.6923 ph21 d5 p1*1.4615 ph21):f1
  d5
  (p1*1.4615 ph23 d5 p1*0.6923 ph23 d5 p1*0.2308 ph23):f1
  GRADIENT3
  4u pl13:f3 LOCKH_OFF
;---------------------------------------acquisition
  go=2 ph31 cpd3:f3
  100u do:f3 wr #0
  10u LOCKH_OFF
exit


ph1= 1 1 1 1 1 1 1 1
     3 3 3 3 3 3 3 3

ph2= 2 0
ph3= 1
ph4= 3
ph5= 0 0 0 0 2 2 2 2
ph6= 0 0 2 2
ph7= 3 3 3 3 3 3 3 3
     3 3 3 3 3 3 3 3
;for testing
;     1 1 1 1 1 1 1 1
;     1 1 1 1 1 1 1 1
ph31=0 2 2 0 2 0 0 2
     2 0 0 2 0 2 2 0
;for testing
;     2 0 0 2 0 2 2 0
;     0 2 2 0 2 0 0 2



ph18=2

ph20=0
```

```
ph21=1
ph22=2
ph23=3
```

Off-resonance CW decoupling for ^{13}C ν_1 calibration (Chapter 4)

Sample: selectively methyl labeled $^{13}CHD_2$

```
;13C field strength measurements with 2H decoupling
;G. Bodenhausen ans D.J. Ruben, Chem. Phys. Lett. 69, 185 (1980)
;D.R. Muhandiram et al, JMR B102, 317-321 (1993)


;pl1   : power for 1H
;pl3   : power for 15N
;pl4   : power for 2H
;pl2   : power for 13C hard
;pl12  : power for 13C CW decoupling (check probe abilities!)

;p1    : 90 degree hard pulse 1H
;p3    : 90 degree hard pulse 13C
;p4    : 13C pulse, 225deg for 500/600, 180deg for 750/900
;p5    : 90 degree hard pulse 15N
;pcpd4 : 90 deg cpd-pulse 2H

;p21   : 1m (Gradient in first INEPT)
;p22   : 800u (Gradient in first INEPT)
;p23   : 1m (Gradient for z-filter)
;p24   : 1m (Gradient for second INEPT)

;cnst3 : o2p
;cnst13: off-res CW dec (ppm)
;gpz1  : 19%
;gpz2  : 30%
;gpz3  : 65%
;gpz4  : 15%

;d1    : relaxation delay
;d2    : 1H-13C INEPT delay (1.7m)
;d5    : delay 3-9-19=1/(Hz between nulls)
;in0   : 1/2*SW(in Hz)

;cnst21: CO chemical shift (offset, in ppm)

#include <Avance_dl.incl>

define delay INEPT_1
define delay INEPT_2

#define GRADIENT0  10u p20:gp0 200u
#define GRADIENT1  10u p21:gp1 200u
#define GRADIENT2  10u p22:gp2 200u
#define GRADIENT3  10u p23:gp3 200u
#define GRADIENT4  10u p24:gp4 200u
```

```
"p2=p1*2"
"p6=p5*2"

;"spoff13=bf2*(cnst23/1000000)-o2"

"in0=inf1/2"


"d0=in0/2-p3*2/3.1415"
"INEPT_1=d2-(p21+210u)"
"INEPT_2=d2-(p24+210u)-10u"


1  10u ze
   10m LOCKDEC_ON
   10u H2_PULSE
2  1m
   10u do:f2
   10u do:f4
   10u fq=cnst3 (bf ppm):f2 ;o2p
   10m H2_LOCK
   10u LOCKH_OFF
   20u
   d1
   10u do:f1
   10u pl1:f1
   10u pl2:f2
   10u pl14:f4
;   20u pl3:f3
   20u LOCKH_ON
;----------------------------------------Boltzmann
   (p3 ph20):f2
   GRADIENT0
   10m
   10u H2_PULSE
;   10u cpd4:f4
;----------------------------------------first INEPT
   (p1 ph20):f1
   GRADIENT1
   INEPT_1
   (center (p2 ph20):f1 (p3 ph20 2u p4 ph21 2u p3 ph20):f2)
   GRADIENT1
   INEPT_1
   (p1 ph21):f1
   GRADIENT2
   10u cpd4:f4
;----------------------------------------13C evolution
9  (refalign (p3 ph1 d0 d0 p3 ph20):f2 center(p2 ph20):f1)
   10u do:f4
   GRADIENT3
   (p1 ph20):f1
;----------------------------------------second INEPT
   GRADIENT4
   INEPT_2
   10u
   (center (p2 ph20):f1 (p3 ph20 2u p4 ph21 2u p3 ph20):f2)
   GRADIENT4
```

```
   10u fq=cnst13 (bf ppm):f2 ;off-dec ppm
   INEPT_2 pl12:f2
;---------------------------------------acquisition
   go=2 ph31 cw:f2
   1m do:f2 mc #0 to 2 F1PH(ip1, id0)
   10u do:f1
   10u do:f2
;   10u do:f3
   10u do:f4
   10m H2_LOCK
   10m LOCKH_OFF
   10m LOCKDEC_OFF

;   10u LOCKH_OFF
exit

ph1= 0 2
ph20=0
ph21=1
ph22=2
ph23=3
ph31=2 0
```

Off-resonance CW decoupling for ^{1}H ν_1 calibration (Chapter 4)

Sample: selectively methyl labeled $^{13}CHD_2$

```
;G. Bodenhausen ans D.J. Ruben, Chem. Phys. Lett. 69, 185 (1980)
;D.R. Muhandiram et al, JMR B102, 317-321 (1993)

;cnst1 : off-res 1H dec (ppm)
;cnst11: o1p (ppm)

;pl1   : power for 1H
;pl11  : power for off-res 1H dec
;pl3   : power for 15N
;pl4   : power for 2H
;pl2   : power for 13C hard
;pl12  : power for 13C GARP decoupling
;sp12  : power for selective C=O pulse

;p1    : 90 degree hard pulse 1H
;p3    : 90 degree hard pulse 13C
;p4    : 13C pulse, 225deg for 500/600, 180deg for 750/900
;p5    : 90 degree hard pulse 15N
;pcpd4 : 90 deg cpd-pulse 2H


;p21   : 1m (Gradient in first INEPT)
;p22   : 800u (Gradient in first INEPT)
```

```
;p23   : 1m (Gradient for z-filter)
;p24   : 1m (Gradient for second INEPT)

;gpz1  : 19%
;gpz2  : 30%
;gpz3  : 65%
;gpz4  : 15%

;d1    : relaxation delay
;d2    : 1H-13C INEPT delay (1.7m)
;d5    : delay 3-9-19=1/(Hz between nulls)
;in0   : 1/2*SW(in Hz)

;cnst21: CO chemical shift (offset, in ppm)

#include <Avance_dl.incl>

define delay INEPT_1
define delay INEPT_2
define delay INEPT_R

#define GRADIENT0  10u p20:gp0 200u
#define GRADIENT1  10u p21:gp1 200u
#define GRADIENT2  p22:gp2 190u
#define GRADIENT3  10u p23:gp3 200u
#define GRADIENT4  10u p24:gp4 200u
#define GRADIENT5  10u p25:gp5 200u
#define GRADIENT6  10u p26:gp6 200u
#define GRADIENT7  p27:gp7 190u

"p2=p1*2"
"p6=p5*2"

;"spoff13=bf2*(cnst23/1000000)-o2"

"in0=inf1/2"


"d0=in0/2-p3*2/3.1415"
"INEPT_1=d2-(p21+210u)"
"INEPT_2=d2-(p24+210u)"

"INEPT_R=d2-(p21+210u)"


1  10u ze
   10m LOCKDEC_ON
   10u H2_PULSE
2  1m
   10u do:f2
   10u do:f4
   10m H2_LOCK
```

```
   10u LOCKH_OFF
   20u pl9:f1
   d1 cw:f1
   10u do:f1
   10u pl1:f1
   10u pl2:f2
   10u pl14:f4
   20u LOCKH_ON
;----------------------------------------Boltzmann
   (p3 ph20):f2
   GRADIENT0
   10m
   10u H2_PULSE
;----------------------------------------first INEPT
   (p1 ph20):f1
   INEPT_1
   GRADIENT1
   (center (p2 ph21):f1 (p4 ph20):f2)
   GRADIENT1
   INEPT_1
;----------------------------------------refocused INEPT
  (center (p1 ph21):f1 (p3 ph20):f2)
   INEPT_R
   GRADIENT3
   (center (p2 ph21):f1 (p4 ph20):f2)
   GRADIENT3
   INEPT_R
   (p3 ph21):f2
;---------------------------------let's decouple
   5u fq=cnst1 (bf ppm):f1
   5u pl11:f1
   GRADIENT2
   5u cpd4:f4
   5u cw:f1
;----------------------------------------13C evolution
   (p3 ph1):f2
   d0
   d0
   (p3 ph20):f2
;9  (refalign (p3 ph1 d0 d0 p3 ph20):f2 center(p2 ph20):f1)
   5u do:f1
   5u do:f4
   GRADIENT7
   5u pl1:f1
   5u fq=cnst11 (bf ppm):f1
;----------------------------------------back out
   (p3 ph2):f2
   INEPT_R
   GRADIENT5
   (center (p2 ph21):f1 (p4 ph20):f2)
   GRADIENT5
   INEPT_R
```

```
;-----------------------------------------second INEPT
   (center (p1 ph20):f1 (p3 ph20):f2)
   GRADIENT4
   INEPT_2
   (center (p2 ph20):f1 (p4 ph21):f2)
   GRADIENT4
   INEPT_2 pl12:f2
;---------------------------------------acquisition
   go=2 ph31 cpd2:f2
   1m do:f2 mc #0 to 2 F1PH(ip1, id0)
   10u do:f4
   10u do:f2
   10u do:f1
   10m H2_LOCK
   10m LOCKH_OFF
   10m LOCKDEC_OFF
exit

ph1= 0 2
ph2= 1 1 3 3
ph20=0
ph21=1
ph22=2
ph23=3
ph31=2 0 0 2
```

^{13}C methyl Off-resonance $R_{1\rho}$ (Chapter 4)

Sample: selectively methyl labeled $^{13}CHD_2$

```
;methyl 13C R1rho
;adiabatic ramp pulses for off-res spin-lock
;variable temperature correction
;Brath et al., JACS (2005)

;cnst1 : 1H dec (0.3 ppm)
;cnst11: o1p (ppm)
;cnst25: temp-corr far off-field position (ppm)
;cnst15: off-res spin-lock position (ppm)
;cnst16: o2p (ppm)
;cnst20: w_RF (Hz)
;cnst21: w_MAX (Hz)

;pl1   : power for 1H
;pl11  : power for off-res 1H dec
;pl3   : power for 15N
;pl4   : power for 2H
```

```
;pl2   : power for 13C hard
;pl12  : power for 13C GARP decoupling
;pl14  : power for 2H decoupling
;pl15  : max power for comp
;pl16  : power for spin-lock
;sp1   : power for flip-back
;sp2   : power for flip-back
;sp3   : power for flip-back
;sp15  : power for ramp-on
;sp16  : power for ramp-off

;p1    : 90 degree hard pulse 1H
;p11   : 1.5m flip-back Gauss-128
;p3    : 90 degree hard pulse 13C
;p4    : 13C pulse, 225deg for 500/600, 180deg for 750/900
;p15   : 13C adiabatic ramp on (4ms)
;p16   : 13C adiabatic ramp off (4ms)
;p18   : T_relax/2

;pcpd2 : 90 deg cpd-pulse 13C
;pcpd4 : 90 deg cpd-pulse 2H

;p21   : 1m (Gradient in first INEPT)
;p22   : 800u (Gradient in first INEPT)
;p23   : 1m (Gradient for z-filter)
;p24   : 1m (Gradient for second INEPT)

;gpz1  : 19%
;gpz2  : 30%
;gpz3  : 65%
;gpz4  : 15%

;d1    : relaxation delay
;d2    : 1H-13C INEPT delay (1.7m)
;d5    : delay 3-9-19=1/(Hz between nulls)
;d8    : T_RELAX
;d9    : T_MAX
;d14   : T_HEAT (calculated)
;in0   : 1/2*SW(in Hz)


#include <Avance_dl.incl>

define delay INEPT_1
define delay INEPT_12
define delay INEPT_2
define delay INEPT_R
define delay INEPT_R2

#define GRADIENT0  10u p20:gp0 200u
#define GRADIENT1  10u p21:gp1 200u
#define GRADIENT2  10u p22:gp2 200u
```

```
#define GRADIENT3  10u p23:gp3 200u
#define GRADIENT4  10u p24:gp4 200u
#define GRADIENT5  10u p25:gp5 200u
#define GRADIENT6  10u p26:gp6 200u
#define GRADIENT7  10u p27:gp7 200u
#define GRADIENT8  10u p28:gp8 200u

"p2=p1*2"
"p6=p5*2"

"in0=inf1/2"
"d0=in0/2-p3*2/3.1415"

"INEPT_1=d2-(p21+210u)"
"INEPT_12=d2-(p21+p11+210u+5u)"

"INEPT_2=d2-(p24+210u)"

"INEPT_R=d2-(p21+210u)"
"INEPT_R2=d2-(p25+210u+p11+5u)"

"d11=d1-d14"
"p18=0.5*d8"

"d20=0.001*d9"
"d21=1/cnst20"
"d22=1/cnst21"

1  10u ze
   d20
   d21
   d22
   10m LOCKDEC_ON
   10u H2_PULSE
2  1m
   10u do:f1
   10u do:f2
   10u do:f4
   10m H2_LOCK
   10u LOCKH_OFF
;---------------------------------Temperature compensation
   d11
   10u LOCKH_ON
   10u fq=cnst25 (bf ppm):f2
   10u pl15:f2
   10u cw:f2
   d14
   10u do:f2
   10u fq=cnst16 (bf ppm):f2
;-----------------------------------------
   10u pl1:f1
   10u pl2:f2
```

```
   10u pl14:f4
;---------------------------------------Boltzmann
   (p3 ph20):f2
   GRADIENT0
   10m
   10u H2_PULSE
;-----------------------------------------first INEPT
   (p1 ph20):f1
   INEPT_1
   GRADIENT1
   (center (p2 ph21):f1 (p4 ph20):f2)
   GRADIENT1
   INEPT_1
;---------------------------------------refocused INEPT
   (center (p1 ph21):f1 (p3 ph20):f2)
   INEPT_R2
   (p11:sp1 ph17:r):f1
   5u
   GRADIENT3
   (center (p2 ph21):f1 (p4 ph20):f2)
   GRADIENT3
   INEPT_R
   (p3 ph21):f2
;---------------------------------off-resonance spin-lock
   GRADIENT2
   2u fq=cnst1 (bf ppm):f1
   2u fq=cnst15 (bf ppm):f2
   2u pl1:f1
   2u
   (p15:sp15 ph20):f2
   2u
   2u pl16:f2
   (center (p18 ph20):f2 (p2 ph20):f1)
   (center (p18 ph20):f2 (p2 ph20):f1)
   2u pl2:f2
   2u
   (p16:sp16 ph20):f2
   5u
   2u pl1:f1
   2u fq=cnst16 (bf ppm):f2
   2u fq=cnst11 (bf ppm):f1
   GRADIENT8
;-----------------------------------------13C evolution
   5u cpd4:f4
9  (refalign (p3 ph1 d0 d0 p3 ph20):f2 center(p2 ph20):f1)
   5u
   5u do:f4
   GRADIENT7
;-------------------------------------------back out
   (p3 ph2):f2
   INEPT_R
   GRADIENT5
```

```
   (center (p2 ph21):f1 (p4 ph20):f2)
   GRADIENT5
   INEPT_R2
;-----------------------------------------second INEPT
 ;  (p11:sp3 ph17:r):f1 "for testing, unecesarry"
;   5u
   (center (p1 ph20):f1 (p3 ph20):f2)
   GRADIENT4
   INEPT_2
   (center (p2 ph20):f1 (p4 ph21):f2)
   GRADIENT4
   INEPT_2 pl12:f2
;-----------------------------------------acquisition
   go=2 ph31 cpd2:f2
   1m do:f2 mc #0 to 2 F1PH(ip1, id0)
   10u do:f4
   10u do:f2
   10u do:f1
   10m H2_LOCK
   10m LOCKH_OFF
   10m LOCKDEC_OFF
exit

ph1= 0 2
ph2= 1 1 3 3
ph20=0
ph21=1
ph22=2
ph23=3

ph17=0
ph18=1
ph19=2

ph31=2 0 0 2
```

HEteronuclear ROtatIng-frame Nuclear Exchange (HEROINE) (Chapter 5)

Sample: ^{15}N labeled

```
;Take note of the maximum power and pulse length that is acceptable for
your probe.

;d9    : max T_relax (~0.125 ms, probe dependent)
;d8    : T_relax

;pl1   : power for 1H
;pl2   : power for 13C
;pl3   : power for 15N
;pl13  : power for 15N waltz16 decoupling
;pl16  : spin-lock power level 15N
```

```
;p1    : 90 degree hard pulse 1H
;p3    : 90 degree hard pulse 13C
;p4    : 180 degree hard 13C pulse (225d for 5/600)
;p5    : 90 degree hard pulse 15N
;p11   : 1.5ms Gaussian
;p15   : 0.25*d8
;pcpd3 : 90 deg cpd-pulse15N(waltz16,160u)

;d1    : relaxation delay
;d2    : INEPT delay (~2.7m)
;d5    : delay for 3-9-19=1/(Hz between nulls)
;in0   : 1/(2 SW) (Hz)

;p21   : 500u (Gradient in first INEPT)
;p22   : 500u (Gradient for z-filter)
;p23   : 1m (Gradient for second INEPT)
;gpz1  : 19%
;gpz2  : 30%
;gpz3  : 65%

;cnst11: o3p
;cnst22: off-res SL (ppm)
;cnst21: temp-comp (ppm)
;cnst23: amide region (ppm)
;cnst20: o1p

#include <Avance_dl.incl>

define delay INEPT_W
define delay INEPT_D
define delay INEPT_D2
define delay INEPT_D22
define delay INEPT_2
define delay U_ELEMENT
define delay U_ELEMENT2

#define GRADIENT0  10u p20:gp0 200u
#define GRADIENT1  10u p21:gp1 200u
#define GRADIENT2  10u p22:gp2 200u
#define GRADIENT3  10u p23:gp3 200u
#define GRADIENT4  10u p24:gp4 200u
#define GRADIENT5  10u p25:gp5 200u
#define GRADIENT6  10u p26:gp6 200u
#define GRADIENT7  10u p27:gp7 200u
#define GRADIENT8  10u p28:gp8 200u
#define GRADIENT9  10u p29:gp9 200u

"p2=2*p1"
"p6=2*p5"

"in0=inf1/2"
```

```
"d0=in0/2-p1-p5*2/3.14159"

"d3=d5/2-p5"
"INEPT_D=d2-p21-210u-p11-10u"
"INEPT_D2=d2-p23-210u"
"INEPT_D22=d2-p23-210u-p11-10u"
"INEPT_2=d2-p25-210u"
"INEPT_W=d2-(p23+210u+p1*2.3846+d5*2.5)"

"U_ELEMENT=d2-p24-210u"
"U_ELEMENT2=d2-p24-210u"
"p15=d8*0.25"


"d14=d9-d8"
"d11=d1-d14-20u"

1  10u ze
2  1m do:f3
   d11
   10u pl15:f3
   10u fq=cnst21 (bf ppm):f3
   5u cw:f3
   d14
   5u do:f3
   10u fq=cnst11 (bf ppm):f3
   10u pl1:f1
   10u pl2:f2
   20u pl3:f3
   20u LOCKH_ON
;-----------------------------------BOLTZ
   (p5 ph20):f3
   GRADIENT0
   1m
;----------------------------------------first INEPT
   (p1 ph20):f1
   10u
   (p11:sp1 ph18:r):f1
   GRADIENT1
   INEPT_D pl1:f1
   (center(p2 ph21):f1 (p6 ph20):f3)
   GRADIENT1
   INEPT_D
   (p11:sp1 ph19:r):f1
   5u
   5u pl1:f1
   (p1 ph23):f1
;----------------------------------------SL HzNx
   GRADIENT7
   (p5 ph21):f3
   2u pl16:f3
```

```
   2u fq=cnst23 (bf ppm):f1
   (center (p15 ph20):f3 (p2 ph20):f1)
   (center (p15 ph20):f3 (p2 ph20):f1)
   2u fq=cnst20 (bf ppm):f1
   2u pl3:f3
   (p5 ph23):f3
   GRADIENT8
   (p5 ph21):f3
;----------------------------------------U_element
   U_ELEMENT
   GRADIENT4
   (center (p2 ph21):f1 (p6 ph21):f3)
   GRADIENT4
   U_ELEMENT2
   (p5 ph20):f3
   GRADIENT9
   (p5 ph22):f3
;----------------------------------------SL Ny
   2u pl16:f3
   2u fq=cnst23 (bf ppm):f1
   (center (p15 ph21):f3 (p2 ph20):f1)
   (center (p15 ph21):f3 (p2 ph20):f1)
   2u fq=cnst20 (bf ppm):f1
   2u pl3:f3
   (p5 ph20):f3
   GRADIENT2
;----------------------------------------15N evolution
   (p5 ph1):f3
   d0
   (p2 ph20):f1
   d0
   (p5 ph20):f3
   GRADIENT6
;--------------------------------------
   (p5 ph2):f3
   GRADIENT5
   INEPT_2
   (center(p2 ph3):f1 (p6 ph20):f3)
   GRADIENT5
   INEPT_2
   (p5 ph23):f3
;----------------------------------------second INEPT
   (p1 ph22):f1
   GRADIENT3
   INEPT_W
   (p1*0.2308 ph21 d5 p1*0.6923 ph21 d5 p1*1.4615 ph21):f1
   (d3 p6 ph1 d3):f3
   (p1*1.4615 ph23 d5 p1*0.6923 ph23 d5 p1*0.2308 ph23):f1
   GRADIENT3
   INEPT_W pl13:f3 LOCKH_OFF
;----------------------------------------acquisition
   go=2 ph31 cpd3:f3
```

```
   1m do:f3 mc #0 to 2 F1PH(ip1,id0)
10u do:f1
10u do:f2
10u do:f3
10u LOCKH_OFF
exit

ph1 =0 2 2 0
ph2 =0 0 0 0
ph3 =1 1 3 3
ph31=2 0 0 2

ph20=0
ph21=1
ph22=2
ph23=3

ph16=0
ph17=1
ph18=2
ph19=3
```

CT-CPMG experiment that has equalized heating and can be used in conjunction with HEROINE (Chapter 5)

Sample: ^{15}N labeled

```
;Take note of the maximum power and pulse length that is acceptable for
your probe.

; SET L3 to based on desired v_CPMG and then re-run remember to set
cnst7, d20, d21 from the HEROINE experiment. This is for the
temperature correction

;optimization of water flip back:
;- optimize watergate (o1,sp2,ph26)
;- optimize water flip back (sp1,ph16,ph18,ph17,ph19)

;in0   : 1/(2 SW) (Hz)
;cnst7 : HEROINE SL (Hz)
;cnst21: off-res temp-corr (ppm)
;cnst11: o3p
;pl1   : power for 1H
;pl2   : power for 13C
;pl3   : power for 15N

;sp1   : water flipback power
;sp2   : water flipback power in watergate
;spnam1: 1.5ms Gaussian
;spnam2: 1.5ms Gaussian
```

```
;p1    : 90 degree hard pulse 1H
;p5    : 90 degree hard pulse 15N
;p11   : water flipback pulse (1.5m)
;p50   : Temperature_corr pulse

;p20   : 1m  (Cleaning Gradient )
;p21   : 500u (Gradient in first INEPT)
;p22   : 500u (Gradient in second INEPT)
;p23   : 900u (Gradient in watergate)
;p24   : 500u (Gradient in Z-filter)
;gpz0  : 80%
;gpz1  : 19%
;gpz2  : 15%
;gpz3  : 32%
;gpz4  : 60%


;d1    : relaxation delay
;d2    : INEPT delay (~2.7ms)
;d14   : inter-pulse delay
;d16   : Temp CORR length
;d20   : HEROINE recycle delay
;d21   : HEROINE max T_relax
;d8    : T-constant time CPMG
;l3    : CPMG loop



define delay INEPT1
define delay INEPT2
define delay INEPT3
define delay U1
define delay INEPT_2
define delay INEPT_W

#include <Avance_dl.incl>

#define GRADIENT0   10u p20:gp0 200u
#define GRADIENT1   10u p21:gp1 200u
#define GRADIENT2   10u p22:gp2 200u
#define GRADIENT3   10u p23:gp3 200u
#define GRADIENT4   10u p24:gp4 200u
#define GRADIENT5   10u p25:gp5 200u
#define GRADIENT6   10u p26:gp6 200u
#define GRADIENT7   10u p27:gp7 200u


"p2=2*p1"
"p6=2*p5"
"in0=inf1/2"
"d0=in0/2-p1-p5*2/3.14159"
```

```
"INEPT1=d2-(p21+p11+210u)-10u"
"INEPT_2=d2-p27-210u"
"INEPT_W=d2-(p23+210u+p1*2.3846+d5*2.5)"

"d3=d5/2-p5"
"U1=d2-p11-10u-p26-210u"

;"d13=d1-d8-180u"
"d13=d1-d16-180u"
"d14=d8/(16*l3)-p5"
"p50=d16"
"d58=1/cnst7"
"d59=1/(100000*d21)"
"d60=1/(10000*d20)"
1  10u ze
   d58
   d59
   d60
2  1m
   10u do:f3
   20u pl1:f1
   20u pl2:f2
   20u pl3:f3
   d13
   10u pl15:f3
   10u fq=cnst21 (bf ppm):f3
   (p50 ph20):f3
   10u fq=cnst11 (bf ppm):f3
   10u pl3:f3
   20u pl1:f1
   20u pl2:f2
   20u pl3:f3

   20u LOCKH_ON
;----------------------------------------first INEPT
5  (p5 ph20):f3
   GRADIENT0
   1m
   (p1 ph20):f1
   10u
   (p11:sp1 ph18:r):f1
   GRADIENT1
   INEPT1 pl1:f1
   (center(p2 ph21):f1 (p6 ph20):f3)
   GRADIENT1
   INEPT1
   (p11:sp1 ph19:r):f1
   5u
   5u pl1:f1
   (p1 ph23):f1
```

```
   GRADIENT4


   (p5 ph4):f3
;----------------------------------------CPMG
11 d14
   (p6 ph21):f3
   d14
   d14
   (p6 ph21):f3
   d14
   d14
   (p6 ph20):f3
   d14
   d14
   (p6 ph22):f3
   d14
lo to 11 times l3
;----------------------------------------U element
   GRADIENT6
   U1
   (p11:sp3 ph15:r):f1
   5u
   5u pl1:f1
   (center(p2 ph21):f1 (p6 ph20):f3)
   10u
   (p11:sp3 ph15:r):f1
   GRADIENT6
   U1 pl1:f1
;----------------------------------------CPMG
21 d14
   (p6 ph20):f3
   d14
   d14
   (p6 ph20):f3
   d14
   d14
   (p6 ph21):f3
   d14
   d14
   (p6 ph23):f3
   d14
lo to 21 times l3
   (p5 ph5):f3
   GRADIENT5
;----------------------------------------15N evolution
   (p5 ph1):f3
   d0
   (p2 ph20):f1
   d0
   (p5 ph20):f3
   GRADIENT2
```

```
;---------------------------------------
   (p5 ph2):f3
   GRADIENT7
   INEPT_2
   (center(p2 ph3):f1 (p6 ph20):f3)
   GRADIENT7
   INEPT_2
   (p5 ph23):f3
;----------------------------------------second INEPT
   (p1 ph22):f1
   GRADIENT3
   INEPT_W
   (p1*0.2308 ph21 d5 p1*0.6923 ph21 d5 p1*1.4615 ph21):f1
   (d3 p6 ph1 d3):f3
   (p1*1.4615 ph23 d5 p1*0.6923 ph23 d5 p1*0.2308 ph23):f1
   GRADIENT3
   INEPT_W pl13:f3 LOCKH_OFF
;----------------------------------------acquisition
   go=2 ph31 cpd3:f3
   1m do:f3 mc #0 to 2 F1PH(ip1,id0)
10u do:f1
10u do:f2
10u do:f3
10u LOCKH_OFF
exit


ph1 =0 2 2 0
ph3 =1 1 3 3
ph2 =0 0 0 0
ph4 =0 0 0 0 2 2 2 2
ph5 =1
ph31=2 0 0 2 0 2 2 0


ph10=3 3 3 3
ph11=0 0 0 0
ph12=3 3 3 3


ph15=2
ph16=0
ph17=1
ph18=2
ph19=3

ph20=0
ph21=1
ph22=2
ph23=3

ph26=2
```

CT-CPMG Reference experiment that has equalized heating and can be used in conjunction with HEROINE (Chapter 5)

Sample: ^{15}N labeled

```
;Take note of the maximum power and pulse length that is acceptable for
your probe.

; SET L3 to based on desired v_CPMG and then re-run remember to set
cnst7, d20, d21 from the HEROINE experiment. This is for the
temperature correction

;optimization of water flip back:
;- optimize watergate (o1,sp2,ph26)
;- optimize water flip back (sp1,ph16,ph18,ph17,ph19)

;in0   : 1/(2 SW) (Hz)
;cnst7 : HEROINE SL (Hz)
;cnst21: off-res temp-corr (ppm)
;cnst11: o3p
;pl1   : power for 1H
;pl2   : power for 13C
;pl3   : power for 15N

;sp1   : water flipback power
;sp2   : water flipback power in watergate
;spnam1: 1.5ms Gaussian
;spnam2: 1.5ms Gaussian

;p1    : 90 degree hard pulse 1H
;p5    : 90 degree hard pulse 15N
;p11   : water flipback pulse (1.5m)
;p50   : Temperature_corr pulse

;p20   : 1m  (Cleaning Gradient )
;p21   : 500u (Gradient in first INEPT)
;p22   : 500u (Gradient in second INEPT)
;p23   : 900u (Gradient in watergate)
;p24   : 500u (Gradient in Z-filter)
;gpz0  : 80%
;gpz1  : 19%
;gpz2  : 15%
;gpz3  : 32%
;gpz4  : 60%


;d1    : relaxation delay
;d2    : INEPT delay (~2.7ms)
;d14   : inter-pulse delay
;d16   : Temp CORR length
;d20   : HEROINE recycle delay
```

```
;d21    : HEROINE max T_relax
;d8     : T-constant time CPMG
;l3     : CPMG loop



define delay INEPT1
define delay INEPT2
define delay INEPT3
define delay U1
define delay INEPT_2
define delay INEPT_W

#include <Avance_dl.incl>

#define GRADIENT0   10u p20:gp0 200u
#define GRADIENT1   10u p21:gp1 200u
#define GRADIENT2   10u p22:gp2 200u
#define GRADIENT3   10u p23:gp3 200u
#define GRADIENT4   10u p24:gp4 200u
#define GRADIENT5   10u p25:gp5 200u
#define GRADIENT6   10u p26:gp6 200u
#define GRADIENT7   10u p27:gp7 200u


"p2=2*p1"
"p6=2*p5"
"in0=inf1/2"
"d0=in0/2-p1-p5*2/3.14159"


"INEPT1=d2-(p21+p11+210u)-10u"
"INEPT_2=d2-p27-210u"
"INEPT_W=d2-(p23+210u+p1*2.3846+d5*2.5)"

"d3=d5/2-p5"
"U1=d2-p11-10u-p26-210u"

;"d13=d1-d8-180u"
"d13=d1-d16-180u"
"d14=d8/(16*l3)-p5"
"p50=d16"
"d58=1/cnst7"
"d59=1/(100000*d21)"
"d60=1/(10000*d20)"
1  10u ze
   d58
   d59
   d60
2  1m
   10u do:f3
   20u pl1:f1
```

```
   20u pl2:f2
   20u pl3:f3
   d13
   10u pl15:f3
   10u fq=cnst21 (bf ppm):f3
   (p50 ph20):f3
   10u fq=cnst11 (bf ppm):f3
   10u pl3:f3
   20u pl1:f1
   20u pl2:f2
   20u pl3:f3

   20u LOCKH_ON
;----------------------------------------first INEPT
5  (p5 ph20):f3
   GRADIENT0
   1m
   (p1 ph20):f1
   10u
   (p11:sp1 ph18:r):f1
   GRADIENT1
   INEPT1 pl1:f1
   (center(p2 ph21):f1 (p6 ph20):f3)
   GRADIENT1
   INEPT1
   (p11:sp1 ph19:r):f1
   5u
   5u pl1:f1
   (p1 ph23):f1
   GRADIENT4
   (p5 ph4):f3
;----------------------------------------U element
   GRADIENT6
   U1
   (p11:sp3 ph15:r):f1
   5u
   5u pl1:f1
   (center(p2 ph21):f1 (p6 ph20):f3)
   10u
   (p11:sp3 ph15:r):f1
   GRADIENT6
   U1 pl1:f1
   (p5 ph5):f3
   GRADIENT5
;----------------------------------------15N evolution
   (p5 ph1):f3
   d0
   (p2 ph20):f1
   d0
   (p5 ph20):f3
   GRADIENT2
;---------------------------------------
```

```
   (p5 ph2):f3
   GRADIENT7
   INEPT_2
   (center(p2 ph3):f1 (p6 ph20):f3)
   GRADIENT7
   INEPT_2
   (p5 ph23):f3
;----------------------------------------second INEPT
   (p1 ph22):f1
   GRADIENT3
   INEPT_W
   (p1*0.2308 ph21 d5 p1*0.6923 ph21 d5 p1*1.4615 ph21):f1
   (d3 p6 ph1 d3):f3
   (p1*1.4615 ph23 d5 p1*0.6923 ph23 d5 p1*0.2308 ph23):f1
   GRADIENT3
   INEPT_W pl13:f3 LOCKH_OFF
;---------------------------------------acquisition
   go=2 ph31 cpd3:f3
   1m do:f3 mc #0 to 2 F1PH(ip1,id0)
10u do:f1
10u do:f2
10u do:f3
10u LOCKH_OFF
exit


ph1 =0 2 2 0
ph3 =1 1 3 3
ph2 =0 0 0 0
ph4 =0 0 0 0 2 2 2 2
ph5 =1
ph31=2 0 0 2 0 2 2 0


ph10=3 3 3 3
ph11=0 0 0 0
ph12=3 3 3 3


ph15=2
ph16=0
ph17=1
ph18=2
ph19=3

ph20=0
ph21=1
ph22=2
ph23=3

ph26=2
```

CT-CPMG with TROSY readout for low temperature measurements (Chapter 6)

Sample: ^{15}N labeled

```
;optimization of water flip back:
;- optimize watergate (o1,sp2,ph26)
;- optimize water flip back (sp1,ph16,ph18,ph17,ph19)

;K. Pervushin et al, PNAS, 94, 12366 (1997)

;pl1   : power for 1H
;pl2   : power for 13C
;pl3   : power for 15N

;sp1   : water flipback power
;sp2   : water flipback power in watergate
;spnam1: gauss128_5
;spnam2: gauss128_5

;p1    : 90 degree hard pulse 1H
;p3    : 90 degree hard pulse 13C
;p4    : 180 degree hard pulse 13C (225d for 5/600)
;p5    : 90 degree hard pulse 15N
;p11   : water flipback pulse (1.5m)


;p20   : 1m  (Cleaning Gradient )
;p21   : 500u (Gradient in first INEPT)
;p22   : 500u (Gradient in second INEPT)
;p23   : 900u (Gradient in watergate)
;p24   : 500u (Gradient in Z-filter)
;gpz0  : 80%
;gpz1  : 19%
;gpz2  : 15%
;gpz3  : 32%
;gpz4  : 60%

;d8    : constant-time T_cp
;d14   : Inter-pulse delay
;d16   : inter-pulse during heating
;every refocusing frequency dumps in the same # pi pulses

;d1    : relaxation delay
;d2    : INEPT delay (~2.7ms)
;in0   : 1/(2 SW) (Hz)
;l3    : v_cpmg loop counter
;l11   : l3 + 1
define delay INEPT1
define delay INEPT2
define delay INEPT3
define delay U1
```

```
#include <Avance_dl.incl>

#define GRADIENT0   10u p20:gp0 200u
#define GRADIENT1   10u p21:gp1 200u
#define GRADIENT2   10u p22:gp2 200u
#define GRADIENT3   10u p23:gp3 200u
#define GRADIENT4   10u p24:gp4 200u
#define GRADIENT5   10u p25:gp5 200u
#define GRADIENT6   10u p26:gp6 200u

"p2=2*p1"
"p6=2*p5"
"in0=inf1/2"
"d0=in0/2-(p3*2 + 1.5u)"
"INEPT1=d2-(p21+p11+210u)-14u"
"INEPT2=d2-(p22+p11+210u)-14u"
"INEPT3=d2-(p23+p11+210u)-14u"

"U1=d2-p11-10u-p26-210u"



"l2 = 1"

"l4=l11-l3"

"d13=d1-d8"

"d14=d8/(16*l3)-p5"


"d16=d8/(16*l4)-p5"


1  10u ze
2  1m
   20u pl1:f1
   20u pl2:f2
   20u pl3:f3
   d13*0.5
   10u
;-----------------------temp-corr
4  d16
   (p6 ph21):f3
   d16
   d16
   (p6 ph21):f3
   d16
   d16
   (p6 ph20):f3
   d16
   d16
```

```
   (p6 ph22):f3
   d16
   d16
   (p6 ph20):f3
   d16
   d16
   (p6 ph20):f3
   d16
   d16
   (p6 ph21):f3
   d16
   d16
   (p6 ph23):f3
   d16
lo to 4 times l4
   d13*0.5
   20u pl1:f1
   20u pl2:f2
   20u pl3:f3

   20u LOCKH_ON
;----------------------------------------first INEPT
5  (p5 ph20):f3
   GRADIENT0
   1m
   (p1 ph20):f1
   10u
   (p11:sp1 ph18:r):f1
   GRADIENT1
   INEPT1 pl1:f1
   (center(p2 ph21):f1 (p6 ph20):f3)
   GRADIENT1
   INEPT1
   (p11:sp1 ph19:r):f1
   5u
   5u pl1:f1
   (p1 ph23):f1
   GRADIENT4


   (p5 ph4):f3
;---------------------------------------CPMG
11 d14
   (p6 ph21):f3
   d14
   d14
   (p6 ph21):f3
   d14
   d14
   (p6 ph20):f3
   d14
   d14
```

```
   (p6 ph22):f3
   d14
lo to 11 times l3
;----------------------------------------U element
   GRADIENT6
   U1
   (p11:sp3 ph15:r):f1
   5u
   5u pl1:f1
   (center(p2 ph20):f1 (p6 ph20):f3)
   10u
   (p11:sp3 ph15:r):f1
   GRADIENT6
   U1 pl1:f1
;----------------------------------------CPMG
21 d14
   (p6 ph20):f3
   d14
   d14
   (p6 ph20):f3
   d14
   d14
   (p6 ph21):f3
   d14
   d14
   (p6 ph23):f3
   d14
lo to 21 times l3
   (p5 ph5):f3
   GRADIENT5
;D.LEE readout
;----------------------------------------15N evolution
if "l2 %2 == 1" goto 31
   (p5 ph2):f3
goto 32
31 (p5 ph1):f3
32 d0
   (p3 ph23 1.5u p4 ph20 1.5u p3 ph23):f2
   d0
;----------------------------------------second INEPT
   (p1 ph10):f1
   10u
   (p11:sp1 ph17:r):f1
   GRADIENT2
   INEPT2 pl1:f1
   (center(p2 ph20):f1 (p6 ph20):f3)
   GRADIENT2
   INEPT2
   (p11:sp1 ph16:r):f1
   5u
   5u pl1:f1
   (center(p1 ph20):f1 (p5 ph12):f3)
```

```
;----------------------------------------WATERGATE
   GRADIENT3
   INEPT3
   (p11:sp2 ph26:r):f1
   5u
   5u pl1:f1
   (center(p2 ph20):f1 (p6 ph20):f3)
   10u
   (p11:sp2 ph26:r):f1
   GRADIENT3
   INEPT3 LOCKH_OFF
   (p5 ph11):f3
;----------------------------------------acquisition
   go=2 ph31
   1m mc #0 to 2 F1EA(ip10*2 & ip12*2 & ip17*2 & iu2,id0)
10u do:f1
10u do:f2
10u do:f3
10u LOCKH_OFF
exit

ph1 =1 3 2 0
ph2 =1 3 0 2
ph4 =0 0 0 0 2 2 2 2
ph5 =1
ph31=1 3 2 0 3 1 0 2


ph10=3 3 3 3
ph11=0 0 0 0
ph12=3 3 3 3


ph15=2
ph16=0
ph17=1
ph18=2
ph19=3

ph20=0
ph21=1
ph22=2
ph23=3

ph26=2
```

CT-CPMG Reference experiment with TROSY readout for low temperature measurements (Chapter 6)

Sample: ^{15}N labeled

```
;set l3 = 0
;optimization of water flip back:
;- optimize watergate (o1,sp2,ph26)
;- optimize water flip back (sp1,ph16,ph18,ph17,ph19)

;K. Pervushin et al, PNAS, 94, 12366 (1997)

;pl1   : power for 1H
;pl2   : power for 13C
;pl3   : power for 15N

;sp1   : water flipback power
;sp2   : water flipback power in watergate
;spnam1: gauss128_5
;spnam2: gauss128_5

;p1    : 90 degree hard pulse 1H
;p3    : 90 degree hard pulse 13C
;p4    : 180 degree hard pulse 13C (225d for 5/600)
;p5    : 90 degree hard pulse 15N
;p11   : water flipback pulse (1.5m)


;p20   : 1m  (Cleaning Gradient )
;p21   : 500u (Gradient in first INEPT)
;p22   : 500u (Gradient in second INEPT)
;p23   : 900u (Gradient in watergate)
;p24   : 500u (Gradient in Z-filter)
;gpz0  : 80%
;gpz1  : 19%
;gpz2  : 15%
;gpz3  : 32%
;gpz4  : 60%

;d8    : constant-time T_cp
;d14   : Inter-pulse delay
;d16   : inter-pulse during heating
;every refocusing frequency dumps in the same # pi pulses

;d1    : relaxation delay
;d2    : INEPT delay (~2.7ms)
;in0   : 1/(2 SW) (Hz)
;l3    : v_cpmg loop counter
;l11   : l3 + 1
define delay INEPT1
define delay INEPT2
define delay INEPT3
define delay U1

#include <Avance_dl.incl>

#define GRADIENT0   10u p20:gp0 200u
```

```
#define GRADIENT1   10u p21:gp1 200u
#define GRADIENT2   10u p22:gp2 200u
#define GRADIENT3   10u p23:gp3 200u
#define GRADIENT4   10u p24:gp4 200u
#define GRADIENT5   10u p25:gp5 200u
#define GRADIENT6   10u p26:gp6 200u

"p2=2*p1"
"p6=2*p5"
"in0=inf1/2"
"d0=in0/2-(p3*2 + 1.5u)"
"INEPT1=d2-(p21+p11+210u)-14u"
"INEPT2=d2-(p22+p11+210u)-14u"
"INEPT3=d2-(p23+p11+210u)-14u"

"U1=d2-p11-10u-p26-210u"



"l2 = 1"

"l4=l11-l3"

"d13=d1-d8"

"d14=d8/(16*l3)-p5"


"d16=d8/(16*l4)-p5"


1  10u ze
2  1m
   20u pl1:f1
   20u pl2:f2
   20u pl3:f3
   d13*0.5
   10u
;-----------------------temp-corr
4  d16
   (p6 ph21):f3
   d16
   d16
   (p6 ph21):f3
   d16
   d16
   (p6 ph20):f3
   d16
   d16
   (p6 ph22):f3
   d16
   d16
```

```
   (p6 ph20):f3
   d16
   d16
   (p6 ph20):f3
   d16
   d16
   (p6 ph21):f3
   d16
   d16
   (p6 ph23):f3
   d16
lo to 4 times l4
   d13*0.5
   20u pl1:f1
   20u pl2:f2
   20u pl3:f3

   20u LOCKH_ON
;----------------------------------------first INEPT
5  (p5 ph20):f3
   GRADIENT0
   1m
   (p1 ph20):f1
   10u
   (p11:sp1 ph18:r):f1
   GRADIENT1
   INEPT1 pl1:f1
   (center(p2 ph21):f1 (p6 ph20):f3)
   GRADIENT1
   INEPT1
   (p11:sp1 ph19:r):f1
   5u
   5u pl1:f1
   (p1 ph23):f1
   GRADIENT4

   (p5 ph4):f3
;----------------------------------------U element
   GRADIENT6
   U1
   (p11:sp3 ph15:r):f1
   5u
   5u pl1:f1
   (center(p2 ph20):f1 (p6 ph20):f3)
   10u
   (p11:sp3 ph15:r):f1
   GRADIENT6
   U1 pl1:f1
;----------------------------------------CPMG
   (p5 ph5):f3
   GRADIENT5
;D.LEE readout
```

```
;----------------------------------------15N evolution
if "l2 %2 == 1" goto 31
   (p5 ph2):f3
goto 32
31 (p5 ph1):f3
32 d0
   (p3 ph23 1.5u p4 ph20 1.5u p3 ph23):f2
   d0
;----------------------------------------second INEPT
   (p1 ph10):f1
   10u
   (p11:sp1 ph17:r):f1
   GRADIENT2
   INEPT2 pl1:f1
   (center(p2 ph20):f1 (p6 ph20):f3)
   GRADIENT2
   INEPT2
   (p11:sp1 ph16:r):f1
   5u
   5u pl1:f1
   (center(p1 ph20):f1 (p5 ph12):f3)
;----------------------------------------WATERGATE
   GRADIENT3
   INEPT3
   (p11:sp2 ph26:r):f1
   5u
   5u pl1:f1
   (center(p2 ph20):f1 (p6 ph20):f3)
   10u
   (p11:sp2 ph26:r):f1
   GRADIENT3
   INEPT3 LOCKH_OFF
   (p5 ph11):f3
;----------------------------------------acquisition
   go=2 ph31
   1m mc #0 to 2 F1EA(ip10*2 & ip12*2 & ip17*2 & iu2,id0)
10u do:f1
10u do:f2
10u do:f3
10u LOCKH_OFF
exit

ph1 =1 3 2 0
ph2 =1 3 0 2
ph4 =0 0 0 0 2 2 2 2
ph5 =1
ph31=1 3 2 0 3 1 0 2


ph10=3 3 3 3
ph11=0 0 0 0
ph12=3 3 3 3
```

```
ph15=2
ph16=0
ph17=1
ph18=2
ph19=3

ph20=0
ph21=1
ph22=2
ph23=3

ph26=2
```

Curriculum Vitae

Education

Current – Ph.D. Student, **Max-Planck Institute for Biophysical Chemistry**, Göttingen, Germany

B.S. (*Cum Laude*), Biochemistry and Biophysics **Rensselaer Polytechnic Institute**, Troy, NY, 2009

B.S. (*Cum Laude*), Biomedical Engineering, **Rensselaer Polytechnic Institute**, Troy, NY, 2009

Work Experience

Doctoral Student: *Accessing kinetics from the supra-τ_c range via relaxation dispersion NMR spectroscopy*. Department of NMR-based Structural Biology at the Max-Planck Institute for Biophysical Chemistry with Prof. Dr. Christian Griesinger, 2010-Present.

Undergraduate Research Assistant: *NMR based studies of splicing and cleavage mutants from Mycobacterium tuberculosis RecA inteins.* Department of Biology at Rensselaer Polytechnic Institute with Prof. Chunyu Wang, 2007-2009.

Undergraduate Research Assistant: *Computational analysis of tissue growth from mechanically-loaded dental implants*. Department of Biomedical Enigeering at Rensselaer Polytechnic Institute with Prof. John Brunski, Summer 2007.

Publications

Ban D., Mazur A., Carneiro M.G., Sabo T.M., Giller K., Koharudin M.I., Becker S., Gronenborn A.M., Griesinger C., Lee D., **Enhanced accuracy of kinetic information from CT-CPMG experiments by transverse rotating-frame**. Submitted.

Sabo T.M., Smith C.A., Ban D., Mazur A., Lee D., Griesinger C., **ORIUM: Optimized RDC-based Iterative and Unified Model-free analysis**. Submitted.

Ban D., Gossert A.D., Giller K., Becker S., Griesinger C., Lee D., **Exceeding the limit of dynamics studies on biomolecules using high spin-lock field strengths with a cryogenically cooled probehead**. J. Magn. Reson., 221 (2012) 1-5.

Ban D., Funk M., Gulich R., Egger D., Sabo T.M., Walter K.F.A., Fenwick R.B., Giller K., Pichierri F., de Groot B.L., Lange O.F., Grubmüller H., Salvatella X., Wolf M., Loidl A., Kree R., Becker S., Lakomek N.A., Lee D., Lunkenheimer P., Griesinger C., **Kinetics of conformational sampling**. Angew. Chem. Int. Ed., 50 (2011) 11437-11440.

Du Z., Liu Y., Ban D., Lopez M.M., Belfort M., Wang C., **Backbone dynamics and global effects of an activating mutation in minimized Mtu RecA inteins**. J. Mol. Biol., 400 (2010) 755-767.